

TRANSVERSE IONIZING SHOCK WAVES IN A PLANAR  
ELECTROMAGNETIC SHOCK TUBE

by

Sing Lee

Thesis submitted for the degree of Doctor of  
Philosophy in the Australian National  
University.

October 1969

This work is a thesis submitted for the degree  
of Doctor of Philosophy in the Australian National  
University.

Title: Transverse Ionizing Shock Waves in a  
Planar Electromagnetic Shock Tube.

Candidate: Sing Lee, B. Sc.(Hons), M.Sc.

The contents of this thesis, except as described  
in the Acknowledgement, and where credit is indicated  
by a reference, are entirely my own work.

(Sing Lee)

ACKNOWLEDGEMENT

It is a pleasure to record my deep appreciation for the general guidance, stimulation and cooperation given to me by Dr R.J. Sandeman, in all the aspects of my research, and in the writing of this thesis. In particular the experimental arrangements, of both the channelled spectra method, and the single wavelength method of Mach Zehnder interferometry, were entirely his work.

This thesis has been made possible by the Research Scholarship from the University, and the excellent research facilities provided by the Physics Department. I express also, my thanks, to the members of the Aerophysics Group for the many stimulating discussions I have been privileged to attend; to Mr G. Allen, for help with the computer programmes, to Mr R. Kennett, for cooperation in the channelled spectra experiment; to Mr R. Storey and Mr F. Parchi for the construction of the apparatus used in the experiments, and to Mr K. Smith for the two Figures of the shock tube.

This acknowledgement would not be complete without recording my thanks to my wife, Sau San, and our children Suzie and Shannon, for their continuous loving support, and patient understanding.

ABSTRACT

The Kunkel-Gross-Chapman-Jouguet hypothesis for the propagation of normal ionizing shock waves, was adapted for the description of the transverse ionizing shock waves in the planar electromagnetic shock tube. This was made possible by the adoption of an ohmic dissipation model for the expansion wave, resulting in the choice of the isentropic sound speed as the small disturbance speed. The validity of this choice was established by bow shock measurements. Transverse ionizing shock equilibrium solutions were obtained, based on this C-J model; with extension to the hydromagnetic and the gasdynamic regimes.

A new method of Mach Zehnder interferometry, using multi-channel spectra, was used to obtain more accurate measurements, of the electron density and the density ratio, than could be attained by conventional M-Z methods. An approximate probe theory was developed to account for the influence of the bow shock on the measurement of the transverse magnetic field and the total pressure. The pre-shock electric field was also measured.



The experiments showed that, in the C-J ionizing regime, the C-J solutions were in fair to good agreement with the measured helium shock properties; and that, when the inclined shock effect was taken into account, similar agreement was observed for the argon shock. In the limit of zero bias field, however, gasdynamic behaviour was not observed. This was attributed to the failure of the shock front to separate from the expansion drive current.

A distinction was made between an incomplete separation of the shock front from the expansion current, and a complete separation. Incomplete separation was observed for helium, generally; whilst complete separation was observed for both helium and argon in the C-J ionizing regime; but not in the gasdynamic limit.

It was postulated that the presence of an expansion current makes a complete gasdynamic separation impossible; and further, that, at sufficiently high velocities an expansion current may not be required, in which case a complete gasdynamic separation may become possible.

In addition, the coupling and decoupling of the back emf's, associated with the motions of the shock

front and expansion current, were examined in some detail. A qualitative theory was also proposed to explain the differences between the observed tilts of the helium and argon current sheets.

## CONTENTS

	<u>Page</u>
Acknowledgement	I
Abstract	II
Introduction	1
Chapter 1	
Electromagnetic Shock Tubes	3
1.1 General development	3
1.2 Shock tube geometries	5
1.3 Bias fields	7
1.4 Shock wave studies	9
Chapter 2	
Theory of the Transverse Ionizing Shock Wave	11
2.1 Classification	11
2.2 Equilibrium shock jump equations	13
2.3 Structural limits to solutions	20
2.4 Closure of the system of shock jump equations	22
2.4.1 Structural methods	22
2.4.2 Chapman Jouguet model	26
2.4.2.1 Justification of the C-J model	27
2.5 Small disturbance speeds	31

	<u>Page</u>
2.5.1 Derivation of small disturbance speeds-dissipationless approximation	33
2.5.2 Small disturbance speed in a dissipative plasma	36
2.5.2.1 Magnetogasdynamic equations	36
2.5.2.2 Order of magnitude comparison for choice of dissipation coefficients	37
2.5.2.3 Gas characterised by $\chi = \nu = 0, \nu_m \neq 0$	42
2.5.3 Summary	44
2.6 Analysis of the transverse C-J model	45
2.7 Current required to drive shock	49
2.8 Numerical solutions of the transverse ionizing C-J shock	52
2.8.1 Computation procedure	56
2.8.2 Discussion of numerical results	58
 Chapter 3	
The Experimental Arrangement	64
3.1 The shock tube and vacuum system	66
3.1.1 Description	66
3.1.2 Vacuum performance	69
3.1.3 Electrode maintenance	70
3.2 The condenser banks and control electronics	70
3.2.1 The main condenser bank	70

	<u>Page</u>
3.2.2 The bias field bank	73
3.2.3 Switching units	74
3.3 Diagnostics	75
3.3.1 Electrical measurements	76
3.3.1.1 Voltage measurements	76
3.3.1.2 Current measurements	80
3.3.2 Magnetic probes	84
3.3.3 The pressure probe	88
3.3.3.1 The detection of mass and mass flow	88
3.3.3.2 The bow shock and the stagnation region	92
3.3.3.2.1 The bow shock	92
3.3.3.2.2 The stagnation regi	97
3.3.3.2.3 Field and flow distributions	100
3.3.3.3 Design considerations	108
3.3.3.4 Probe construction	109
3.3.3.5 Probe maintenance	110
3.3.3.6 Probe sensitivity	111
3.3.3.7 Probe calibration-I	113
3.3.3.8 Probe calibration-II	114
3.3.4 Mach Zehnder Interferometry and high speed photography	116

	<u>Page</u>
3.3.4.1 Refractivity of the plasma species	117
3.3.4.2 Fringe shift estimates	119
3.3.4.3 Single wavelength interferometry	120
3.3.4.4 Channelled spectra interferometry	121
3.3.4.4.1 The $P\Delta\lambda$ path difference	124
3.3.4.4.2 The $\lambda\Delta P$ path difference	125
3.3.4.4.3 Analysis of the interferograms	128
 Chapter 4	
Experimental Results	133
4.1 Velocity measurements	133
4.1.1 Streak photographs	134
4.1.2 The velocity-time relationship	135
4.1.3 Velocity measurements and momentum balance	137
4.2 Pressure and magnetic field distributions	139
4.2.1 Distributions for 0.1 torr Ar, 5 KV, $B_1 = 0$	142
4.2.2 Distributions for 0.1 torr Ar, 5 KV, $B_1 = 2.5$ KG	144
4.2.3 Distributions in helium, 5 KV, 0.25 torr	146
4.3 Magnetic field measurements	147

	<u>Page</u>
4.3.1 Measurement technique	148
4.3.2 Results of $B_2$ measurements	149
4.4 Electric field measurements	150
4.4.1 Electric field results	155
4.5 Electron density and heavy particle density measurements	158
4.5.1 The channelled spectra measurements	158
4.5.1.1 Comparison of $N_e$ , $\Gamma$ , $P$ and $B$ profiles	162
4.5.1.2 Summary of results and comparison with theory	165
4.5.2 Single wavelength Mach Zehnder interferometry	172
4.5.2.1 Argon interferograms	175
4.5.2.2 Helium interferograms	177
4.5.2.3 Summary and discussion of interferograms	182
4.6 The inclined pressure front and the shock solutions	189
4.7 Observation of the bow shock	196
4.7.1 Significance of the bow shock	197
4.8 Shock and non-shock effects	198
4.8.1 Observation of a pure gas separation	199
4.8.2 Reverse current loops and the back emf	202

	<u>Page</u>
Chapter 5	
Conclusions	209
5.1 Experimental verification of the C-J model	209
5.2 The identification of a shocked 'gas sample'	216
References	223
Nomenclature	229
List of Tables	236
List of Figures	237



## INTRODUCTION

This thesis describes an experimental study of shock wave-current sheet propagation in a planar electromagnetic shock tube, with the application of a steady uniform magnetic field transverse to the direction of propagation, as well as to the direction of current flow in the propagating current sheet. The main purpose of this study is twofold.

In the gas ionizing regime of electromagnetic shock wave propagation, fairly comprehensive experimental studies of normal ionizing shock waves have been reported<sup>1,2,3,4</sup> and a Kunkel-Gross-Chapman-Jouguet model has been found to provide fair agreement with experimental observations. The subject has been reviewed by Gross<sup>5</sup>. For the transverse ionizing shock, little work along these lines have been reported, mainly because no suitable small disturbance speed appears to be applicable<sup>6</sup> when a dissipationless model is used for the flow following the shock wave. The

first objective of this thesis is to propose, that, for the operation of the transverse shock tube in the ionizing shock regime, an ohmic dissipation model is more suitable than a dissipationless model for the expansion wave. Using this model, a suitable small disturbance speed is available for the application of the Chapman-Jouguet condition. The experiment is planned so that the experimental results can be compared with solutions based on this model.

The second objective of this study is to investigate the distribution of mass flow in the shock tube during the various phases of shock wave propagation; and to examine experimentally the concept of the separation of the shock front and the drive current. Reliable information of mass distribution and shock-current separation is necessary in any attempt to produce a 'known gas sample'.

MKS units are used throughout except where otherwise specified.

## CHAPTER 1

### ELECTROMAGNETIC SHOCK TUBES

#### 1.1 General development

Since the first observation of electrically generated shock waves by Fowler<sup>7</sup> in 1951, a large variety of electrically powered shock tubes have been constructed, extending the speed range of shock wave studies from the 5 mm/microsecond typical of pressure driven shock tubes\* to figures an order of magnitude higher. A most important result of this increase in shock speed is the increased electrical conductivity of the post shock gas which enables the shocked gas to interact strongly with the electric and magnetic fields either present in the shock generating discharge or additionally imposed.

Kolb<sup>8</sup> first demonstrated the effect of incorporating the self magnetic field of an electrical discharge in the drive by arranging for the discharge paths to generate a  $\underline{JXB}$  force along the shock tube. Patrick<sup>9</sup> extended this concept by arranging for a

---

\*

A speed of 1.8 cm/microsecond has been produced in the double diaphragm free piston shock tube<sup>82</sup>.

current sheet driven by its self magnetic pressure to propagate down a shock tube, driving a shock wave ahead of it. His magnetic annular shock tube (MAST) geometry is the basis of many electromagnetic shock tubes in operation. In electromagnetic shock tubes, energy is coupled into the driven gas by means of electromagnetic forces; but Joule heating cannot be ignored a priori. However, whereas the former mechanism becomes increasingly efficient with rising electrical conductivity, the latter becomes increasingly inefficient. In tubes where sufficiently high conductivity develops, the drive is predominantly electromagnetic and ohmic processes can approximately be considered as negligible in the calculation of the drive mechanism. Teh and Lee<sup>10</sup> have observed a transition, with increasing shock speed, from Joule heating drive to electromagnetic drive in a low velocity electromagnetic shock tube experiment. This transition point can be estimated by considering the requirement that the convection of the magnetic flux with the fluid motion should exceed the diffusion of the flux through the fluid. This is the requirement for efficient electromagnetic coupling. Putting the relevant terms from the magnetohydrodynamic equations into this

inequality results in the condition that the magnetic Reynolds number  $R_m \gg 1$ .  $R_m = \mu \sigma u d$ , where  $\mu$  is the permeability,  $\sigma$  the electrical conductivity,  $u$  the fluid velocity and  $d$  is a characteristic length usually taken to be the characteristic dimension of the shock tube. Clearly, the first requirement of an electromagnetic shock tube is for this condition to be fulfilled.

## 1.2 Shock tube geometries

The early work of Kolb<sup>11</sup> has shown that one of the first experimental requirements for the production of a really strong shock wave is a fast rate of rise of current. This requirement is particularly stringent for devices with short JXB interaction lengths. However, even for devices with constant drive over the whole length of shock propagation, the largest possible current is required to drive the fastest possible shock wave. The resultant requirement of the lowest possible inductance appears to have dominated the design of electromagnetic shock tubes resulting in the almost exclusive use of the cylindrical coaxial geometry<sup>2,4,6,9,12-15</sup>. From the electrical engineering point of view, such a geometry has also the advantage of fringe free

fields and internally closed field lines. Because of the cylindrical geometry, however, analysis of flow is considerably more complicated than in a one dimensional case. Most calculations<sup>14,16-18</sup> are done on the basis of a one dimensional flow and then applied to the cylindrical geometry either with some modifications to account for the cylindrical geometry<sup>1</sup> or directly<sup>2,3,6,9,14</sup>. Fishman and Petschek<sup>19</sup> have considered the justification of applying one-dimensional calculations to cylindrical geometries.

In shock tubes where the primary aim is not the production of the strongest shocks, the problem of inductance minimization can be relaxed. In fact, for some purposes, a relatively large inductance can be used advantageously. For example, Hoffman<sup>20</sup> has shown theoretically and experimentally that the formation of a pressure pulse with the pressure front at the very front of the current sheet is facilitated by a slow initial current sheet speed corresponding to a small force field Mach number (less than 2 cm/microsecond in 0.5 torr of hydrogen). From the point of view of probe and optical accessibility, uniformity of drive field as well as the direct applicability of one dimensional calculations, a 'one-dimensionalised' MAST geometry is

of advantage. A parallel plate shock tube, consisting of two wide plates with a constant spacing between them and with a large width to spacing ratio, represents such a geometry. The flow in such a shock tube has been investigated by a number of groups<sup>21-24</sup>. More recently Sorrell<sup>81</sup>, using a parallel plate geometry, has obtained shock-current separation in 0.46 torr hydrogen at speeds between 8.0 and 11.6 cm/microsecond.

### 1.3 Bias fields

Externally imposed steady magnetic fields (as opposed to the self magnetic field of the driver current sheet) of various orientations to the direction of propagation have been applied to shock tubes. Besides the use of bias fields for purely technical purposes (for example for insulating the plasma from the shock tube walls<sup>25</sup>), bias fields are also used in investigations of shock wave regimes which from theoretical consideration appear to be particularly interesting. Shock waves with a magnetic field normal to the plane of the shock have been extensively studied<sup>1-4,9,12</sup>, particularly in the regime where switch on shocks<sup>2,3</sup> and separated gas shocks<sup>3</sup> are expected.

Transverse magnetic fields have also been used. Vlases<sup>26,27</sup> has studied the propagation of a cylindrical

expanding shock wave in the inverse pinch with a magnetic field transverse to the direction of propagation but parallel to the direction of current flow in the propagating current front. The situation where a magnetic field is perpendicular to both the direction of propagation and the propagating current path has been investigated by Patrick<sup>9</sup>, Patrick and Pugh<sup>6</sup> and Yasuhara (who uses an unsteady bias field<sup>14</sup>). The term 'transverse shock' will from this point on be reserved for the shock propagating in a magnetic field that is perpendicular to both the direction of propagation and the direction of current flow in the propagating front.

Oblique shocks (shocks propagating into a magnetic field having both transverse and normal components) have been investigated by Patrick<sup>6,9</sup> and Kantrowitz et al.<sup>13</sup> Taussig<sup>17</sup>, in a theoretical comparison of oblique, normal and transverse shocks, found that, for a given total drive current (and a given bias field), the transverse shock has a higher shock speed and develops the highest downstream temperature of all three cases. This is not surprising as the transverse field interacts directly with the drive current producing a further component to the driving force.



#### 1.4 Shock wave studies

As will be discussed in the next chapter, the electrical conductivity ahead of the propagating shock wave is of importance in determining the type and properties of the shock wave. In some experiments, pre-ionization of the gas ahead of the shock is arranged in order to study the behaviour of shocks moving into a conducting gas. Vlases<sup>27</sup> has conducted such experiments in his inverse pinch. Messerle<sup>28</sup> has used an RF discharge to preheat a column of gas into which two opposing shock waves are propagated. In most other experiments reported, the gas ahead of the shock is not pre-ionized (except by precursors which in most cases produce only low levels of conductivity). The main features of this class of gas ionizing shock waves are that the gas ahead, being non-conducting, can support an electric field; and that energy has to be expended by the shock wave in ionizing the gas through which it passes and which it sweeps up. Experimentally, these features were first recognized by Vlases<sup>26</sup> and Brennan, Lehane, Millar and Watson-Munro<sup>12,29</sup>.

At high velocities, however, even when the gas is not pre-ionized, hydromagnetic compression of the shock jump magnetic fields is observed<sup>9,13</sup>, indicating a zero

electric field ahead of the shock. Some theoretical aspects of the gas ionizing and hydromagnetic regimes with particular reference to the transverse shock will be discussed in the next chapter.

## CHAPTER 2

### THEORY OF THE TRANSVERSE IONIZING SHOCK WAVE

#### 2.1 Classification

In the theory of magnetohydrodynamic (MHD) shock waves (for example, Marshall<sup>30</sup>, Kemp and Petschek<sup>18</sup>) the conductivities on both sides of the shock wave are taken as infinite. This allows the infinite conductivity equation  $\vec{E} = -\vec{u} \times \vec{B}$  ( $\vec{E}$ =electric field,  $\vec{B}$ =magnetic induction) to be applied to both sides of the shock wave. This model will be referred to as the hydromagnetic shock wave. A consequence of the infinite conductivities is that  $\vec{B}$  is 'frozen' to the fluid particles during shock compression resulting in the hydromagnetic condition of  $\Gamma = \beta$ , where  $\Gamma$  and  $\beta$  are the density and magnetic induction ratios respectively across the shock.

In distinction, shock waves which move into unionized, non-conducting gas, and ionize it so that the post shock gas is conducting and interacts with the magnetic and electric fields present are generally referred to as ionizing shock waves. Shock waves which

do not interact with magnetic and electric fields are termed pure gas shocks or simply gas shocks\*.

A fundamental difference exists in the three classes of shock waves. This relates to  $E_{LAB}$ , the electric field in laboratory coordinates, ahead of the shock. For the hydromagnetic shock  $E_{LAB}$  is zero. For the ionizing shock  $E_{LAB}$  is non-zero and its magnitude affects the shock solutions. For the gas shock  $E_{LAB}$  is irrelevant since the fields remain unchanged on both sides of the shock. In the limit of vanishingly small fields, ionizing shock solutions become pure gas solutions. From structural consideration (this will be discussed in greater detail in a later section) there is a magnetic Mach number (refer Section 2.6) above which ionizing solutions become hydromagnetic. This means that in the limit of vanishingly small fields, all three solutions must be identical.

Ionizing shock waves are further classified according to the orientation of the magnetic field with respect to the direction of propagation. The terms normal, transverse and oblique have already been introduced.

---

\* Also referred to as gas-dynamic shocks.

## 2.2 Equilibrium shock jump equations

The solution of the transverse ionizing shock wave problem is, in the context of our experiments, the solution for the post shock state given the controllable pre-shock state and the shock velocity as a parameter. The model we assume for the plasma is that of an infinitely conducting, dissipationless gas. For such an MHD model, the following macroscopic equations are applicable:

$$\text{Mass} \quad \frac{\delta \rho}{\delta t} + \nabla \cdot (\rho \mathbf{u}) = 0 \quad , \quad (2-1)$$

$$\text{Momentum} \quad \frac{\delta \mathbf{u}}{\delta t} + (\mathbf{u} \cdot \nabla) \mathbf{u} + \frac{1}{\rho} \nabla P - \frac{1}{\rho} \mathbf{J} \times \mathbf{B} = 0 \quad , \quad (2-2)$$

$$\begin{aligned} \text{Energy} \quad \frac{\delta}{\delta t} \left( \frac{1}{2} \rho u^2 + \rho e + P_* \right) + \nabla \cdot \left[ \rho \mathbf{u} \left( \frac{1}{2} u^2 + e + \frac{P}{\rho} \right) \right. \\ \left. + \frac{1}{\mu} (\mathbf{E} \times \mathbf{B}) \right] = 0 \quad , \quad (2-3) \end{aligned}$$

$$\text{Induction} \quad \frac{\delta \mathbf{B}}{\delta t} = -(\nabla \times \mathbf{E}) \quad , \quad (2-4)$$

$$\text{Maxwell} \quad \mu \mathbf{J} = \nabla \times \mathbf{B} \quad , \quad (2-5)$$

$$\nabla \cdot \mathbf{B} = 0 \quad , \quad (2-6)$$

$$\text{MHD approximation} \quad \mathbf{E} = -\mathbf{u} \times \mathbf{B} \quad , \quad (2-7)$$

$$\text{State} \quad e = e(P, \rho) \quad . \quad (2-8)$$

$$P_* = P + \frac{B^2}{2\mu}$$

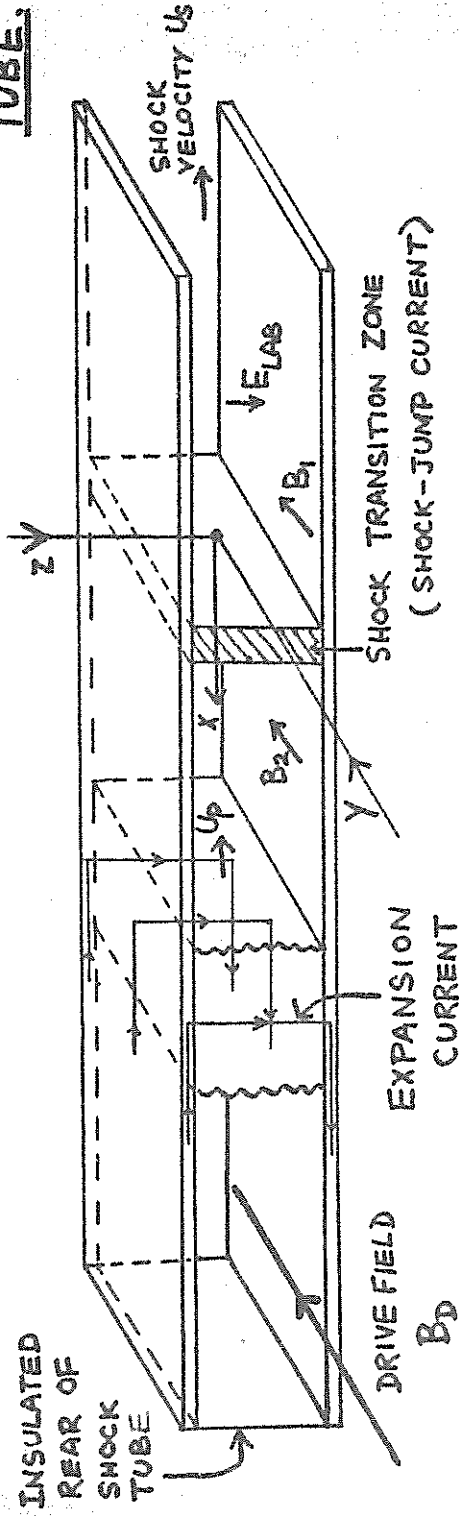
Equations (2-1) to (2-3) are the conservation equations for mass, momentum and energy including, where relevant, electromagnetic terms. Maxwell's equations (2-4) to (2-6) relate the electric field  $\underline{E}$ , the magnetic induction  $\underline{B}$  and the current density  $\underline{J}$ .  $\underline{E}$  is the electric field in coordinates fixed to the fluid which is moving at a velocity  $\underline{u}$  relative to our fixed system of coordinates. The equation of state (2-8) relates the internal energy of the fluid  $e$  to its pressure  $P$  and density  $\rho$ . The displacement current term in (2-5) has been excluded as being insignificant relative to the other terms.

Helliwell and Pack<sup>31</sup> have discussed the integration of the equations (2-1) to (2-4) across the shock transition zone from the pre-shock steady state 1 to the post shock steady state 2, with the assumption of a steady shock transition zone. The resultant equilibrium jump conservation equations number four, the fourth being the conservation of the electric field in the shock fixed coordinates. These jump equations can be most conveniently written in the one-dimensional form which is directly applicable to our planar shock tube. A diagram of the shock fixed coordinates to be used is given in Figure 2.1, with a schematic of the planar



**FIG. 2.1. SCHEMATIC OF THE TRANSVERSE ELECTROMAGNETIC SHOCK**

TUBE.

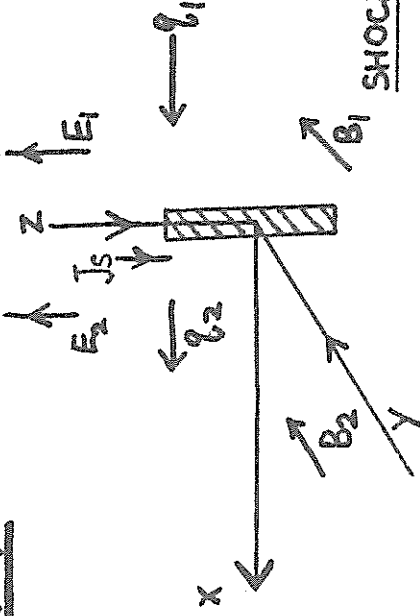


$$\underline{U_p = \underline{q_1 - q_2}}$$

STATE 2

STATE 1

$$\underline{U_S = \underline{q_1}}$$



SHOCK FIXED COORDINATES



shock tube and an idealized representation of the shock tube flow. The relationship between the system of coordinates used and the orientation of the planar shock tube is maintained throughout the subsequent sections of this thesis.

In this system of shock fixed coordinates the jump equations are:

$$\text{Mass} \quad \rho_2 q_2 = \rho_1 q_1 \quad , \quad (2-9)$$

$$\text{momentum} \quad \rho_2 q_2^2 + P_2 + \frac{B_2^2}{2\mu} = \rho_1 q_1^2 + P_1 + \frac{B_1^2}{2\mu} \quad , \quad (2-10)$$

$$\text{energy} \quad \rho_2 q_2 \left( \frac{1}{2} q_2^2 + h_2 \right) - \frac{E_2 B_2}{\mu} = \rho_1 q_1 \left( \frac{1}{2} q_1^2 + h_1 \right) - \frac{E_1 B_1}{\mu} \quad , \quad (2-11)$$

$$\text{electric field} \quad E_2 = E_1 \quad , \quad (2-12)$$

where  $h$  is the enthalpy per unit mass and  $q$  the flow velocity.

The orthogonality of the three vectors  $E_2$ ,  $B_2$  and  $q_2$  are implicit in the assumption of infinite conductivity behind the shock, so that:

$$\vec{E}_2 = -q_2 \times \vec{B}_2$$

can be written as:

$$E_2 = -q_2 B_2 \quad . \quad (2-13)$$

Chu<sup>32</sup> has proved from shock structure considerations that the angle between  $E_1$  and  $B_1$  must be equal to  $90^\circ$ . This enables the right hand term of (2-11) to be written as  $\frac{E_1 B_1}{\mu}$ , since  $\sin\theta = 1$ , where  $\theta$  is the angle between  $E_1$  and  $B_1$ .

The assumption of a zero conductivity  $\sigma$  ahead of the shock implies that an electric field  $E_{LAB}$  can exist ahead of the shock. The transform equation (to laboratory coordinates) is:

$$E_{LAB} = E_1 + q_1 B_1. \quad (2-14)$$

Kulikovskii and Lyubimov<sup>33</sup> and Chu<sup>32</sup> have suggested that the electric field ahead of the shock is governed by the electromagnetic radiation propagating ahead of the shock and cannot be arbitrarily specified. This is a crucial point because it means that  $E_{LAB}$  is not equal to the electric field originally imposed ahead of the shock by external means or by circuit parameters; but is in fact a function of the shock structure. Gross<sup>5</sup> has discussed the importance of this concept, and has summarized the limits of the electric field within which steady solutions can be found in the case of normal ionizing shock waves.

Practically, the existence of a non zero  $E_{LAB}$  means that one more unknown  $E_1$  (or  $E_{LAB}$ ) has to be included in the problem.

To complete the set of equations describing the shock jump, we have the equation of state, the enthalpy equation and as many Saha equations as the number of degrees of ionization being considered.

$$\text{State} \quad P_2 = \rho_2 R T_2 \left( 1 + \sum_{r=1}^{r=n} r \alpha_r \right) \quad (2-15)$$

$T_2$  is the post shock temperature,  $n$  is the number of degrees of ionization being considered and  $\alpha_r$  is the  $r$ th ionization fraction.  $R$  is the gas constant  $k/M_w$ , where  $k$  is the Boltzmann constant and  $M_w$  the molecular weight of the gas. This relation expresses the fact that the total kinetic pressure in the gas is the sum of the partial pressures developed by the heavy particles (ions and neutrals) and the electrons.

The enthalpy,  $h$ , being the sum of the random thermal energy and the internal energies (ionization and excitation) is given by:

$$\begin{aligned} \text{Enthalpy } h_2 = & \frac{5}{2} \left( 1 + \sum_{r=1}^{r=n} r \alpha_r \right) RT_2 + \frac{1}{M_w} \sum_{r=1}^{r=n} \alpha_r I_r^f \\ & + \frac{1}{M_w} \sum_{r=0}^{r=n} \alpha_r \bar{E}_r \end{aligned} \quad (2-16)$$

Here  $I_r^f$  is the total energy required to raise one ion from its unionized state to its  $r$ th ionized state and  $\bar{E}_r$  is the average excitation energy per  $r$ th ionized ion. The ionization potentials are known quantities whilst the excitation energies are temperature dependent and can be computed from the tabulated values of atomic and ionic energy levels and the statistical weights of these levels<sup>34</sup>, once a suitably converging summation scheme is adopted<sup>35</sup>.

Corresponding to each of the ionization fractions  $\alpha_r$ , a Saha relation<sup>36</sup> exists connecting  $\alpha_r$  with  $\alpha_{r-1}$  namely,

$$\text{Saha } \frac{\alpha_{r+1}}{\alpha_r} = \frac{\sum_{s=1}^{s=n} s \alpha_s}{\sum_{s=1}^{s=n} \alpha_s} = \frac{2 M_w}{h^2} \left[ \frac{2 \pi m k}{h^2} \right]^{\frac{3}{2}} \frac{Z_{r+1}}{Z_r \rho_2} T_2^{\frac{3}{2}} \exp \left[ - \frac{[I_r - \delta_r]}{k T_2} \right] \quad (2-17)$$

*$I_r$  = ionization energy from  $r \rightarrow r+1$  stage*

Here  $m$  is the electronic mass,  $\delta_r$ , the reduction of ionization potential due to the coulomb interaction

of an ion with its neighbours within its Debye neighbourhood; and the  $Z_r$ 's are the partition functions. Equation (2-17) represents a set of  $n$  equations, with  $r=1\dots r=n$ . The first equation, with  $r=1$ , has the fraction of neutrals  $\alpha_0$  given by:

$$\alpha_0 = (1 - \sum_{s=1}^{s=n} \alpha_s) \quad .$$

The set of equations (2-9) to (2-13) and (2-15) to (2-17) are therefore available to solve for the  $n+8$  unknowns of the shock jump problem, namely,  $\rho_2$ ,  $q_2$ ,  $P_2$ ,  $h_2$ ,  $T_2$ ,  $E_2$ ,  $B_2$ ,  $E_1$  and the  $n$   $\alpha'_s$ .  $P_1$ ,  $h_1$ ,  $\rho_1$ ,  $B_1$  and  $q_1$  are specified pre-shock quantities. Since there are only  $n+7$  equations for the  $n+8$  unknowns, the system of equations is not closed.

One method of producing solutions is to treat one of the unknowns, for example,  $E_1$ , as a parameter and to study the solutions with the variation of  $E_1$ . Taussig<sup>16</sup>,<sup>17</sup> has made a comprehensive study of such parametric solutions for the case of the normal ionizing shock waves. The main problem with this method is that a choice has to be made, from the family of solutions, of the one that is most likely to be physically observable.

A simpler method is to choose a suitable closing equation. This will be discussed in a later section.

### 2.3 Structural limits to solutions

Before proceeding to the closure of the system of shock jump equations, it is pertinent to discuss the limits within which we can expect the values of  $E_1$  to lie. Unlike gas shocks (without energy release or absorption within the shock) for which every solution satisfying the criterion of entropy increase can be proved to be physically observable, not all ionizing shock solutions (obtained, for example, by the parametric variation of  $E_1$ ) are physically observable. In general, solutions are said to be physically observable if they are stable with respect to small disturbances and if they possess a finite structure. This latter means that if we include a dissipation parameter in the shock equations, a continuous solution can be found linking the two states of the gas, and further, that this continuous solution tends to the jump solution in the limit when the dissipation parameter tends to zero. Chu<sup>32</sup> has examined the shock jump equations (with dissipation terms) and obtained limits (necessary, but not sufficient) within which

solutions have a finite structure. These limits for the electric field are:

$$\text{structural limits } -q_1 B_1 < E_1 < -\left(\frac{\gamma-1}{\gamma+1}\right) q_1 B_1 \quad , \quad (2-18)$$

where  $\gamma$  is the ratio of specific heats. We define  $\gamma$  in relation to the enthalpy (see Section 2.8.2 for justification):

$$h_2 = \frac{P_2}{\rho_2} + \frac{P_2}{\rho_2(\gamma-1)} \quad ,$$

definition of  $\gamma$        $\gamma = \frac{h_2}{h_2 - P_2/\rho_2} \quad ,$

(2-19)

where  $h_2$ ,  $P_2$ , and  $\rho_2$  are already independently defined.

We express the structural limits of (2-18) in terms of  $\beta = \frac{B_2}{B_1}$  and  $E_{LAB}$ . We first note from (2-9) that:

$$\Gamma = \rho_2/\rho_1 = q_1/q_2 \quad ,$$

Then in combination with (2-14), equation (2-18) gives:

$$0 < E_{LAB} < \left(\frac{2}{\gamma+1}\right) q_1 B_1 \quad . \quad (2-20)$$

Also, equation (2-18) with (2-9) and (2-12) to (2-14), gives:

$$\Gamma > \beta > \left(\frac{\gamma-1}{\gamma+1}\right) \Gamma \quad . \quad (2-21)$$

The LHS of (2-18), (2-20) and (2-21) are equivalent inequalities as are the RHS. The LHS inequality shows that for ionizing shocks  $E_{\text{LAB}}$  cannot go negative and that the magnetic field compression ratio cannot exceed the density compression ratio. The LHS limit  $\Gamma = \beta$ , corresponds to the hydromagnetic solution.

To identify the limit represented by the RHS of (2-18), (2-20) and (2-21) we note that for a pure gas shock, in the strong shock limit: (Mach number about 10 or greater<sup>37</sup>)

$$\Gamma = \frac{\gamma+1}{\gamma-1} \quad .$$

The RHS is therefore the pure gas limit  $\beta = 1$  and the inequality also states that for an ionizing shock wave, the magnetic induction cannot decrease across the shock.

In summary, we state that ionizing shock solutions must lie between pure gas and hydromagnetic limits.

## 2.4 Closure of the system of shock jump equations

### 2.4.1 Structural methods

Consider an actual situation in which a transverse shock wave is being observed in the laboratory. Suppose



the shock wave is reproducible with a set of observable and reproducible post shock properties  $\rho_2$ ,  $q_2$ ,  $P_2$ ,  $h_2$ ,  $T_2$ ,  $E_2$  and  $B_2$  and  $E_{LAB}$  corresponding to each set of controlled experimental parameters  $\rho_1$ ,  $P_1$ ,  $h_1$ ,  $q_1$ , and  $B_1$ . The very existence of the reproducible shock wave must mean that another relationship must exist connecting some post shock quantities or  $E_{LAB}$  with some pre-shock quantities. Kulikovskii and Lyubimov<sup>33</sup> and Chu<sup>32</sup> have shown that this relationship must take the form:

$$B_1 = B_1 (\rho_2, P_2, q_2, B_2) \quad . \quad (2-22)$$

The actual relation representing (2-22) depends on the relative importance of the dissipative coefficients  $\nu_m$  (magnetic viscosity),  $\nu$  (viscosity) and  $\chi$  (heat conductivity). Kulikovskii and Lyubimov<sup>33,38</sup> have considered a model in which the shock transition zone consists of an incomplete thermal shock followed by a magnetogasdynamic shock. In the thermal shock the gas is hardly ionized and hence electrically non-conducting, so that the flow is purely gas dynamic with  $\nu$  and  $\chi$  dominating the dissipative terms. Behind the thermal shock the gas is sufficiently ionized to interact with the electromagnetic field. An ionizing

temperature  $T_*$  is defined at which the electrical conductivity switches over from a zero value to a non-zero value. May and Tendys<sup>39</sup> have given a more definitive concept of  $T_*$  by defining it as that temperature at which the electrical resistivity begins to become the dominant dissipative mechanism. Using a simple kinetic model they have estimated  $T_*$  as  $kT_* = \frac{1}{2} aI$ , where  $a$  is essentially a constant near unity, and  $I$  is the ionization potential.

Kulikovskii and Lyubimov<sup>33</sup> have obtained the explicit form of (2-22) for the limiting cases:

A.  $v_m \gg v, v_m \gg \chi$

corresponding to a non-conducting gas.

In this case  $B_1 = B_2$

B.  $T_1 = T_*$

corresponding to the hydromagnetic case.

In this case  $E_1 = -q_1 B_1$

C.  $v_m \ll v, v_m \ll \chi$  everywhere that  $\sigma \neq 0$

corresponding to a gas ionizing shock wave.

In this case  $E_1 = -q_* B_1$ , where  $q_*$  is the velocity for which the temperature  $T_*$  is reached in the continuous motion of a non-conducting gas inside the shock transition region.

Kulikovskii and Lyubimov<sup>33</sup> and Allen and Segre<sup>40</sup> have also discussed the role of electromagnetic radiation ahead of the shock front. Chu<sup>32</sup> and May and Tendys<sup>39</sup> have outlined schemes for the solution of ionizing shock waves using the  $T_*$  model. The procedure consists of estimating  $T_*$  and the corresponding  $q_*$  and then using  $E_1 = -q_* B_1$  to close the system of shock jump equations. Perona and Axford<sup>41</sup> have proceeded beyond these techniques by integrating simplified shock structure equations from just behind the thermal shock to the back of the MHD region for a normal ionizing shock wave in argon.

Such shock structure integration techniques are potentially capable of providing accurate solutions, particularly when more accurate information on rate constants, and precursor ionization processes become generally available for inclusion into the structure equations and the boundary conditions. In particular, integration techniques provide information on the variation of properties through the shock transition region. Such information is not provided by equilibrium shock jump calculations. Moreover, it must be remembered that equilibrium solutions cannot be expected to be accurately applicable unless a state of local

thermal equilibrium is observed or expected to exist over a measurable distance behind the shock front. However, there is experimental evidence that the simpler shock jump calculations using a Chapman-Jouguet hypothesis as the closing relation are in fair agreement with observed shock tube behaviour. This will be considered in the next section.

#### 2.4.2 Chapman-Jouguet model

The recent experiments reported by Miller<sup>2</sup> and Levine<sup>3</sup> and the earlier experiments of Brennan, Brown, Millar, and Watson-Munro<sup>12</sup> as analysed by Wood<sup>1</sup> have verified the Chapman-Jouguet model suggested by Kunkel and Gross<sup>42</sup> for the operation of normal ionizing shock tubes in the switch-on (trans-Alfvenic) regime. According to this model, Joule heat energy is deposited in the shock front as a consequence of the switched on transverse magnetic field (associated with which is a shock jump current). This energy is analogous to the combustion heat energy deposited in the detonation wave of gasdynamics. In detonation wave theory, the application of minimum entropy requirement is necessary to remove ambiguity in the solutions; and results in the requirement that the fluid velocity relative to the

front be equal to the local small disturbance speed. Gross<sup>5</sup> has described the physical conditions under which the C-J model might be operative in the electromagnetic shock tube. In the first instance of electrical breakdown across the rear of the shock tube, a large electric field exists along the shock tube. Ideally, immediately, the drive current reaches a constant value and the shock wave reaches a constant velocity. During the short acceleration period, the pre-shock electric field decreases; at the same time the flow velocity out of the shock increases until this flow is choked. This limiting situation is analogous to a C-J detonation wave and the limiting velocity is the local small disturbance speed.

#### 2.4.2.1 Justification of the C-J model

Taussig<sup>17</sup> has examined ionizing shock jump equations and has proved a shock structure restriction which enables the definition of a unique solution for every shock speed. He suggests that this definition can either take the form of a phenomenological assumption such as the C-J hypothesis or can be obtained by a detailed analysis of shock structure. Taussig also shows that the C-J solution corresponds with the largest

pre-shock electric field that is consistent with a steady shock solution at a given shock speed. Cowley<sup>45</sup> has investigated the stability of ionizing shock waves to plane magneto-acoustic disturbances, on the basis of their evolutionarity (evolutionarity<sup>83</sup> is necessary but not sufficient for stability). He concludes that the following two classes of ionizing shock waves are evolutionary:

$$\text{Class I} \quad q_1 > a, \quad q_2 < c_{s2} \quad (2-23)$$

with  $E_{\text{LAB}}$  not restricted by structural requirements. Here  $a$  is the sonic speed ahead of the shock and  $c_{s2}$  is the slow disturbance speed behind the shock front.

Further, when ohmic dissipation dominates in the transition (i.e.  $v_m \gg v$ ,  $v_m \gg \chi$ ), this class of ionizing shock waves has finite structure. The initial ionization preceding the conducting region can be provided either by a pure gas shock or by precursor action.

$$\text{Class II} \quad q_2 > a, \quad c_{f2} \geq q_2 \geq c_{s2} \quad (2-24)$$

with  $E_{\text{LAB}}$  restricted by structural requirements. Here,  $c_{f2}$  is the post shock fast magnetoacoustic speed.

Further, for the condition of predominant ohmic dissipation, this class of shock exhibits only a pure gas transition, with no shock jump current permissible



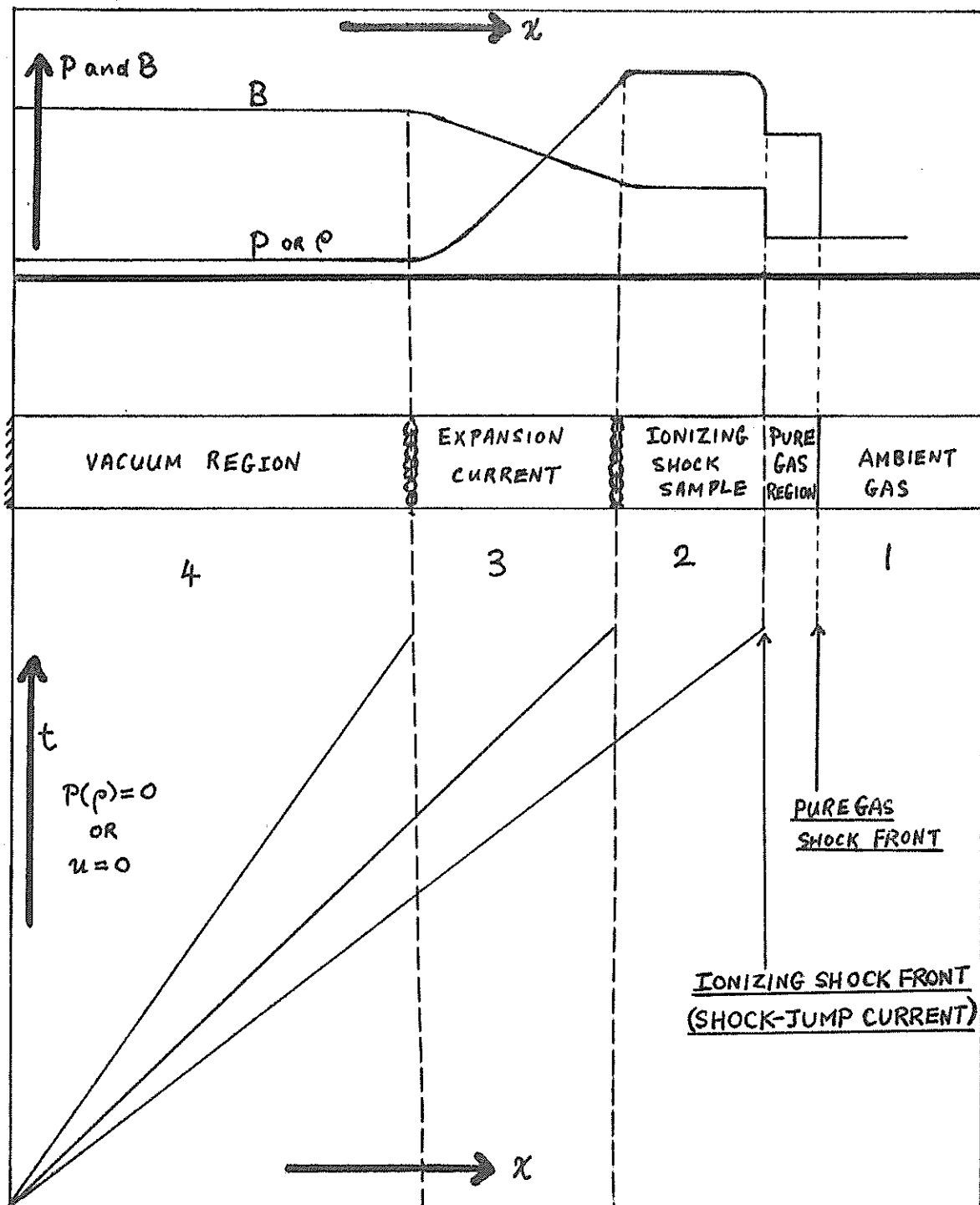


FIG. 2.2 FLOW MODEL OF THE TRANSVERSE IONIZING SHOCK



throughout the whole region of shock transition. However, with the inclusion of sufficient precursor ionization, the shock transition can carry current.

Thus, assuming negligible precursor ionization, ionizing shocks are evolutionary only if (2-23) applies. Taussig<sup>17</sup> has referred to these shocks as weak ionizing shocks in the sense that a pure gas transition is required before the ionizing (shock jump current) region. We note, however, that in the absence of precursors (or when the precursor ionization is of low level) a pure gas transition region, however small, is always required to provide the initial ionization before the conductivity can reach a sufficient level for shock current flow.

Another condition on the flow velocity has been obtained<sup>44</sup> by considering the flow characteristics behind the shock wave in the electromagnetic shock tube. The model to be discussed is shown in Figure 2.2. The ambient gas in region 1 is compressed by the shock to region 2. There can be no mass flow in region 4 because of the boundary condition imposed by the back wall at  $x=0$ . Therefore, in region 4 either  $u=0$  or  $P=0$ . In any case the density must decrease in the transition from 2 to 4 because the flow is away from

the back wall. The magnetic field on the other hand must increase in this transition because the magnetic pressure is driving the flow<sup>18</sup>. We therefore require an expansion wave for the transition from 2 to 4. Friedrichs and Kranzer<sup>46</sup> have shown, for isentropic flow, that the expansion wave connecting regions of uniform flow such as 2 and 4 must be a simple wave. Assuming a 'step function' drive current, region 3 must be a centred simple wave. In the diagram the separation between the  $\rho$  and B jump represents the pure gas transition region.

Taussig<sup>44</sup> has pointed out that in such a situation, since the front of the rarefaction wave moves with the slow magneto-acoustic speed  $c_{s2}$  with respect to the fluid, the criterion for the existence of steady shock solution is:

$$q_2 \geq c_{s2} \quad (2-25)$$

A combination of (2-23) and (2-25) results in the C-J condition:

$$q_2 = c_{s2} \quad (2-26)$$

There is thus justification for the application of the C-J hypothesis for ionizing shock wave in electromagnetic shock tubes for which the model

illustrated in Figure 2.2 is applicable. For large ohmic dissipation and when precursor ionization is negligible, the ionizing shock solution corresponding to (2-26) is evolutionary and possesses finite structure. The C-J condition is a necessary one under these circumstances.

However, when sufficient precursor ionization exists, (2-24) also yields an evolutionary ionizing shock solution. In this case the C-J condition is a physically possible, but not necessary, one.

## 2.5 Small disturbance speeds

In the case of a transverse ionizing shock wave, the choice of a small disturbance speed suitable to the problem is not at all obvious and we shall give it careful consideration here. Kalikman<sup>49</sup> has studied a dissipationless flow problem with arbitrary field ( $B(x,y,z)$ ) direction. These modes of magneto-acoustic disturbances can propagate:

1. The Alfven mode having velocity

$$c_A = b = \left[ \frac{B^2}{\mu \rho} \right]^{\frac{1}{2}} . \quad (2-27)$$

This wave propagates along the B lines.

2. The fast and slow magnetoacoustic modes, having velocity

$$c = \pm \left[ \frac{b^2 + a^2 \pm [(b^2 + a^2)^2 - 4a^2 b_n^2]^{\frac{1}{2}}}{2} \right]^{\frac{1}{2}}, \quad (2-28)$$

where the two absolute values of (2-28) correspond to the fast and slow speed  $c_f$  and  $c_s$  with the condition that  $c_f \geq c_s$ . This wave can propagate in any direction.

Here,  $b_n = \left[ \frac{B_n^2}{\mu\rho} \right]^{\frac{1}{2}}$  where  $B_n$  is the field component along the direction of propagation. We note that the relevant speeds for application to the C-J condition are those in the direction of propagation of the shock wave.

For normal ionizing shocks, these speeds are directly applicable by putting  $b = b_x = \left[ \frac{B^2}{\mu\rho} \right]^{\frac{1}{2}} = b_n$ , since  $B_x = B = B_n$ .

In the case of the transverse ionizing shock ( $B = B_y$ ):

$$b_n = 0, \quad ,$$

$$b = b_y = \left[ \frac{B^2}{\mu\rho} \right]^{\frac{1}{2}}, \quad ,$$

$$c_A = 0, \quad ,$$

$$c_s = 0, \quad ,$$

and

$$c_f = (b^2 + a^2)^{\frac{1}{2}}. \quad (2-31)$$

Kantrowitz and Petschek<sup>50</sup> have discussed comprehensively the properties of these waves with the aid of Friedrichs diagrams. They have also shown that for the fast mode, the magnetic pressure increases when gas density increases. For the slow mode the magnetic pressure increases when the density decreases. The fast speed  $c_f$  as given by (2-31) is therefore not applicable for our model of Figure 2.2. We are thus left with  $c_s=0$  for our rarefaction wave of region 3.

#### 2.5.1 Derivation of small disturbance speeds-dissipationless approximation

To see the significance of  $c_s=0$  we have to look at the flow equation governing region 3. These are the one-dimensional form of equations (2-1), (2-2) and (2-4) together with the isentropic equation of state:

$$P = \text{constant} \times \rho^\gamma \quad . \quad (2-32)$$

With (2-31) in place of the energy equation, we have:

$$\text{Mass} \quad \frac{\delta \rho}{\delta t} + u \frac{\delta \rho}{\delta x} + \rho \frac{\delta u}{\delta x} = 0 \quad , \quad (2-33)$$

$$\text{momentum} \quad \rho \frac{\delta u}{\delta t} + \rho u \frac{\delta u}{\delta x} + a^2 \frac{\delta \rho}{\delta x} + \frac{B}{\mu} \frac{\delta B}{\delta x} = 0 \quad , \quad (2-34)$$

$$\text{induction} \quad \frac{\delta B}{\delta t} + u \frac{\delta B}{\delta x} + B \frac{\delta u}{\delta x} = 0 \quad . \quad (2-35)$$

where (2-32) has been used to eliminate  $\frac{\delta P}{\delta x}$  from the momentum equation.

Equations (2-33) to (2-35) belong to a general class of conical problems<sup>46</sup> in which all the flow quantities depend on only one variable  $\xi = \frac{x}{t}$ . Conical expansions are simple waves and in the centred simple wave of Figure 2.2 flow properties are constant along lines passing through the origin and can change only across these lines. In such a wave changes in the flow move with the velocity relative to the laboratory coordinate or with the velocity  $c=\xi-u$  relative to the fluid. Transforming to the  $\xi$  coordinate, equations (2-33) to (2-35) become (noting that  $\frac{\delta}{\delta x} = \frac{1}{t} \frac{\delta}{\delta \xi}$  ,

$$\frac{\delta}{\delta t} = -\frac{\xi}{t} \frac{\delta}{\delta \xi} ):$$

$$\text{mass} \quad \rho u' - c\rho' = 0 \quad , \quad (2-36)$$

$$\text{momentum} \quad \frac{B}{\mu} B' - c\rho u' + a^2 \rho' = 0 \quad , \quad (2-37)$$

$$\text{induction} \quad -cB' + Bu' = 0 \quad . \quad (2-38)$$

The superscript dash refers to differentiation with respect to  $\xi$ . This is a system of three homogenous equations with the three partial derivatives  $B'$ ,  $u'$ , and  $\rho'$  as the unknowns. The condition for the existence of a non-zero solution for the unknowns is that the determinant of the coefficients be identically equal to zero. This gives the equation:

$$c(c^2 \rho - a^2 \rho - \frac{B^2}{\mu}) = 0 \quad (2-39)$$

and hence the two speeds of (2-30) and (2-31).

The relationship between  $B'$ ,  $u'$ , and  $\rho'$  can be obtained in ratio form by algebraic arrangement of equations (2-36) to (2-38); resulting in:

$$\frac{B'}{\rho(c^2 - a^2)} = \frac{u'}{(cB/\mu)} = \frac{\rho'}{(\rho B/\mu)} \quad (2-40)$$

As expected, putting  $c=c_f$  of (2-3) into (2-40) produces  $B'$  and  $\rho'$  of the same sign. Putting  $c=c_s=0$  into (2-40) gives  $B'$  and  $\rho'$  of opposite sign, which is what is physically required in the rarefaction wave of region 3.

With  $c=0$ , (2-40) gives

$$\delta u = 0 \quad \text{and} \quad -\frac{B}{\mu} \delta B = \delta P$$

(since  $\rho' = P' \frac{\delta \rho}{\delta P} = \frac{P'}{a^2}$  where  $a = (\frac{\delta P}{\delta \rho})^{\frac{1}{2}}$  is the isentropic sound speed); which with boundary conditions integrate to:

$$u = 0 \quad \text{and} \quad \frac{B^2}{2\mu} + P = \text{constant}.$$

The speed  $c_s=0$  therefore corresponds to the snow-plow limit with an infinitesimally thin current sheet right behind the shock front, compressing all the mass

swept up and carrying all the current in this infinitesimally small region. Such an infinitesimally thin current sheet is not consistent with the assumption of zero dissipation. Experimental observations in the transverse shock tube show that the drive current region is not small (this will be shown in Chapter 4), but is in fact distributed for several centimetres behind the shock front. The general pattern of current flow is very similar to that observed behind normal ionizing shock waves (for example, by Heywood<sup>4</sup>). We therefore inquire if a suitable (non-zero) small disturbance speed may be found when the assumption of zero dissipation is removed.

## 2.5.2 Small disturbance speeds in a dissipative plasma

### 2.5.2.1 Magnetogasdynamic equations

The equations governing the flow in which viscosity  $\nu$ , heat conductivity  $\chi$  and magnetic viscosity  $\nu_m = \frac{1}{\mu\sigma}$  are not negligible are:

$$\text{Mass} \quad \frac{\delta \rho}{\delta t} + \rho \frac{\delta u}{\delta x} + u \frac{\delta \rho}{\delta x} = 0 \quad , \quad (2-41)$$

$$\text{Momentum} \quad \rho \frac{\delta u}{\delta t} + \rho u \frac{\delta u}{\delta x} + \frac{\delta P}{\delta x} + \frac{B}{\mu} \frac{\delta B}{\delta x} - \frac{4}{3} \frac{\delta}{\delta x} \left( \nu \frac{\delta u}{\delta x} \right) = 0 \quad , \quad (2-42)$$



$$\begin{aligned} \text{Energy} \quad & \rho \frac{\delta h}{\delta t} + \rho u \frac{\delta h}{\delta x} - \frac{\delta P}{\delta t} - \frac{4}{3} \frac{\delta}{\delta x} \left( \nu u \frac{\delta u}{\delta x} \right) - \frac{\delta}{\delta x} \left( \chi \frac{\delta T}{\delta x} \right) \\ & + \frac{\delta B}{\delta x} \left( \frac{uB}{\mu} - \frac{\nu_m}{\mu} \frac{\delta B}{\delta x} \right) = 0, \end{aligned} \quad (2-43)$$

$$\text{Induction} \quad \frac{\delta B}{\delta t} + u \frac{\delta B}{\delta x} + B \frac{\delta u}{\delta x} - \frac{\delta}{\delta x} \left( \nu_m \frac{\delta B}{\delta x} \right) = 0, \quad (2-44)$$

$$\text{State} \quad P(\rho, S) = \quad (2-45)$$

where  $S$  is the entropy and where the terms containing  $\nu_m$ ,  $\nu$  and  $\chi$  are the dissipative terms. Assuming changes in the rarefaction wave are gradual, for an order of magnitude estimate we can make the approximation that  $\frac{\delta}{\delta x} = \frac{\Delta}{\Delta x}$  and  $\frac{\delta}{\delta x} \left( \frac{\delta}{\delta x} \right) = \frac{\Delta}{(\Delta x)^2}$ . We can then compare a dissipative term with a non-dissipative term in the same equation, using estimated values of the variables occurring in the terms.

#### 2.5.2.2 Order of magnitude comparison for choice of dissipation coefficients

We compare the following terms, where the D terms and the S terms are the dissipative and non-dissipative terms respectively. In the momentum equation (2-42), we compare

$$D_1 = \frac{4}{3} \nu \frac{\Delta u}{(\Delta x)^2}, \text{ with } S_1 = \frac{B}{\mu} \frac{\Delta B}{\Delta x};$$

in the induction equation (2-44), we compare

$$D_2 = v_m \frac{\Delta B}{(\Delta x)^2} , \text{ with } S_2 = u \frac{\Delta B}{\Delta x} ;$$

and in the energy equation (2-43), we compare

$$D_3 = \frac{4}{3} v \left[ u \frac{\Delta u}{(\Delta x)^2} + \left( \frac{\Delta u}{\Delta x} \right)^2 \right] ,$$

$$D_4 = \chi \left[ \frac{\Delta T}{(\Delta x)^2} \right] , \quad \text{and}$$

$$D_5 = \frac{v_m}{\mu} \left[ \frac{\Delta B}{\Delta x} \right]^2 ,$$

with each other and with  $S_3 = \frac{uB}{\mu} \left[ \frac{\Delta B}{\Delta x} \right]$  .

The following order of magnitude estimates of total change in properties  $\Delta u$ ,  $\Delta B$ , and  $\Delta T$  across the rarefaction wave of width  $\Delta x$  are used:

$$\begin{aligned} u = \Delta u &= 10^4 , & B = \Delta B &= 1 , \\ \Delta T &= 10^4 & \text{and } \Delta x &= 0.1 . \end{aligned}$$

With these values, the D and S terms are:

$$\text{Momentum} \quad D_1 = 10^6 v \quad , \quad S_1 = 10^7 \quad ,$$

$$\text{Induction} \quad D_2 = 10^2 v_m \quad , \quad S_2 = 10^5 \quad ,$$

$$\begin{aligned} \text{Energy} \quad D_3 &= 10^{10} v \quad , \\ D_4 &= 10^6 \chi \quad , \\ D_5 &= 10^8 v_m \quad , \quad \text{and } S_3 = 10^{11} . \end{aligned}$$

For the dissipative terms to be negligible compared to the non-dissipative terms the following inequalities are necessary:

$$\nu \ll 10 \quad , \quad (2-46)$$

$$\chi \ll 10^5 \quad , \quad (2-47)$$

$$\nu_m \ll 10^3 \quad . \quad (2-48)$$

To estimate  $\nu$ ,  $\chi$  and  $\nu_m$  we need to know the values of  $\omega_i \tau_i$  and  $\omega_e \tau_e$  in order to choose the correct equations for calculating  $\nu$ ,  $\chi$  and  $\nu_m$ <sup>51</sup>, where  $\omega_i$  and  $\omega_e$  are the ion and electron gyration frequencies respectively and  $\tau_i$  and  $\tau_e$  are the ion-ion and electron-electron collision times respectively. Combining equations given in Spitzer<sup>51</sup>, we have:

$$\omega_e \tau_e = 8.9 \times 10^5 B T^{\frac{3}{2}} / n_e \quad (2-49)$$

$$\omega_i \tau_i = 2.1 \times 10^{14} B T^{\frac{3}{2}} / (n_i Z^2 A^{\frac{1}{2}}) \quad (2-50)$$

where  $Z$  and  $A$  are the ionic charge and mass number respectively, and  $n_e$  and  $n_i$  are the number densities of electrons and ions respectively.

For estimated conditions of  $T = 20,000^\circ\text{K}$ ,  $n_e = n_i = 10^{21}$ ,  $B = 0.5$  and  $Z = 1$ ,  $A = 40$  for the argon ion, we have:

$$\omega_e \tau_e \sim 20 \quad ,$$

$$\text{and } \omega_i \tau_i \sim 0.07 \quad .$$

We note that  $\omega_e \tau_e \gg 1$  is the criterion for electrons to be strongly coupled to the magnetic field and  $\omega_i \tau_i \gg 1$  is the criterion for the ions to be strongly coupled to the magnetic field. Thus, for the viscosity and thermal conductivity, which are ion dominated mechanisms, we choose the weak magnetic field equations given by Spitzer<sup>51</sup>. Similarly, for  $\sigma$  which is electron dominated we choose the strong magnetic field equation. These are:

$$\nu = \frac{2.2 \times 10^{-16} T^{\frac{5}{2}} A^{\frac{1}{2}}}{Z^4 \ln \Lambda} \quad , \quad (2-51)$$

$$\chi = 5 \times 10^{-10} \frac{T^{\frac{5}{2}}}{Z \ln \Lambda} \quad , \quad (2-52)$$

$$\frac{1}{\sigma} = 1.3 \times 10^2 \frac{Z \ln \Lambda}{T^2} \quad , \quad (2-53)$$

where  $\ln \Lambda = 6.5$ , for our conditions.

We thus have the following dissipation coefficients:

$$\nu \approx 2 \times 10^{-5} \quad ,$$

$$\chi \approx 10 \quad ,$$

$$\text{and } \nu_m \approx 5 \times 10^2 \quad .$$

Comparing these estimates with the inequalities of (2-46) to (2-48) we note that our order of magnitude calculations show that the dissipation terms due to  $\nu$  and  $\chi$  are smaller than the corresponding non-dissipation terms by the factor of  $10^{-4}$ , whilst the magnetic viscous term is of the order of the corresponding non-dissipative terms. We also note that equations (2-51) to (2-53) are only very slightly density dependent through the  $\ln \Lambda$  factor, and that up to  $T=50,000^\circ\text{K}$  the conclusions regarding the relative magnitudes of the dissipative and non-dissipative terms remain valid.

We note further that in the estimates, the current sheet width  $\Delta x$  is taken as 10 cm. If this width reduces to 1 cm. or less, the ohmic (magnetic viscous) term may become larger than the non-dissipative terms whilst the other two dissipative mechanisms are still negligible. This is a very good indication that the correct model for the region 3 of Figure 2.2. cannot be a dissipationless one, but in fact should be characterised by:

$$\nu = \chi = 0 \quad \text{and}$$

$$\nu_m \neq 0 \quad .$$

### 2.5.2.3 Gas characterised by $v = \chi = 0$ , $v_m \neq 0$

Pai<sup>53</sup> has considered the problem of finding the characteristic directions of the one-dimensional unsteady flow of magnetogasdynamics governed by equations (2-41) to (2-45). He concludes that for inviscid fluids ( $v = 0$ ), the magnetic field has influence on the characteristics only when  $v_m = 0$  as well. For all other conditions, the characteristics of magnetogasdynamics are the same as those of the corresponding ordinary gasdynamic problems. Following Pai<sup>53</sup>, and putting  $v = \chi = 0$ , we write (2-41) to (2-44) as:

$$\text{Momentum} \quad \rho \left( \frac{\delta u}{\delta t} + u \frac{\delta u}{\delta x} \right) + P_\rho \frac{\delta \rho}{\delta x} + \frac{B}{\mu} \frac{\delta B}{\delta x} + P_S \frac{\delta S}{\delta x} = 0 \quad , \quad (2-54)$$

$$\text{Mass} \quad \rho \frac{\delta u}{\delta t} + \left( \frac{\delta \rho}{\delta t} + u \frac{\delta \rho}{\delta x} \right) = 0 \quad , \quad (2-55)$$

$$\text{Induction} \quad B \frac{\delta u}{\delta x} + \left( \frac{\delta B}{\delta t} + u \frac{\delta B}{\delta x} \right) - \frac{\delta Q}{\delta x} = 0 \quad , \quad (2-56)$$

$$\text{Energy} \quad \rho T \left( \frac{\delta S}{\delta t} + u \frac{\delta S}{\delta x} \right) = 0 \quad , \quad (2-57)$$

$$\text{and} \quad v_m \frac{\delta B}{\delta x} = Q \quad ; \quad (2-58)$$

where, from the equation of state (2-45), we have

written  $P_\rho = \frac{\delta P}{\delta \rho}$  and  $P_S = \frac{\delta P}{\delta S}$  which are used to eliminate  $\frac{\delta P}{\delta x}$  from the momentum equation. The second differential of B has been transformed to a first differential by

(2-58). The equation of the characteristics can be written as  $\psi(x, t) = \text{constant}$ . Using the notation  $\psi_x = \frac{\delta\psi}{\delta x}$ , and  $\psi_t = \frac{\delta\psi}{\delta t}$ , the characteristic condition of (2-54) to (2-58) is then written as the following determinantal equation, formed by the coefficients of the first derivatives of this set of simultaneous equations:

$$\begin{vmatrix} \rho\psi_t + \rho u\psi_x & P_\rho \psi_x & \frac{B}{\mu} \psi_x & P_S \psi_x & 0 \\ \rho\psi_x & \psi_t + u\psi_x & 0 & 0 & 0 \\ B \psi_x & 0 & \psi_t + u\psi_x & 0 & -\psi_x \\ 0 & 0 & 0 & \rho T (\psi_t + u\psi_x) & 0 \\ 0 & 0 & \frac{v_m}{\mu} \psi_x & 0 & 0 \end{vmatrix} = 0 \quad (2-59)$$

which reduces to:

$$(\psi_t + u\psi_x) \psi_x^2 \rho^2 T \frac{v_m}{\mu} \left[ (\psi_t + u\psi_x)^2 - \psi_x^2 P_\rho \right] = 0,$$

and finally:

$$\rho^2 T \frac{v_m}{\mu} \psi_x^2 (\psi_t + u\psi_x) \left[ \psi_t + (u+a) \psi_x \right] \left[ \psi_t + (u-a) \psi_x \right] = 0$$

where  $a = P_\rho$

The three characteristics are:

1.  $\psi_x = 0$

or  $t = \text{constant},$

a characteristic with infinite signal speed;

$$2. \quad \psi_t + u\psi_x = 0 \quad \text{which is}$$

$$\frac{dx}{dt} = \frac{-\psi_t}{\psi_x} = u \quad .$$

This is the streamline.

$$3. \quad \psi_t + (u \pm a) \psi_x = 0 \quad \text{which is}$$

$$\frac{dx}{dt} = u \pm a \quad .$$

This is the line of propagation of small disturbances with the velocity - a, relative to the fluid. The velocity - a, is therefore the speed with which the front of the expansion wave in region 3 of Figure 2.2 moves relative to the fluid. Since, for  $v = \chi = 0$ ,  $v_m \neq 0$ , the magnetic field has no influence on the flow characteristics; the situation is analogous to the gasdynamic situation in which the front of an expansion wave always travels at the local small disturbance speed.

### 2.5.3 Summary

We have seen that in the dissipationless approximation no suitable small disturbance speed is available for the application of the Chapman Jouguet condition to the solution of the transverse ionizing



shock wave. Applying the expansion model (as has been successfully applied to normal ionizing shock tubes) to the transverse shock tube leads to an infinitesimally thin snow plow type current sheet, which is neither consistent with the dissipationless assumption nor experimentally observed.

We have made order of magnitude estimates which indicate that the conditions existing behind the transverse ionizing shock wave may be most consistent with the large ohmic dissipation model of  $v = \chi = 0$ , and  $v_m \neq 0$ . With this model of the plasma the magnetic field does not affect the flow characteristics and the small disturbance speed is purely gasdynamic. We propose to use this speed-a, as the C-J speed for the transverse ionizing shock wave.

## 2.6 Analysis of the transverse C-J model

As a simplification we write:

$$a = \left[ \frac{\gamma P}{\rho} \right]^{\frac{1}{2}},$$

and use for the C-J condition:

$$q_2 = \left[ \frac{\gamma P_2}{\rho_2} \right]^{\frac{1}{2}}. \quad (2-61)$$

The set of equations (2-9) to (2-13), and (2-15) to (2-17) and (2-61) forms a closed set of  $8+n$  equations which we shall refer to as the C-J model for transverse ionizing shocks. An analysis using the conservation equations and the C-J condition together with each structural limit of (2-21) shows that the range of C-J solutions is characterised by limiting values of  $\Gamma$  and magnetic Mach number  $M_A$  dependent only upon  $\chi$ .

First,  $P_2$  is eliminated from the momentum (2-10) and energy (2-11) equations by the mass equation (2-9) and the C-J condition (2-61) giving:

$$\text{C-J momentum} \quad \frac{W}{\Gamma} \left( \Gamma - 1 - \frac{1}{\gamma} \right) = \frac{B_2^2}{2\mu} - \frac{B_1^2}{2\mu} \quad , \quad (2-62)$$

$$\text{C-J energy} \quad \frac{W}{\Gamma} \left( \frac{1}{\gamma-1} + \frac{1}{2} [1-\Gamma^2] \right) = \frac{B_2^2}{\mu} (B_1 - B_2) \quad , \quad (2-63)$$

where  $W = \rho_1 q_1^2$  and  $\gamma$  is defined by (2-19).

Next  $B_2$  is eliminated from (2-62) and (2-63) by the hydromagnetic limit  $\Gamma = \beta = \frac{B_2}{B_1}$  , (2-63A)

giving:

$$\left\{ \begin{array}{l} \text{C-J momentum} \\ \text{hydromagnetic limit} \end{array} \right. \quad P_B = \frac{W}{\Gamma(1-\Gamma^2)} \left( \frac{1}{\gamma} - \Gamma + 1 \right) \quad , \quad (2-64)$$

$$\left\{ \begin{array}{l} \text{C-J energy} \\ \text{hydromagnetic limit} \end{array} \right. \quad P_B = \frac{W}{2\Gamma^2(1-\Gamma)} \left[ \frac{1}{\gamma-1} + \frac{1}{2}(1-\Gamma^2) \right] \quad , \quad (2-65)$$

where the pre-shock magnetic pressure  $\frac{B_1^2}{2\mu}$  is denoted by  $P_B$ .

The forms of (2-64) and (2-65) enable  $P_B$  and  $W$  to be simultaneously eliminated when (2-64) and (2-65) are combined, giving:

C-J hydromagnetic limit  $\Gamma^3 - 3\Gamma^2 - \gamma_a \Gamma - \Gamma_G = 0$  , (2-66)  
for  $\Gamma$

where  $\gamma_a = \frac{4+\gamma-3\gamma^2}{\gamma(\gamma-1)}$  ,

$$\Gamma_G = \frac{\gamma+1}{\gamma-1} . \quad (2-67)$$

It should be noted that  $\Gamma_G$  is the pure gas density ratio.

In the range  $\gamma = 1.10$  to  $\gamma = 1.50$ , (2-66) yields only one positive root ranging from  $\Gamma = 5.880$  to  $\Gamma = 3.293$ .

The same procedure applied to the gas shock limit yields the equation:

C-J pure gas limit  $(\Gamma_r - 1)(\Gamma_r^3 + \gamma_f \Gamma_r^2 + \gamma_g \Gamma_r - \gamma_e) = 0$ , (2-68)  
for  $\Gamma$

where  $\gamma_f = \frac{\gamma_G^{-4}}{\Gamma_G}$  ,  $\gamma_g = \frac{7-\Gamma_G}{\Gamma_G(\Gamma_G+1)}$  ,  $\gamma_e = \frac{1}{\Gamma_G}$

and  $\Gamma_r = \frac{\Gamma}{\Gamma_G}$  .

As is to be expected the only root of interest here is  $\Gamma_r = 1$ , or  $\Gamma = \Gamma_G$ .



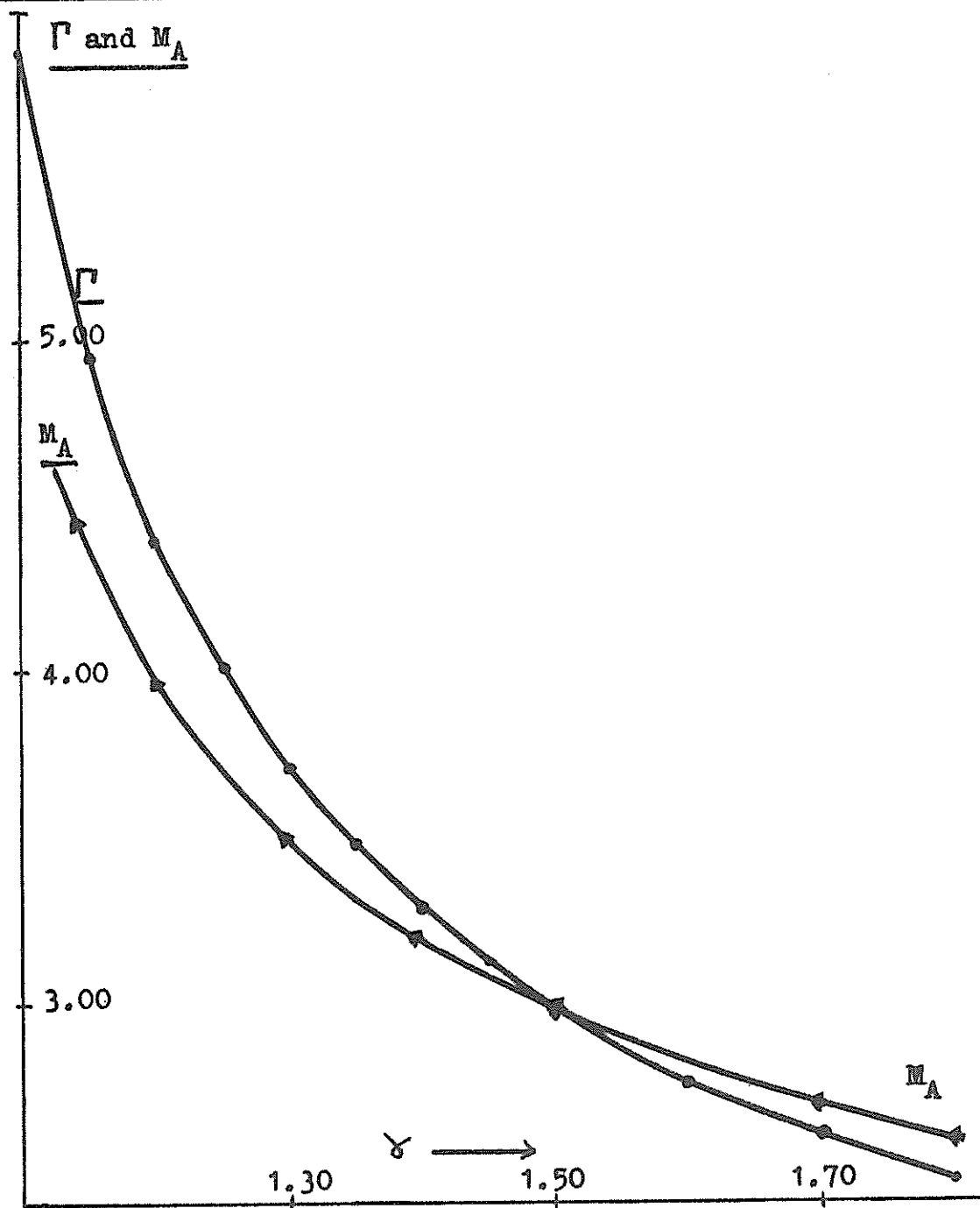


Fig.2.3 Values of  $\Gamma$  and  $M_A$  in the hydromagnetic  
limit of the Transverse Ionizing C-J Model

The limits in magnetic Mach number  $M_A$ , where

$$M_A = q_1 / b, \quad b^2 = \frac{B_1^2}{\rho_1 \mu},$$

is found by dividing (2-62) by  $B_1^2/2\mu$  and then combining with the structural limit of (2-21), giving:

$$\begin{array}{l} \text{C-J model} \\ \text{structural} \\ \text{limits} \\ \text{for } M_A \end{array} \quad \begin{array}{c} \text{hydromagnetic} \\ \frac{(\Gamma^2 - 1)\gamma\Gamma}{2[\gamma(\Gamma - 1) - 1]} \geq M_A^2 > \frac{\gamma\Gamma}{2} \left\{ \frac{\left[\frac{\Gamma}{\Gamma_G}\right]^2 - 1}{\gamma(\Gamma - 1) - 1} \right\} \end{array} \quad \begin{array}{c} \text{pure gas} \\ \end{array} \quad (2-69)$$

Thus the  $\Gamma$  limits of the C-J model for the transverse ionizing shock are given by (2-66) and (2-68) whilst (2-69) gives the corresponding values of  $M_A$  at these limits. At values of  $M_A$  (for a given  $\gamma$ ) larger than  $M_H$  where  $M_H$  is the quantity on the LHS of (2-69) the behaviour of the transverse shock is hydromagnetic and the appropriate closing relation is  $\Gamma = B_2/B_1$ . At shock speeds for which  $M_A$  is less than  $M_H$ , the transverse shock exhibits C-J behaviour. At small values of  $M_A$  (low shock speeds), solutions become gas dynamic, with  $B_1 = B_2$ . As  $B_1 \rightarrow 0$  (or for very high values of  $M_A$ ), the pure gas and hydromagnetic solutions merge.

Figure 2.3 shows graphs of  $\Gamma$  and  $M_A$  at the C-J hydromagnetic limit as a function of  $\gamma$ .



→ MOTION OF SYSTEM

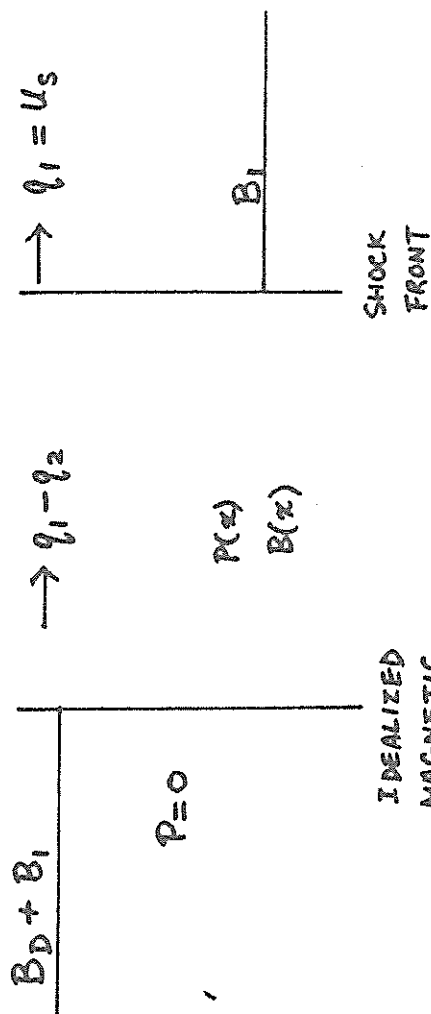


FIG. 2.4 'STRUCTURELESS' MOMENTUM BALANCE MODEL



## 2.7 Current required to drive shock

For calculating the drive current required, a momentum exchange model is used without considering the structure of the current carrying zone; i.e. we consider a magnetic interface with magnetic field  $B_D + B_1$  driving the shocked gas which moves at a speed  $q_1 - q_2$  behind the shock front moving at a speed  $q_1$ . Ahead of the shock front  $B = B_1$ ,  $P = P_1 \approx 0$ ; behind the magnetic interface  $B_T = B_D + B_1$ ,  $P = 0$ . With this structureless model (Figure 2.4), the difference in magnetic pressures across the current carrying region is available to balance the rate of momentum imparted to the gas swept up into the region, which is  $\rho_1 q_1 \times (q_1 - q_2)$ . Hence, the momentum balance equation is:

$$\frac{B_T^2}{2\mu} - \frac{B_1^2}{2\mu} = \rho_1 q_1 (q_1 - q_2),$$

which gives a quadratic in  $B_D$ :

$$B_D^2 + 2 B_1 B_D - 2\mu W \left( \frac{\Gamma-1}{\Gamma} \right) = 0, \quad (2-70)$$

with a positive root:

$$B_D = \left[ B_1^2 + 2\mu W \left( \frac{\Gamma-1}{\Gamma} \right) \right]^{\frac{1}{2}} - B_1 \quad (2-71)$$

which is the field required to drive the shock. The shock speed for a given  $B_D$  and  $\beta_D = \frac{B_D}{B_1}$  is:

$$q_1^2 = \frac{B_D^2}{2\rho_1\mu} \left(\frac{\Gamma}{\Gamma-1}\right) \left[1 + \frac{2}{\beta_D}\right] \quad . \quad (2-72)$$

The bias field has increased the shock speed by the factor  $\left[1 + \frac{2}{\beta_D}\right]^{\frac{1}{2}}$ . For example, a 71 per cent increase in shock speed is expected for  $\beta_D = 1$ , as compared with the 'unbiased' case with  $\frac{1}{\beta_D} = 0$ .

It is also instructive to express (2-70) as a relationship between  $M_A$  and  $\beta_D$  by dividing throughout by  $B_1^2$ . This gives:

$$\beta_D^2 + 2\beta_D - 2M_A^2 \left(\frac{\Gamma-1}{\Gamma}\right) = 0 \quad , \quad (2-73)$$

which is useful for estimating the drive-bias field ratio  $\beta_D$  required to attain a given shock speed-magnetic speed ratio  $M_A$ . Thus, for example, for a typical value of  $\gamma = 1.14$ , the C-J hydromagnetic limit is reached at  $\Gamma = 5.11$ ,  $M_A = 4.45$  (Figure 2.3). With these values of  $\Gamma$  and  $M_A$ , the required field ratio is  $\beta_D = 4.75$ . With a smaller field ratio, shock behaviour is ionizing, and with a larger field ratio, hydromagnetic.

Returning to the model of Figure 2.2, and the shock jump equations (2-10) and (2-11), we note that the magnetic induction is, in general, required to jump in

magnitude across the shock front from the equilibrium pre-shock value  $B_1$  to the equilibrium post-shock value  $B_2$ . The magnetic field then rises further through the expansion to reach the value  $B_T$ . The relationship between current and induction gradient is given by equation (2-5); which in our geometry becomes:

$$\mu J_A = -\frac{\delta B}{\delta X} \quad ,$$

so that 
$$\int_{x_1}^{x_2} J_A \delta x = \frac{1}{\mu} (B_{x_2} - B_{x_1}) \quad , \quad (2-74)$$

where we have written  $J_A$  to denote current density per unit area (area in the x-y plane) and where  $B_{x_2}$  and  $B_{x_1}$  are the magnetic induction in the y direction at the axial points  $x_2$  and  $x_1$ . Where the magnetic induction rises with a reasonably uniform gradient so that  $J_A$  can be assumed uniform between  $x_2$  and  $x_1$  we can approximate (2-74) with:

$$J_A (x_2 - x_1) = \frac{1}{\mu} (B_{x_2} - B_{x_1}) \quad ,$$

which is 
$$J = \frac{1}{\mu} (B_{x_2} - B_{x_1}) \quad , \quad (2-75)$$

where  $J$  is the current per unit current sheet width.

With this approximation, the various current densities are:

$$\begin{array}{ll} \text{shock} & J_S = \frac{1}{\mu} (B_2 - B_1) \\ \text{current} & \end{array} \quad , \quad (2-76)$$

$$\begin{array}{ll} \text{expansion} & J_E = \frac{1}{\mu} (B_D + B_1 - B_2) \\ \text{current} & \end{array} \quad , \quad (2-77)$$

$$\begin{array}{ll} \text{total drive} & J_D = J_S + J_E = \frac{1}{\mu} B_D \\ \text{current} & \end{array} \quad . \quad (2-78)$$

The term current partitioning will be used to refer to the separation of the shock current from the expansion current.

## 2.8 Numerical solutions of the transverse ionizing C-J shock

Transverse ionizing shock jump solutions are numerically calculated for argon and helium, over a range of  $\rho_1$ ,  $B_1$  and  $q_1$  selected mainly for comparison with experimental results. The system of n+8 equations made up of (2-9) to (2-13), (2-15) to (2-17) and either (2-61) or (2-63A) are used to solve for the n+8 unknowns  $\rho_2$ ,  $q_2$ ,  $P_2$ ,  $h_2$ ,  $T_2$ ,  $E_2$ ,  $B_2$ ,  $E_1$  and the  $n \alpha$ 's. When  $E_{LAB} > 0$  the C-J condition (2-61) is used and this is replaced by the hydromagnetic equation (2-63A) when the limit  $E_{LAB}=0$  is reached in the C-J calculations. ( $E_{LAB}$  is defined in (2-14)). The pure gas limit (RHS of (2-21)) equivalent to  $B_1 = B_2$  is used for the calculation when  $B_1 \rightarrow 0$ .

For helium,  $n=2$  is used for the whole range of calculations whilst for argon,  $n=4$  Saha equations have to be used for the higher velocity calculations. The main problems encountered are numerical ones concerning (2-16) and (2-17) which require the evaluation of the partition functions and excitation energies.

The calculation of the partition functions has been described by Griem<sup>35</sup>. The formula relating the  $r$ th partition function to the energy levels  $E_n$  and corresponding statistical weight  $g_n$  of the  $r$ th ionized atom is:

$$Z_r = \sum g_n \exp \left[ \frac{-E_n}{kT_2} \right], \quad (2-79)$$

where the summation is over all energy levels subject to a truncation criterion, which is necessary because the summation, as it stands, is a divergent one since the number of discrete levels is infinite as the ionization limit is approached. The number of levels actually contributing to the partition functions is however limited to those whose energies are below the reduced ionization limit. The summation should therefore be carried on up to a value  $n_{\max}$ ; where  $n_{\max}$  is the maximum principal quantum number for those

levels whose energies are below the reduced ionization limit. The hydrogenic formula for  $n_{\max}$  is:

$$n_{\max} = \left[ \frac{(r+1)^2 I_H}{\delta_r} \right]^{\frac{1}{2}}, \quad (2-80)$$

where  $I_H$  is the ionization potential of the hydrogen atom. The ionization reduction energy  $\delta_r$  is, for a Debye plasma:

$$\delta_r = \frac{(r+1)e^2}{4\pi\epsilon\rho_D}, \quad (2-81)$$

where  $\epsilon$  is the permittivity. The Debye radius  $\rho_D$  is given by:

$$\rho_D^2 = \frac{\epsilon k T_2}{N_2 e^2 \sum_{r=1}^{r=n} ([r+r^2] \alpha_r)}, \quad (2-82)$$

where  $N_2$  is the total heavy particle density in the post shock region; i.e.:

$$N_2 = \rho_2 / M_w = \frac{\rho_1 q_1}{q_2 M_w}. \quad (2-83)$$

With  $n_{\max}$  thus determined from (2-80) to (2-83) the summation of  $Z_r$  can then be done using tabulated values of  $E_n$  and  $g_n$ <sup>34</sup>. However, these tables do not always contain all values of  $E_n$  up to  $n_{\max}$  especially for the higher degrees of ionization. It is thus necessary to make a further approximation by summing

to the levels available (corresponding to quantum number  $n'$ ) according to equation (2-79) and then resorting to a hydrogenic formula, accounting for the appropriate multiplicity, for the remainder of the summation to  $n_{\max}$ . The summation for  $Z_r$  then becomes:

$$Z_r = \sum_{n=1}^{n=n'} g_n \exp \left[ \frac{-E_n}{kT_2} \right] + (2S+1)(2L+1) \sum_{n=n'+1}^{n=n_{\max}} 2n^2 \exp \left[ \frac{-[I_r - (r+1)^2 I_H / n^2]}{k T_2} \right], \quad (2-84)$$

where  $S$  and  $L$  are the spin and orbital momentum of the ground state of the  $(r+1)$ th ionization stage.

Similarly the excitation energy of the  $r$ th ionized atom is:

$$\bar{E}_r = \frac{1}{Z_r} \sum_{n=1}^{n=n'} E_n g_n \exp \left[ \frac{-E_n}{kT_2} \right] + \frac{1}{Z_r} (2S+1)(2L+1) \sum_{n=n'+1}^{n=n_{\max}} E'_n 2n^2 \exp \left[ \frac{-[I_r - (r+1)^2 I_H / n^2]}{k T_2} \right].$$

where  $E'_n = (I_r - (r+1)^2 I_H / n^2)$  (2-85)

The equations (2-80) to (2-85) define  $Z_r$ ,  $\bar{E}_r$  and  $\delta_r$  as functions of the post shock unknowns  $T_2$ ,  $\rho_2$  and  $\alpha_r$  ( $r=1 \dots n$ ). These equations have ignored external magnetic and electric field effects, which is

justifiable because the Zeeman and Stark effects involved for the range of fields used are small; at least in the sense that any resultant inaccuracies in  $Z_r$ ,  $\bar{E}_r$  and  $\delta_r$  do not affect equations (2-15) to (2-17) sufficiently to cause significant errors in the solutions.

### 2.8.1 Computation procedure

For  $n=4$  the set of jump equations are reduced to a seven dimension vector  $\tilde{F}(\tilde{a}) = 0$  with the unknowns  $\tilde{a}$  as  $q_2$ ,  $T_2$ ,  $B_2$ ,  $\alpha_1$ ,  $\alpha_2$ ,  $\alpha_3$ , and  $\alpha_4$ . An initial search point  $\tilde{a}'$  is estimated and checked for accuracy by evaluating the sum of the squares of the residuals

$$|\tilde{F}|^2 = \sum_{r=1}^{r=7} [\tilde{F}_r(\tilde{a}')]^2.$$

The values of  $\tilde{a}$ , are then adjusted and  $|\tilde{F}|^2$  again calculated. This is done iteratively until  $|\tilde{F}|^2$  is sufficiently small; the main problem being to ensure convergence during the iterations. A Fortran residue-minimization sub-routine (VAO2A) is used to provide the iterative procedure on an IBM 360. This sub-routine is described by Osborne<sup>54</sup> and by Allen<sup>48</sup> as specifically applied to gas shock calculations.



The transverse ionizing shock equations are written as:

$$\text{Momentum } F(1) = \frac{(A_s + 1) R T_2}{\frac{q_2}{\rho_1 q_1} (\rho_1 q_1 [q_1 - q_2] - \frac{B_2^2}{2\mu} + \frac{B_1^2}{2\mu} + P_1)} - 1, \quad (2-86a)$$

$$\text{Energy } F(2) = \frac{q_2 B_2 (B_2 - B_1)}{\mu \rho_1 q_1 (\frac{1}{2} [q_1^2 - q_2^2] - [h_2 - h_1])} - 1, \quad (2-86b)$$

$$\text{C-J or Hydro-magnetic } F(3) = \frac{q_2^2}{\gamma R T_2 (1 + A_s)} - 1 \text{ or } F(3) = \frac{q_2 B_2}{q_1 B_1} - 1, \quad (2-86c)$$

$$\text{Saha } F(4) = \frac{\alpha_1}{\alpha_0} \frac{A_s}{A_t} \frac{Z_1}{Z_0} \text{EXP} \left[ \frac{\delta_1 - I_1}{k T_2} \right] - 1, \quad (2-86d)$$

$$F(5) = \frac{\alpha_2}{\alpha_1} \frac{A_s}{A_T} \frac{Z_2}{Z_1} \text{EXP} \left[ \frac{\delta_2 - I_2}{k T_2} \right] - 1, \quad (2-86e)$$

$$F(6) = \frac{\alpha_3}{\alpha_2} \frac{A_s}{A_T} \frac{Z_3}{Z_2} \text{EXP} \left[ \frac{\delta_3 - I_3}{k T_2} \right] - 1, \quad (2-86f)$$

$$F(7) = \frac{\alpha_4}{\alpha_3} \frac{A_s}{A_T} \frac{Z_4}{Z_3} \text{EXP} \left[ \frac{\delta_4 - I_4}{k T_2} \right] - 1, \quad (2-86g)$$

where  $A_s = 1 + \alpha_1 + 2\alpha_2 + 3\alpha_3 + 4\alpha_4$ ,  $A_T = 1 - \alpha_1 - \alpha_2 - \alpha_3 - \alpha_4$ .

Starting with a set of values of  $T_2$ ,  $q_2$ ,  $B_2$ ,  $\alpha_1$ ,  $\alpha_2$ ,  $\alpha_3$ ,  $\alpha_4$ ;  $\rho_D$  is first calculated from (2-82),  $\delta_r$  from (2-81),  $n_{\max}$  from (2-80), and then  $Z_r$  and  $\bar{E}_r$  are summed using equations (2-84) and (2-85);  $h_2$  is then calculated

from (2-16) and  $\gamma$  from (2-15) and (2-19). The resultant values of  $\gamma$ ,  $h_2$ ,  $\delta_r$ ,  $Z_r$  and  $E_r$  are returned for the calculation of the F values using equations (2-86). The values of  $T_2$ ,  $q_2$ ,  $B_2$ ,  $\alpha_1$ ,  $\alpha_2$ ,  $\alpha_3$ ,  $\alpha_4$  are then adjusted and the procedure repeated. The optimization, i.e. the adjustment of  $T_2$ ,  $B_2$ ,  $q_2$ ,  $\alpha_1$ ,  $\alpha_2$ ,  $\alpha_3$ , and  $\alpha_4$  whilst ensuring convergence, is done by VAO2A.

For maximum efficiency, the least number of Saha equations required for accuracy should be used. Thus for 0.1 Torr of argon, between  $14,000^\circ\text{K}$  and  $29,000^\circ\text{K}$ , the first two Saha equations are used with  $\alpha_3 = \alpha_4 = 0$ , since the inclusion of the third and fourth Saha equations results in  $\alpha_3$  and  $\alpha_4$  of value less than 0.01, which makes no difference to the values of  $P_2$  and  $h_2$ . Between  $29,000^\circ\text{K}$  and  $42,000^\circ\text{K}$  the first three Saha equations are required and all four Saha equations are required between  $42,000^\circ\text{K}$  and  $61,000^\circ\text{K}$ .

### 2.8.2 Discussion of numerical results

Calculations for 0.1 Torr of argon are shown in Figure 2.5 to Figure 2.11. A range of magnetic induction is covered from the gas dynamic limit  $B_1 = 0$  ( $B_1=B_2$ ) to  $B_1 = 0.6$ . Over the range of velocity covered, two sets of results, ( $B_1 = 0.05$  and  $B_1 = 0.1$ ) extend past the hydromagnetic limit. For  $B_1 = 0.05$ ,  $b = 0.3 \times 10^4$  m/sec,

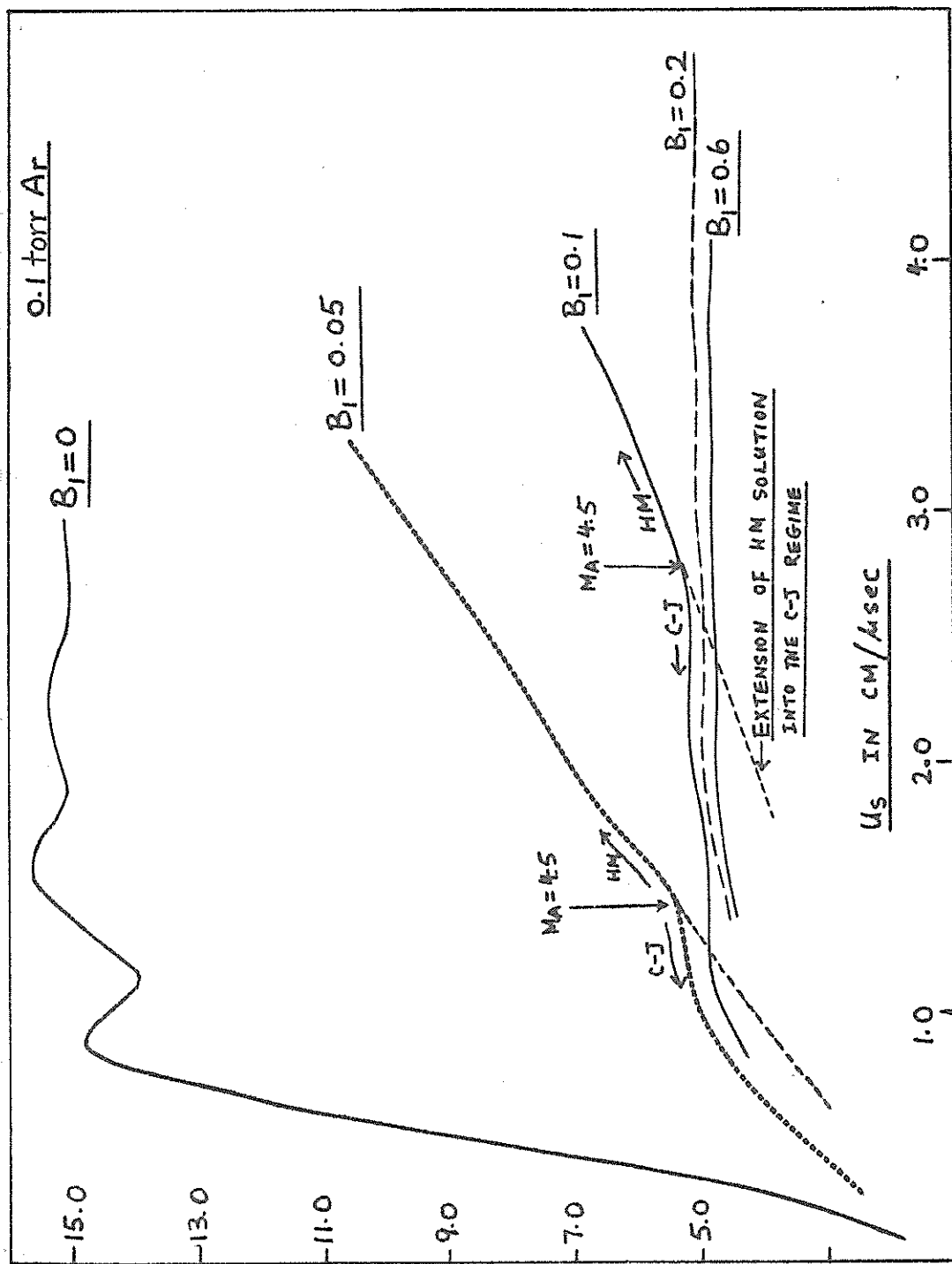


FIG. 2.5  $\Gamma$  AS FUNCTION OF  $U_s$ , TRANSVERSE C-J MODEL

and the hydromagnetic limit is reached at  $M_A = 4.6$  corresponding to the shock velocity of  $U_s = 1.38 \times 10^4$  m/sec. Below this speed, the solutions are C-J type and above this speed, because  $E_{LAB}$  goes negative with the continued application of the C-J condition, the hydromagnetic solutions are plotted. For  $B_1 = 0.1$ , the solutions become hydromagnetic at  $U_s = 2.8 \times 10^4$  m/sec. For  $B_1 = 0.2$  and greater, the hydromagnetic limit lies beyond the range of the graphs; for example, for  $B_1 = 0.2$  the limit is reached at approximately  $U_s = 5.6 \times 10^4$  m/sec.

For the solutions of  $\Gamma$ , it can be seen on Figure 2.5 that the C-J solutions are all in the neighbourhood of  $\Gamma = 4.9$  except at the lower velocity and when  $\Gamma$  begin to drop to smaller values. For  $B_1 = 0.2$  and above, the graphs are horizontal line between  $U_s = 1.7$  cm/microsecond to  $U_s = 5.0$  cm/microsecond and beyond, starting to rise only when the hydromagnetic limits are reached. In contrast the pure gas solution with  $B_1 = 0$  rises steeply to about 15 and then rises and falls successively about this value as the velocity increases to 3 cm/microsecond. The first peak occurs as first ionization is almost completed and second ionization begins to take over. The succeeding peaks similarly



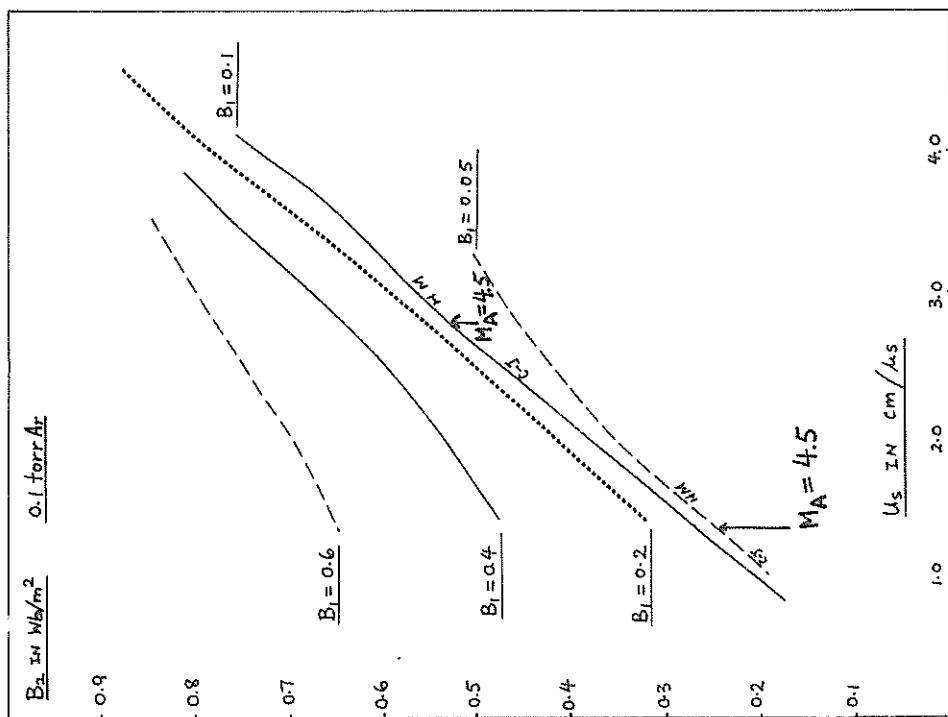


FIG. 2.6  $B_2$  AS FUNCTION OF  $U_5$ , TRANSVERSE C-J MODEL

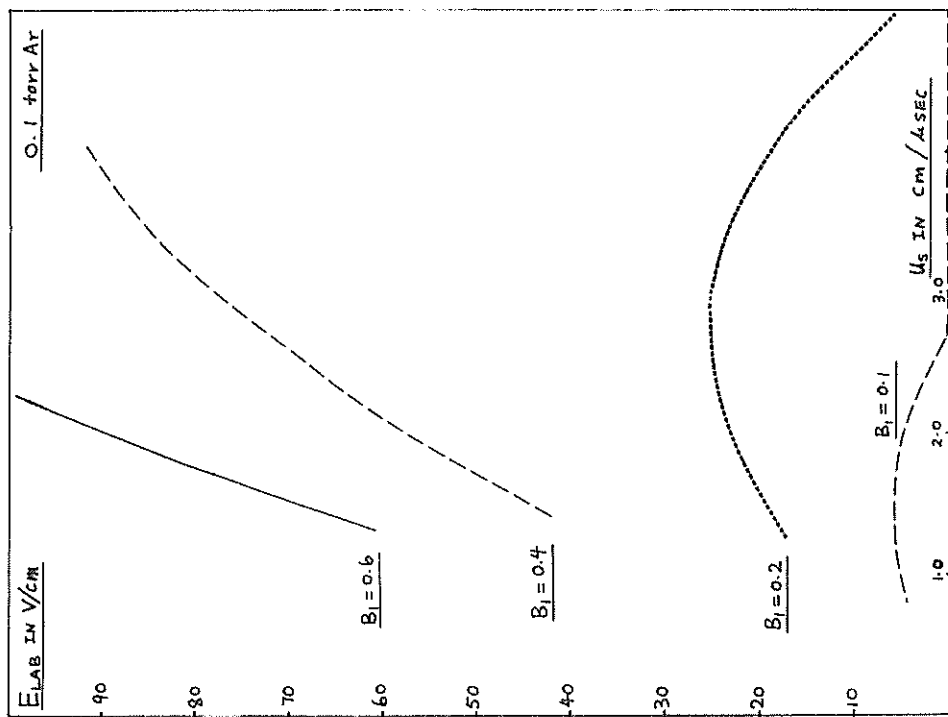


FIG. 2.7  $E_{LAB}$  AS FUNCTION OF  $U_5$ , TRANSVERSE C-J MODEL

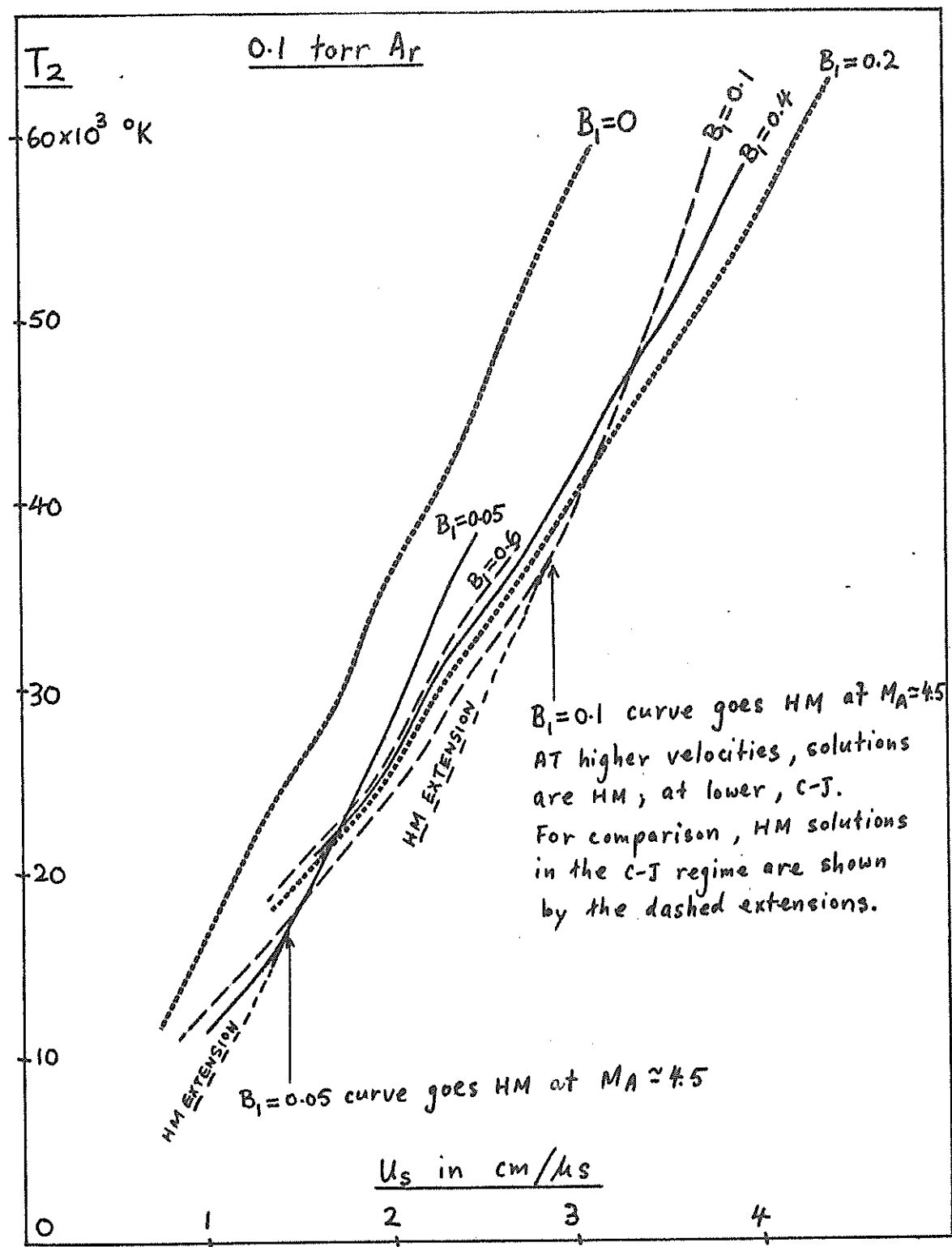


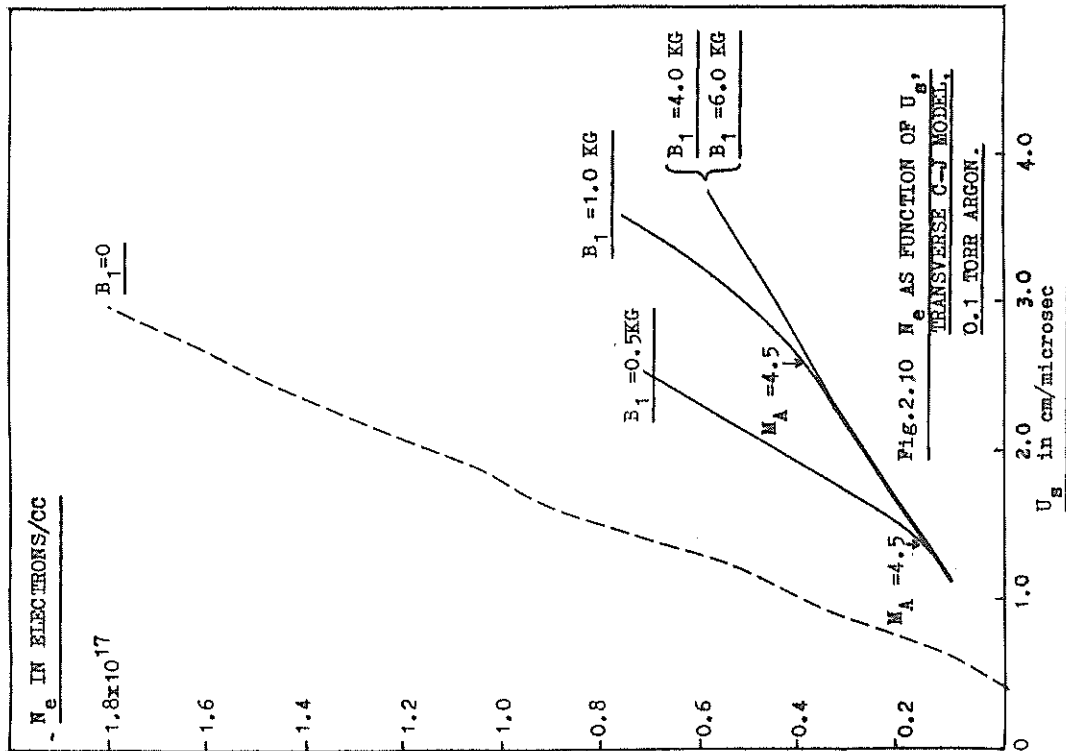
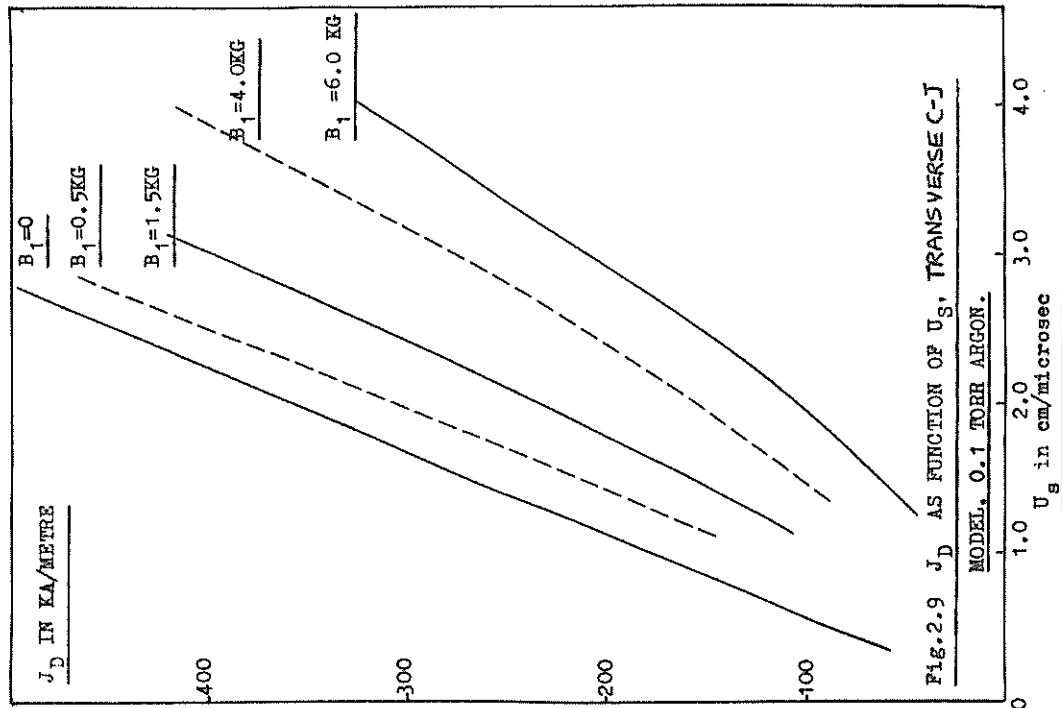
FIG. 2.8 TEMPERATURE AS FUNCTION OF  $U_s$ , TRANSVERSE C-J MODEL

indicate the start of a higher degree of ionization. The hydromagnetic solutions rise at an almost constant slope and the effect of succeeding degrees of ionization is hardly perceptible. Increasing the bias field lowers the density ratio.

The solutions of  $B_2$  are displayed in Figure 2.6 where it is noticed that the C-J solutions proceed into the hydromagnetic branch smoothly without any distinguishing feature. The  $E_{LAB}$  solutions are more interesting, in that the graph for each bias field has a maximum beyond which the value of  $E_{LAB}$  falls to zero at the hydromagnetic limit. Increasing the bias field increases the values of  $E_{LAB}$  and displaces the maximum in the direction of higher  $U_s$ .

The bias field lowers the post shock temperature at any given shock velocity. In the C-J branches, at a given shock velocity, the smaller the bias field, the lower the temperature. Beyond the hydromagnetic limit however, each graph turns upwards to climb more steeply and cuts across the graphs of the higher bias field solutions which have not yet reached the limit. After this cross-over, the solutions have the correct  $B_1$  dependence; with higher temperatures for the smaller bias fields, so that the solutions merge smoothly

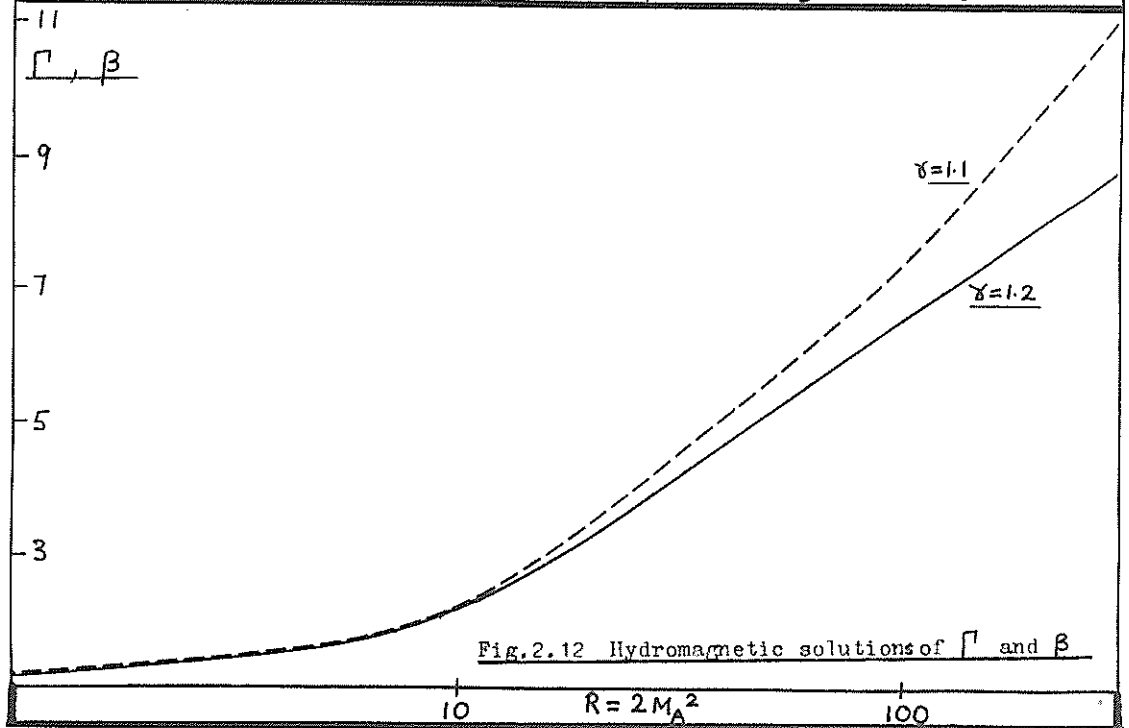
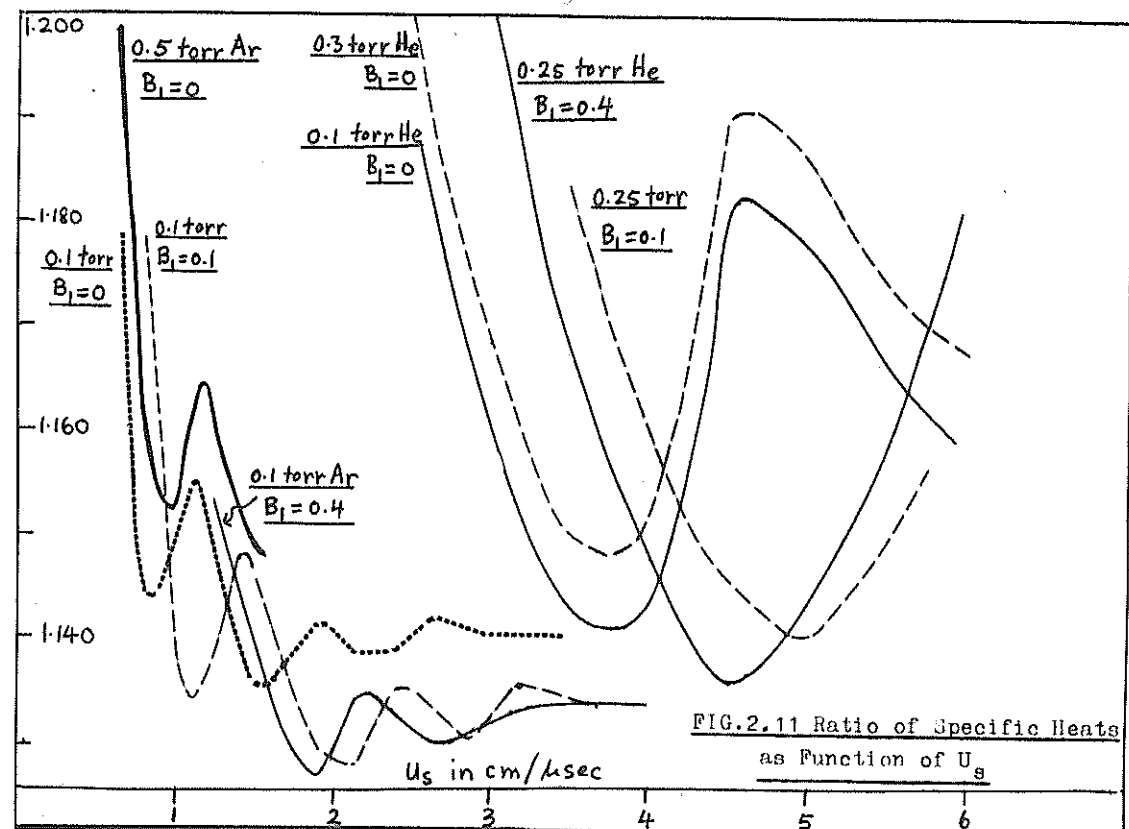




into the pure gas solutions at vanishingly small bias fields.

Figure 2.9 shows the currents required as a function of shock speed and bias field, whilst Figure 2.10 displays the electron densities.

The value of  $\gamma$  can be considered as an index descriptive of the number of degrees of freedom for the partitioning of the increasing energy of the gas. For an ideal gas,  $\gamma$  is a constant and the temperature increases proportionately with the enthalpy. When a gas begins to ionize, energy is required for the ionization and the increase in temperature corresponding to a given increase in enthalpy is less than the case when ionization is not considered. Once ionization is not negligible, however, the number of degrees of freedom cannot increase indefinitely and in a freely ionizing gas,  $\gamma$  will be almost constant, over fairly wide ranges of temperatures. This is illustrated in Figure 2.11, where, for 0.1 Torr argon with  $B_1 = 0.1$ , the value of  $\gamma$  is seen to lie between 1.142 and 1.135 above 1.3 cm/microsecond. The magnetic field has only a small effect on  $\gamma$ , reducing the average value of 1.140 ( $B_1 = 0$ ) to 1.133 ( $B_1 = 0.4$ ). Similarly the pressure has a slight effect. Hence, for approximate



calculations, it is justifiable, where the gas is known to be freely ionizing, to use (2-19) for the enthalpy calculation instead of the more precise equation of (2-16).

For example, using (2-19) for the enthalpy, an expression for  $\Gamma = \frac{\rho_2}{\rho_1}$  in terms of  $\gamma$  can be obtained by eliminating  $E_1$ ,  $E_2$ ,  $h_2$ ,  $P_2$ ,  $q_2$ ,  $B_2$  from the momentum equation (2-10), using, in addition, the energy, mass and electric field equations (2-9) and (2-11) to (2-13) and a closing relation depending on the model being considered. Thus, for hydromagnetic calculations, using (2-63a), the momentum and energy equations are written as:

$$\text{Energy} \quad P_2 + \frac{B_1^2}{\mu \gamma_a} \Gamma(\Gamma - 1) + \frac{1}{2} W \left( \frac{1 - \Gamma^2}{\Gamma} \right) \frac{1}{\gamma_a} = 0 \quad ,$$

$$\text{Momentum} \quad P_2 + \frac{B_1^2}{2\mu} (\Gamma^2 - 1) + W \left( \frac{1 - \Gamma}{\Gamma} \right) = 0 \quad ;$$

the difference of which gives:

$$\text{Hydromagnetic equation} \quad \Gamma^3 + a\Gamma^2 + b\Gamma + c = 0 \quad , \quad (2-87)$$

$$\text{where} \quad a = \frac{1}{2\gamma_a} (4 P_B + W)/d \quad , \quad P_B = \frac{B_1^2}{2\mu} \quad ,$$

$$b = -(P_B + W)/d \quad , \quad W = \rho_1 q_1^2 \quad ,$$

$$c = \frac{W}{d} \left[ 1 - \frac{1}{2\gamma_a} \right] , \quad \gamma_a = \frac{\gamma}{\gamma - 1} ,$$

$$\text{and} \quad d = 2 P_B \left[ \frac{1}{2} - \frac{1}{\gamma_a} \right] .$$

This technique is used in a later section for estimating the effect of the bow shock on probe measurements in a hydromagnetic flow. It is noted that the freely ionizing region, for argon, is between  $23,000^\circ\text{K}$  to the temperature required for the complete ionization of the atom. For helium, this region lies between  $18,000^\circ\text{K}$  and  $86,000^\circ\text{K}$  (corresponding to 2.3 cm/microsecond and 8.0 cm/microsecond for  $B_1 = 0$ ). Above that, helium quickly becomes ideal with a  $\gamma$  tending towards 1.66 above  $150,000^\circ\text{K}$  (9.4 cm/microsecond).

The values of  $\Gamma$  calculated from (2-87) are shown in Figure 2.12 as a function of  $R$  where  $R = \frac{W}{P_B} = 2M_A^2$ .

### CHAPTER 3

#### THE EXPERIMENTAL ARRANGEMENT

The design of the shock tube used in these experiments was based on preliminary work with a one metre long planar shock tube of 6 cm x 6 cm cross section. In this tube, the basic electrical and magnetic behaviour of the propagating discharge was studied. Current sheet velocity was measured and sheet structure studied by streak and framing photography and with magnetic probes. It was found that, with a typical operating point of 0.25 torr helium, and 140 KA, a well defined current sheet was formed which remained flat and thin over the first 4 cm of travel before developing an anode lead and an inclined though still well defined front<sup>56</sup>. Approximate matching of the dynamic impedance of the shock tube to the transmission line condenser bank, of characteristic impedance 60 milliohm and characteristic time 26 microsecond, was observed and a consistent energy balance in the first cycle of discharge was obtained in terms of gas flow energy, inductive storage in the shock tube and transmission line, and energy dissipation in expanding

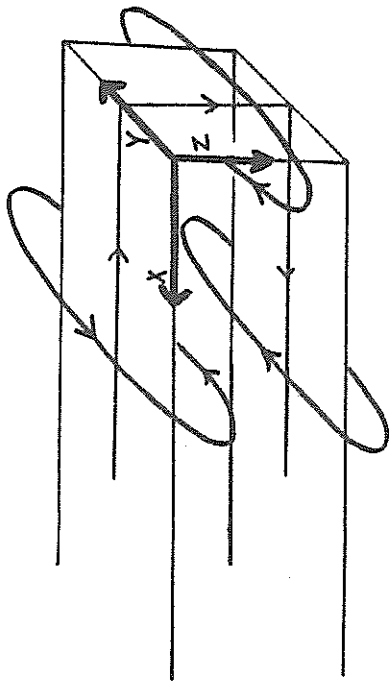
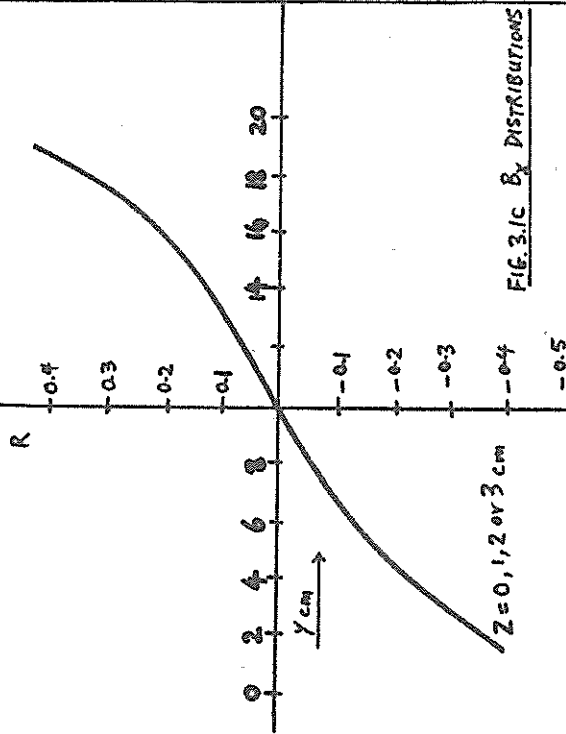
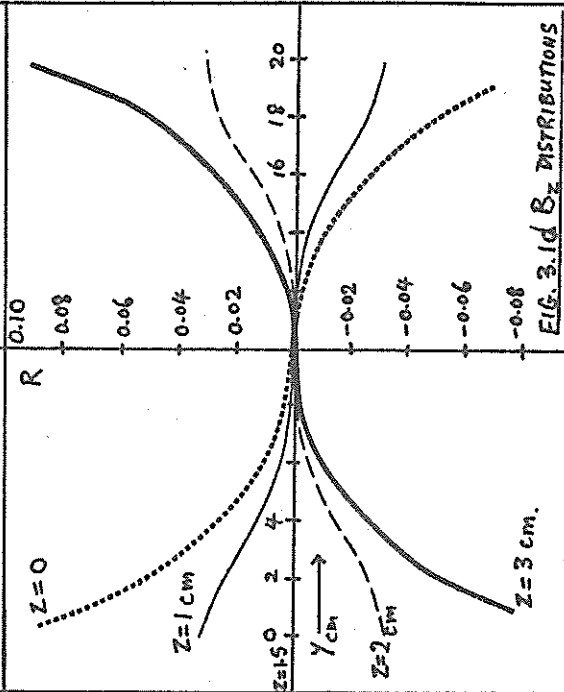
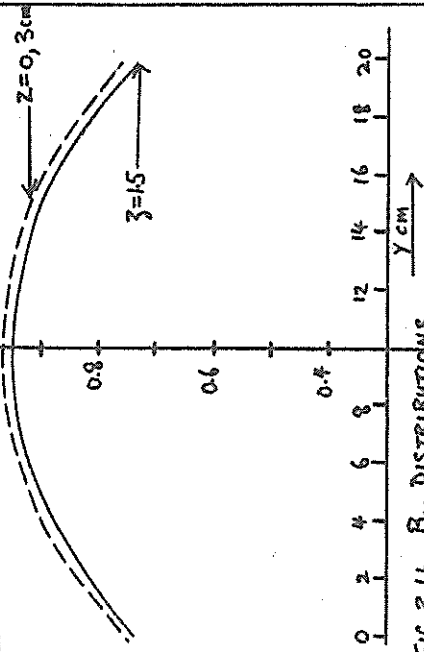


FIG. 3.1a COORDINATES OF MAGNETIC FIELD

COMPUTATIONS



RATIO OF FIELD TO  
'IDEAL' FIELD - R



and contracting (on reflection of the first current sheet from the end wall) current loops<sup>57</sup>. From this work, a shock tube of larger width to gap ratio, namely a width of 20 cm and a gap of 3 cm, was decided upon as a compromise between sufficient drive field, uniformity of field and a large path for interferometry.

The magnetic field distribution over the back surface of the current sheet was computed, assuming an ideal, flat and thin current sheet between two semi-infinite current return surfaces.

For the coordinates shown in Figure 3.1a, at the position  $(0+, y, z)$  where  $0+$  indicates the position  $x \rightarrow 0$  from the back of the current sheet, the three components of the total magnetic field are:

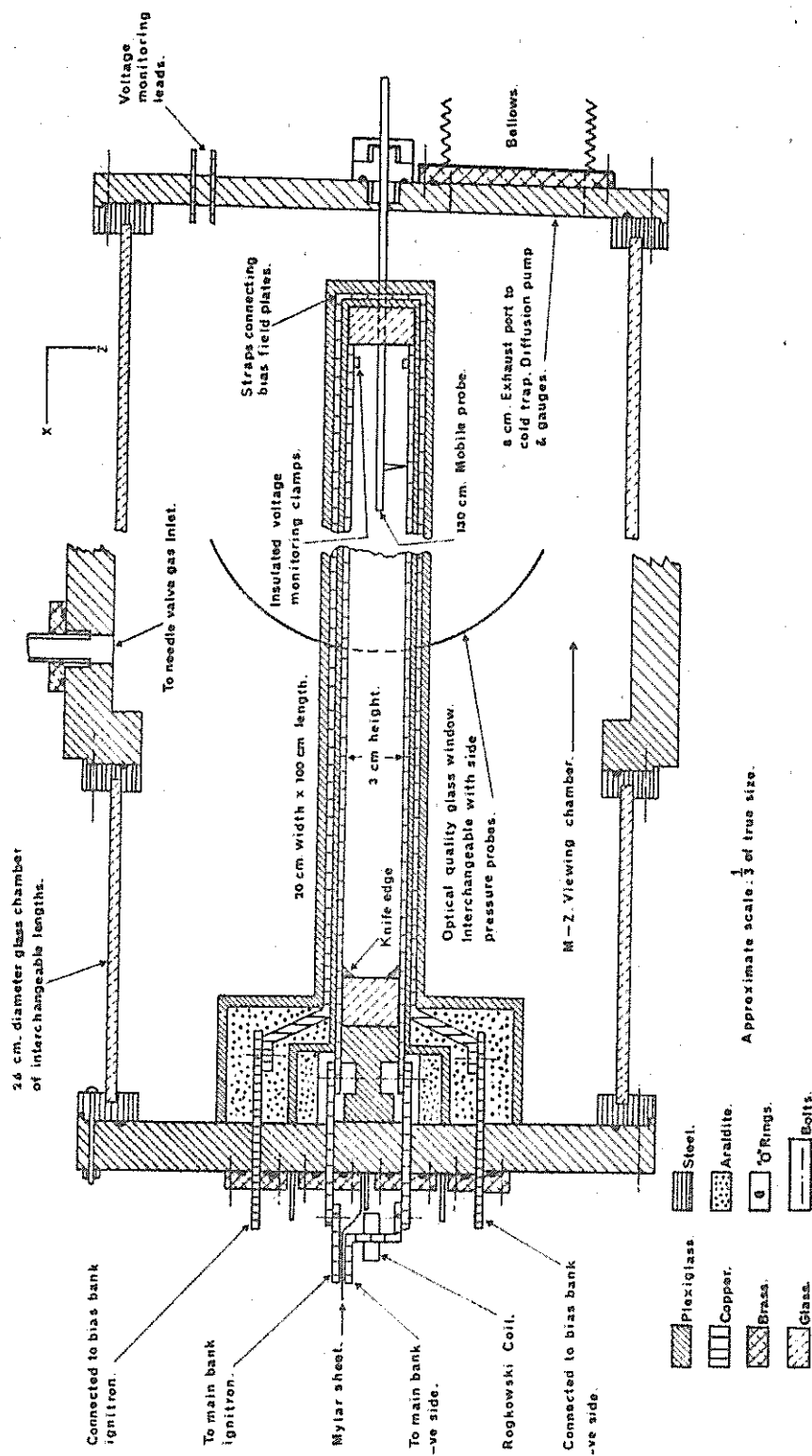
$$B_y = \frac{\mu I}{4\pi w} \left[ 2\pi + \tan^{-1} \left( \frac{y}{z} \right) + \tan^{-1} \left( \frac{w-y}{z} \right) + \tan^{-1} \left( \frac{y}{g-z} \right) + \tan^{-1} \left( \frac{w-y}{g-z} \right) \right], \quad (3-1)$$

$$B_x = \frac{\mu I}{4\pi w} \ln \left[ \frac{y^2}{(w-y)^2} \right], \quad (3-2)$$

$$B_z = \frac{\mu I}{8\pi w} \left\{ \ln \left[ \frac{z^2 + y^2}{z^2 + (w-y)^2} \right] + \ln \left[ \frac{(g-z)^2 + y^2}{(g-z)^2 + (w-y)^2} \right] \right\}. \quad (3-3)$$

Generally, these equations are not applicable near the edges of the current surfaces; as can be seen





PLANAR ELECTROMAGNETIC SHOCK TUBE.

Fig 3.2

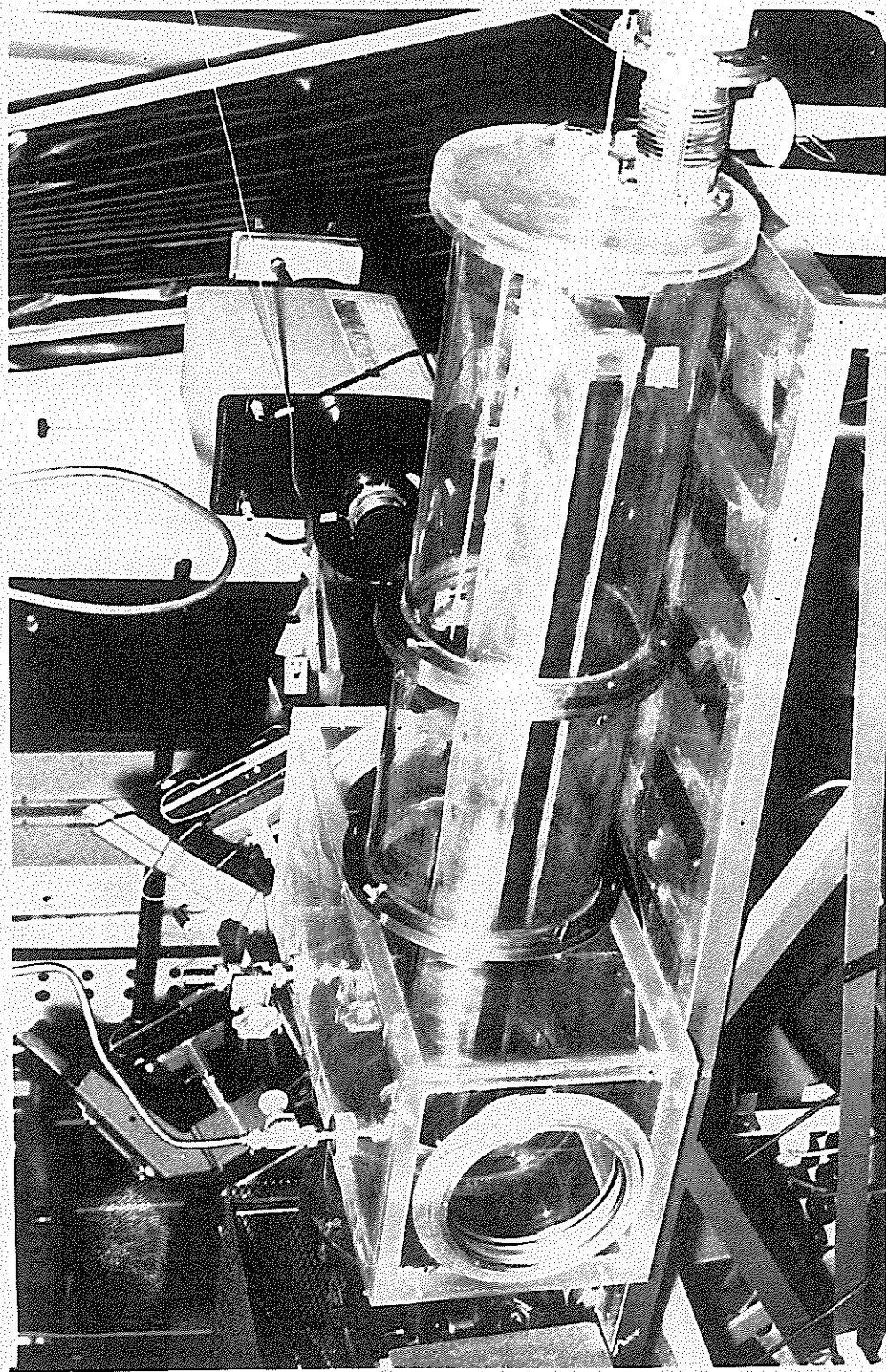


FIG. 3.3 THE SHOCK TUBE

from the expressions (3-2) and (3-3), when either  $g \rightarrow z$ , or  $w \rightarrow y$ .

The distributions on the  $y$ - $z$  plane along the back surface of the current sheet are shown in Figure 3.1b to Figure 3.1d.

### 3.1 The shock tube and vacuum system

#### 3.1.1 Description

The shock tube consisted of two  $\frac{1}{16}$  inch copper plates, 100 cm long (in the  $x$  direction) by 20 cm wide ( $y$ ), fixed parallel to each other at a uniform distance of 3 cm apart ( $z$ ). A diagram in the  $x$ - $z$  plane of the shock tube is shown in Figure 3.2 whilst Figure 3.3 shows the three dimensional aspects of the shock tube in its vacuum chamber with the rectangular Mach Zehnder (MZ) viewing chamber attached. At the drive end of the shock tube, copper knife edges (to localise breakdown) were provided, sitting flush against a flat glass plate. At the far end of the shock tube, the copper plates terminated at a glass block, serving as a supporting spacer as well as a reflecting surface for the shock waves. The sides of the shock tube were open, the plates being placed in a chamber consisting of 26 cm (i.d.) glass cylinders with  $1/4$  inch wall thickness

and of interchangeable lengths in 17 cm increments. The MZ viewing chamber could thus be positioned at variable distances from the knife edges. This chamber was made of 1 inch plexiglass and was fitted with two optical quality windows 20 cm in diameter to accommodate the 17 cm field of view of the interferometer.

The bias field current was carried by two  $\frac{1}{8}$  inch copper plates placed parallel to and having the same dimensions as the shock tube plates. The bias field plates were separated from the shock tube plates by  $\frac{1}{16}$  inch plexiglass and were completely insulated from the shock tube plates by: wrappings of 0.0005 inch mylar; plexiglass strips for the edges and araldite epoxy resin applied on the inner (i.e., unexposed) surfaces. All connections to the bias plates were likewise completely insulated. Two 1-cm wide copper straps, placed 5 cm apart, connected the bias plates together behind the far end glass block. A hole in this block along the centre line of the shock tube allowed a probe to enter the shock tube between the bias plate connecting straps.

This probe entered the vacuum through a sliding O ring seal on the circular back flange. This arrangement allowed positioning of the probe head

anywhere along the centre line of the shock tube, without disturbing the vacuum. The optical glass windows were replaceable with plexiglass windows containing similar sliding vacuum entry points for side probes for the traversal of the shock tube in the y-direction. A pair of insulated clamps near the reflection plate were connected to voltage monitoring leads passing through the back flange via vacuum seals.

The gas inlet port was connected through a needle valve to a variety of gas bottles, including dry air, argon, helium and nitrogen. The shock tube was evacuated by a 1250 litre/sec oil diffusion pump through a cold trapped baffle. The diffusion pump was backed by a 900 litre/min rotary pump.

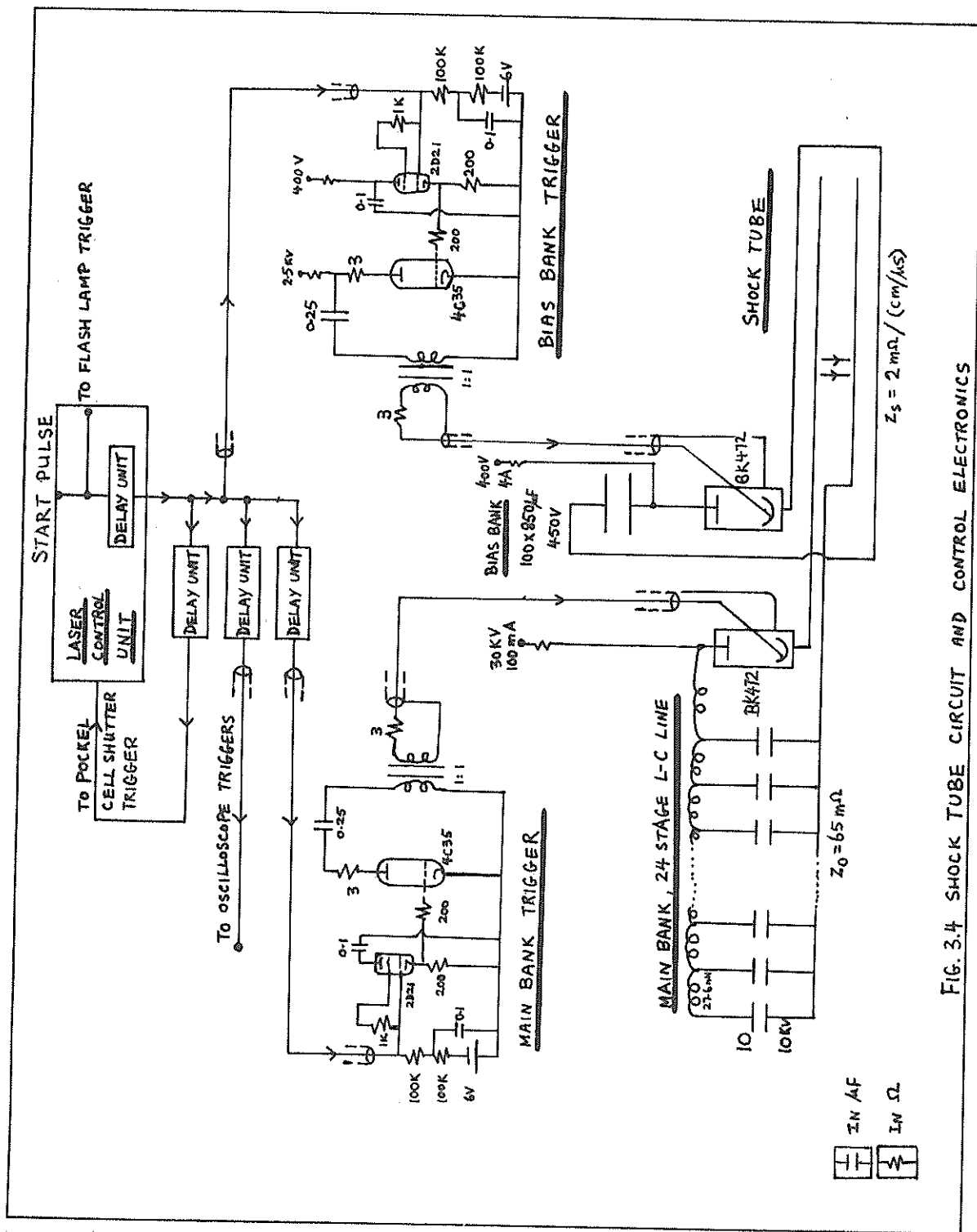
The main problem with the construction of the shock tube was that of vacuum feedthrough for the two sets of current carrying plates. Both electrical insulation and vacuum sealing had to be maintained whilst a compromise had to be made on the separation of the plates to facilitate the assembly of the tube, and at the same time not introducing intolerably large inductances. A completely boxed-in structure was found to be suitable within the vacuum chamber, with each plate boxed in completely with plexiglass sheets

and the spaces filled up with epoxy resin. The final vacuum seal to the end flange was provided by non-circular O rings compressed by rectangular brass flanges through which the current carrying copper plates pass.

### 3.1.2 Vacuum performance

A thermistor gauge with a useful range of 0.01 to 0.4 torr was used to indicate pressure drifts whilst the pressures recorded in the experiments were read on two 'cold trapped' vacustats with useful ranges of 0.005 to 1.0 torr and 0.05 to 10.0 torr respectively. Base pressures were recorded by a calibrated Pirani-Penning gauge with a range of  $10^{-3}$  to  $3 \times 10^{-5}$  torr. The base pressure attainable was better than  $3 \times 10^{-5}$  torr, with an initial pressure rise rate of 0.001 torr a minute to a pressure of 0.08 torr. Above 0.08 torr this rate decreased to  $0.06 \times 10^{-3}$  torr a minute.

The operating procedure was designed to eliminate the introduction of large impurity levels due to the high initial pressure rise rate. From base pressure the shock tube was filled rapidly with the test gas up to around 0.3 torr or higher and then pumped down to the



desired pressure. The effective pressure rise rate was thus kept down to  $0.06 \times 10^{-3}$  torr a minute.

### 3.1.3 Electrode maintenance

The shock tube copper plates and knife edges were examined every fifty shots and rubbed over with a soft cloth. After two hundred shots at about 100 KAmper, slight pitting of the knife edges and slight marking of the reflection glass plate were observed. This did not appear to affect the performance of the shock tube, and except for rubbing over with a cloth every fifty to two hundred shots, no maintenance of the knife edges and copper surfaces was required.

## 3.2 The condenser banks and control electronics

### 3.2.1 The main condenser bank

The condenser bank consisted of twelve BICC 10 KV, 2 x 10 microfarad condensers arranged to run as a 24 stage L-C line (Figure 3.4). The inductance per stage  $L_o$  is controlled by the width  $w_o$ , separation  $g_o$  and length  $d_o$  of the connecting plates between the condensers by the equation:

$$L_o = \mu \frac{g_o}{w_o} d_o \quad . \quad (3-4)$$



This formula is strictly accurate only for infinite parallel plates, but for a width-gap ratio greater than 4, the accuracy is better than 85 per cent. With the most frequently used dimensions of  $g_o = 1.5$  cm,  $w_o = 5.6$  cm and  $d_o = 13.8$  cm;  $L_o = 27.6$  nH, giving a characteristic impedance of :

$$\left(\frac{L_o}{C_o}\right)^{\frac{1}{2}} = Z_o = 0.065 \Omega \quad .$$

The constant current region had a characteristic time of

$$\tau_o = 2n (L_o C_o)^{\frac{1}{2}} = 25 \text{ microsec.}$$

This square pulse type behaviour is modified by stray inductances  $L_s$  which exists mainly in the connections between the transmission line and the shock tube as well as in the ignitron switch. The pulse shape is also modified by the inductive loading of the shock tube as the current loop increases in area with the propagation of the current sheet down the length of the tube. This inductance is 19 nH/10 cm of the tube. With an initial voltage  $V_o$  on the bank, the constant current  $I_o$  in the tube is determined by the sum of the bank impedance and the shock tube impedance  $Z_s$ ;

$$I_o = \frac{V_o}{Z_o + Z_s} \quad . \quad (3-5)$$

The impedance of the shock tube is determined by the rate of increase of inductively stored energy in the tube. When the current is constant:

$$Z_s = L' u \quad , \quad (3-6)$$

where  $L' = \mu g_0 / w_0$  is the inductance per metre and  $u$  is the velocity of the current sheet. Thus at a current sheet speed of  $5 \times 10^4$  m/sec, with  $L' = 1.9 \times 10^{-7}$ , we have  $Z_s = 9.5$  milliohm.

At current sheet speeds below  $5 \times 10^4$  m/sec, the load impedance is less than 13 per cent of the total impedance. This ensures that slight variations in current sheet velocity do not affect the value of the current. The bank delivered 90 Kamp at 6 KV corresponding to a drive field of  $0.57 \text{ Wb/m}^2$ .

A number of methods of switching the bank were considered. One switch used was a four electrode air gap switch with strip geometry and swinging cascade switching sequence<sup>58,59</sup>; employing a Blumlein type generator<sup>60</sup> for providing fast rising 20 KV triggering pulses. However, it was found that an EE BK472 ignitron fitted with a coaxial mounting, matched to the parallel plate transmission line, was much simpler to use; requiring no maintenance at up to 140 Kamp. In

its coaxial mounting, the BK472 had an estimated inductance of 40 nH compared to the 15 nH for the strip air gap, and about 40 nH for the rest of the plates connecting the condenser bank to the switch and the shock tube. The use of the ignitron increased the current rise time by about 1 microsec, and the switching time by about 1 microsec. The switching jitter was, however, almost comparable to the air gap, being less than 50 nsec. The stability in holding off the bank voltage throughout the whole range of operation and the ability to switch voltages as low as 25 volts make ignitron switching a really simple matter, compared to air gap switching.

### 3.2.2 The bias field bank

The bias field bank consisted of 100 x 850 microfarad electrolytics (Ducon ENP850) rated at 450 V, which were connected in parallel to two 1m x 1m copper plates, and fed into the shock tube bias field plates by means of parallel plate lines. This bank was switched by a second coaxially mounted BK472. The shock tube bias plate inductance was 220 nH and the inductance of the rest of the circuit and the ignitron switch was approximately 400 nH. The characteristic

impedance of the bank was 2.8 milliohm. Operated in the under-damped mode, the bank had a current constant of 21.3 Kamp/100V with a maximum current of about 96 Kamp. The corresponding bias field figures are 0.133 Wb/m<sup>2</sup>/100V with a maximum field of 0.6 wb/m<sup>2</sup> (6.0 KG). The risetime of the discharge was 250 microsec with a peak region of 50 microsec during which the current was steady to within 2 per cent. The ignitron switched the bank reliably at voltages as low as 25V so that the lowest bias field available was 0.33 KG.

### 3.2.3 Switching units

The basic switching unit consisted of a 2.5 KV 0.25 microfarad discharge into a 4 ohm load and coupled by a 1:1 transformer (designed for 15 KV single pulse insulation) onto the triggering electrode of the ignitron. The switch of this unit was a 4C35 hydrogen thyratron<sup>78</sup> (Figure 3.4). Timing and synchronization were provided by a transistor multivibrator delay unit with a 40V, 2 microsec square pulse output, and a delay, variable from 0.7 microsec to 2 millisec, with a jitter of less than 0.2 per cent in the range of 10 to 300 microsec. The use of up to four of these delay units allowed a large variety of triggering sequences involving the two condenser banks, the exploding wire

light source, the pockel cell switched ruby laser, the STL image converter camera and up to six oscilloscopes, operated simultaneously. Overall synchronization accuracy between the switching of the main bank and the subsequent triggering of diagnostic equipment was better than 0.1 microsec.

A typical triggering sequence with details of the circuits is shown in Figure 3.4. Figure 3.5 shows oscilloscope traces of the bias bank, whilst the main bank current trace can be seen in Figure 4. .

### 3.3 Diagnostics

Instrumentation of the shock tube included electrical measurements of current and voltage, measurement of the electric field ahead of the shock wave, probe measurements of magnetic field and pressure, streak and framing photography of the flow luminosity using an image converter camera and time resolved Mach Zehnder interferometry for the measurement of electron density and heavy particle density. As many measurements as possible were made simultaneously to obtain reliable comparison of pressure, magnetic field and luminosity profiles and of pressure, magnetic field, electron density and heavy particle density.

### 3.3.1 Electrical measurements

#### 3.3.1.1 Voltage measurements

Voltage measurements were made with two high impedance Tektronix probes, the P6013A (12KV, 100 M $\Omega$ , 3pf) and the P6015 (40KV, 100 M $\Omega$ , 2.7 pf), and a low impedance (500 ohm) 10:1 resistive divider, the ratio of which could be increased by the use of standard Tektronix BNC attenuation pads. The time response of the probes were tested and found to be better than 20 ns. The calibration factors were checked from time to time by means of the voltage calibration unit on a Tektronix 585 oscilloscope.

Measurements of voltages and electric fields have to be considered in terms of generating impedances so as not to inadvertently load the sources of the voltages. In the case of the shock tube circuit (Figure 3.6), the voltage behind the current sheet consists of both inductive and resistive components. Ahead of the shock, the inductive component is not present because no current flows. An electric field  $E_{\text{LAB}}$  of the type discussed in ionizing shock wave theory, the magnitude of which is determined by shock structure, must be associated with an electrostatic charge distribution in the section of the shock tube

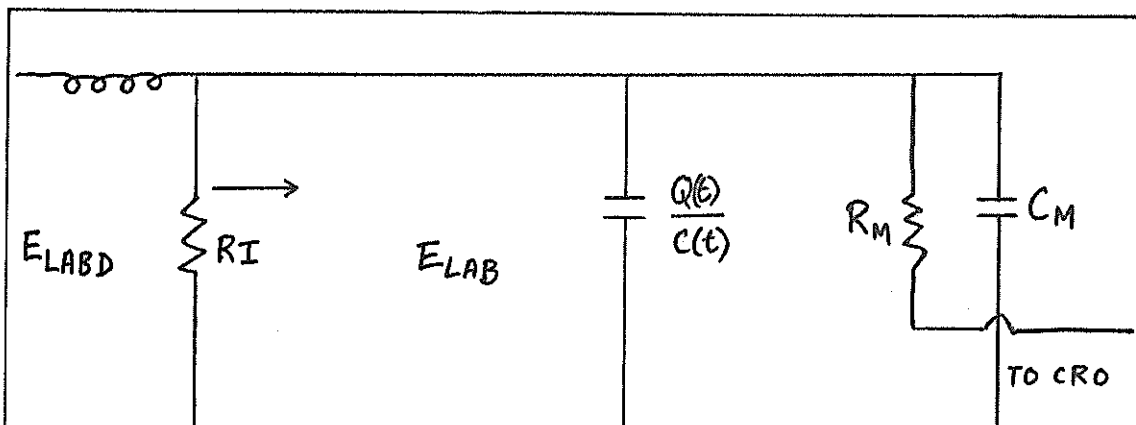


FIG.3.6 EQUIVALENT CIRCUIT FOR SHOCK TUBE  
VOLTAGES

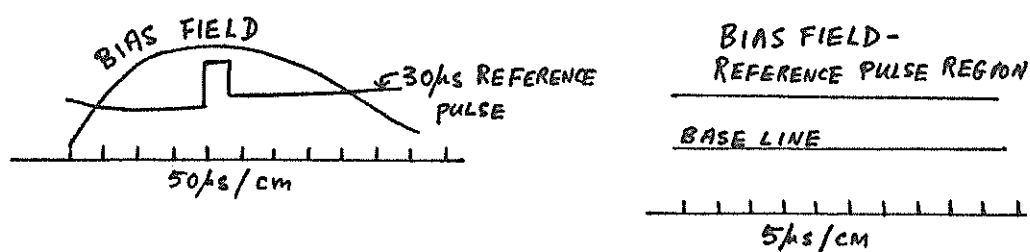


FIG. 3.5 BIAS FIELD OSCILLOGRAM TRACES

ahead of the propagating shock wave<sup>5</sup>. The equivalent circuit is shown in Figure 3.6.

Behind the current sheet, the electric field in laboratory coordinates is:

$$E_{\text{LABD}} = \frac{1}{g} \left( \frac{IdL}{dt} + RI \right) , \quad (3-7)$$

when  $I$  is a constant.  $R$  is the ohmic resistance of the current sheet. The first term in (3-7) is just:

$$\frac{1}{g} I \mu \frac{g}{w} \frac{dx}{dt} = B_D u_p , \quad (3-8)$$

where  $u_p$  is the current sheet velocity in the laboratory coordinate. This is the infinite conductivity electric field equation (2-13) transformed to the laboratory coordinates. The generating impedance is therefore

$$Z_{gD} = (I \mu g \frac{u_p}{w} + RI) / I = \frac{\mu g u_p}{w} + R . \quad (3-9)$$

$Z_{gD}$  of (3-9) is always less than one ohm and the measurement of  $E_{\text{LABD}}$  is a straight forward matter.

The electric field ahead of the shock has a much higher impedance since it is capacitative, having the constant of 59 pf/metre. During steady state propagation, this capacitance ahead of the shock is being decreased at a constant rate so that charge must be released in order to maintain a steady electric



field in this decreasing region. When a probe is connected to the shock tube electrodes as shown in Figure 3.6, this charge that is released is available to feed the probe; and provided the probe does not drain more current than is available from this charge release, the presence of the probe will not influence the field. We can write the capacitance of the preshock region as  $C=C'x$  where  $C'$  is the capacitance per metre. Then the rate of charge  $Q$  released is:

$$\frac{dQ}{dt} = \frac{d(CV)}{dt} = g_{LAB1}^E C' \frac{dx}{dt} = g_{LAB1}^E C' U_s \quad (3-9)$$

In a steady situation, this current released is constant. With this current feeding the probe, a finite time  $t_c$  is required to charge the probe up to the voltage  $g_{LAB1}^E$ . Equating the charge provided in the time  $t_c$  to the charge required, we have:

$$g_{LAB1}^E C' U_s t_c = g_{LAB1}^E C_M \quad ,$$

$$C_M = C' U_s t_c \quad .$$

If the probe is in position from the start of the discharge, the probe voltage will be in equilibrium with the preshock voltage, and  $t_c$  can be regarded as a characteristic time for voltage changes during the period of observation  $t_{ob}$ . With  $t_c$  thus defined, the criterion for the choice of  $C_M$  can be written as:

$$C_M \leq C' U_s t_c, \quad (3-10)$$

$$\text{with } R_M C_M \gg t_{ob}. \quad (3-11)$$

If these criteria are not satisfied, then more current will be drawn by the probe than can be supplied by the charge released by the decrease of capacitance as described by (3-9). The excess required current would then have to be drawn from the shock front-current sheet region. Using the P6015 probe with  $C_M = 2.7$  pf and  $R_M = 10^8$ , and with negligible capacitance in the connections between the shock tube electrodes and the probe, we have  $C_M R_M = 270$  microsec which satisfies (3-11). And with  $C' = 59 \times 10^{-12}$ , and  $U_s = 2 \times 10^4$ , equation (3-10) is satisfied for  $t_c \geq 2.3 \mu\text{sec}$ . This means that for an observation time much less than 270  $\mu\text{sec}$ , and for a steady  $E_{LAB1}$  (with fluctuations occurring with characteristic times greater than 2.3  $\mu\text{sec}$ ) the presence of the probe is not felt at all by the shock-current sheet system.

If a pair of floating electrodes is used to measure  $E_{LAB1}$ , it must be noted that this pair of electrodes is charged electrostatically by being immersed in this electric field. If the capacitance of this pair of electrodes is  $C_e$ , then the measuring

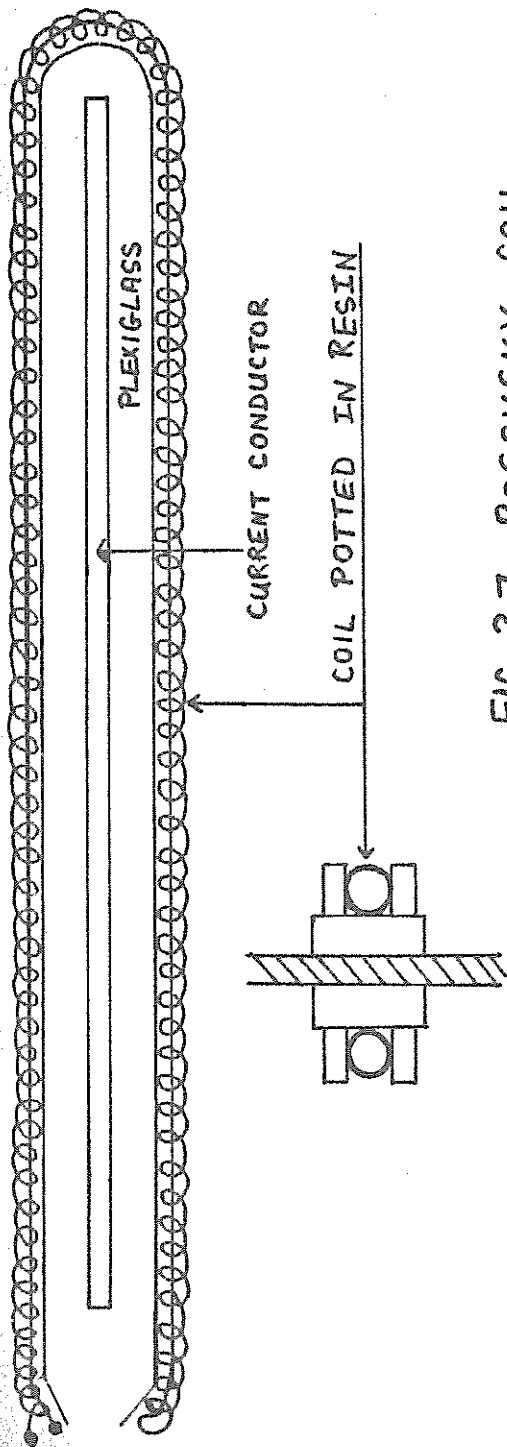


FIG. 3.7 ROGOVSKY COIL

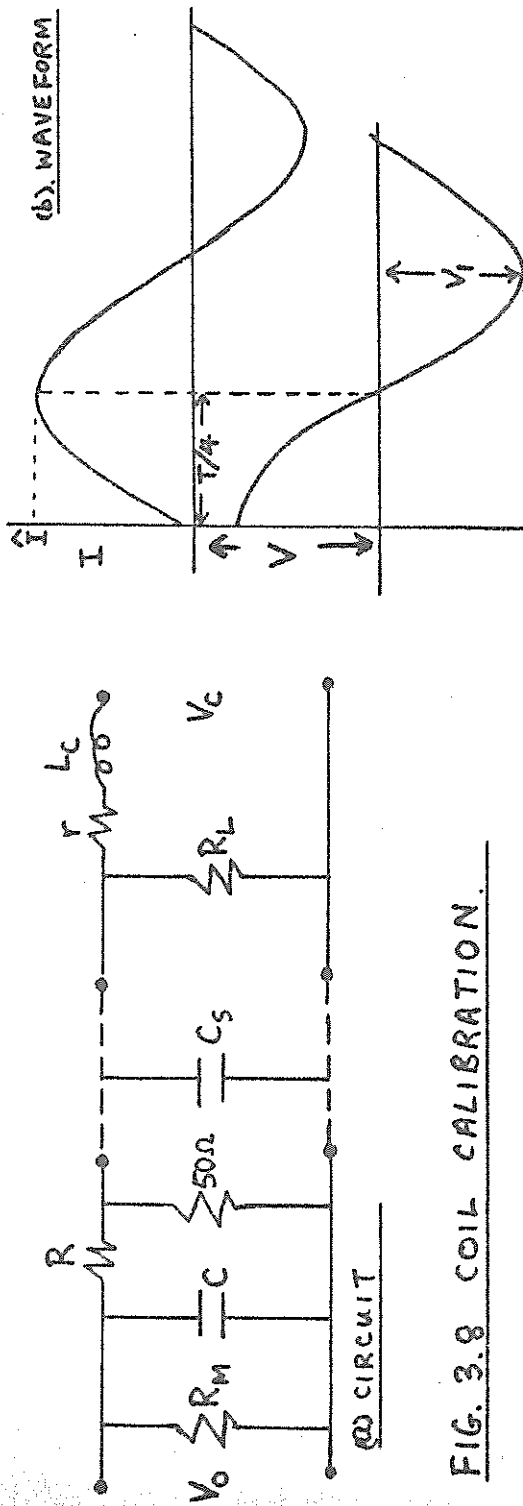


FIG. 3.8 COIL CALIBRATION.

capacitance  $C_M$  has to draw current from  $C_e$ ; and another criterion, in addition to (3-10) and (3-11), has to be fulfilled, namely:

$$C_e \gg C_M \quad .$$

This necessitates electrode capacitance of the order of 10 pf or more. This difficulty is avoided by making connections direct on to the shock tube electrodes. Levine<sup>3</sup> has successfully measured the pre-shock electric field in this way.

### 3.3.1.2 Current measurements

A parallel plate low inductance current shunt was developed to measure current, but because of contact problems between the resistive element and the clamping copper plates, this shunt was used only for confirming the calibration of the Rogovsky coils.

The wide parallel plate geometry of the transmission line plates required coils of non-circular major radii for both the banks. The geometry of the main bank coil is shown in Figure 3.7, and the equivalent circuit of the measurement system is given in Figure 3.8. The theory of the Rogovsky coil has been described by Leonard<sup>61a</sup> and Grives et al.<sup>62</sup>, and its high frequency limitations by Cooper<sup>63</sup>. Provided the current path

does not approach the minor turns of the coil too closely and provided the major circumference of the coil is topologically equivalent to a torus encircling the current path, the voltage induced across the coil  $V_c$  as in Figure 3.8a, can be written conveniently as:

$$V_c = \mu \frac{NA}{S} \frac{dI}{dt} \quad , \quad (3-12)$$

where  $N$  is the number of minor turns,  $A$  the area of a minor turn and  $S$  the circumference of the major loop. On integration, the voltage  $V_o$  appearing on the oscilloscope is:

$$V_o = \frac{NA}{S} \left( \frac{1}{RC} \right) I \quad , \quad (3-13)$$

where  $I$  is the current flowing through the coil and  $RC$  is the integration time constant.

The following design criteria<sup>62</sup> have to be met to ensure proper integration and matching:

1.  $L_c \omega \ll R_L + r \quad ,$
  2.  $\frac{1}{\omega_s} \ll RC \quad ,$
  3.  $R \ll R_m \quad ,$
- and
4.  $L_c C_s \ll \frac{1}{\omega^2} \quad , \quad (3-14)$

where  $\omega$  and  $\omega_s$  are respectively the highest and lowest significant angular frequencies to be observed,

$L_c$  and  $r$  are the coil inductance and resistance,  $R_L$  the load inductance,  $C_s$  the capacitance of the cable joining the coil to the integrator and  $R$  and  $C$  are the integrator resistance and capacitance. A further design consideration was observed in order to eliminate resonant oscillations, namely:

$$5. \quad 4 C_s L_c < \left[ \frac{L_c}{R_L} \right]^2 \quad . \quad (3-15)$$

The main bank coil had the following constants:

$$\begin{aligned} N &= 620 \quad , \\ \text{minor radius} \quad a &= 3 \times 10^{-3} \text{ m} \quad , \\ S &= 0.46 \text{ m} \quad , \\ \text{and} \quad RC &= 2.72 \times 10^{-3} \text{ sec} \quad . \end{aligned}$$

The calculated sensitivity is 57 Kamp/Volt. The coil was calibrated by disconnecting all but the first stage of the condenser bank (i.e. the stage nearest the shock tube) and putting a shorting conductor across the input terminals of the shock tube. This formed a simple L-C-R circuit whilst maintaining the operating geometry and position of the coil. The discharge current in this circuit was a slightly damped sinusoid with half period  $T/2$  (averaged over the first half cycle). If the voltage on the condenser at  $t = 0$  is  $V$  and at  $t = T/2$  is  $V_1$ ; where  $V_1 \leq V$  due to the slight

damping. The initial charge on the condenser is  $Q = CV$  and at  $t = T/2$  the condenser is negatively charged with  $Q_1 = CV_1$ . The total charge that has flowed in the circuit in this period of  $T/2$  seconds is:

$$Q_S = Q + Q_1 = Q(1 + V_1/V)$$

For slight damping we can assume that:

$$\begin{aligned} Q_S &= \int_0^{\frac{T}{2}} \hat{I} \sin \omega t \, dt \quad \text{where } \omega = \frac{2\pi}{T} \\ &= \frac{2\hat{I}}{\omega} \end{aligned}$$

$$\text{Thus} \quad \hat{I} = \frac{\pi \left(1 + \frac{V_1}{V}\right) CV}{T} \quad (3-16)$$

For a more exact result, the damping can be included in the integration of  $Q_S$ . The difference is slight if  $V_1 > 0.9V$ . A measurement of  $V$ ,  $V_1$ ,  $T/2$  and a separate measurement of  $C$  using a bridge, enabled  $\hat{I}$  to be calculated and compared with the peak coil voltage  $\hat{V}_0$  observed at the oscilloscope.

The measured constant for the main bank is: 60.0 Kamp/V ( $\pm 4$  per cent).

The bias bank coil was similar in construction, and had an integration constant of 4.5 msec and calibration constant of: 71 Kamp/V ( $\pm$  4 per cent).

### 3.3.2 Magnetic probes

The use of coils for measuring magnetic fields has been discussed in some detail by Lovberg<sup>61b</sup>. Essentially, a coil of N turns, each of area A, when placed in a varying magnetic field threading the coil, has an induced voltage, which on integration yields:

$$V_o = \frac{NAB}{RC}, \quad (3-16)$$

where RC is the integration time constant.

The risetime of the coil is given by:

$$t_r = \frac{L_c}{R_o}, \quad (3-17)$$

where  $L_c$  is the coil inductance and  $R_o$  is the load impedance. This load impedance is the characteristic impedance of the terminated cable connecting the coil to the integrator. Ferrari and Zuckers<sup>64</sup> have discussed coil distortion of signals in terms of coil inductance and distributed capacitance  $C_c$ . They concluded that less than 10 per cent distortion should occur when the highest frequency of interest is less than  $\frac{1}{10}$  of the resonant frequency of the coil; i.e.



$$< \frac{1}{10} (L_c C_c)^{\frac{1}{2}} \quad . \quad (3-18)$$

Lovberg<sup>61b</sup> has discussed the finite time for flux diffusion into the coil interior. In the case of a coil placed in a solid probe of radius  $r_p$ , flux has to diffuse from the plasma surrounding the probe into the probe in order to be 'counted' by the coil. The diffusion time is:

$$t_d = \frac{\mu \sigma r_p^2}{4} \quad , \quad (3-19)$$

where  $\sigma$  is the plasma conductivity.

Miller<sup>65</sup> has examined the integration of the rate of change of  $B$  as observed by a coil of radius  $a$  and concludes that the formula (3-16), which results from the time integrating of the coil voltage, is accurate only when:

$$w_b \gg a \quad , \quad (3-20)$$

$$\text{and} \quad u \tau_r \gg a \quad , \quad (3-21)$$

where  $w_b$  is the smallest distance over which  $\frac{\delta^2 B}{\delta x^2}$  has a significant value,  $u$  the velocity of the flux and  $\tau_r$  is the smallest time over which  $\frac{\delta B}{\delta x}$  has a significant value.

In terms of (3-20) and (3-21) it is seen that for  $u = 2 \times 10^4$  m/sec, and  $a = 1.5 \times 10^{-3}$  m, these criteria are approximately satisfied when  $\tau_r = 0.3$   $\mu$ sec or larger. This can be interpreted as meaning that, as the current sheet sweeps past, changes occurring in less than 0.3  $\mu$  sec will not be accurately displayed by a passive integration system. With a probe radius  $r_p$  of 3 mm, a capacitance  $C_c$  of the order of picofarads and a maximum estimate of  $\sigma$  of  $10^5$ , it is seen that the various times of true response represented by (3-17) to (3-19) are all smaller than 0.3  $\mu$ sec. Hence the criteria they represent are all satisfied for rise times greater than 0.3  $\mu$ sec. This is converted to a distance response of 6 mm (that is, structure occurring over distances less than 6 mm will not be accurately discerned by the probe). This 6 mm response is not limited only to the velocity of  $2 \times 10^4$  used in the estimation of  $\tau_r$  but is applicable for all speeds since  $u$  and  $\tau_r$  varies inversely in the criterion (3-21).

Other perturbations introduced into the plasma by the probe have also been described by Lovberg; including fringing of the field lines caused by the probe, cooling of the plasma in the region around the probe and the introduction of impurities into the

plasma from the probe. Another aspect of perturbation especially relevant to a shock wave-current sheet is the bow shock that forms over the head of the probe. This will be discussed in the section on pressure probes.

The coils used in the experiments were close wound from SWG 44 enamelled wire on polythene formers. They had the following constants:

$$\begin{aligned} n &= 30 \quad , \\ a &= 1.8 \text{ mm} \quad , \\ R_o &= 50 \text{ ohm} \quad , \\ \text{and} \quad L_c &= 3 \text{ } \mu\text{H} \quad . \end{aligned}$$

Two integration constants were used, one of which was 500  $\mu\text{sec}$  and the other 2.72 msec. The corresponding sensitivities are 66 KG/V (calculated) and 360 KG/V (calculated).

For calibration, the coils were placed in the central region of a parallel plate loop of the following dimensions: width ( $w$ ) = 20 cm, gap ( $g$ ) = 3 cm and length = 30 cm. A slightly damped discharge in this loop was monitored by a calibrated Rogovsky coil and the magnetic field was calculated from the formula:

$$B = \frac{\mu I}{w} \quad , \quad (3-22)$$

where  $f$  is a correction factor due to non-infinite geometry.

Using the coordinates of Figure 3.1a, this correction factor was obtained from an extension of (3-1) as:

$$f = \frac{2}{4\pi} \left[ \tan^{-1}\left(\frac{y}{z}\right) + \tan^{-1}\left(\frac{w-y}{z}\right) + \tan^{-1}\left(\frac{y}{g-z}\right) + \tan^{-1}\left(\frac{w-y}{g-z}\right) \right], \quad (3-23)$$

giving  $f = 0.9$  for the central position of  $y = 10$ ,  $z = 1.5$ .

For the coil used in most of the measurements, the calibrated sensitivity is: 68 KG/V (RC = 500  $\mu$ sec) and 270 KG/V (RC = 2.72 msec), with an uncertainty of  $\pm 5$  per cent.

### 3.3.3 The pressure probe

#### 3.3.3.1 The detection of mass and mass flow

As a shock wave moves down a gas pressure driven shock tube, the gas it encounters is swept up between the shock front and the contact surface. The 'slug' of shocked gas continually increases in mass and moves behind the shock front at a lower velocity than the shock velocity. In the electromagnetic shock tube the 'contact surface' is generally not so well defined,

in comparison with the gas pressure driven shock tube. The presence of currents and electromagnetic interactions increases the types of internal structure that the mass of shocked gas may possess. In general, the effect of a strong field may be expected to 'smear' out the 'slug'. Under these circumstances, the presence of a well defined slug cannot be assumed, although, often, mass flow structures have been inferred from luminosity, electric field, magnetic field and electron density measurements. Thus, Lovberg<sup>61b</sup> using magnetic and floating electric field probes has presented evidence of efficient snowplowing of mass by his current sheet. MacLelland et al.<sup>23</sup> has revealed complex electron density structures in the current sheet by means of schlieren photography. Eckbreth<sup>24</sup> used a combination of high speed photography, electric and magnetic probes to infer regions of mass flow corresponding to two distinct drive modes. Levine<sup>3</sup> has used a reflected shock luminosity technique combined with magnetic field measurements and spectroscopic measurements of electron density, to deduce the presence of a current free shock heated gas sample, in his normal shock experiment, operated at super-Alfvenic speeds.

Interferometric methods are a more direct method for the evaluation of mass when the flow is sufficiently dense and little ionized. However, since the refractivity of electrons is an order of magnitude higher than the refractivity of the argon ion and atom, the problem of estimating a small 'positive' fringe shift due to the heavy particles in the presence of a much larger 'negative' fringe shift due to electrons is a difficult one, when the level of ionization is greater than 20 per cent. Helium, with an even lower refractivity presents an even more formidable problem, with electron contribution to the fringe shift completely swamping the heavy particle contribution when the ionization is about one per cent.

A direct method of measuring mass flow is by means of a pressure sensing probe, which, regardless of the degree of ionization, indicates the flow of the heavy particles (atoms and ions), since the momentum of the electron is negligible. Pressure measurements using a piezoelectric element is a well established technique in pressure driven shock tubes<sup>66</sup>, but in an electromagnetic shock tube, because of large voltages and rapidly varying magnetic fields, the design of a

suitable probe presents a number of technical problems. Chang<sup>67</sup> has used a piezoelectric quartz crystal to help confirm the presence of a shock wave in his coaxial plasma gun. Hoffman<sup>20</sup> used a pressure and a magnetic probe for comparing the positions of the shock front and current sheet in an inverse pinch. In these studies however, the probes only indicated the arrival time of the pressure pulse as all other information was lost in the internal oscillations following the start of the pressure pulse. Rudderlow<sup>68</sup> has reported a particularly efficient probe. He has used this probe in a coaxial electromagnetic shock tube to compare the measured pressure with the Newtonian impact pressure (defined in the next section). He found that the measured pressure is 0.3 to 0.8 of the impact pressure over the ambient pressure range of 0.05 to 0.2 torr in air. His experiments were in the normal shock super-Alfvenic regime with an Alfven Mach number of 6.6. Recently, Sorrell<sup>81</sup> has deduced from probe measurements that shock front-current sheet separation can be achieved in hydrogen at a shock speed of 11.4 to 8.0 cm/microsec but not below 8.0 cm/microsec.

As pressure and magnetic probe measurements are becoming of increasing use and importance in the electromagnetic shock tube, it is pertinent, in fact, necessary, to look into the flow perturbation in the region of the probe on a more quantitative basis than has been discussed in section 3.3.2. It should be noted immediately that a bow shock can be expected to stand in front of the probe in the electromagnetic shock tube, under most operating conditions (experimental evidence of this will be shown in a later section). It is necessary to estimate the effect of the bow shock on both pressure and magnetic field measurements.

### 3.3.3.2 The bow shock and the stagnation region

#### 3.3.3.2.1 The bow shock

The term total pressure is generally used by gasdynamicists<sup>69c</sup> to describe the stagnation pressure, whereas it is generally used by magnetohydrodynamicists<sup>80</sup> as the sum of the magnetic and the static pressure. We shall use the term total pressure  $P_T$  as the sum of the magnetic pressure  $P_B$ , the static pressure  $P$  and the Newtonian impact pressure  $P_N = \rho q^2$ . In addition, we shall use a term total gas pressure  $P_G$  as the sum of  $P$  and  $P_N$ .



In an incompressible pure gas flow, the pressure exerted at the stagnation point on a surface normal to the flow is the total gas pressure  $P_G$ . However, when the gas is compressible, the pressure exerted at the stagnation point on that surface is not  $P_G$  but the stagnation pressure  $P_0$ , which is the static pressure developed when the flow is brought to a stop isentropically. We want to consider two processes in our probe problem. The first is the solution of the bow shock jump conditions, and the second, the isentropic compression of the gas, from immediately behind the bow shock, to the stagnation point. In both these processes the density ratio increases. If we assume that the flow is hydromagnetic, the magnetic induction ratio is the same as the gas density ratio. The magnetic pressure increases as the square of the magnetic induction whilst the magnetic energy per unit mass increases as the magnetic induction. In both these processes, therefore, the magnetic energy must increase at the expense of the gas enthalpy. In the transverse shock (as we shall see), the transverse field can dominate the pressure and energy terms in the stagnation region, even when the magnetic pressure is initially (before\* the bow shock) less than the static pressure.

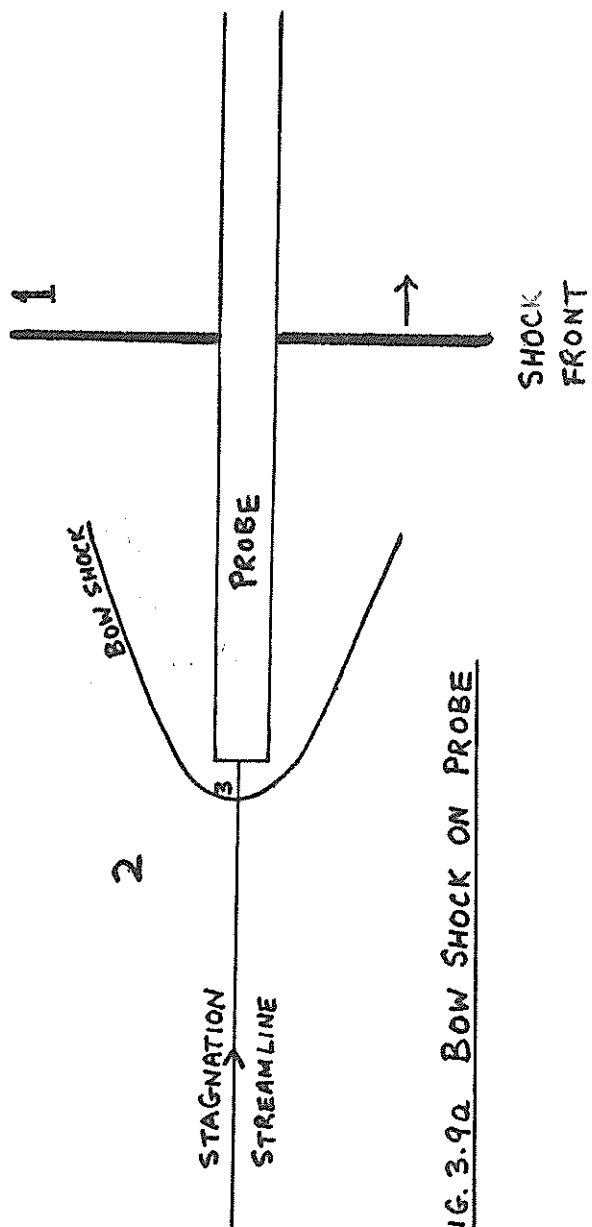


FIG. 3.9a BOW SHOCK ON PROBE

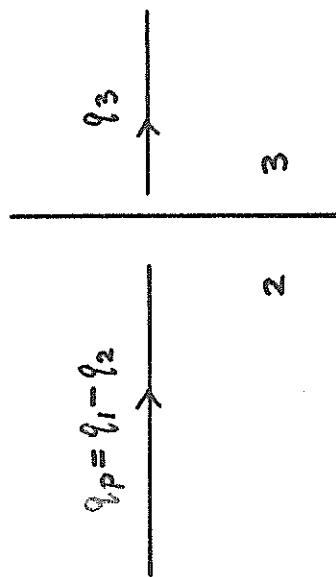


FIG. 3.9b ONE-DIMENSIONALIZED DETACHED SHOCK

We make the following assumptions:

1. The detached bow shock is stationary with respect to laboratory coordinates.
2. The flow is one dimensional and normal to the detached shock. This assumption is only accurate along the stagnation streamline.
3. The flow is hydromagnetic on both sides of the detached shock.
4. The gas on both sides of the shock is freely ionizing, in the sense discussed in section 2.8.2, i.e. the value of  $\gamma$  is frozen on both sides of the shock.

The situation is as depicted in Figure 3.9, where state 1 is the ambient gas, state 2 is the freestream flow behind the state 2 to state 1 shock and state 3 is the region immediately after the detached shock, on the probe side. The coordinates of the detached shock will be used and these coincide with the laboratory coordinates. The flow velocity into the detached shock is  $q_p = q_1 - q_2$ , where the subscript p is used to denote state 2 quantities transformed to the detached shock coordinates, wherever such a transformation is necessary. State 2 and state 1 are connected by the jump equations (2-9) to (2-13)

and either (2-61) or (2-63A) depending on the regime the 2 to 1 shock is in. Applied to the detached shock, the shock jump equations (2-9) to (2-13) can be re-written as:

$$\begin{aligned}
 \text{Mass} \quad & \rho_2 q_p = \rho_3 q_3 \quad , \\
 \text{Electric field} \quad & E_p = E_3 = -q_p B_2 \quad , \\
 \text{hydromagnetic} \quad & E_3 = -q_3 B_3 \quad , \\
 \text{so that we have:} \quad & \Gamma_3 = \beta_3 = \frac{\rho_3}{\rho_2} = \frac{B_3}{B_2} = \frac{q_p}{q_3} \quad . \quad (3-24)
 \end{aligned}$$

For a freely ionizing gas, we write:

$$h = \frac{P}{\rho} \frac{\gamma}{\gamma - 1}$$

with  $\gamma_2 = \gamma_3 = \gamma$ . The momentum and energy equations can then be written as:

$$\begin{aligned}
 \text{Momentum} \quad & P_2 + P_{N2} \left( \frac{\Gamma_3^{-1}}{\Gamma_3} \right) + P_{B2} (1 - \Gamma_3^2) - P_3 = 0 \quad , \\
 & (3-25)
 \end{aligned}$$

$$\begin{aligned}
 \text{Energy} \quad & \Gamma_3 P_2 + \frac{1}{2} P_{N2} \left( \frac{\gamma - 1}{\gamma} \right) \left( \frac{\Gamma_3^{2-1}}{\Gamma_3} \right) \\
 & + 2 P_{B2} \left( \frac{\gamma - 1}{\gamma} \right) \Gamma_3 (1 - \Gamma_3) - P_3 = 0 \quad , \quad (3-26)
 \end{aligned}$$

$$\text{where } P_{N2} = \rho_2 q_p^2, \quad P_{B2} = \frac{B_2^2}{2\mu} \quad .$$

Taking the difference in these equations eliminates  $P_3$ , and results in the following equation:

$$a \Gamma_3^3 + b \Gamma_3^2 + c \Gamma_3 + d = 0 \quad , \quad (3-27)$$

$$\text{where } a = \frac{2-\gamma}{\gamma} \quad ,$$

$$b = r_p + \frac{\gamma-1}{2\gamma} (4 + r_N) \quad ,$$

$$c = -(r_p + r_N + 1) \quad ,$$

$$d = \frac{1+\gamma}{2\gamma} r_N \quad ,$$

$$r_p = \frac{P_2}{P_{B2}} \quad ,$$

$$\text{and } r_N = \frac{P_{N2}}{P_{B2}} \quad . \quad (3-28)$$

This gives the value of  $\Gamma_3$  in terms of  $\gamma$ , and the ratios  $r_p$  and  $r_N$ ; so that with the properties of state 2 known, state 3 can be calculated. From the momentum equation (3-25), we have:

$$\frac{P_3}{P_2} = \gamma_3 = 1 + \frac{r_N}{r_p} \left( \frac{\Gamma_3^{-1}}{\Gamma_3} \right) + \frac{1}{r_p} (1 - \Gamma_3^2) \quad . \quad (3-29)$$

To help with the numerical calculations, we write down the following relations between  $r_p$  and  $r_N$ :

$$\text{C.J. For } \gamma = 1.135 \quad ,$$

$$M_A < 4.5 \quad ,$$

$$r_p < 0.3 \quad ,$$

$$r_N = \gamma(\gamma-1)^2 r_p \approx 16.2 r_p \quad . \quad (3-30)$$

(since  $\Gamma \sim 4.9$  for C.J. regime)

For  $r_p > 0.3$ , the 1 to 2 shock is in the hydromagnetic regime and:

$$\text{Hydromagnetic} \quad r_N = r_p (\Gamma - 1) + \frac{(\Gamma^2 - 1)(\Gamma - 1)}{\Gamma^2} . \quad (3-31)$$

The ratio  $\Gamma$  is not a constant in the hydromagnetic regime, but increases rapidly from the C-J value of about 4.9 to the pure gas value of 15.8 (for argon). Above  $r_p = 2.0$ , we can put  $r_N = 15 r_p$  approximately.

Values of  $\Gamma_3$  are computed and displayed in Figure 3.11a, from  $r_p = 0.1$  to  $r_p = 100$ . It is seen that  $\Gamma_3$  goes from a value of 1.0 in the large magnetic field limit ( $r_p \rightarrow 0$ ) to a value of 7.3 in the small magnetic field limit ( $r_p \rightarrow \infty$ ).

### 3.3.3.2.2 The stagnation region

Having found the conditions in state 3, we can next use an isentropic compression to estimate the conditions at the stagnation point. The total energy per unit mass in region 3 is:

$$H_{T3} = \frac{p_3}{\rho_3} \frac{\gamma}{\gamma-1} + \frac{B_3^2}{\rho_3 \mu} + \frac{1}{2} q_3^2 .$$

The total energy per unit mass at the stagnation point is:

$$H_{T03} = \frac{P_{03}}{\rho_{03}} \frac{\gamma}{\gamma-1} + \frac{B_{03}^2}{\rho_{03} \mu} \quad .$$

Equating these, we have:

$$\frac{P_{03}}{\rho_{03}} \frac{\gamma}{\gamma-1} + \frac{2P_{B03}}{\rho_{03}} = \frac{P_3}{\rho_3} \frac{\gamma}{\gamma-1} + \frac{2P_{B3}}{\rho_3} + \frac{1}{2} a_3^2 \quad . \quad (3-31)$$

Multiplying by  $\frac{\rho_3}{P_3} \frac{\gamma-1}{\gamma}$  and putting  $\Gamma_{03} = \frac{\rho_{03}}{\rho_3}$  and  $Y_{03}$

$= \frac{P_{03}}{P_3}$ , (3-31) is re-arranged as:

$$\frac{Y_{03}}{\Gamma_{03}} + \frac{2P_{B3}}{P_3} (\Gamma_{03} - 1) \frac{\gamma-1}{\gamma} = 1 + \frac{\gamma-1}{2\gamma} \frac{P_{N3}}{P_3} \quad ,$$

$$\begin{aligned} \text{and as: } \frac{Y_{03}}{\Gamma_{03}} + \frac{2\Gamma_3^2}{Y_3} \left( \frac{\gamma-1}{\gamma} \right) \times \frac{1}{r_p} \Gamma_{03} - \frac{2\Gamma_3^2}{Y_3} \left( \frac{\gamma-1}{\gamma} \right) \times \frac{1}{r_p} \\ = 1 + \frac{\gamma-1}{2\gamma} \times \frac{1}{\Gamma_3 Y_3} \frac{r_N}{r_p} \quad . \quad (3-32) \end{aligned}$$

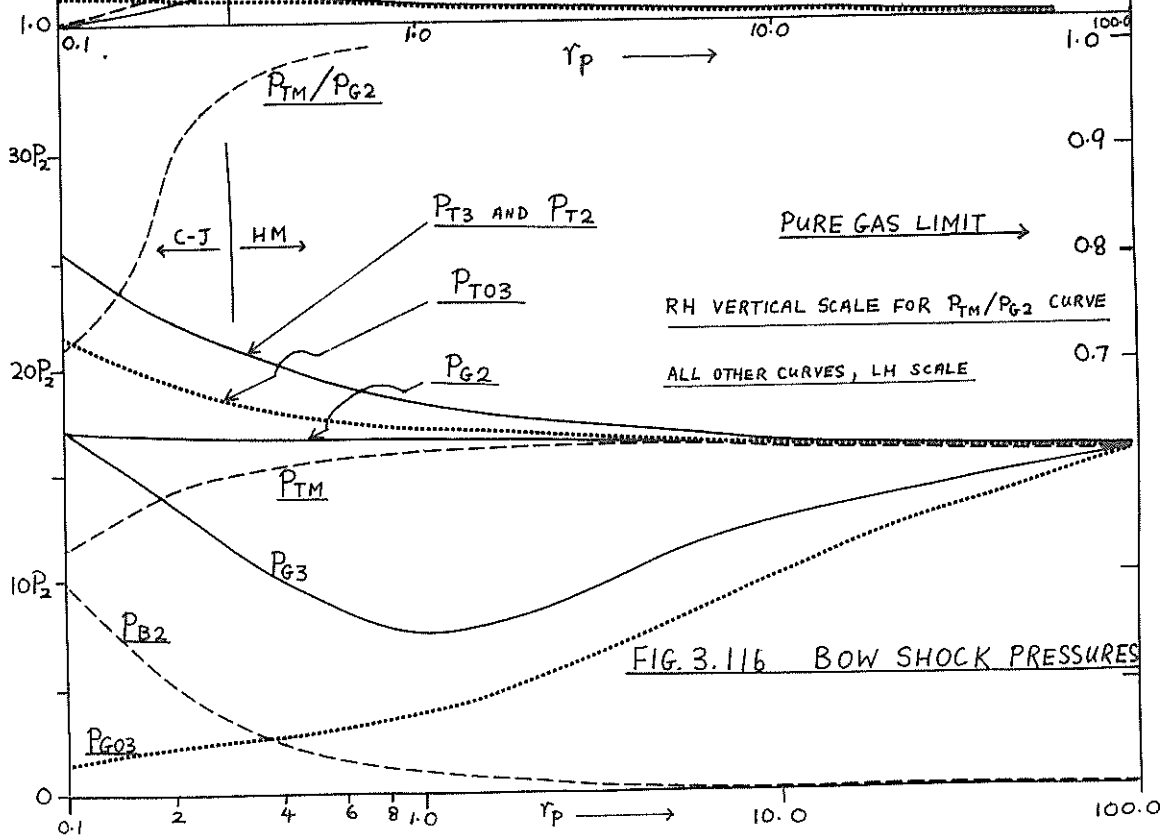
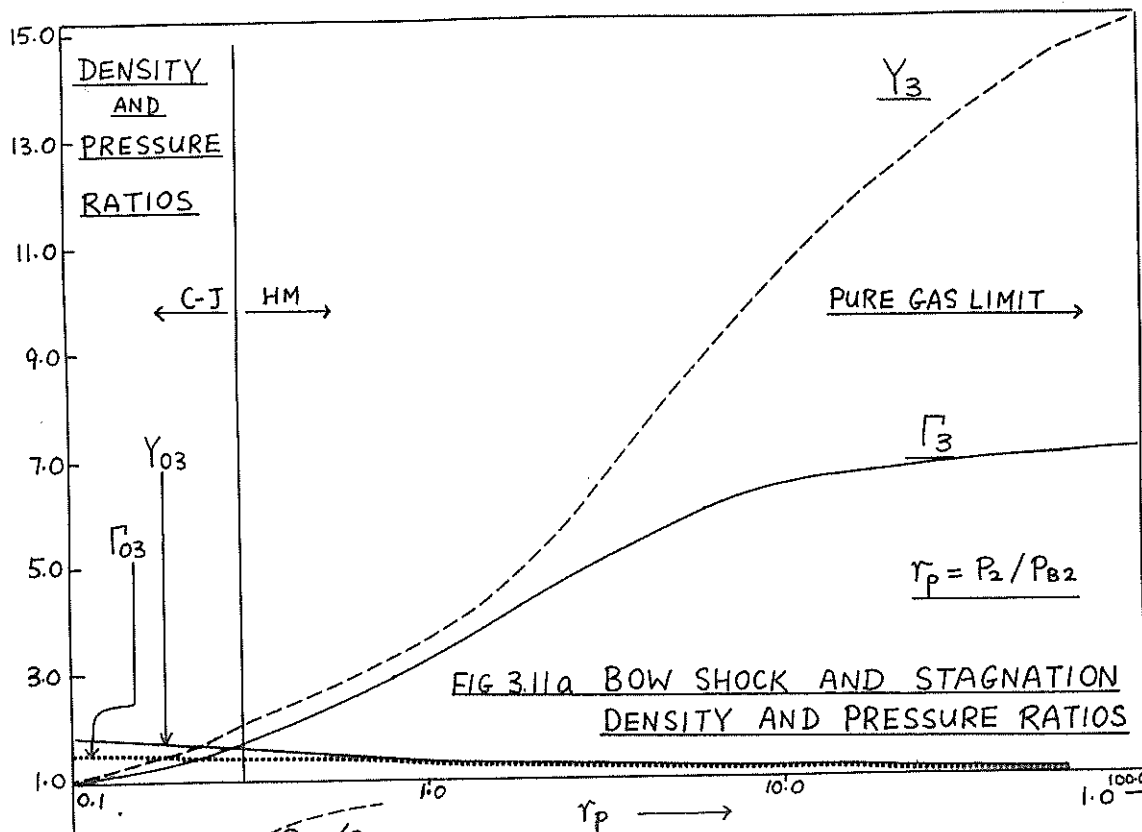
The assumption of an isentropic compression and a frozen value of  $\gamma$  allows us to write:

$$\frac{P_{03}}{P_3} = \left( \frac{\rho_{03}}{\rho_3} \right)^\gamma \quad \text{i.e.} \quad Y_{03} = (\Gamma_{03})^\gamma \quad . \quad (3-33)$$

With (3-33), equation (3-32) reduces to:

$$(\Gamma_{03})^{\gamma-1} + a\Gamma_{03} + b = 0 \quad , \quad (3-34)$$

the coefficients of which depend only on state 3 conditions. These are:





$$a = 2\left(\frac{\gamma-1}{\gamma}\right) \frac{\Gamma_3^2}{Y_3} \times \frac{1}{r_p}, \quad ,$$

$$\text{and} \quad b = -(a + 1 + \frac{\gamma-1}{2\gamma} \times \frac{1}{\Gamma_3 Y_3} \frac{r_N}{r_p}) \quad . \quad (3-35)$$

The values of  $\Gamma_{03}$  and  $Y_{03}$  are evaluated from equations (3-33) and (3-34) and shown on Figure 3.11a.  $\Gamma_{03}$  and  $Y_{03}$  tend to 1.06 and 1.07 respectively at the low magnetic field limit. In order to compare the relative values of the magnetic and gas pressures, the following pressures are also evaluated, using  $P_2$  as a normalizing factor:

$$P_{G2} = P_2 \left(1 + \frac{r_N}{r_p}\right) \quad , \quad (3-36)$$

$$P_{T2} = P_2 \left(1 + \frac{r_N}{r_p} + \frac{1}{r_p}\right) \quad , \quad (3-37)$$

$$P_{G3} = P_2 \left(Y_3 + \frac{r_N}{\Gamma_3 r_p}\right) \quad , \quad (3-38)$$

$$P_{T3} = P_2 \left(Y_3 + \frac{r_N}{\Gamma_3 r_p} + \frac{\Gamma_3^2}{r_p}\right) \quad , \quad (3-39)$$

$$P_{G03} = P_2 (Y_{03} Y_3) \quad , \quad (3-40)$$

$$\text{and} \quad P_{T03} = P_2 \left(Y_{03} Y_3 + \frac{\Gamma_{03}^2 \Gamma_3^2}{r_p}\right) \quad . \quad (3-41)$$

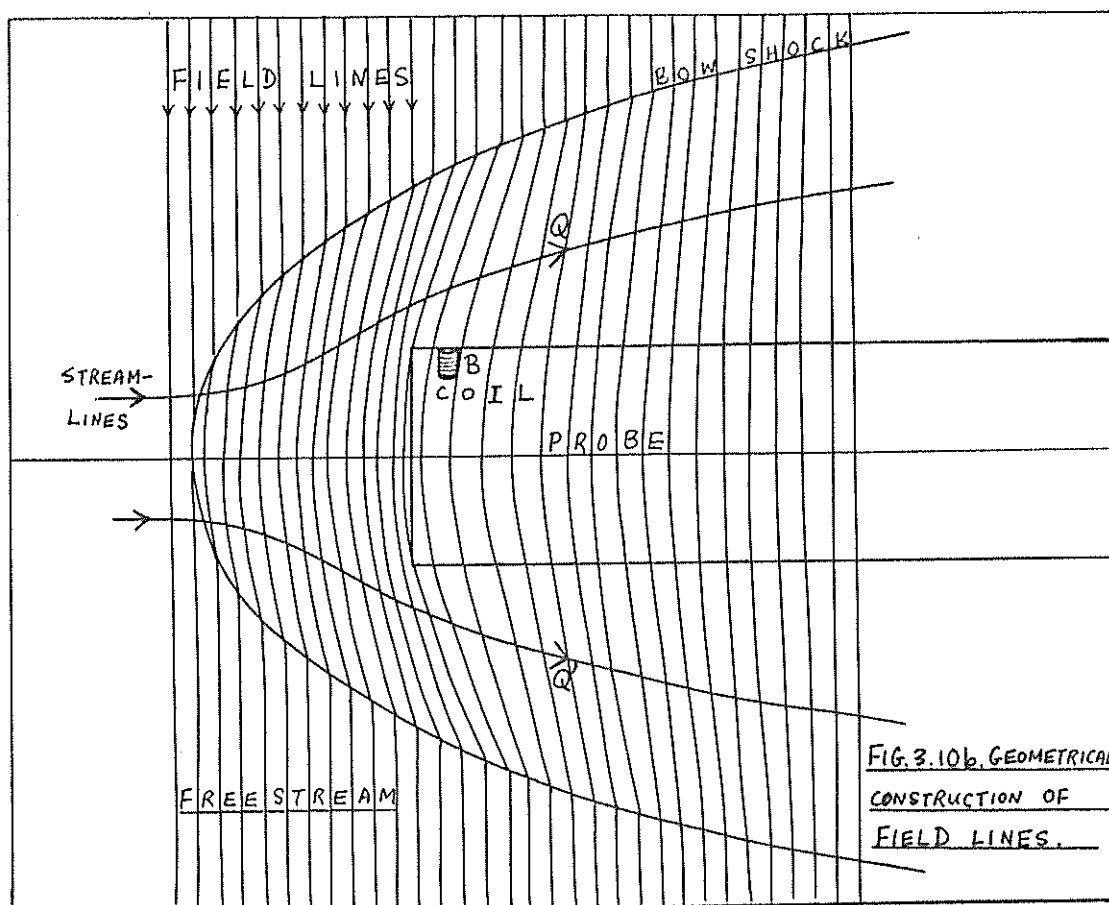


FIG. 3.10b. GEOMETRICAL  
CONSTRUCTION OF  
FIELD LINES.

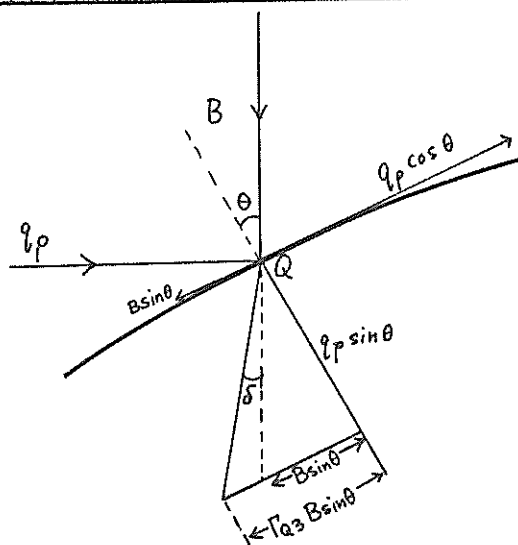


FIG. 3.10a. BOW SHOCK FLOW AND FIELD COMPONENTS

These are plotted on Figure 3.11b. The magnetic field has a marked effect on the total gas pressure. For example, for  $r_p = 1$ , in state 2 the magnetic pressure is equal to  $P_2$ , whilst the total gas pressure is about  $16.5 P_2$ . Across the bow shock, the total gas pressure has dropped to  $7.5 P_2$ , whilst the magnetic pressure increases to  $10 P_2$ . Compressing to the stagnation point, the total gas pressure has dropped further to  $3.7 P_2$ , whilst the magnetic pressure has increased to  $13 P_2$ . The corresponding density ratios are 3.2 across the bow shock and about 1.2 from the bow shock to the stagnation point.

#### 3.3.3.2.3 Field and flow distributions

The calculations of section 3.3.3.2.1. apply only along the stagnation streamline. We shall briefly discuss the effect of the bow shock curvature as we leave the stagnation streamline, in terms of the distribution of field and flow lines. For simplicity, we consider the x-y plane passing through the stagnation streamline as shown in Figure 3.10b. We assume, for a start, that the probe body is made of non-conducting material, so that the magnetic field lines can pass through the probe unimpeded.

At point Q (Figures 3.10a and 3.10b), off the probe axis where the flow enters the shock at an angle  $\frac{\pi}{2} - \theta$  to the shock normal, the velocity component normal to the shock surface is  $q_p \sin \theta$ , and the component tangential to the shock surface is  $q_p \cos \theta$ . Through the shock, the normal component is reduced whilst the tangential component remains unchanged. The streamline therefore bends away from the stagnation streamline, as shown in Figure 3.10b. Similarly, the tangential component of the induction  $B \sin \theta$  is increased to  $\Gamma_{Q3} B \sin \theta$  across the shock, whilst the normal component is unaffected ( $\Gamma_{Q3}$  is the density ratio across the bow shock at the point Q). The B lines will therefore bend slightly upstream. However, because of the symmetry of the flow about the axis of the probe in the x-y plane, the field line passing through Q must also pass through its image Q' on the other side of the bow shock. The actual path taken by the B line between Q and Q' will be affected by its interaction with the flow.

Without going into the details of this interaction, we can estimate this path by using the stagnation condition (which we know), and the knowledge that the density ratios (of both the fluid particles and the

field lines compared to the freestream densities) are greatest along the stagnation streamline, and decreases towards Q. In the ionizing shock regime (Figure 3.11a), along the stagnation streamline, the density ratio across the bow shock is about 1.4 (value of  $\Gamma_3$ ) and increases to about 1.9 at the stagnation point (the product of  $\Gamma_3$  and  $\Gamma_{03}$ , since we are considering density ratios compared with the freestream density). We can estimate the field line curvatures required to conform with these density ratios if we assume that the detachment distance (i.e. between the bow shock and the stagnation point along the stagnation streamline) is of the order of the probe diameter, that the bow shock shape is as illustrated in Figure 3.10b, and that the density ratio at Q is 1 (this value of  $\Gamma_{Q3}$  will give the biggest curvature). The problem is now to geometrically fit the field lines into the spaces to give the correct relative densities at the stagnation region and in the region around Q and Q'. This gives a field line distribution of the order illustrated in Figure 3.10b. We also note that in the limit of very low fields, the combination of increased stagnation densities (Figure 3.11a and b) and decreased detachment distance (see for example Pai and Kornowski<sup>85</sup>

for estimates of detachment distances) will result in much larger curvatures. In that limit, the distribution will be quite different from that shown in Figure 3.10b and the following estimates will not apply.

With the field distribution as shown in Figure 3.10b it is now necessary to estimate the magnetic field density in the probe just behind the stagnation point and also the magnetic field component in the y-direction passing through the coil, positioned as shown in Figure 3.10b. We first note that  $\Gamma_{Q3}$  is less than  $\Gamma_3 \approx 1.4$ , and write down the relationship between  $\Gamma_{Q3}$  and the angle  $\delta$  through which the magnetic induction B is deflected through the bow shock (Figure 3.10a); i.e.:

$$\tan (\delta + \theta) = \frac{\Gamma_{Q3} B_2 \sin \theta}{B_2 \cos \theta} = \Gamma_{Q3} \tan \theta . \quad (3-42)$$

For a Mach 3.5 flow in the freestream, a maximum estimate of  $30^\circ$  can be set for  $\theta$ , which for  $\Gamma_{Q3} = 1.4$  gives  $\delta = 9^\circ$ . The maximum estimate of the magnetic induction at Q after passing through the bow shock is therefore:

$$\begin{aligned} B_{\max} &= B_2 (\cos^2 \theta + \Gamma_{Q3}^2 \sin^2 \theta) \\ &\approx 1.24 B; \end{aligned} \quad (3-43)$$

and the component in the y-direction is

$$B_{y\max} = B_2(\cos^2 \theta + \Gamma_{Q3}^2 \sin^2 \theta) \cos \delta$$

$$\approx 1.22 B \quad . \quad (3-44)$$

As the field lines approach the surface of the probe, it is necessary for them to spread apart. This can be seen from two points of view. The first considers the path of the streamlines approaching the face of the probe. These deflect to go to the side of the probe. In the subsequent expansion, a gasdynamic analysis, see for example Liepmann and Roshko<sup>69b</sup>, shows that the density ratio (compared to freestream) decreased to below unity. In the second method, we refer again to Figure 3.10b. The field lines far to the right of the probe face are seen to be almost undisturbed compared to the freestream distribution. Near the front of the probe, the field lines are compressed into the stagnation region. It is thus necessary for the field density just behind the stagnation point to be less than the freestream value.

We can now write down the pressure exerted on the stagnation point of the pressure probe front face as:

$$P_{TM} = P_{T03} - P_{B2} = P_2 \left( Y_{03} Y_3 + \frac{\Gamma_{03}^2 \Gamma_3^2}{r_p} - \frac{1}{r_p} \right), \quad (3-45)$$

where the error involved, in taking  $P_{B2}$  as the pressure behind the front surface of the probe, is small.

Finally, we have to estimate the effect of the conductivity of the probe body on the distribution of the field lines. The maximum effect is in the case when the probe wall is perfectly conducting. Then all the field lines which should be in the volume of the probe to maintain the distribution shown in Figure 3.10b are now displaced from this volume and squeezed into the exterior of the probe. However, in reality, field diffusion through the conducting walls of the probe occurs, governed by the equation:

$$\frac{\delta B}{\delta t} = \frac{\delta}{\delta x} \left( \frac{1}{\mu\sigma} \frac{\delta B}{\delta x} \right) \quad (3-46)$$

the solution of which is, for times of our interest, dominated by a factor  $e^{-\frac{\mu\sigma x^2}{4t}}$ . Denoting  $t_d = \frac{\mu\sigma d^2}{4}$ , where  $d$  is the thickness of the conducting wall of the probe, we note that, if originally the field lines are entirely outside the volume of the probe, then after a time of  $4t_d$ , the magnetic field has diffused into the probe to the extent that the interior of the probe has now a field of  $e^{-0.25} = 0.78$  of the field at



the external point. At this time, 22 per cent of the field lines, which should be within the volume for an undistorted distribution, are still excluded from the volume of the probe. If we assume that the 22 per cent of field is displaced into an external volume 5 times the size of the volume of the probe (i.e., a cylinder coaxial with the probe and with a diameter 2.5 times that of the probe), then the external field distribution is distorted by less than  $4\frac{1}{2}$  per cent. Thus, for times longer than  $4 t_d$ , or for field variations occurring in the freestream with a characteristic time greater than  $4 t_d$ , the re-distribution of field lines within the probe, occurs sufficiently rapidly to allow less than 22 per cent distortion of the field for an interior point, and less than  $4\frac{1}{2}$  per cent for an external point. In this connection, we note that a coil, sitting in a cavity drilled through the conducting wall of the probe, can be treated as being on the exterior of the probe.

For the probe discussed in the next section, the front face was shielded by 0.07 mm of brass, giving a  $4 t_d$  of 0.1 microsec. For the 0.12 mm brass wall of the cylinder the value of  $4 t_d$  was 0.3 microsecond.

In view of the above analysis, we propose to use the following expressions for  $B_M$  and  $P_{TM}$ , the induction observed by the coil, and the total pressure measured by the pressure probe front surface:

$$B_M \approx B_2, \quad (3-47)$$

and (3-4) for  $P_{TM}$ ; with a reliable response time of 0.3 microsec. We note that (3-47) is likely to be an overestimate, since Figure 3.10b shows that the field density at the coil is slightly less than the freestream density. Equation (3-45) is also an overestimate, since  $P_{T03}$  is derived for the stagnation point. For small bias fields, in particular, the actual measured field can be expected to be considerably less than  $B_2$ , since the field line curvature at the coil will be much more than represented in Figure 3.10b.

A more rigorous calculation is necessary in order to obtain more reliable estimates than given by (3-47) and (3-45). It is further noted that, for pressure and magnetic field measurements in other bias field geometries, bow shock effects may have to be taken into account; particularly in view of its ability to deflect field lines.

### 3.3.3.3 Design considerations

In order to obtain as much information as possible about the shock front and flow, a probe was designed to have the following characteristics:

1. Small physical size (i.e. small area presented to the flow), keeping to a minimum the perturbation of the flow and the field distribution in the shock tube;
2. efficient electrostatic and electromagnetic shielding to reduce external noise levels; particularly, the high frequency noise associated with the triggering pulses;
3. good electrical and mechanical contact and acoustic matching between the surfaces to reduce internally generated noise in the form of acoustic reflections and oscillations;
4. a fast response time and a sufficiently long decay (charge leakage time) to accommodate the period of observation;
5. mobility, to enable the probing of different parts of the shock tube.

A number of probes were constructed for axial (x) probing, side (y) probing and a three prong probe was also constructed to measure the pressure distribution from the top plate to the bottom plate in an attempt

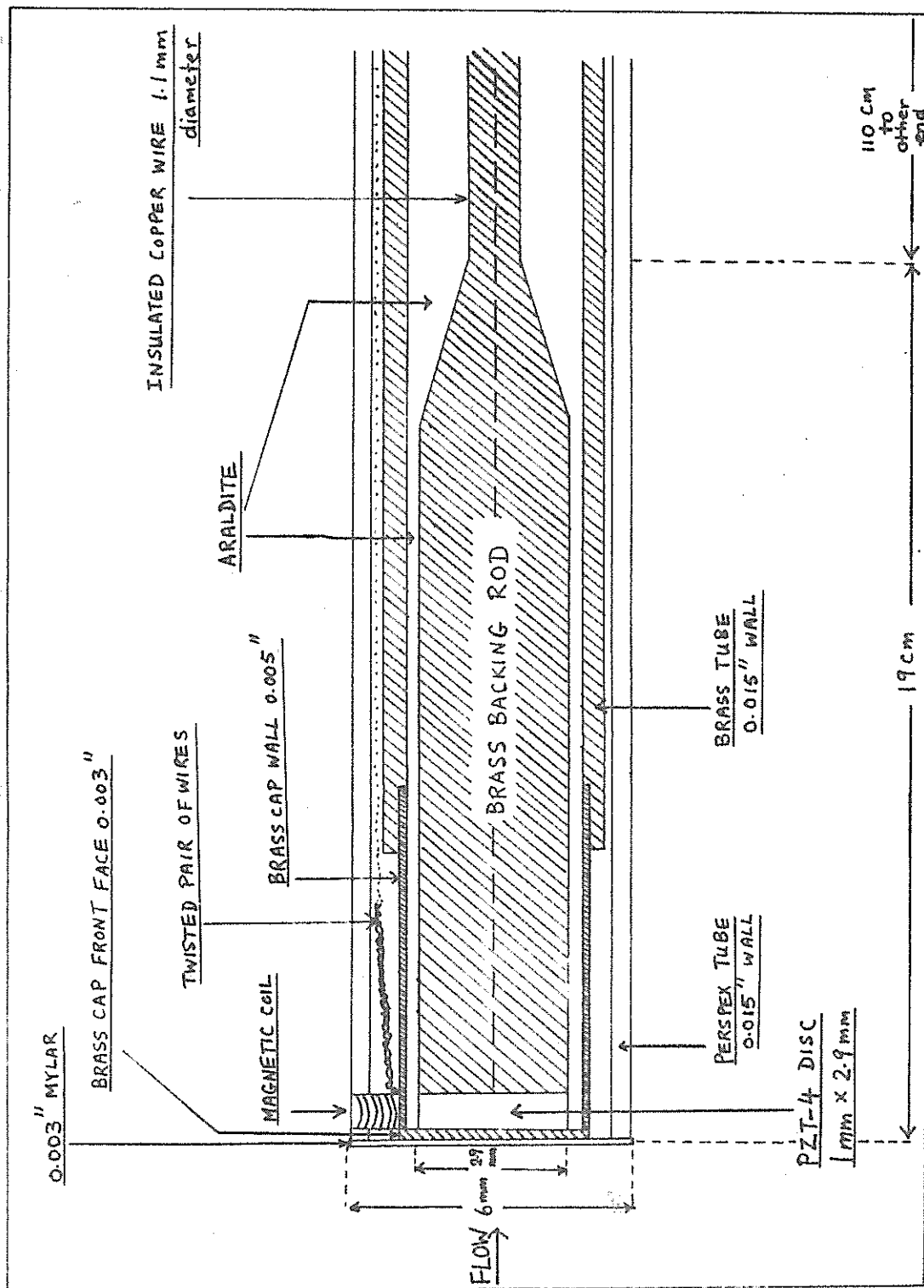


FIG. 3.12 COMBINATION TOTAL PRESSURE AND MAGNETIC PROBE

to correlate vertical ( $z$ ) pressure profile with current sheet tilt. The basic construction of a probe is illustrated in Figure 3.12. The one illustrated is an axial probe of total length 130 cm.

#### 3.3.3.4 Probe construction

The pressure sensing element was a PZT-4 disc, the size of which was chosen as a compromise between the various requirements of fast rise time, sensitivity, small probe area (normal to flow) and reasonable ease of handling. The front electrode face of the crystal was stuck evenly with conducting araldite to the inner face of a brass cap which served as a coaxial return providing efficient shielding against the high frequency triggering noises. This coaxial geometry was continued by the brass tubing (Figure 3.12) which continued along the whole length of the probe emerging in a shielded box with coaxial sockets attached. The other electrode face was stuck onto a brass rod which served as an electrical conductor as well as a backing rod. Brass provided a sufficiently good acoustic match; mismatch reflections being found experimentally to be less than 5 per cent. (This is subject, most critically, to the condition that the joint between

the crystal face and the brass surface is uniform and air free.) The two way transit time of stress waves between the crystal face to the far end of the brass backing rod was 50 microsec, enabling observations to be made within this period without interference from this source; which was further reduced by partially matching the brass rod to a thinner copper wire by way of a tapered transition.

A 0.003 inch thick mylar film was stuck evenly onto the front face of the brass cap. The brass tubing and cap were then enclosed in a plexiglass tubing of 0.5 mm wall thickness, which together with the mylar shield completely insulated the outer conductor of the pressure probe from the flow. A magnetic coil was positioned 1 mm behind the mylar sheet in a cavity drilled into the plexiglass wall and was held in position and insulated by a spot of araldite. The transit time of the stress wave through the mylar and brass cap front was estimated to be 60 nsec.

#### 3.3.3.5 Probe maintenance

The mylar face was unmarked, when examined, after about twenty discharges at 100 Kamp. A thin sooty film was wiped off the mylar surface after about 100

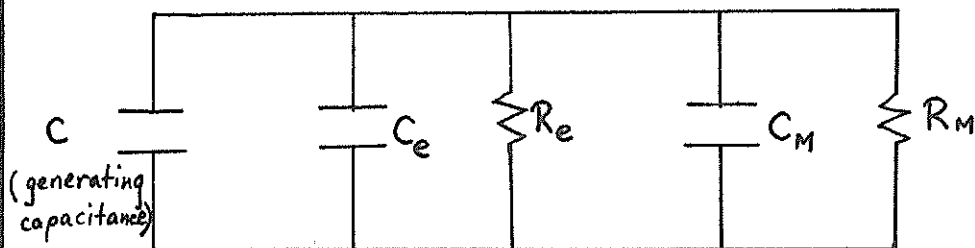


FIG. 3.13 PRESSURE MEASURING CIRCUIT

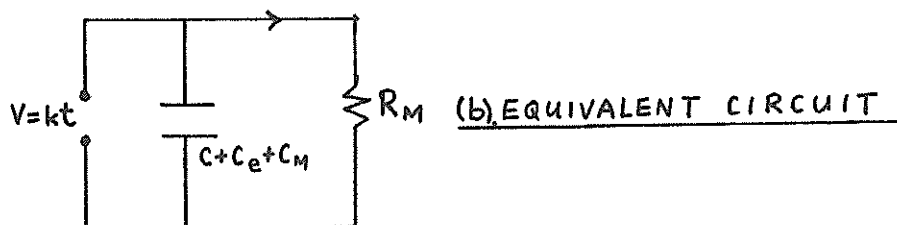
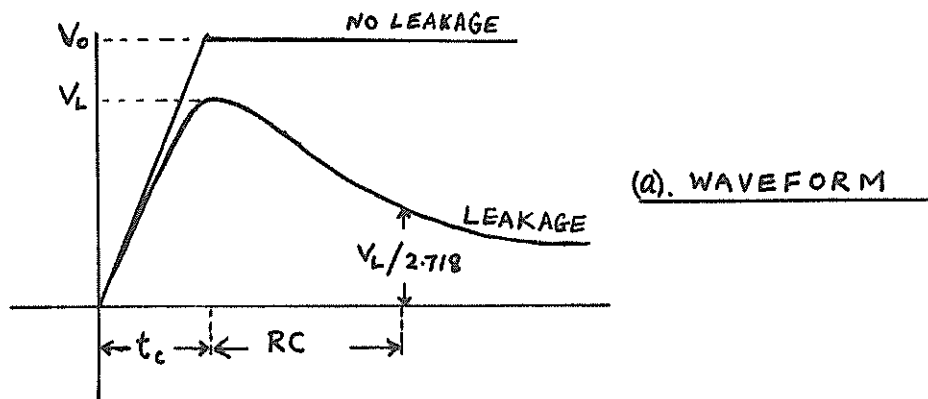


FIG. 3.14 LOW FREQUENCY PROBE CALIBRATION

discharges. Otherwise, the head of the probe did not appear to be affected by discharges (up to 140 Kamp) except for a slight gradual smoothing of the edge of the mylar sheet where it was stuck onto the plexiglass tubing.

### 3.3.3.6 Probe sensitivity

The sensitivity  $S$  of the probe can be considered in the following manner.

$$S_d = F_s t \quad (3-48)$$

where  $S_d$  is the sensitivity of the disc in volts/Newton/m<sup>2</sup>) under no load condition,  $F_s$  is the sensitivity factor supplied by the manufacturer and  $t$  is the thickness of the disc in metres.

When the disc of capacitance  $C$  is positioned in the probe and connected to an oscilloscope of input capacitance  $C_M$  and resistance  $R_M$ , the equivalent circuit is as shown in Figure 3.13 where  $C_e$  is the total capacitance of the transmission system and  $R_e$  is the leakage resistance of the probe and transmission system measured at the oscilloscope end. Since  $C$  is the generating capacitance, the measuring sensitivity  $S$  is then related to the no load sensitivity  $S_d$  by:

$$S = S_d \left( \frac{C}{C + C_e + C_M} \right) \quad , \quad (3-49)$$



under no leakage condition, i.e. when the time of measurement  $\tau_M$  obeys the criterion:

$$\tau_M \ll R_M (C + C_e + C_M) , \quad (3-50)$$

assuming that  $R_e \gg R_M$ .

$C$  and  $C_e$  were both calculated and found consistent with the measured values, and for the axial probe most frequently used (PB-1) with the Tektronix 585 oscilloscope, these constants were:

$$\begin{aligned} C &= 70 \text{ pf} , \\ C_e &= 430 \text{ pf} , \\ C_M &= 15 \text{ pf} , \\ R_M &= 10^6 , \\ \text{and } R_e &= 10^9 . \end{aligned}$$

Thus,

$$\text{Calculated: } S = 0.41 / (10^5 \text{ Newtons/m}^2) \pm 0.04 ,$$

with a RC decay time of 790 microsec. This allowed an observation time of 40 microsec with less than 5 per cent loss of signal amplitude due to RC leakage. The estimated error was based on the low frequency measurement of the capacitances.

### 3.3.3.7 Probe calibration-I

For the calibration of the probes, two methods were used. The first method used a high impedance electrometer to monitor probe output when the probe was subjected to a pressure pulse released from a reservoir (of variable pressure) by means of a mechanical valve with an estimated opening time of  $\frac{1}{2}$  second. The waveform was recorded on an oscilloscope, and indicated leakage, even in the voltage rising part of the waveform, due to the low leakage impedance of the probe. A correction can be made to obtain the no-leakage amplitude  $V_0$  from the observed peak  $V_L$ . This correction is based on the signal risetime  $t_c$  and the RC decay time (Figure 3.14), assuming a linear (with time) pressure rise. The equivalent circuit of Figure 3.13 is reduced to Figure 3.14b. The voltage equation governing this circuit is:

$$i R + \frac{q}{C} - kt = 0 \quad , \quad (3-51a)$$

where  $q$  is the charge. The linear voltage generating term is  $kt$ , so that  $k = \frac{V_0}{t_c}$ . On differentiating (3-51a) and then integrating the resulting differential equation with respect to time, we have, upon re-arranging:

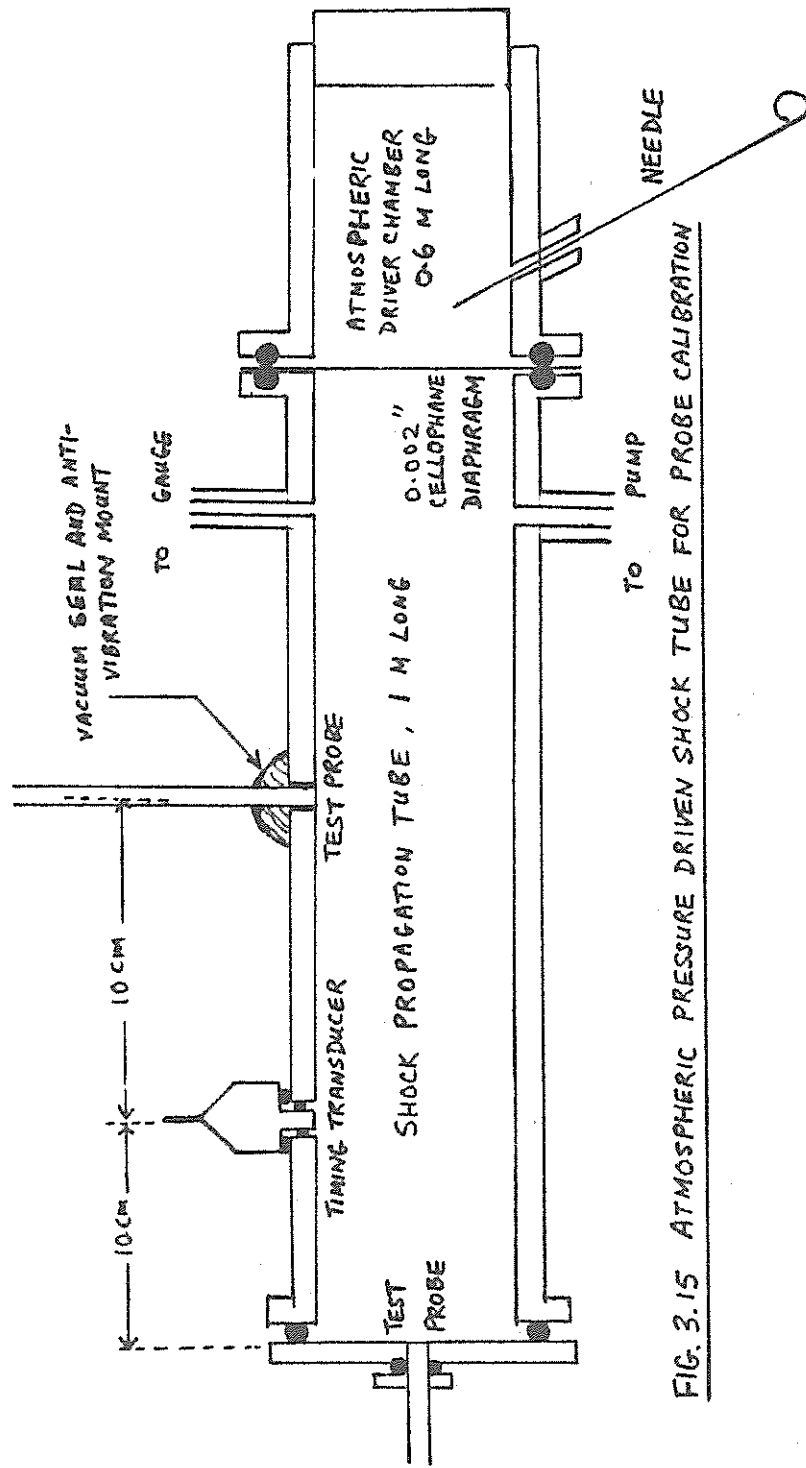


FIG. 3.15 ATMOSPHERIC PRESSURE DRIVEN SHOCK TUBE FOR PROBE CALIBRATION

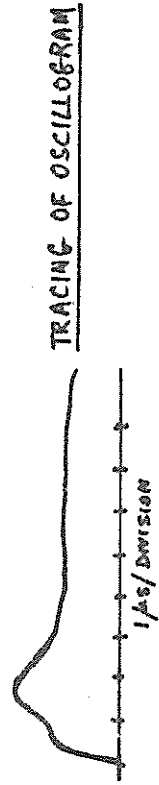


FIG. 3.16 PRESSURE RECORD OF PROBE AT END PORT

$$V_o = V_L \frac{t_c}{RC(1 - e^{-t_c/RC})}, \quad (3-51)$$

which is the desired relationship between  $V_o$  and  $V_L$ .

For PB-1, the calibration was conducted over a pressure range of 0.3 to  $3 \times 10^5$  Newtons/m<sup>2</sup> and gave the following sensitivity of:

Measured:  $S = 0.52V/(10^5 \text{ Newtons/m}^2) \pm 0.05$ .

### 3.3.3.8 Probe calibration-II

A 1 inch (i.d.) by 36 inch long, atmospheric pressure driven, diaphragm controlled shock tube was constructed to provide a known pressure pulse for calibrating the pressure probes. This tube had an end port for monitoring reflected shock pressure and two side ports for shock timing and static pressure measurements (Figure 3.15). The theory and design of diaphragm shock tubes are treated comprehensively by a number of authors including Lukasiewicz<sup>70</sup> and Wright<sup>37</sup>, whilst a discussion of suitable diaphragm materials (found to be critical for the operation of this shock tube) is given in Bradley<sup>71</sup>.

A typical operating point of the tube was  $P_c = 720$  torr,  $P_1 = 20$  torr. ( $P_c$  is the reservoir pressure.)

Using the theory as given, for example, by Wright<sup>37</sup>, we have:

$$\begin{aligned}\frac{P_2}{P_1} &= y = 4.5 & , \\ M &= 2.0 & , \\ &= 2.67 & , \\ P_2 - P_1 &= 0.91 \times 10^4 & , \\ P_r - P_1 &= 3.7 \times 10^4 & , \\ \text{and } P_G - P_1 &= 2.65 \times 10^4 & ,\end{aligned}$$

where  $P_r$  and  $P_G$  are the reflected and total pressures respectively.

At this operating point the Mach number was measured to be  $M2.00 \pm 0.08$ . A typical probe response when facing the flow is shown in Figure 3.16. The pressure rise time across the shock is known to be less than 0.2 microsec which was the 10 to 90 per cent rise time of the steep front of the probe signal. The probe P-B 1 therefore had a risetime of 0.2 microsec for a gas dynamic shock. The hump following the pressure front was the most disturbing feature of the calibration, and has been reported before, e.g., by Rudderlow<sup>68</sup>. The pressure level was taken to be the average over the first 10 microsecond. For P-B 1 the calibration constant was obtained from four measurements each of the static and total pressure rise and is:

Measured:  $S = 0.40V/(10^5 \text{ Newtons/m}^2) \pm 0.07$  .

### 3.3.4 Mach Zehnder Interferometry and high speed photography

A Mach Zehnder interferometer with a 7 inch field of view was used for time resolved studies using the following two methods:

1. Single wavelength interferometry using a Korad 200 MW (max), pockel cell Q switched, ruby laser as a light source. Using this method a 15 nsec exposure was obtained, of the region between the shock tube electrodes, for 18 cm (axial length) of the shock tube.
2. Channelled spectra interferometry using an exploding wire to provide a long duration (50 microsec) continuum light source, with the interferometric output viewed through a spectrometer so that a channelled spectra was displayed over a spectral range of 4500 Å to 5600 Å. An image converter streak camera (normally operated with a 20 microsec sweep) provided a time resolution of 0.1 microsec.

In other studies, the STL image converter camera was used by itself either in the streak or framing mode for studying the self luminosity of the plasma.

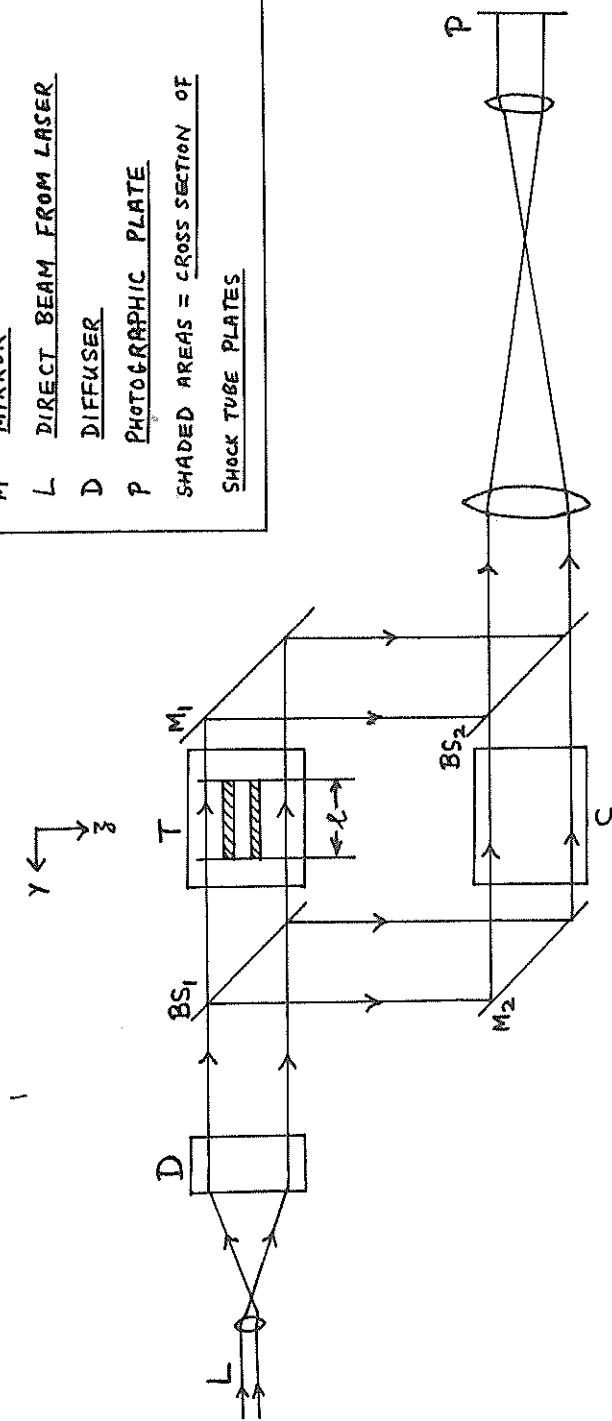


FIG. 3.17 OPTICAL SET UP FOR SINGLE WAVELENGTH M-Z INTERFEROMETRY

### 3.3.4.1 Refractivity of the plasma species

The two light paths of the Mach Zehnder  $BS_1-M_1-BS_2$  and  $BS_1-M_2-BS_2$  are illustrated in Figure 3.17, with the two mirrors and the two beam splitters BS. Also shown are the compensation chamber C and the test chamber T. Through T ran the shock tube whose width  $w$  is indicated. With the arrival of a shock wave the optical path of that path of the beam passing through the shock wave was changed. This produced a fringe shift at the recombined beam. The change in optical path was:

$$\delta = (\mu_r - 1) L \quad , \quad (3-52)$$

where  $\mu_r$  is the refractive index of the gas and  $L$  the path length of the gas through which the beam passed. For electrons<sup>72</sup>:

$$(\mu_r - 1) = -4.49 \times 10^{-22} \lambda^2 N_e \quad , \quad (3-53)$$

where  $\lambda$  is in  $\text{\AA}$  and  $N_e$  in electrons  $\text{cm}^{-3}$ .

For atoms and ions, over the visible spectrum  $(\mu_r - 1)$  can be represented by a one term Cauchy formula<sup>72</sup>:

$$(\mu_r - 1) = A \left( 1 + \frac{B}{\lambda^2} \right) N \quad , \quad (3-54)$$



where A and B are Cauchy coefficients, N the particle density in particles  $\text{cm}^{-3}$  and  $\lambda$  in Å. Values of A and B are tabulated in Table 3.1.

Table 3.1

Species	A	B	Source
ArI	$1.04 \times 10^{-15}$	$5.6 \times 10^5$	Allen <sup>73</sup>
ArII	$0.71 \times 10^{-15}$	$5.6 \times 10^5$	Alpher and White <sup>72</sup>
He I	$1.3 \times 10^{-16}$	$2.3 \times 10^5$	Allen <sup>73</sup>
HeII	$2.7 \times 10^{-17}$	$2.3 \times 10^5$	Van Vleck <sup>74</sup>

The value of A for the singly ionized helium HeII is obtained from the ratio of the molar susceptibilities  $\kappa$  of HeI and HeII given by Van Vleck<sup>74</sup>:

$$\frac{\kappa_{\text{HeI}}}{\kappa_{\text{HeII}}} = 0.207 \quad .$$

Since  $(\mu_r - 1)$  is proportional to the magnetic susceptibility<sup>72</sup>, the value of  $(\mu_r - 1)$  for HeII is then obtained from the value of  $(\mu_r - 1)$  for HeI.

For plasmas of densities of interest to our experiments, the total  $(\mu_r - 1)$  is the sum of the individual contributions, i.e.:

$$(\mu_r - 1)_T = \sum (\mu_r - 1) \quad , \quad (3-55)$$

where the summation is over all the species contributing.

### 3.3.4.2 Fringe shift estimates

For a monochromatic beam of wavelength  $\lambda$  <sup>o</sup> A, the fringe shift  $\delta'$  due to a gas of  $(\mu_r - 1)$  occupying the path length L is:

$$\delta' = L (\mu_r - 1) / \lambda \quad . \quad (3-56)$$

At 6944 <sup>o</sup> A (wavelength of ruby laser output), with L = 20 cm, the particle density required to produce  $\frac{1}{10}$  fringe shift can be obtained using (3-53) for the electrons, and (3-54) for the neutrals and ions.

Putting  $\delta' = \frac{1}{10}$  in equation (3-56), we have:

$$N_e = 1.6 \times 10^{15} / (0.1 \text{ fringe shift}) \quad ,$$

$$N_{ArI} = 3.34 \times 10^{16} / (0.1 \text{ fringe shift}) \quad ,$$

$$N_{ArII} = 4.85 \times 10^{16} / (0.1 \text{ fringe shift}) \quad ,$$

$$N_{HeI} = 2.68 \times 10^{17} / (0.1 \text{ fringe shift}) \quad ,$$

and  $N_{HeII} = 1.29 \times 10^{18} / (0.1 \text{ fringe shift}) \quad .$

If we take  $\frac{1}{10}$  of a fringe shift as the smallest shift measurable, then each of these figures represents

the smallest density detectable in the corresponding single species gas.

### 3.3.4.3 Single wavelength interferometry

Equations (3-53) and (3-54) show that, in an ionized gas, the fringe shift due to the electrons is opposite to that due to the heavy particles. Thus, in argon at  $6940 \text{ \AA}$ , at 4.8 per cent ionization, the fringe shift due to the electrons (in the direction of decreasing refractivity) equals the fringe shift due to the ArI and ArII; and the net fringe shift is zero. In helium, this crossover point occurs at 0.6 per cent ionization. The level of ionization in our tube is higher than these figures at most of the operating points; and at these points, shifts in the direction of decreasing refractivity are expected, giving information on the electron density profile only. The Mach Zehnder was operated in two modes:

1. Infinite fringe: This mode was operated by rotating the mirrors in such a manner as to increase the fringe spacing until a single fringe filled the field of view. The fringes that appeared, when the flow arrived, were then lines of constant density<sup>69a</sup>. The Mach Zehnder is extremely sensitive to slight

vibrations and temperature changes, and the fringe pattern is subject to slight drifts even over a period of minutes. In the infinite fringe mode such slight drifts are not permissible and careful adjustments of the mirrors had often to be made just before the shot.

2. Finite fringe pattern: This mode was obtained by rotating the mirrors until a system of straight fringes were positioned parallel to the shock tube axis. Usually, about ten to twenty fringes were positioned between the shock tube plates. Generally, the more fringes used, the greater is the spatial resolution, but the less is the accuracy in obtaining the fringe shift at each of these fringes.

#### 3.3.4.4 Channelled spectra interferometry

From (3-52) to (3-54) and Table 3.1, we can express the change in optical path due to a multiply ionized gas as:

$$\delta_r = C \lambda_r^2 N_e + A \left( 1 + \frac{B}{\lambda_r^2} \right) (N_{AI} + d N_{AII} + e N_{AIII} \dots) \quad , \quad (3-56)$$

where C, A, B, d, e etc. are constants. If two wavelengths  $\lambda_1$  and  $\lambda_2$  are used, a measurement of  $\delta_1$

and  $\delta_2$  enables the two unknowns  $N_e$  and  $(N_{AI} + d N_{AII} + e N_{AIII} \dots)$  to be found by solving the two resulting simultaneous equations<sup>72</sup>. Where the electron contribution to  $\delta$  is much larger than the heavy particle contribution, the error involved in determining the value of  $(N_{AI} + d N_{AII} + e N_{AIII} \dots)$  is large.

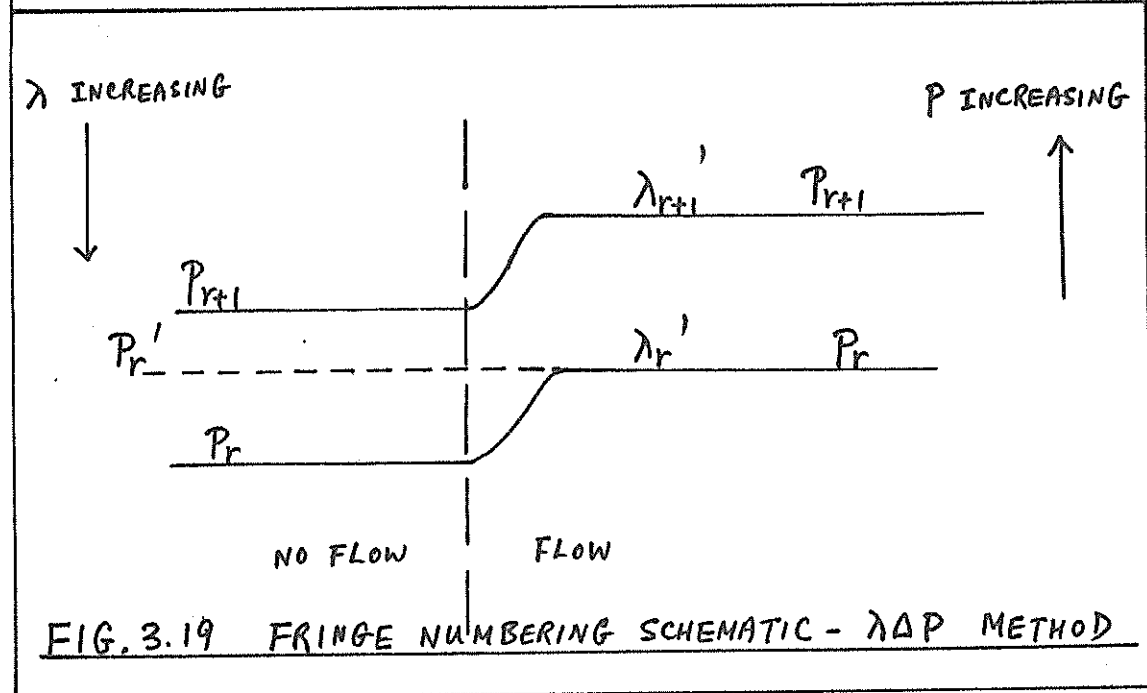
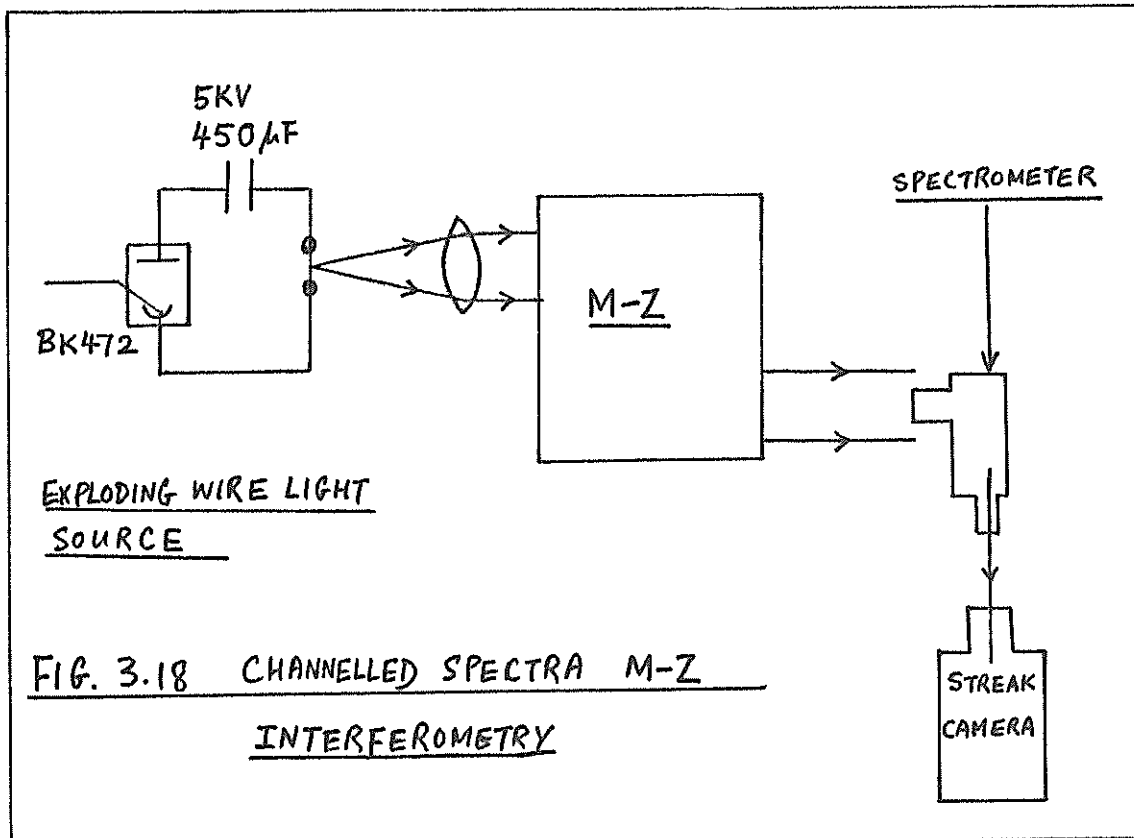
Sandeman<sup>75</sup> has suggested that, by imaging the shock tube onto the slit of a spectrometer and using a continuum light source, the interferometer can be adjusted to a fixed path difference  $\delta_0$ , to produce a channelled spectra; that is, dark fringes parallel to the slit, where

$$P\lambda = \delta_0, \quad P = \text{a half integer.}$$

When the shock passes the slit of the spectrometer, the channels are changed in wavelength position by

$$\Delta\lambda = \frac{\delta}{P}, \quad \text{where the } \delta \text{ is as given in (3-56).}$$

By using as large a number  $m$ , of channels as is consistent with the resolution of the spectrometer, a statistical analysis of the resulting  $m$  equations can be used to reduce the uncertainty in the determination of the electron and heavy particle densities. Another potential advantage of the method is that, if the



Cauchy coefficients of the  $N_{AI}$ ,  $N_{AII}$ ,  $N_{AIII}$ , etc. are separately known, instead of being used in the approximate coupled form of (3-56), then the unknowns  $N_{AI}$ ,  $N_{AII}$ ,  $N_{AIII}$ , etc. can be treated as variables, independent of one another. In that case, solution of the system of channel equations will enable the determination of each of the particle density. Used in the form of (3-56), however, the heavy particle densities cannot be separated. For a three component system consisting of electrons, atoms and first ionized ions, this is no disadvantage, since, with  $N_e$  calculated,  $N_{AII}$  can be equated to  $N_e$ , and hence  $N_{AI}$  found from the calculated value of  $(N_{AI} + d N_{AII})$ .

The experimental arrangement is shown in Figure 3.18. A small x-z section of the shock tube (1mm x 1mm) was imaged onto the entrance slit of a constant deviation spectrometer and a series of channels is produced on the spectrum, by introducing a path difference between the reference and test beams. This image was photographed on HP4 film through an image converter; the image being streaked in the direction of the channels to provide time resolution. Measurements of the no flow and the flow wavelengths were used to compute the optical path difference,  $\delta$ , due to the gas flow.

### 3.3.4.4.1 The $P\Delta\lambda$ path difference

The dark channels are numbered from the long wavelength end, with the fringe having the longest wavelength numbered as  $P_1$ . Then, if  $d$  is the difference in the optical paths of the two beams of the Mach Zehnder, we can write down the following interferometric relations:

$$P_r \lambda_r = d \quad \text{where} \quad P_r = P_1 + \frac{r}{2} \quad (3-57)$$

$$\text{and} \quad r = 1, 2, \dots, (n-1), n.$$

Incrementing  $P_r$  by half integers means that we are considering both the bright and dark channels. When the flow arrives, the path difference between the two arms changes by an amount  $\delta$ , due to the gas refractivity, so that for a given  $P_r$ , the wavelength  $\lambda_r$  is now  $\lambda_r'$ , and

$$P_r \lambda_r' = d + \delta \quad . \quad (3-58)$$

Subtracting the  $r$ th equation of (3-57) from the  $r$ th equation of (3-58), we have the system of  $n$  equations:

$$P_r \Delta\lambda_r = \delta \quad , \quad (3-59)$$

where  $\Delta_r = \lambda_r' - \lambda_r$ ; and  $r$  goes from 1 to  $n$ .

It must be noted that the optical path difference  $d$  between the two arms of the Mach Zehnder interferometer has been taken as a constant for the two wavelengths



$\lambda_r$  and  $\lambda_r'$ ; so that in the subtraction,  $d$  is eliminated. This is not accurate because the lengths of dispersive elements (e.g. glass) in the two beams (excluding the test gas) are not equal, so that  $d$  will be partially dispersive. Thus, (3-59) should have another term on the RHS, this being the difference in  $d(\lambda_r)$  and  $d(\lambda_r')$ , where  $d$  is wavelength dependent. This expression is not suitable for computation purposes since the function  $d(\lambda)$  is not easily determined.

#### 3.3.4.4.2 The $\lambda\Delta P$ path difference

To remove the function  $d(\lambda)$  from the equation, it is necessary to consider the fringe shift from a constant wavelength point of view<sup>75</sup>. Figure 3.19 illustrates the method of numbering the fringes. Consider a flow fringe of wavelength  $\lambda_r'$  and half integer fringe order  $P_r$ . Before the flow arrives, this wavelength  $\lambda_r'$  does not correspond to a half integer  $P$  number but to a number  $P_r'$ , lying, in the example illustrated, between half integer values  $P_r$  and  $P_{r+1}$ . The  $P$ - $\lambda$  relationship can now be written as:

$$\text{Flow} \quad P_r \lambda_r' = \delta + d(\lambda_r') ,$$

$$\text{No flow} \quad P_r' \lambda_r' = d(\lambda_r') ,$$

$$\text{and subtraction gives: } \lambda_r' \Delta P_r = \delta ,$$

$$\text{exactly; where} \quad \Delta P_r = P_r - P_r' . \quad (3-60)$$

Equations (3-60) and (3-56), together with the constants contained in (3-53) and Table 3.1, can now be used to compute the particle densities. For a three component argon system we can write:

$$\lambda_r' \Delta P_r = -8.98 \times 10^{-21} (\lambda_r')^2 N_e + 2.08 \times 10^{-14} \times$$

$$\left[ 1 + \frac{5.6 \times 10^5}{(\lambda_r')^2} \right] [N_{ArI} + 0.69 N_{ArII}] , \quad (3-61)$$

where  $n$  maxima and minima in the fringe system are used in the computation so that  $r$  goes from 1 to  $n$ . The two unknowns  $N_e$  and  $(N_{ArI} + 0.69 N_{ArII})$  can now be solved from this system of  $n$  equations, using a best fit method. With the assumption that  $N_e = N_{ArII}$ , the value of  $N_{ArI}$  can then be computed from the value of  $(N_{ArI} + 0.69 N_{ArII})$ . Statistically, it is advantageous to make  $n$  as large as possible, but practically, the larger  $n$  is, the smaller is each fringe spacing and the bigger the relative error in the measurement of the

corresponding fringe shift. The optimum number of fringes to be used is given by the following equation<sup>75</sup>:

$$n_{\text{opt}} = (\lambda_i - \lambda_j) \frac{\epsilon_1}{\epsilon_2} \quad (3-61a)$$

where  $\lambda_i$  and  $\lambda_j$  are the limits of the spectral range of the spectrometer,  $\epsilon_1$  is the error in estimating the channel centre relative to the channel spacing and  $\epsilon_2$  is the absolute error in converting the channel centres to wavelengths. For these experiments, taking account of the loss of resolution due to the image converter camera, we estimate

$$\epsilon_1 = \frac{1}{10} \quad ,$$

$$\epsilon_2 = 5 \overset{\circ}{\text{A}} \quad ,$$

and with  $\lambda_i - \lambda_j = 1100 \overset{\circ}{\text{A}}$ , the calculated value of  $n_{\text{opt}}$  is  $n_{\text{opt}} = 22$ .

The optimum number of full fringes is 22, or the optimum number of half fringes is 44.

For the measurement of wavelengths, a Hg-Cd-Zn reference spectrum was exposed on the start and the centre of the streak before the shot. A fibre-optic was arranged to image a tiny spot of light onto one end of the reference spectrum. This spot of light was

'tapped' from the exploding wire luminosity and provided a datum line which acted as an extension to the reference spectrum over the entire length of the streak.

The resulting interferograms were measured on a Joyce Loebel recording microdensitometer. Suitably spaced scans were made in order to follow the time profile of the fringe shifts. The viewing slit of the microdensitometer was adjusted to give an equivalent time resolution of 0.1 microsec, the interferogram scale being 50 mm = 20 microsec.

#### 3.3.4.4.3 Computer analysis of the Interferograms

The solution of the  $n$  equations of (3-61), where typically  $n = 35$ , was performed on an IBM 360 computer. The input to the programme included the following measurements made on the densitometric traces:

1. The distances ( $x$ ) of the reference spectrum lines from the datum line,
2. the distances of the  $n$  no flow fringes from the datum line, and
3. the distances of the  $n$  flow fringes (at a fixed time) from the datum line.

The steps performed by the programme are summarized:

1. The distances of the flow and no flow fringes are converted to wavelengths using an Aitken interpolation method<sup>76</sup>, with the reference spectrum providing the  $\lambda$ -x function.
2. The value of  $P_1$  is obtained from the n no flow equations given in (3-57) using the least square subroutine LLSQ<sup>79</sup>. The arrangement of (3-57) in a suitable form for input into LLSQ is the same as that discussed in the next step.
3. Having calculated  $P_1$ , the set of equations (3-61) can now be solved for the best fit values of the densities. The equations are written in the following form:

$$a_{1r}N_e + a_{2r}N_A = b_r \quad (3-62)$$

where the coefficients  $a_{1r}$ ,  $a_{2r}$  form a  $n \times 2$  matrix A, and the coefficients  $b_r$  form a  $n$  dimension column vector B. This is then fed into a standard matrix least square subroutine LLSQ which effectively calculates the value of  $N_e$  and  $N_A$  for which the summation

$$\sum_{r=1}^{r=n} (a_{1r} N_e + a_{2r} N_A - b_r)^2$$

is a minimum.

4. An estimate of the probable errors in the densities is made from the scatter in the measurements of the coefficients.

We note from (3-61) that the coefficients  $a_{1r}$ ,  $a_{2r}$ , and  $b_r$  all depend for their accuracy on the measurement of  $\lambda$ . In particular,  $a_{2r}$  is almost a constant,  $a_{1r}$  is proportional to  $\lambda^2$ , and  $b_r$  is proportional to  $\lambda \Delta P$  which is approximately proportional to  $\lambda \Delta \lambda$ . The fractional errors of these terms due to the error  $\delta \lambda$  in the measurement of  $\lambda$  are of the following magnitudes:

$$\begin{aligned} \frac{\delta(a_{2r})}{a_{2r}} &= \text{negligible} , \\ \frac{\delta(a_{1r})}{a_{1r}} &\sim \frac{2(\delta \lambda_r)}{\lambda_r} , \\ \frac{\delta b_r}{b_r} &\sim \frac{\delta(\Delta \lambda_r)}{\Delta \lambda_r} \sim \frac{2\delta \lambda_r}{\lambda_{r'} - \lambda_r} \sim 100 \left( \frac{2\delta \lambda_r}{\lambda_r} \right) . \quad (3-63) \end{aligned}$$

Equation (3-62) is now written as<sup>77</sup>:

$$\begin{aligned} (a_{1r} \pm \delta a_{1r}) (N_e \pm \delta N_e) + (a_{2r} \pm \delta a_{2r}) \\ (N_A \pm \delta N_A) = b_r \pm \delta b_r ; \end{aligned}$$

$$\begin{aligned} \text{i.e. } \pm a_{1r} \delta N_e \pm N_e \delta a_{1r} \pm a_{2r} \delta N_A \pm N_A \delta a_{2r} \\ = \pm \delta b_r . \end{aligned}$$

Dividing by  $b_r$ , we get:

$$\begin{aligned} & \pm \frac{a_{1r} \delta N_e}{b_r} \pm \frac{N_e \delta a_{1r}}{a_{1r} N_e} \pm \frac{a_{2r} \delta N_A}{b_r} \pm \frac{N_A \delta a_{2r}}{b_r} \\ & = \pm \frac{\delta b_r}{b_r} \quad , \end{aligned} \quad (3-64)$$

for the case where  $|a_{1r} N_e| \gg |a_{2r} N_A|$ .

From (3-63) we note that the second and fourth term of the LHS of (3-64) are negligible compared with the RHS. The error equation reduces to:

$$\pm a_{1r} \delta N_e \pm a_{2r} \delta N_A = \pm \delta b_r \quad ,$$

which we can write in the 'most probable' form<sup>77</sup> as:

$$(a_{1r} \delta N_e)^2 + (a_{2r} \delta N_A)^2 = (\delta b_r)^2 \quad . \quad (3-65)$$

For the estimation of  $\delta N_e$  and  $\delta N_A$  we define  $\delta b_r$  as:

$$\delta b_r = B_r - b_r \quad \text{where}$$

$$B_r = a_{1r} N_e + a_{2r} N_A \quad , \quad (3-66)$$

and the values of  $N_e$  and  $N_A$  are the ones calculated from the least square method as described in step 3.

With the coefficients of the  $n$  equations of (3-65)

thus defined, the least square method is applied to

(3-65) for estimating the most probable errors of  $N_e$

and  $N_A$ . We note that these estimated errors relate

to the internal consistency or precision<sup>77</sup> of the

measurements on the  $n$  fringes, independently of the consideration of instrumental accuracy.



## CHAPTER 4

### EXPERIMENTAL RESULTS

#### 4.1 Velocity measurements

It was desirable to record the shock velocity for every run since there was a 5 per cent scatter (experimentally measured) in shock velocity corresponding to any operating point. This was usually done by recording the pressure pulse on an oscilloscope triggered by a pulse whose position in time relative to the start of the current discharge was known accurately. Where the shock front carried current, the velocity could also be measured from the record of magnetic probe output. Streak photographs were particularly useful for the measurement of fairly constant velocities provided the pressure front could be identified from the various other luminosity features due to precursor light fronts and current sheets. (Precursor light fronts are here referred to as light fronts not detected by the pressure probe and carrying little or no current.)

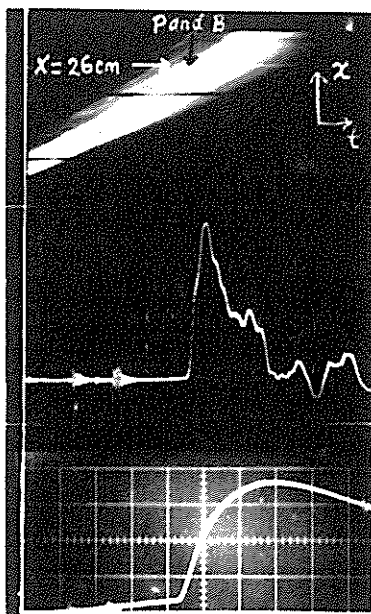


Fig.4.1 Comparison of Streak(S), Pressure(P) and Magnetic Field(B) Signals, 0.1 torr Ar,  $B_1=0$ , 5KV.

Probe position:  $x=26$  cm.

All horizontal axes:  $2.0 \mu\text{sec/cm}$  (1 large division of graticule = 1 cm).

Top: Streak photograph, black markers are 10 cm apart.

Mid: Pressure probe output,  $(1.3 \times 10^5 \text{ N/m}^2)/\text{cm}$ .

Bot: Magnetic probe output, 1.36 KG/cm.

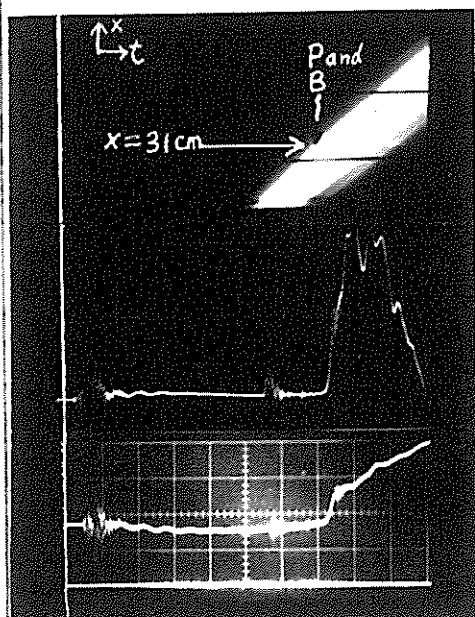


Fig.4.2 Comparison of S,P and B signals, 0.1 torr Ar,  $B_1=2.5\text{KG}$ , 5 KV.

Probe position:  $x=31$  cm.

All horizontal axes:  $2.0 \mu\text{sec/cm}$ .

Top: Streak photograph, black markers are 10 cm apart.

Mid: Pressure probe output,  $(1.3 \times 10^5 \text{ N/m}^2)/\text{cm}$ .

Bot: Magnetic probe output, 1.36 KG/cm (bias field requires correction factor).

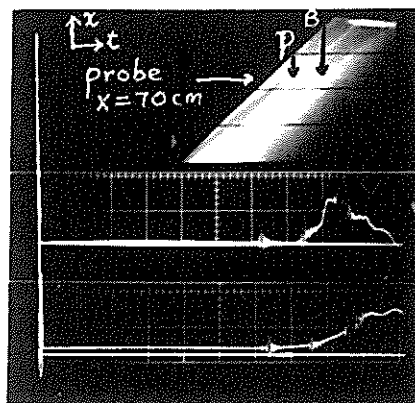


Fig.4.3 S, P and B signals,  
0.25 torr He,  $B_1=0$ , 5KV.

Top: Streak photograph, black markers are 5 cm apart.

Mid: Pressure probe output,  
 $(1.3 \times 10^5 \text{ N/m}^2)/\text{cm}$ .

Bot: Magnetic probe output,  
 $1.36 \text{ KG/cm}$ .

All horizontal axes:  $2.0 \mu\text{sec/cm}$ .

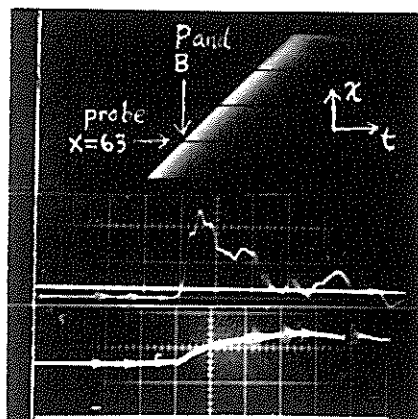


Fig.4.4 S,P and B signals,  
0.25 torr He,  $B_1=2.5 \text{ KG}$ , 5KV.

All horizontal axes:  $2.0 \mu\text{sec/cm}$ .

Top: Streak photograph, black markers are 5 cm apart.

Mid: Pressure probe output,  
 $(1.3 \times 10^5 \text{ N/m}^2)/\text{cm}$ .

Bot: Magnetic probe output,  
 $1.36 \text{ KG/cm}$ .

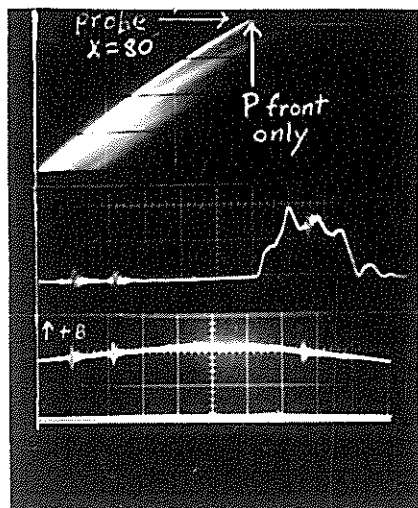


Fig.4.5 S, P and B signals,  
0.1 torr Ar,  $B_1=2.5 \text{ KG}$ , 5KV.

All horizontal axes:  $2.0 \mu\text{sec/cm}$ .

Top: Streak photograph, black markers are 5 cm apart.

Mid: Pressure probe output,  
 $(1.3 \times 10^5 \text{ N/m}^2)/\text{cm}$ .

Bot: Magnetic probe output,  
 $1.36 \text{ KG/cm}$ .

#### 4.1.1 Streak photographs

Streak and framing photographs were taken for a variety of operating conditions, and at different distances down the shock tube. Simultaneously with each photograph, records of the magnetic and pressure probe outputs, time synchronised with the photograph, were obtained. These photographs showed the following features:

1. Precursor luminosity in argon, with no bias field, exhibited filamentary structure, with no definite front, as shown in Figure 4.1. With a bias field, the precursor luminosity either disappeared, or became uniform in appearance, with a definite front (Figure 4.2).
2. The precursor luminosity in helium, with no bias field, had a clearly defined front (Figure 4.3), which was dramatically eliminated when a bias field of 2.5 KG was applied (Figure 4.4).
3. Where the current sheet was well formed (magnetic and pressure probes at  $x = 26$  cm), a bright streak\*, (1.5 cm wide in Figure 4.1 and 0.5 cm wide in Figure 4.2) of fairly constant width, carried most of the current, as can be seen by a comparison between the streak photographs and the magnetic coil outputs. In addition

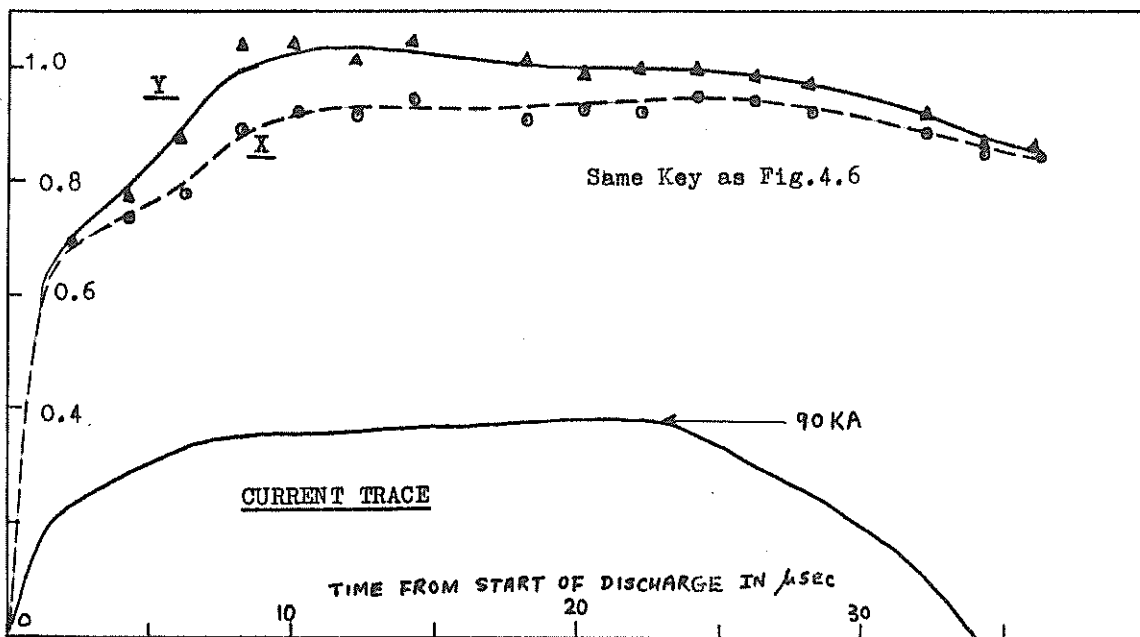
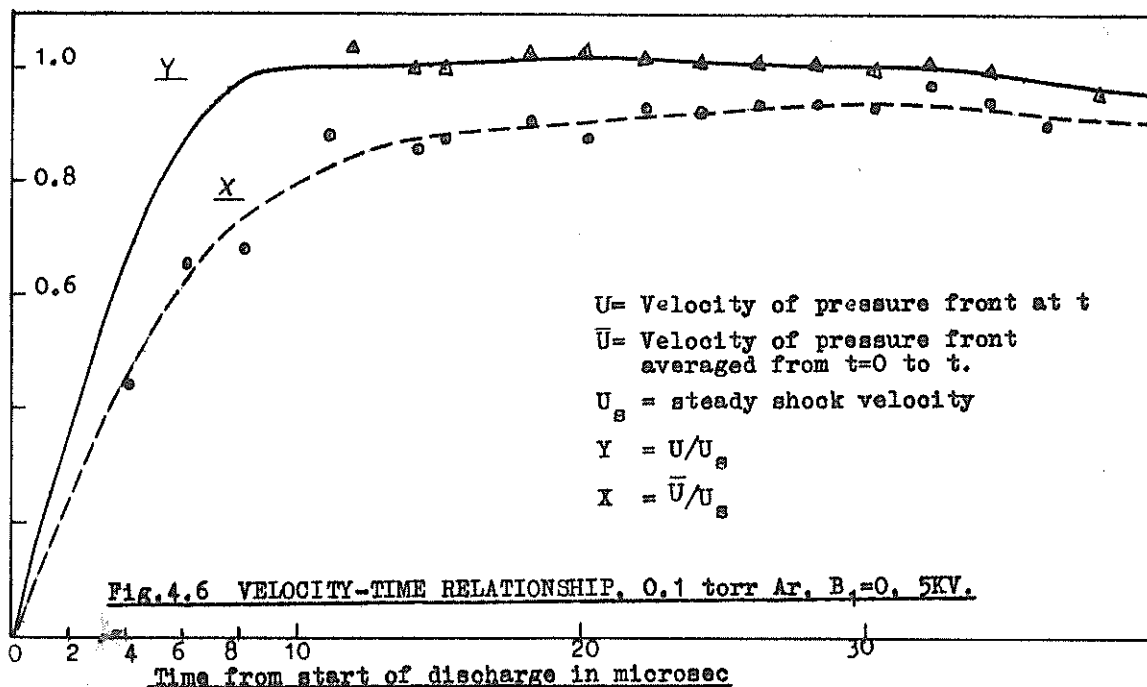
\* The bright, narrow streaks of Figs. 4.1 and 4.2 are clearly distinguishable in the polaroid originals, but have been lost in the reproduction. They extend all along the luminous fronts, and their locations are indicated by the black lines.

Figure 4.2 shows a second current region, 12 cm wide. On the streak photograph the first narrow bright streak correlates with the sharp current jump indicated by the magnetic coil, and the second broader luminous region correlates with the broad region of current increase following the first sharp current jump.

4. In Figure 4.1 and 4.2, the pressure fronts coincide with the regions of maximum current density and no separate feature can be distinguished on the streak photographs. Where the pressure front separates from the main current sheet as in Figure 4.3 and Figure 4.5 (probes at  $x = 70$  cm and  $x = 80$  cm respectively) the pressure front stands out clearly on the streak photograph as a thin line, with the current sheet as a more diffused and broad region starting several cm behind. In the case shown in Figure 4.5, the current density flowing behind the pressure pulse was below the measurable level of approximately 5 KA/metre on reaching  $x = 80$  cm, where the probe measurements were made.

#### 4.1.2 The velocity-time relationship

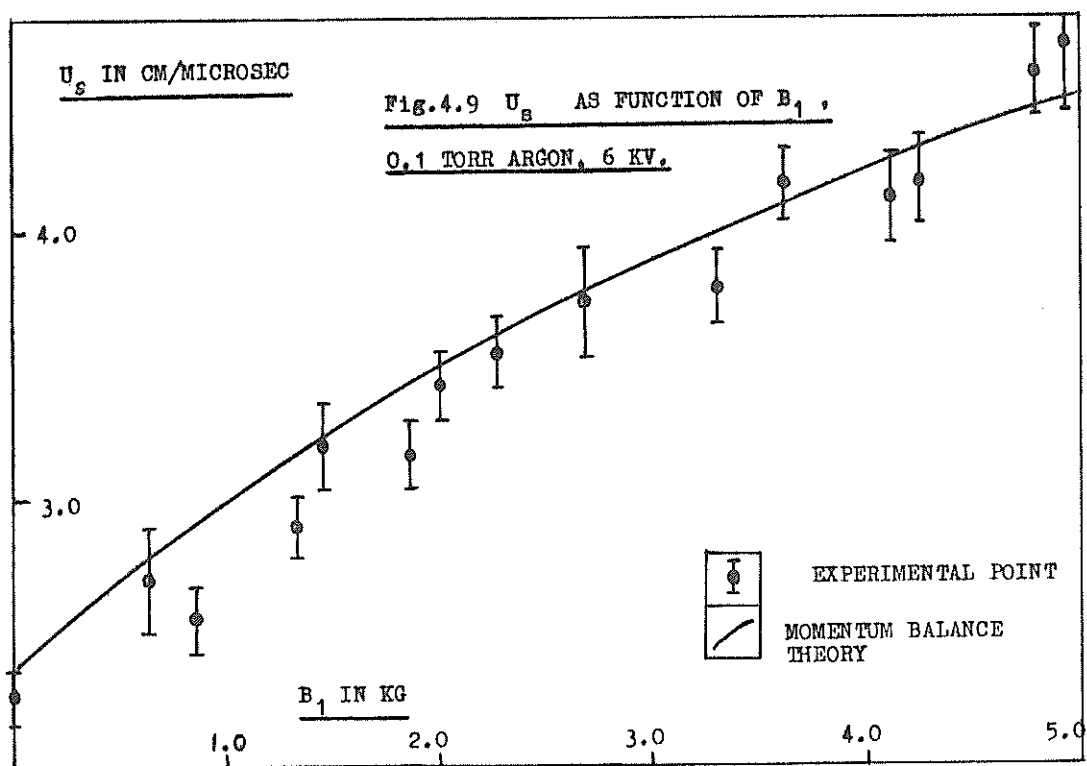
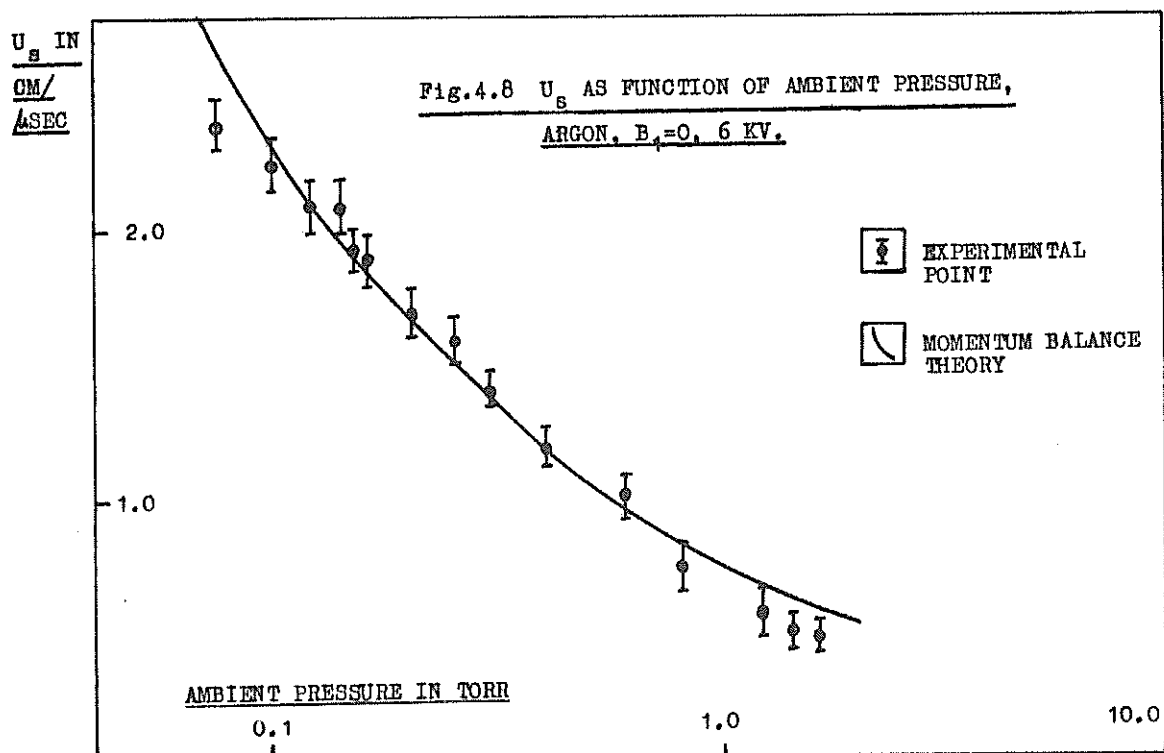
With these distinctions of the various luminosity features noted, streak photographs were confidently used for velocity measurements, complementary to



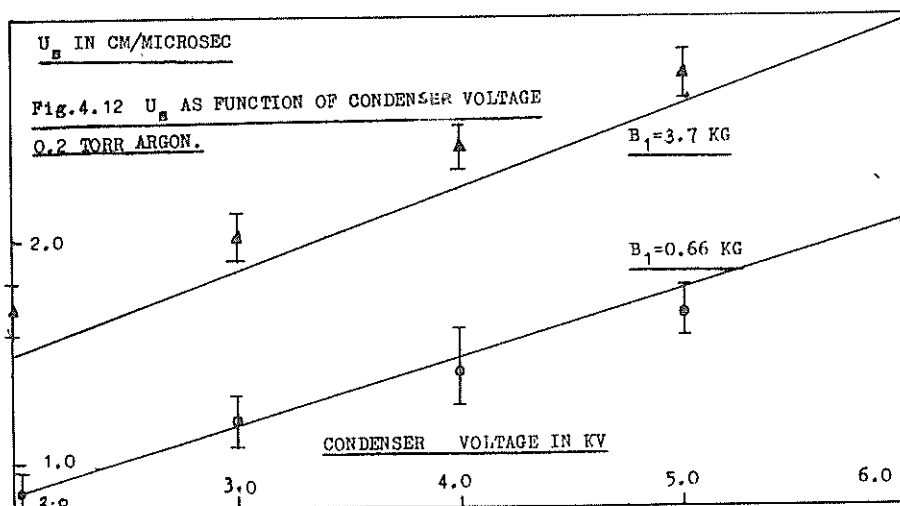
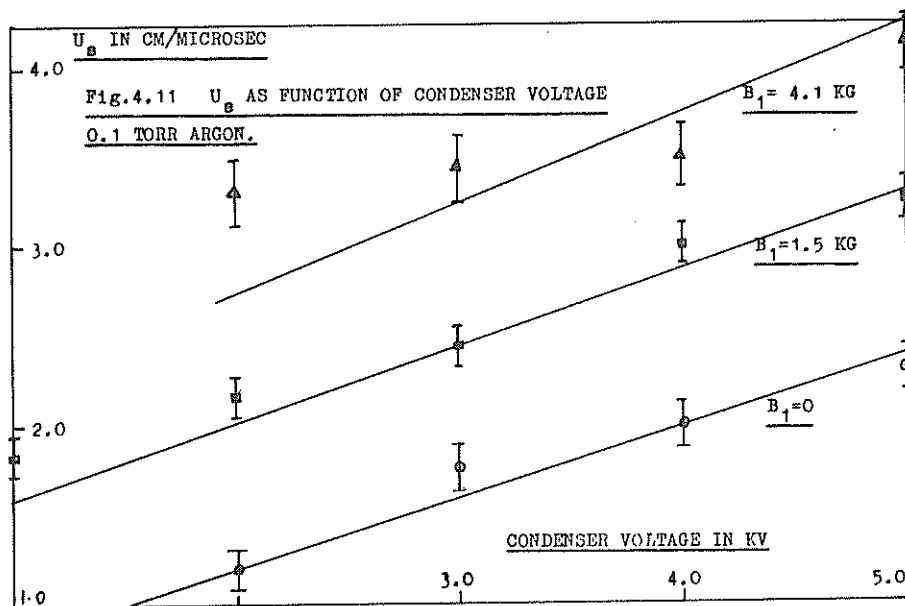
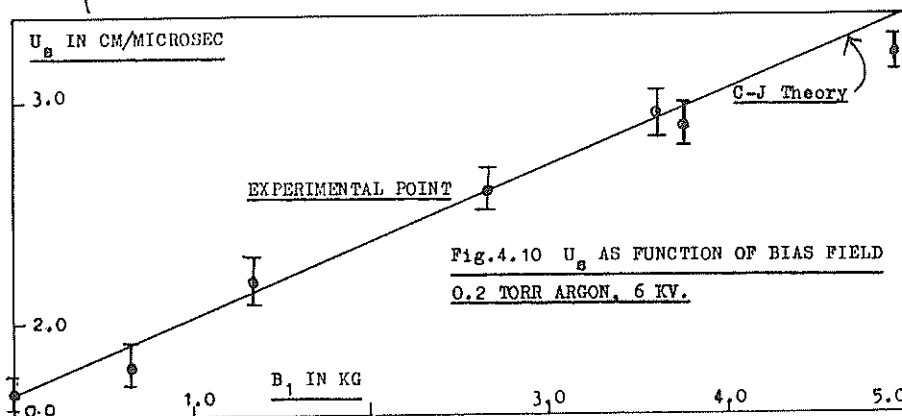
**Fig.4.7 VELOCITY-TIME RELATIONSHIP, 0.1 torr Ar,  $B_1=2.5$  KG, 5 KV.**

pressure probe measurements. Examples of the pressure front velocity versus time relationship are shown on Figure 4.6 and Figure 4.7. We note that the region of constant velocity lasted almost throughout the whole of the period of current decrease, when the bias field was zero. With a bias field the velocity began to drop at the same time approximately as the current began to drop.

In most of the shots during which Mach Zehnder interferometer measurements were made, the velocity monitored was the average velocity. This was obtained by dividing the distance from the knife edge to the probe, by the time between arrival of the pressure front at the probe and the start of the current flow. A correction factor was required to convert this average velocity to the constant shock velocity or to the actual velocity at the time of arrival, if this time was outside the constant velocity period. This correction factor was obtained from data such as shown in Figure 4.6 and Figure 4.7, and the error introduced in the use of the method is estimated as 2 per cent, which is below the experimental scatter of the shock velocity.







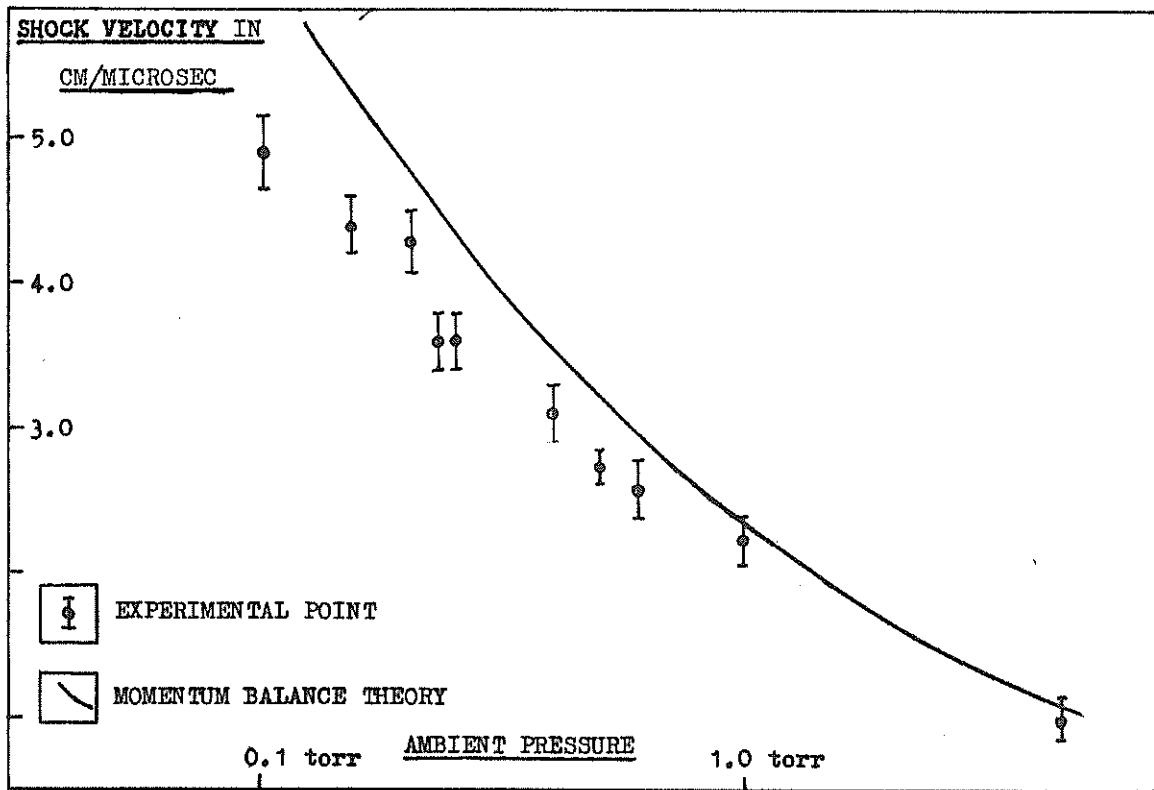


Fig.4.13 SHOCK VELOCITY AS FUNCTION OF FILLING PRESSURE, He,  $B_1=0$ , 6 KV.

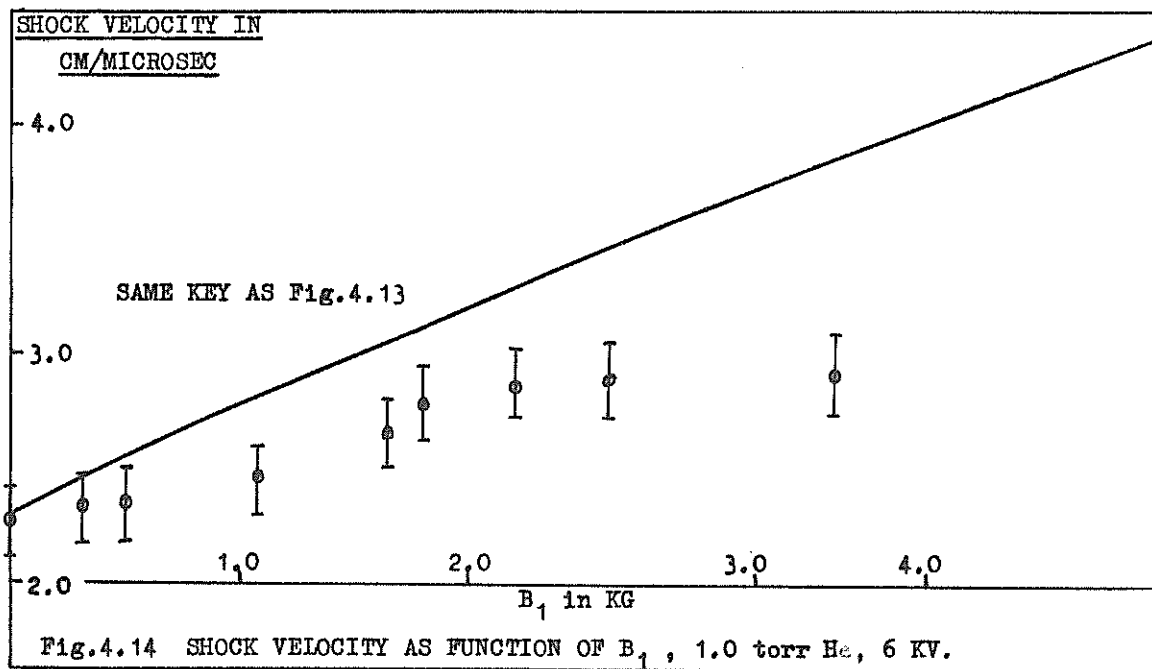


Fig.4.14 SHOCK VELOCITY AS FUNCTION OF  $B_1$ , 1.0 torr He, 6 KV.

#### 4.1.3 Velocity measurements and momentum balance

The influence of initial pressure, drive current and bias field on the shock velocity were compiled from the entire series of experiments and are displayed in Figure 4.8 to Figure 4.14. For comparison, the calculated velocities using the momentum balance equations (2-71) and (2-78) are shown by the solid lines in the figures. The error bars represent either shot to shot scatter (measured typically from 3 to 6 shots at each operating point) or the expected error of the measuring technique, whichever was the bigger at the point considered. In argon, above 0.1 torr and over the entire range of operating conditions, reasonable agreement with theory was observed. In helium, however, agreement with theory was observed only for low bias fields and for ambient pressures near to and above 1.0 torr. These low observed speeds may be due to impurities, either from the back wall, or the electrodes, affecting the momentum balance. The difference between theory and experiment in Figure 4.13 is consistent with a constant impurity level of  $0.4 \pm 0.1$  torr - atomic mass (e.g. 0.0063 torr of an impurity of mass number 63.5). However, reference to Figure 4.14 shows that, at 1 torr helium, the velocity also fell below the

momentum balance velocities as the bias field was increased.

This effect therefore can hardly be ascribed to impurities, and rather indicates a poor coupling of the magnetic pressure to the gas. This could happen if part of the drive current was left behind at the knife edges, or if the current sheet was thick and diffused. Support for this view is obtained by comparing the argon streak of Figure 4.1 and the helium streak of Figure 4.3 and with reference to the corresponding magnetic probe outputs. These show that whilst more than half the total drive current was carried in a distinct and intense current sheet in argon, the current sheet in helium was much more diffuse. With a bias field on, this diffuse nature was even more pronounced (see Figure 4.4). This figure shows an example where no shock jump current was distinguishable from the expansion current, in contrast to Figure 4.2. However, in those helium shots where such current partitioning was observed, the same relatively diffuse nature of the expansion current sheet was observed.

#### 4.2 Pressure and magnetic field distributions

Using a calibrated pressure and magnetic combination probe, a systematic survey along the centre line of the shock tube was made at 3-cm intervals. At each position, the time variation of total pressure and magnetic induction, during a discharge, were recorded together with a streak photograph. The operating point was kept constant for each series of discharges. Four series were studied, all at a drive field of 4.9 KG. Two of these were in 0.1 torr argon, with bias fields of  $B_1 = 0$  and  $B_1 = 2.5$  KG respectively. The other two were in 0.25 torr helium with  $B_1 = 0$  and  $B_1 = 2.5$  KG respectively. For each series, from the time variations at different positions of  $x$ , the distributions of pressure, magnetic field and luminosity along the shock tube at different instants of time were reconstructed. The profiles thus obtained were subject to two smoothing factors, namely:

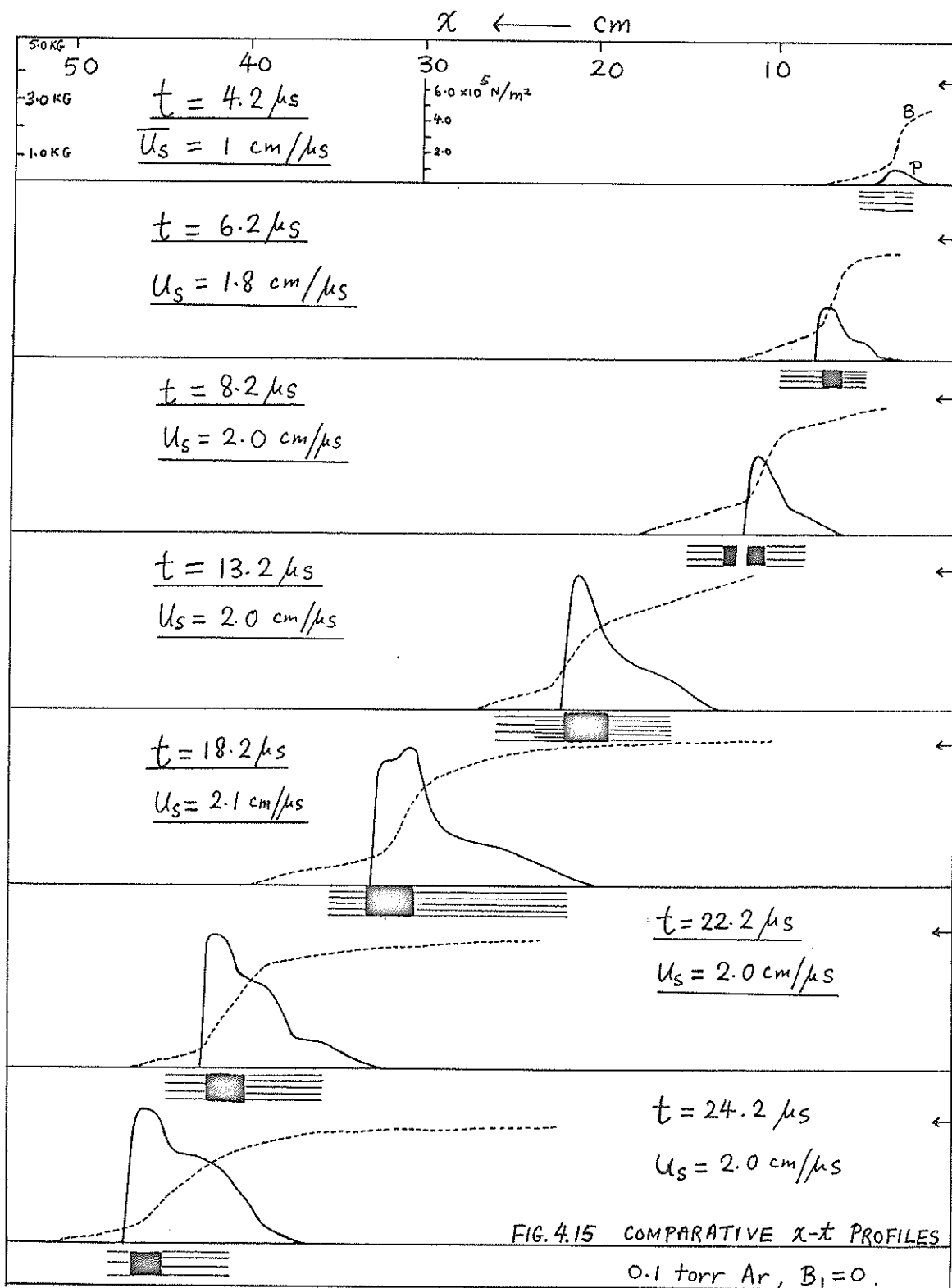
1. Shot to shot scatter, of about 3 per cent, required averaging over the profile.
2. The data was recorded at 3-cm intervals. This limited the resolution in the profiles to 3 cm, for any chosen instant of time. However, if a feature was steady (i.e. consistently observed in the time profiles

at three consecutive positions), but was lost because of the resolution of 3 cm, then it was included in the distance profile by direct reconstruction, averaging over the three consecutive positions.

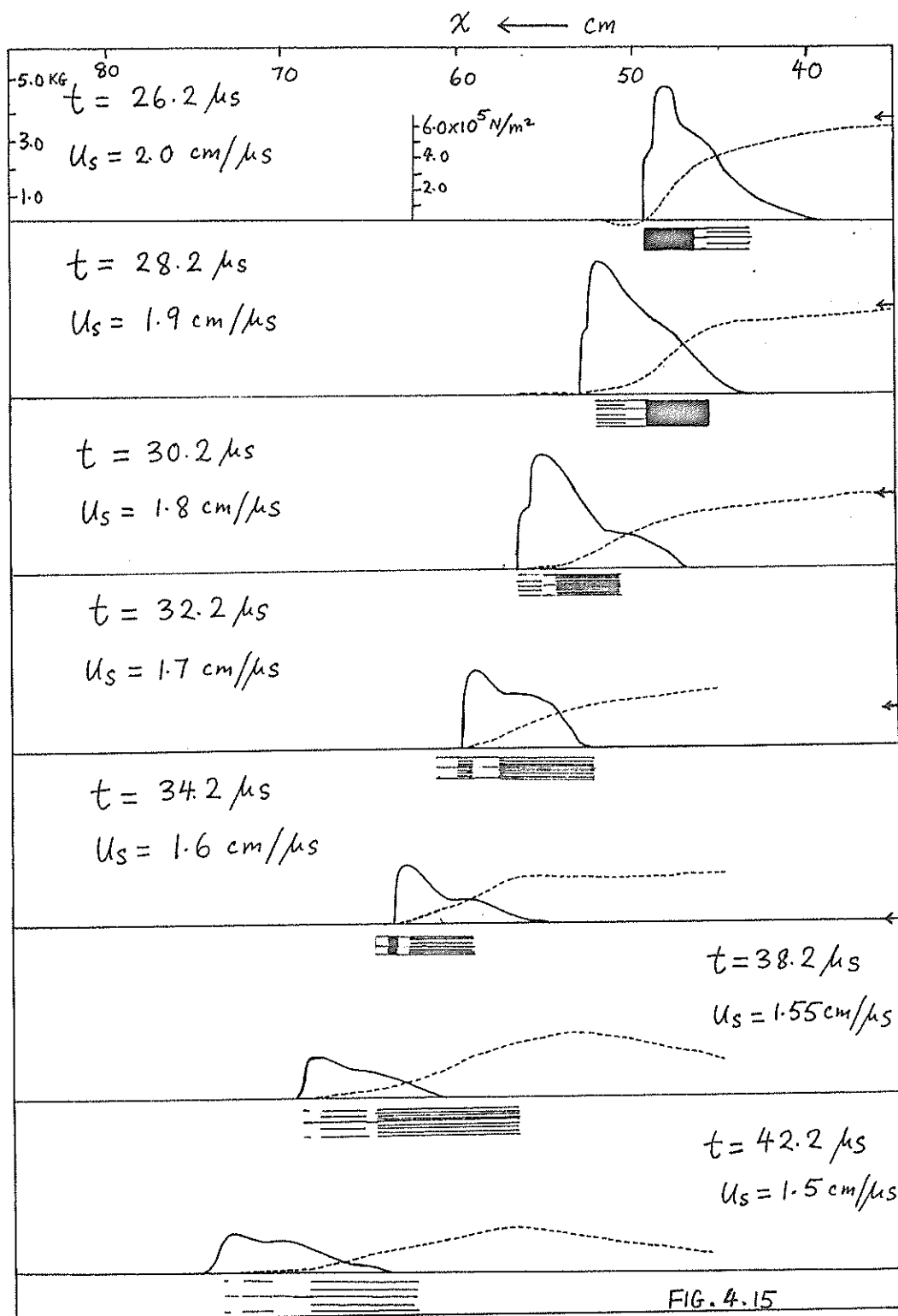
The resultant profiles are a good representation of the build up of the pressure pulse and current sheet during the acceleration phase, the propagation during the constant velocity phase and also some details of the final phase of decay. The main features represented are quantitatively reliable to an estimated accuracy, in amplitude, of 20 per cent for the pressure pulse and 7 per cent for the magnetic induction. For accurate comparison of the positions of the leading edges, the time bases of the two Tektronix 585's were adjusted to be identical to better than 1 per cent and the individual calibration checked for linearity with a Tektronix time mark generator. The triggering of the two oscilloscopes was synchronised to better than 15 nsec. The relative positions of the pressure and current fronts were thus determined to a typical accuracy of 3 mm by a careful comparison of the leading edges of the individual oscillograms, the main uncertainty being that of determining the start of the current sheet from the magnetic trace. The

absolute accuracy of the distances was 5 mm for the leading edges and about 2 cm for the diffusion current front and the trailing portion of the pressure profile.

No attempt was made to include a number of features that were consistently present on the pressure probe output behind the pressure front, which indicated sharply defined structures in the pressure pulse occurring over distances of the order of 5 mm or less. These features were distinguishable from the various modes of oscillation that occurred because of imperfect acoustic matching along the various axes of the pressure crystal. In the interpretation of the probe signals, account was taken of the estimated probe response of 0.3 microsec for both the magnetic and the pressure probes due to the probe cylinder distortion discussed in section 3.3.3.2.2. and the integration effect discussed in section 3.3.2. A study of a large number of probe outputs under different operating conditions indicate that the reliable response time was better than 0.3 microsec, and probably closer to 0.2 microsec. This experimentally observed figure was not in conflict with the earlier estimate as the latter was an upper limit estimate.







#### 4.2.1 Distributions for 0.1 torr Ar, 5 KV, $B_1=0$

The magnetic field and pressure distributions for this operating point are shown on Figure 4-15. The luminosity profiles, from synchronised streak photographs, are included for comparison. The darker the shading, the brighter was the appearance on the streak photograph. The completely black bands represent intensely bright and sharply defined streaks that were usually associated with argon current sheets. The level of the magnetic field due to the condenser current (as measured by the Rogovsky coil) is indicated by an arrow on the right hand side of the diagrams.

From the magnetic field distributions, it is observed that the current propagation down the tube occurred in three distinct regions. Firstly, a diffuse region carrying up to 20 per cent of the total current extended some 5 cm ahead of the pressure front. This was followed by a high density region of  $1\frac{1}{2}$  to 2 cm carrying 50 per cent of the total current. The remainder of the current was spread over a distance of 5 cm (typically) behind the intense sheet.

By  $t=13.2$  microsec, the pressure pulse had built up to a fairly constant structure with a front region about 2 cm wide, within which resided the peak pressure

of  $6 \times 10^5$  Newtons/m<sup>2</sup>; and a trailing region of about 5 cm width. The gross structure of the front region remained reasonably constant throughout the constant velocity region up to  $t=26.2$  microsec. The front of the pressure pulse carried the main current sheet, whilst the rear region carried the remainder of the current. As the drive current began to decrease after  $t=23$  microsec, the relative position of the pressure front and current sheet front began to undergo a dramatic change. The front of the main current sheet became less steep and began to draw back from the pressure front. At the same time, the diffuse current sheet ahead of the pressure front decreased. By  $t=28.2$  microsec, the main current sheet was 4 cm thick and had pulled back to such an extent that the current in the first 2 cm of the pressure pulse was only 3 KA compared to the 40 KA that was flowing in this region at the time of constant drive. The maximum magnetic pressure in this region was now less than 1 per cent of that at the time of constant drive, whilst the pressure pulse and velocity were attenuated by less than 10 per cent over a distance of 8 cm.

After  $t=30.2$  microsec, as the condenser current rapidly dropped to zero and then swung negative, the

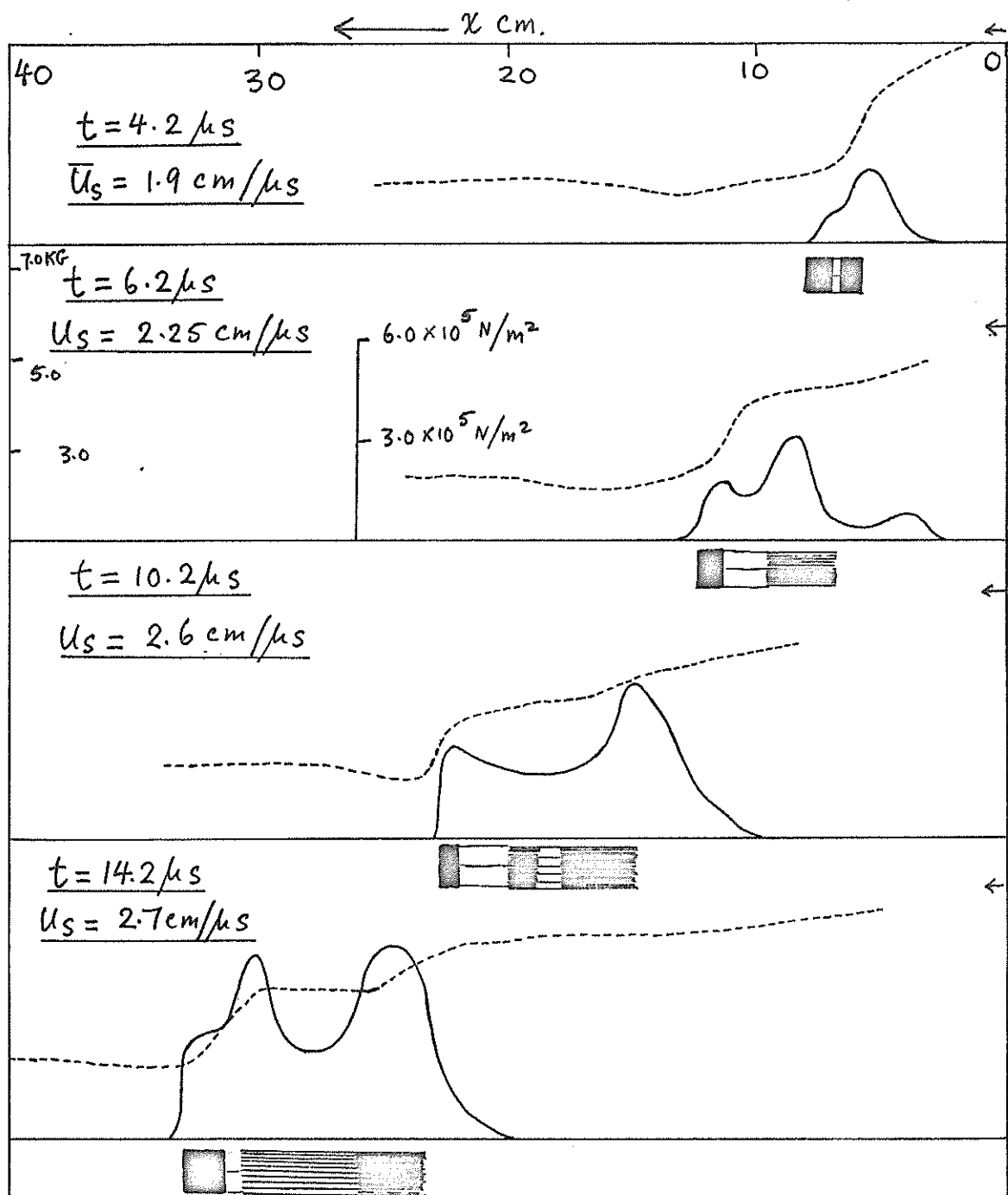
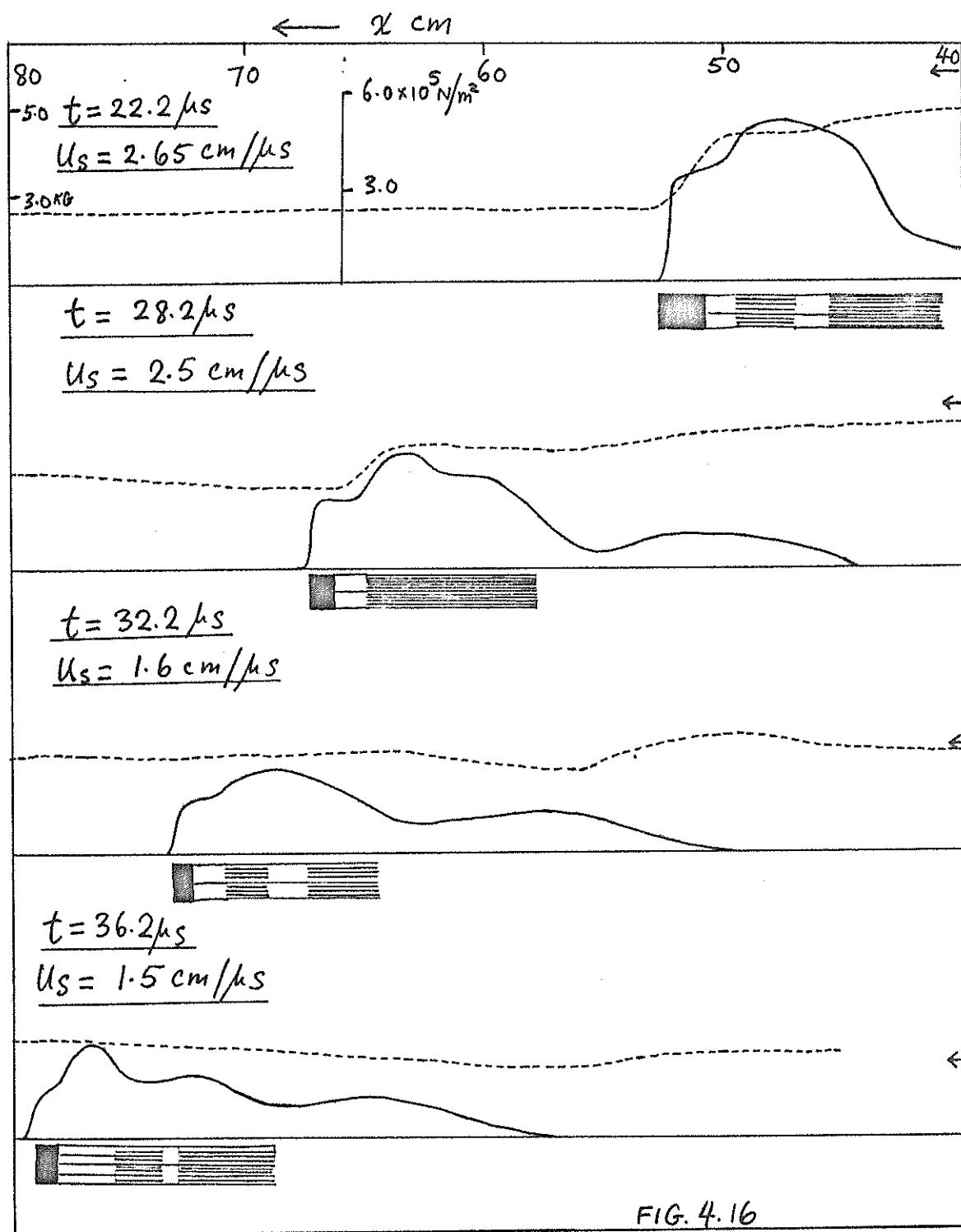


FIG. 4.16 COMPARATIVE  $x$ - $t$  PROFILES 0.1 torr Ar  $B_i = 2.5 \text{ KG}$



decaying current sheet pursuing the pressure pulse became decoupled from the condenser current and formed a closed loop. The formation of this loop had been studied in the 6 cm x 6 cm x 1 m tube, discussed in Chapter 3. In that tube the other end of this loop was a current sheet that was formed a few cm from the starting end of the shock tube. This became distinguishable on the streak photographs about 2.5 microsec before current reversal and moved towards the starting end. The region behind the decaying pressure pulse was therefore a closed and expanding loop of decreasing magnetic flux, until the current reversal. A second current sheet then moved into the tube, pushing the closed loop of remnant flux ahead of it.

#### 4.2.2. Distributions for 0.1 torr Ar, 5 KV, $B_1=2.5$ KG

These are shown in Figure 4.16. In the constant velocity period, the magnetic field profile shows four distinct regions. The magnetic field just ahead of the pressure front was equal to the bias value, but increased to a slightly higher value over a distance of about 3 cm ahead of the pressure front. Behind the pressure front, the magnetic field rose by 3 KG, corresponding to a current of 46 KA, over the first  $1\frac{1}{2}$

decaying current sheet pursuing the pressure pulse became decoupled from the condenser current and formed a closed loop. The formation of this loop had been studied in the 6 cm x 6 cm x 1 m tube, discussed in Chapter 3. In that tube the other end of this loop was a current sheet that was formed a few cm from the starting end of the shock tube. This became distinguishable on the streak photographs about 2.5 microsec before current reversal and moved towards the starting end. The region behind the decaying pressure pulse was therefore a closed and expanding loop of decreasing magnetic flux, until the current reversal. A second current sheet then moved into the tube, pushing the closed loop of remnant flux ahead of it.

#### 4.2.2. Distributions for 0.1 torr Ar, 5 KV, $B_1=2.5$ KG

These are shown in Figure 4.16. In the constant velocity period, the magnetic field profile shows four distinct regions. The magnetic field just ahead of the pressure front was equal to the bias value, but increased to a slightly higher value over a distance of about 3 cm ahead of the pressure front. Behind the pressure front, the magnetic field rose by 3 KG, corresponding to a current of 46 KA, over the first  $1\frac{1}{2}$

cm. This was followed by a region of negligible current. Behind this latter region, the rest of the current, about 30 KA, flowed. Of this, 23 KA flowed in the first 6 cm, with the other 7 KA distributed all the way back to the knife edges.

Corresponding to the three regions of shock-jump current, no current, and expansion current, the pressure pulse exhibited distinct structure. The shock current was carried in a pressure pulse of about the same length whilst the zero current region resided in a more or less flat top region of pressure. The rearward expansion current region coincided with the trailing end of the pressure pulse, which, after  $t=14.2$  microsec, also exhibited a trailing hump of small amplitude extending some 12 cm behind the main pressure structure, which itself was about 10 cm long.

As the condenser current began to drop, the front portion of the pressure pulse (about 1 cm) became gasdynamic, i.e. the magnetic field remained unchanged through it. The velocity decreased slightly to 2.5 cm/microsec at  $t=28.2$  microsec, from the earlier constant value of 2.6 cm/microsec. As the condenser current approached zero, the speed dropped sharply, and was 1.6 cm/microsec at  $t=32.2$  microsec. At this time, the



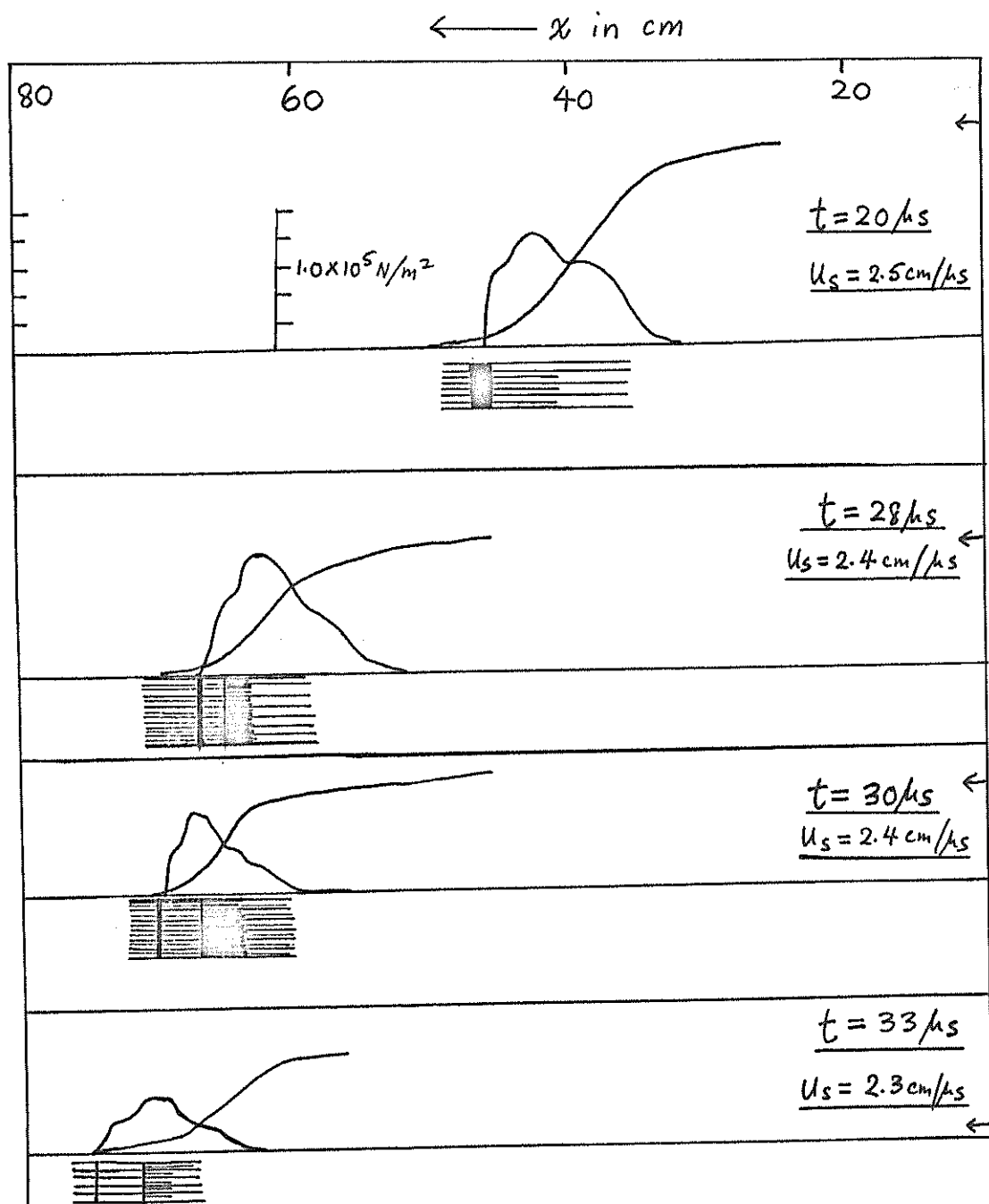


FIG. 4.17 a. COMPARATIVE  $x$ - $t$  PROFILES. 0.25 torr He  $B_1 = 0$

first 6 cm of the pressure pulse was gasdynamic; with a small B rise over the next 4 cm, followed by a slight decrease (just measureable) and then an increase of field over 10 cm. At later times (e.g. at  $t=36.2$  microsec), the magnetic field was 3.5 KG ahead of the pressure front, indicating field compression ahead of the shock from the ambient bias value of 2.5 KG. This field remained practically unchanged through 3 to 4 cm of the pressure pulse, then dropped to about 2.5 KG, over some 18 cm, before rising to about 2.9 KG in a further 5 cm\*.

#### 4.2.3 Distributions in helium, 5 KV, 0.25 torr

Figure 4.17a shows the distributions in helium for the case of zero bias field. Compared to the distributions in argon, it is immediately noticeable that the current sheet in helium was much wider, rising almost linearly for a distance of 10 cm at  $t=22$  microsec. This compares with the argon current sheet width of about 2 cm in which 70 per cent of the current was carried. At  $t=20$  microsec, which was during the constant current region, the first  $1\frac{1}{2}$  cm of the pressure pulse carried less than 5 per cent of the total current.

---

\* This behaviour is consistent with a model to be discussed in section 4.8.2.

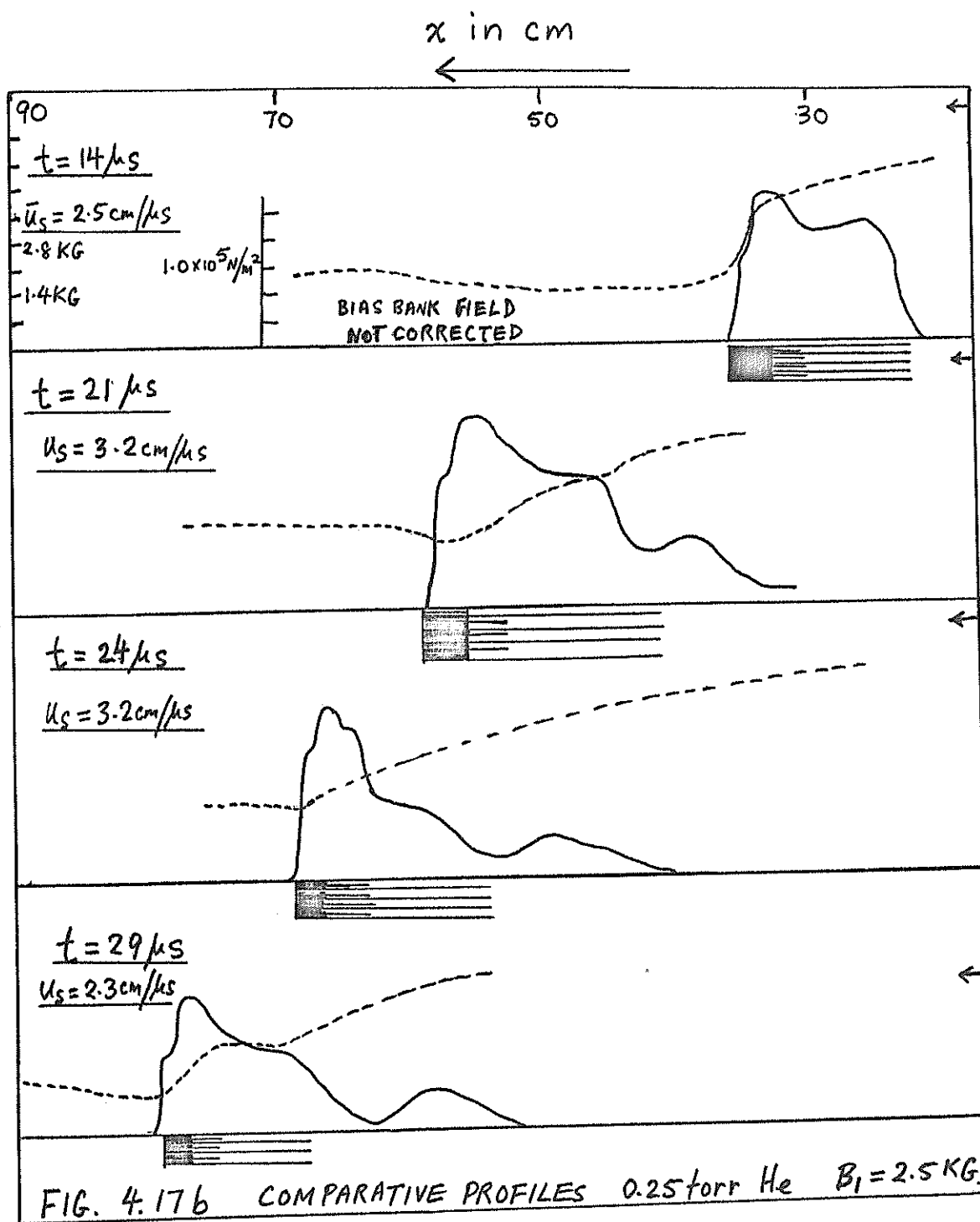


Figure 4.17b shows the distributions in helium for the case when  $B_1 = 2.5$  KG. At  $t = 14.0$   $\mu$ sec microsec, a sharp shock-jump current carrying 70 per cent of the total current in a distance of 2 cm was observed. Further down the tube, at  $x = 60$  cm, corresponding to a time of  $t = 18$  microsec, which was in the constant current period, the shock-jump current sheet had become much thicker. The region ahead of the pressure front had a reversed current. The first 2 cm of the pressure pulse was gasdynamic, followed by the diffuse shock-jump current of 4 cm length; then a 3 cm region of negligible current, followed by the expansion current spread out over some 7 cm.

#### 4.3 Magnetic field measurements

As seen in section 4.1, when the expansion current is separated from the shock-jump current, the two separated regions can be clearly distinguished both from the magnetic coil output and from the streak photograph (see Figure 4.2). This separation is also reflected in the pressure pulse structure.

Figure 4.18 to Figure 4.20 show other examples in which a shock-jump current can be distinguished from the expansion current. In each case, the pressure pulse

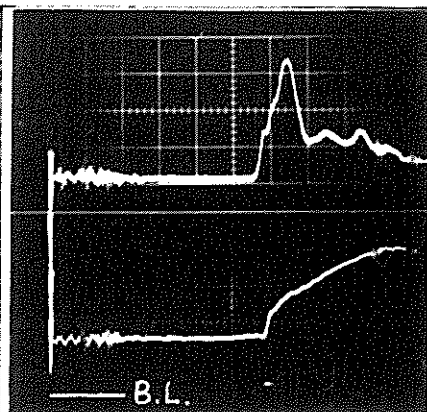


FIG. 4.18 P and B TRACES, 0.25 TORR

He,  $B_1 = 1.9$  KG, 5 KV.

$x = 65$  cm, START =  $9.4 \mu\text{sec}$  .  
 $\mu\text{sec/cm}$ .

Top: P,  $(1.3 \times 10^5 \text{ N/m}^2)/\text{cm}$ .

Bottom: B,  $0.68 \text{ KG/cm}$ .

B.L. = BASE LINE

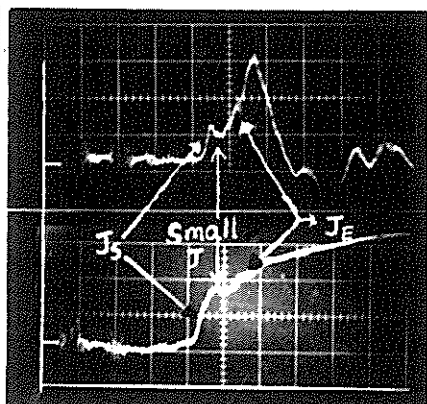


FIG. 4.19 P and B TRACES, 0.10 TORR

Ar,  $B_1 = 2.5$  KG, 5 KV.

$x = 14$  cm.  
 $\mu\text{sec/cm}$ .

Top: P,  $(1.7 \times 10^5 \text{ N/m}^2)/\text{cm}$ .

Bottom: B,  $1.36 \text{ KG/cm}$ .

$J_S \equiv$  region of shock jump current

$J_E \equiv$  region of expansion current

Small J  $\equiv$  region of low J, separating  $J_S$  and  $J_E$ .

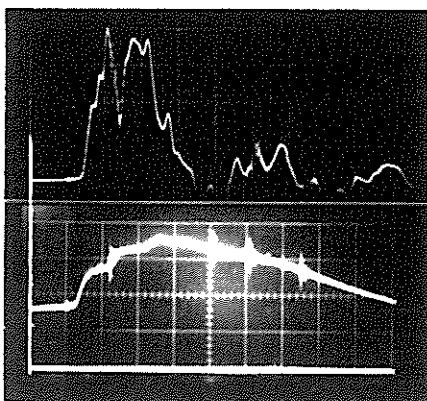
FIG. 4.20 P AND B TRACES, 0.10 TORR

Ar,  $B_1 = 2.5$  KG, 5 KV.

$x = 40$  cm.  
 $\mu\text{sec/cm}$ .

Top: P,  $(1.7 \times 10^5 \text{ N/m}^2)/\text{cm}$ .

Bottom: B,  $1.36 \text{ KG/cm}$ .



exhibits distinguishing features in the separate current regions. Figure 4.19 and 4.20 were argon shots displaying a clear separation, of about 1 microsec, between the two regions. A region of negligible current existed between the two regions. In Figure 4.18, a helium shot, two regions are distinguishable by the clearly different current densities carried by them. No separation in the form of a zero current region is observed, however. We also notice that in Figure 4.18, the first  $\frac{1}{2}$  microsec of the pressure, corresponding to more than 1 cm, was current free, and appears as a distinctive step feature.

#### 4.3.1 Measurement technique

In general, a current free region separating the two main current regions was frequently observed in argon, and also in helium. In other cases, two regions of distinctly different current densities, as in Figure 4.18, could be observed. When such a distinguishable region of shock-jump current was observed on the magnetic coil output, a measurement of the shock-jump magnetic induction was made, subject to the uncertainty of deciding at which points the shock-jump field started and stopped. The error due

to this decision was usually small, as the start and end of the shock-jump current region were usually quite abrupt. The unperturbed bias field was separately measured, as in Figure 3.5, and compared to the field just ahead of the shock-jump current region, to check if field compression or expansion existed ahead of the shock.

Two integrating constants were used in the measurements, one of 500 microsec and the other of 2700 microsec. These were sufficient for the integration of signals with characteristic times of the order of 20 microsec or less. For signals with longer rise or fall times, correction factors were used. These factors were obtained by comparing the signals (using 500 and 2700 microsec constants) with those obtained by using a 10,000 microsec integrating circuit with a 20x gain amplifier. For the bias field, with a rise time of 250 microsec, the correction factor for the 2700 microsec circuit was found to be 1.05 and that for the 500 microsec circuit, 1.46.

#### 4.3.2 Results of B<sub>2</sub> measurements

Those results that can be concisely compared in graphical form with the C-J theory are shown on

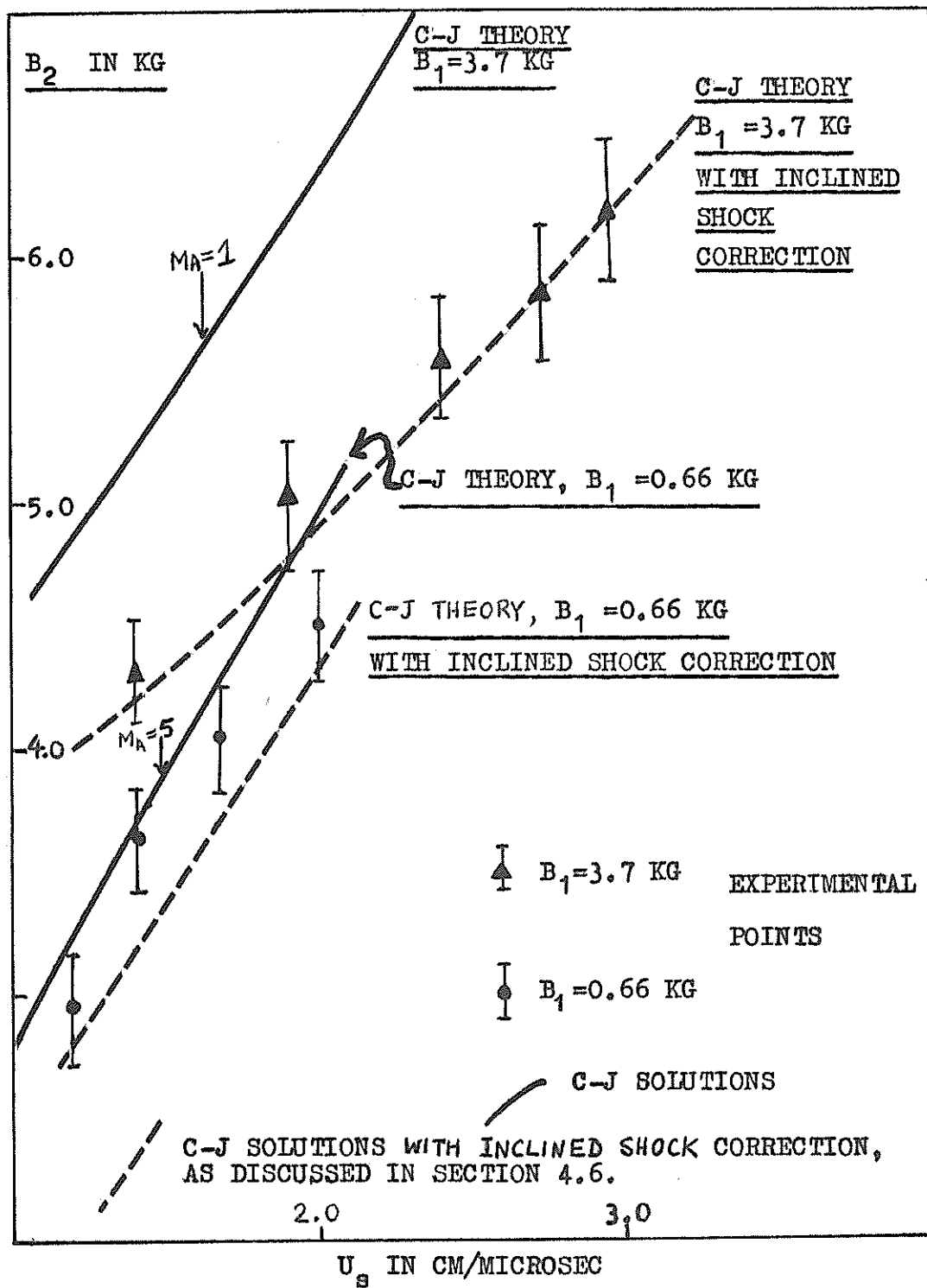


Fig.4.21  $B_2$  AS FUNCTION OF  $U_s$ , 0.2 TORR ARGON.



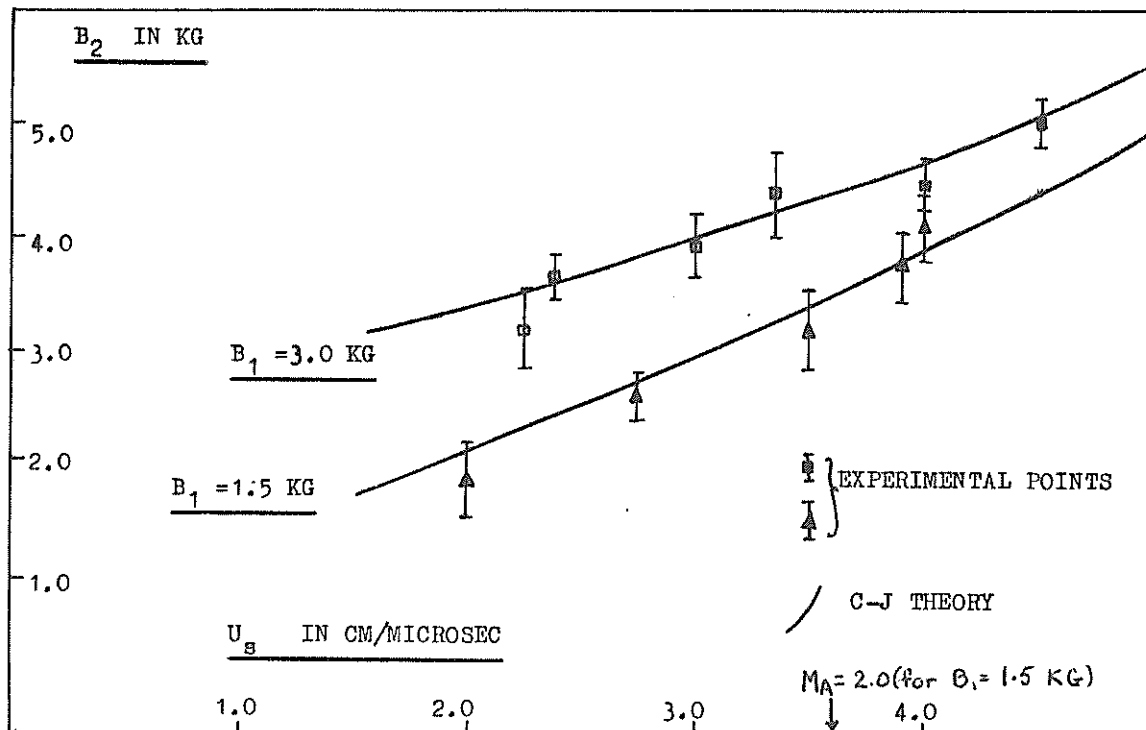
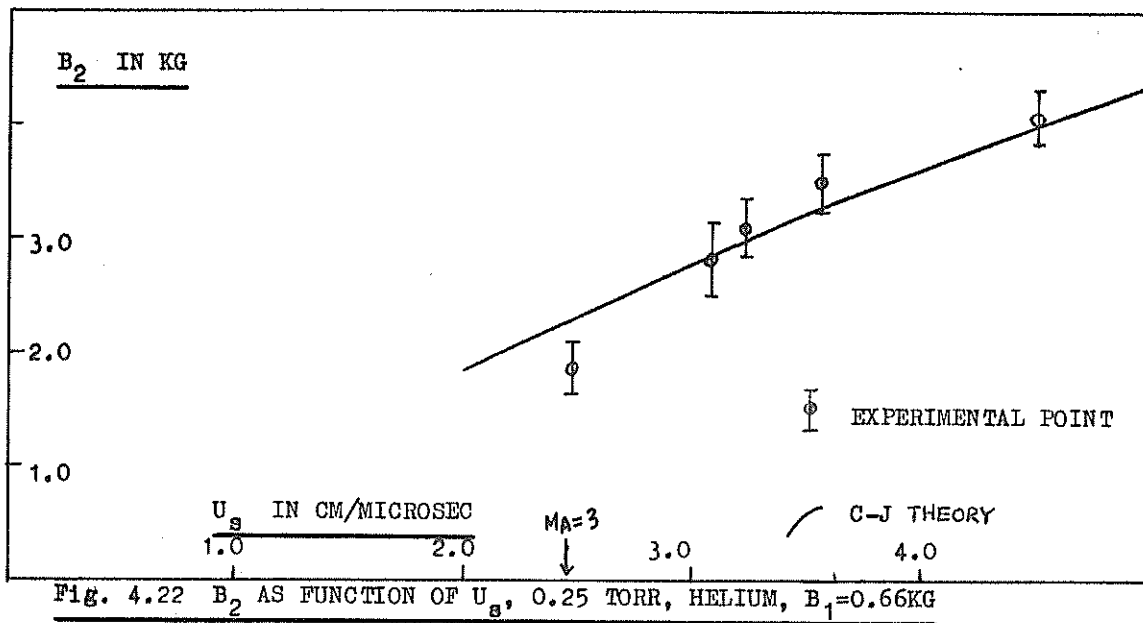


Figure 4.21 to Figure 4.23. The others are presented in Tables 4.1 and 4.2. The helium results are in general agreement with the C-J theory over the whole range investigated with the exception of the point  $B_1=0.69$  KG, 0.1 torr. The agreement is typically better than 20 per cent.

In argon, however, at 0.1 torr, with bias fields between 0.66 to 1.5 KG, a typical disagreement of 40 per cent is observed, whilst above 2.5 KG, the agreement with the C-J theory is better, though still not as good as the helium results. Two sets of results, taken with 0.2 torr argon, show better agreement at  $B_1=0.66$  KG (typically 10 per cent disagreement) than at  $B_1=3.7$  KG (typically 25 per cent disagreement). All the measured values of  $B_2$  in argon are lower than the C-J values.

For comparison, the hydromagnetic values of  $B_2$  (from Figure 2.12) are included in Tables 4.1 and 4.2

#### 4.4 Electric field measurements

Voltage measurements made at the knife edge end of the shock tube showed a constant shape and phase relation with the current trace, under all operating

FIG.4.24  $V_1$  and  $V_D$  Traces, 0.25

TORR He,  $B_1=0$ .

All horizontal axes: 10  $\mu\text{sec/cm}$ .

a,b,and c :  $V_1$  measurements,

100V/cm.

a1,b1, and c1:  $V_D$  measurements,

200 V/cm.

a and a1: 5 KV

b and b1: 4 KV

c and c1: 3 KV.

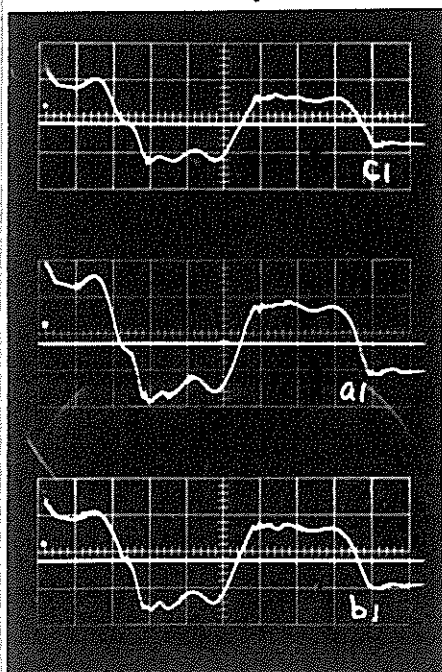
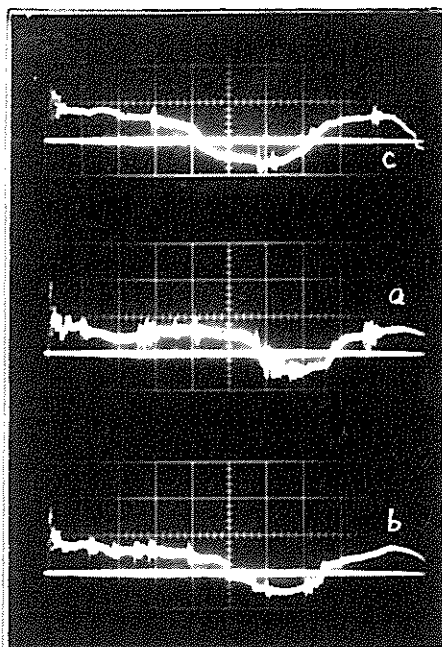


Table 4.1: Results of B<sub>2</sub> measurements -  
Ar, 0.1 torr

Measured				Theory		Comparison with C-J
B <sub>1</sub> (KG)	U <sub>s</sub> (cm/μs)	M <sub>A</sub>	B <sub>2</sub> (KG)	HM(KG)	C-J(KG)	Per cent
0.66	2.70	6.8	2.8±0.3	4.6	4.6	-39
0.66	2.18	5.5	3.0±0.3	3.9	3.9	-23
0.66	1.80	4.6	2.0±0.2	3.4	3.4	-41
1.5	3.20	3.7	3.5±0.4	6.0	6.1	-43
1.5	3.00	3.5	3.0±0.3	5.7	5.8	-48
1.5	2.56	2.9	3.0±0.3	4.8	5.0	-40
1.5	2.32	2.7	2.6±0.3	4.2	4.5	-42
1.5	1.84	2.1	2.1±0.2	3.1	3.7	-43
2.5	2.60	1.8	5.4±0.5	4.4	5.5	- 2
2.7	3.75	2.3	4.8±0.5	6.5	6.9	-30
2.7	3.05	1.9	4.7±0.5	5.0	6.0	-22
2.7	2.48	1.55	4.2±0.4	4.4	5.1	-18
2.7	2.18	1.36	3.8±0.4	4.0	4.7	-19
3.6	3.50	1.62	5.2±0.5	5.9	7.3	-29
4.1	4.60	1.87	6.7±0.7	7.4	9.0	-26
4.1	3.50	1.42	6.3±0.6	6.6	7.6	-17
4.1	2.85	1.16	4.9±0.5	6.0	6.6	-26
4.1	2.70	1.10	4.4±0.4	5.7	6.3	-30

The negative sign in the comparison column indicates that the measured value is below the predicted value.

HM Hydromagnetic.

conditions. Only the amplitude was altered, depending on the initial condenser voltage. The voltage first went negative at t=25 microsec (see Figure 4.24, a1, b1, c1), corresponding to the time when the current

Table 4.2: Results of B<sub>2</sub> measurements - Helium

Measured					Theory		Comparison with C-J
B <sub>1</sub> (KG)	P <sub>1</sub> (torr)	U <sub>s</sub> (cm/ $\mu$ s)	M <sub>A</sub>	B <sub>2</sub> (KG)	HM (KG)	C-J (KG)	Per cent
0.69	0.10	3.86	2.9	1.22 $\pm$ 0.1	2.07	2.2	-45
1.4	0.10	3.96	1.47	1.97 $\pm$ 0.2	2.24	2.7	-26
2.4	0.1	5.20	1.12	3.26 $\pm$ 0.3	3.36	3.8	-13
2.8	0.1	5.35	1.00	3.90 $\pm$ 0.4	3.80	4.10	- 5
2.8	0.1	5.60	1.04	3.54 $\pm$ 0.4	3.80	4.20	-17
1.68	0.25	3.65	1.78	2.86 $\pm$ 0.3	3.02	3.75	-23
2.80	0.25	3.42	1.00	4.0 $\pm$ 0.4	3.78	4.00	0
3.20	0.25	2.98	0.76	4.4 $\pm$ 0.4	3.80	4.10	+ 7
3.50	0.25	3.90	0.91	4.5 $\pm$ 0.5	4.55	4.90	- 8
1.60	0.50	2.78	2.01	2.8 $\pm$ 0.3	3.10	3.50	-20
2.40	1.00	2.50	1.71	6.0 $\pm$ 0.6	4.20	4.80	+20
1.80	0.075	4.00	1.00	3.0 $\pm$ 0.3	2.40	2.70	+12

began to fall from its constant value. This negative voltage at the input end of the shock tube, together with a positive decreasing current flowing through the propagating current sheet provided a suitable condition for the formation of a closed current loop, decoupled from the condenser bank. The propagation of each current sheet was recorded with the polarity associated with the current sheet until just prior to the

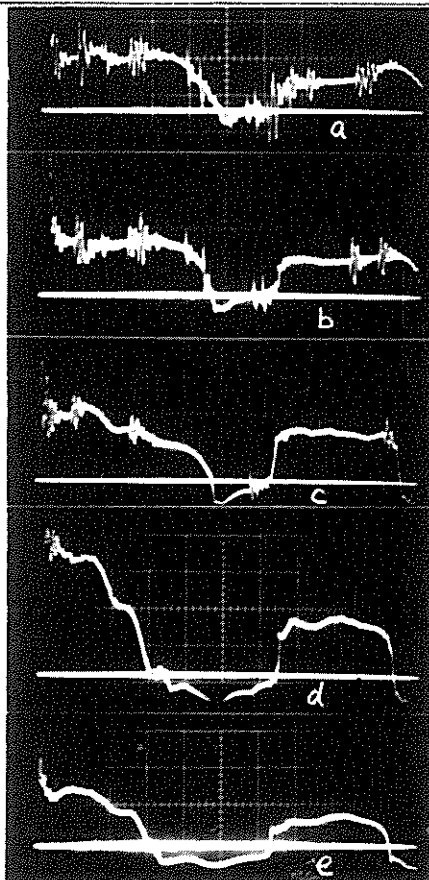


Fig.4.25 Pre-shock voltage ( $V_1$ )

Measurements, 0.1 torr Ar,  $B_1=1.5\text{KG}$

All horizontal axes: 10  $\mu\text{sec/cm}$ .

All vertical axes : 50 V/cm.

Discharge voltages:

a. 6 KV

b. 5 KV

c. 4 KV

d. 3 KV

e. 2 KV

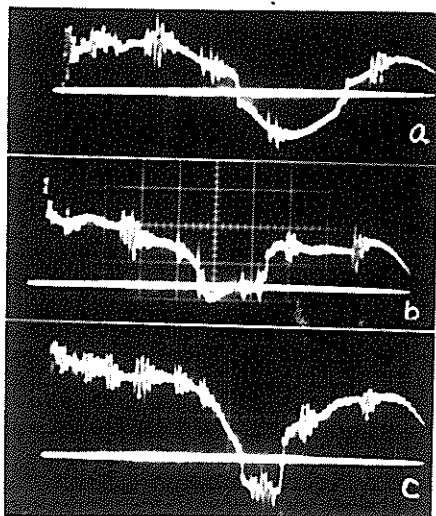


Fig.4.26  $V_1$  measurements, 0.1

Torr Ar, 5 KV.

All horizontal axes: 10  $\mu\text{sec/cm}$ .

All vertical axes : 50 V/cm.

Bias fields:

a. 0

b. 1.5 KG

c. 4.1 KG

formation of the next. In this sense, the input voltage was in phase with the rear-most current sheet.

The electric field at the reflection plate end of the shock tube was the electric field ahead of the forward-most shock wave-current sheet system. This can be seen in Figure 4.24 a, b, c; which are voltage measurements ( $V_1$ ) made at this end of the shock tube. The voltage went to zero at  $t=57$  microsec, for the 5 KV shot. For lower voltage cases,  $V_1$  went negative at earlier times; e.g., at  $t=42$  microsec for the 3 KV shot in helium. These periods, of approximately steady  $V_1$ , corresponded to periods in which a distinguishable pressure pulse originating from the first half cycle of current discharge was detected by the pressure probe. When  $V_1$  had dropped to zero, either the pressure pulse associated with the first current sheet had reached the back wall, or it had been overtaken by the second current sheet. This second current sheet-shock wave system had negative fields associated with it, both in front and at the back. For low voltage operations in a relatively large bias field (e.g., Figure 4.25e, with 2 KV,  $B_1=1.5$  KG) streak photographs show that the first pressure pulse underwent severe attenuation once the condenser current decreased; and also that the

second pressure pulse-current sheet system hardly left the knife edge region. In such a case, the voltage  $V_1$  went negative when the first pressure pulse had sufficiently attenuated for the effects of the second system\* to predominate; in the case of Figure 4.25e, this happened at  $t=28$  microsec.

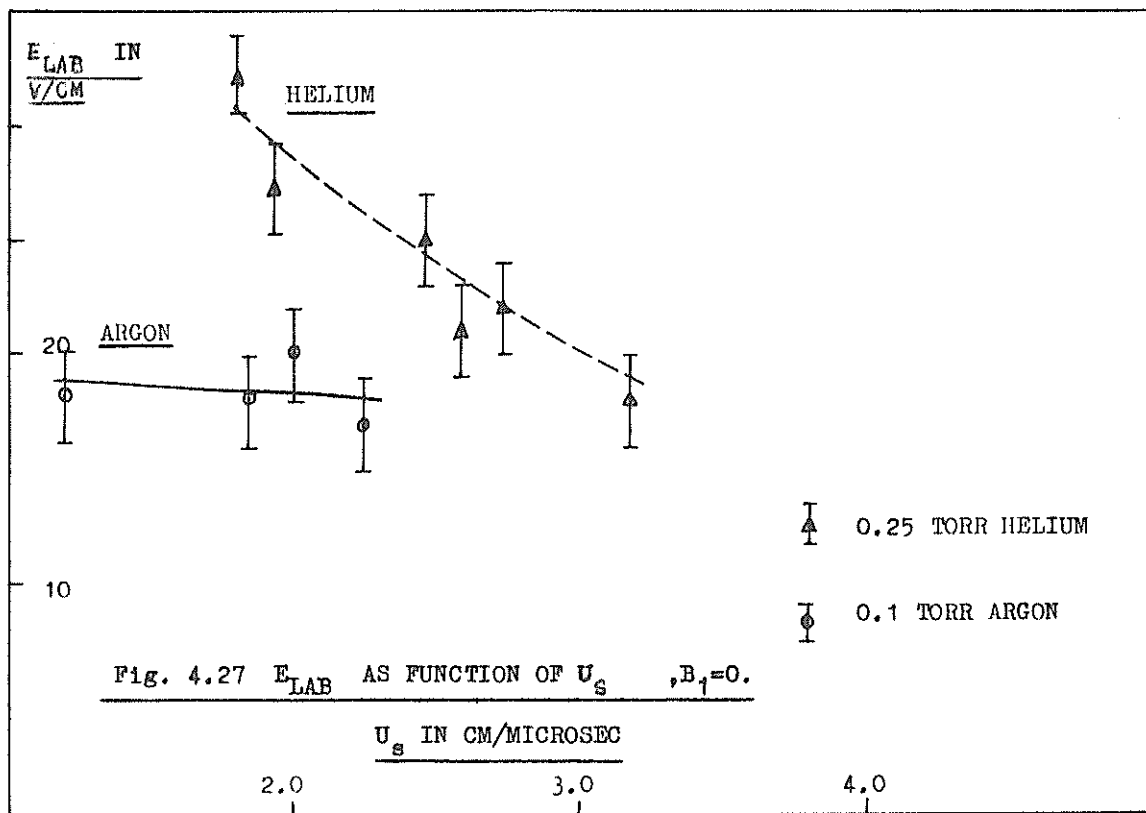
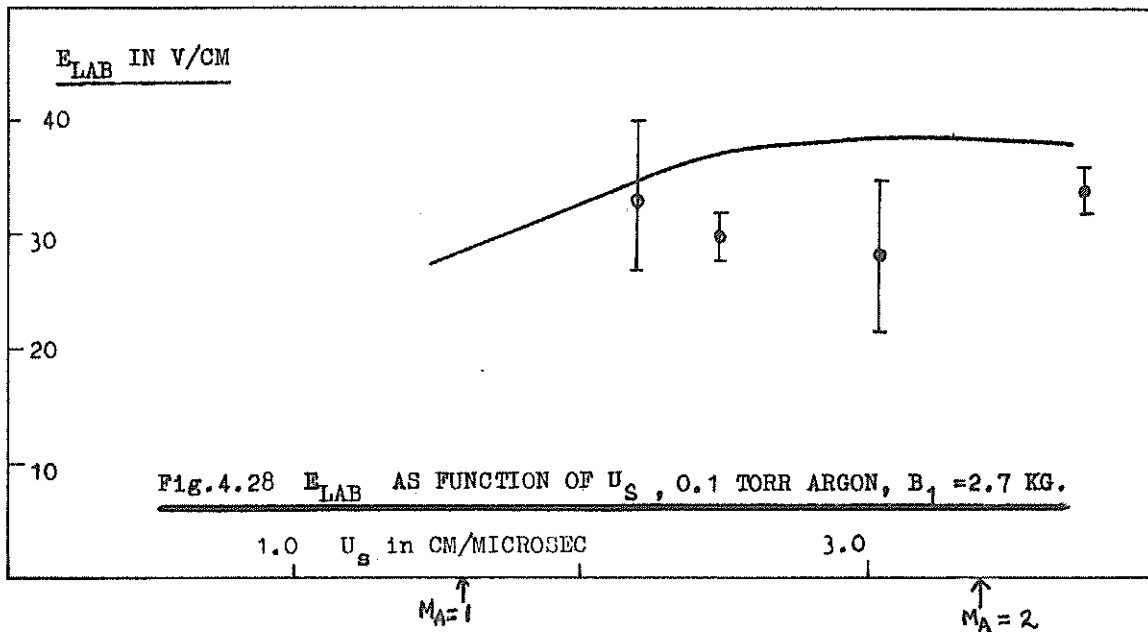
Figure 4.25 shows measurements of  $V_1$  at 0.1 torr argon,  $B_1=1.5$  KG, with the discharge voltage varied from 6 to 2 KV. The amplitudes of  $V_1$  increased as discharge voltage was reduced from 6 to 3 KV; and then decreased as the discharge voltage was further reduced to 2 KV. The length of the period of steady  $V_1$ , however, decreased monotonically with decreasing discharge voltage.

An unexplained feature of interest is the oscillations on the  $V_1$  traces at 6 to 4 KV. These were not present below 3 KV and so cannot be attributed to triggering circuit oscillations. They were also not associated with the condenser current, because they were not present on the  $V_D$  traces (voltage measured at the input end) under all operating conditions (see e.g., Figure 4.24 a1, b1, c1). Levine<sup>3</sup> has observed these oscillations in his normal shock experiments.

---

\* or the negative condenser voltage





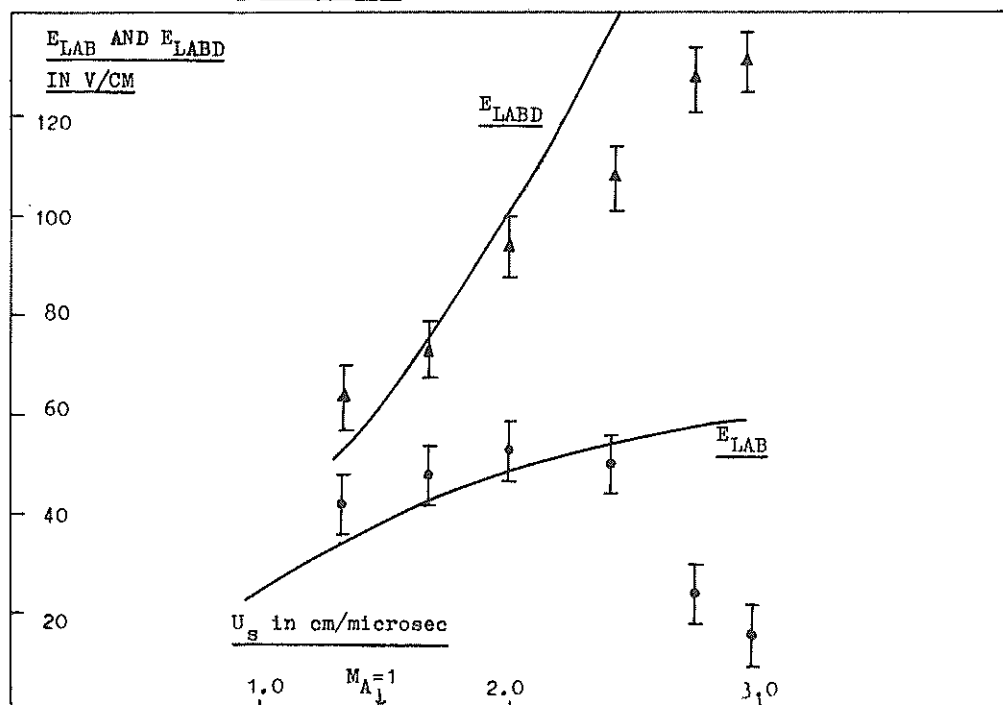
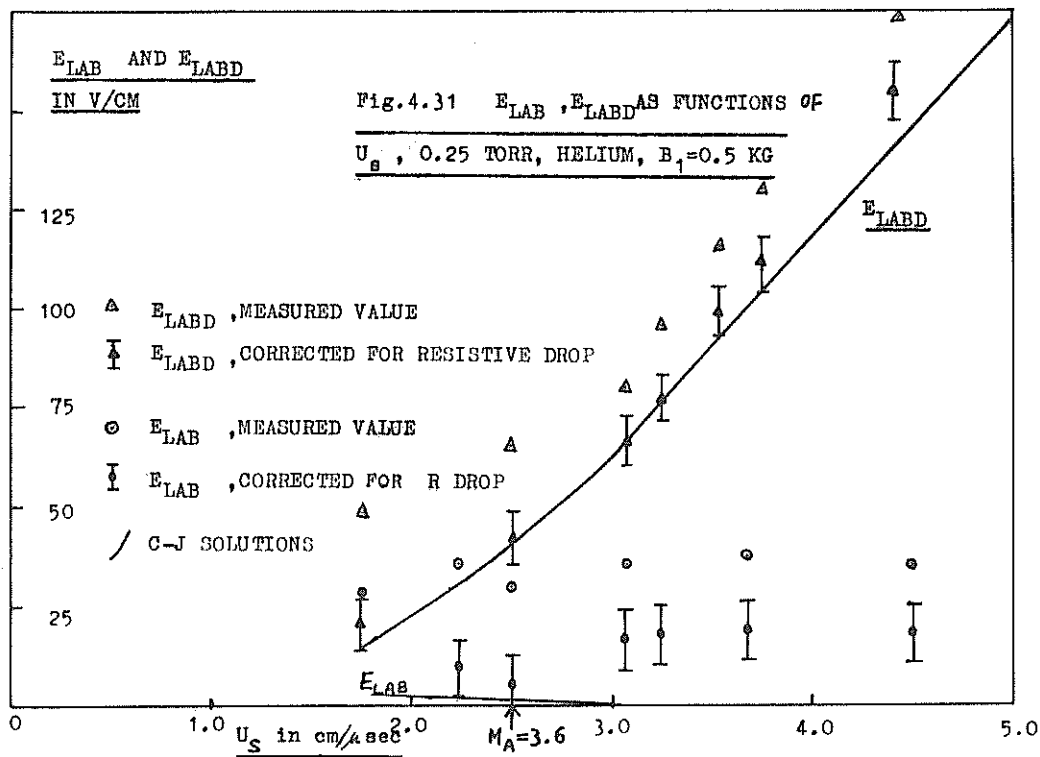


Fig. 4.29  $E_{LAB}$ ,  $E_{LABD}$  AS FUNCTIONS OF  $U_s$ , 0.2 TORR ARGON,  $B_1 = 3.7$  KG.

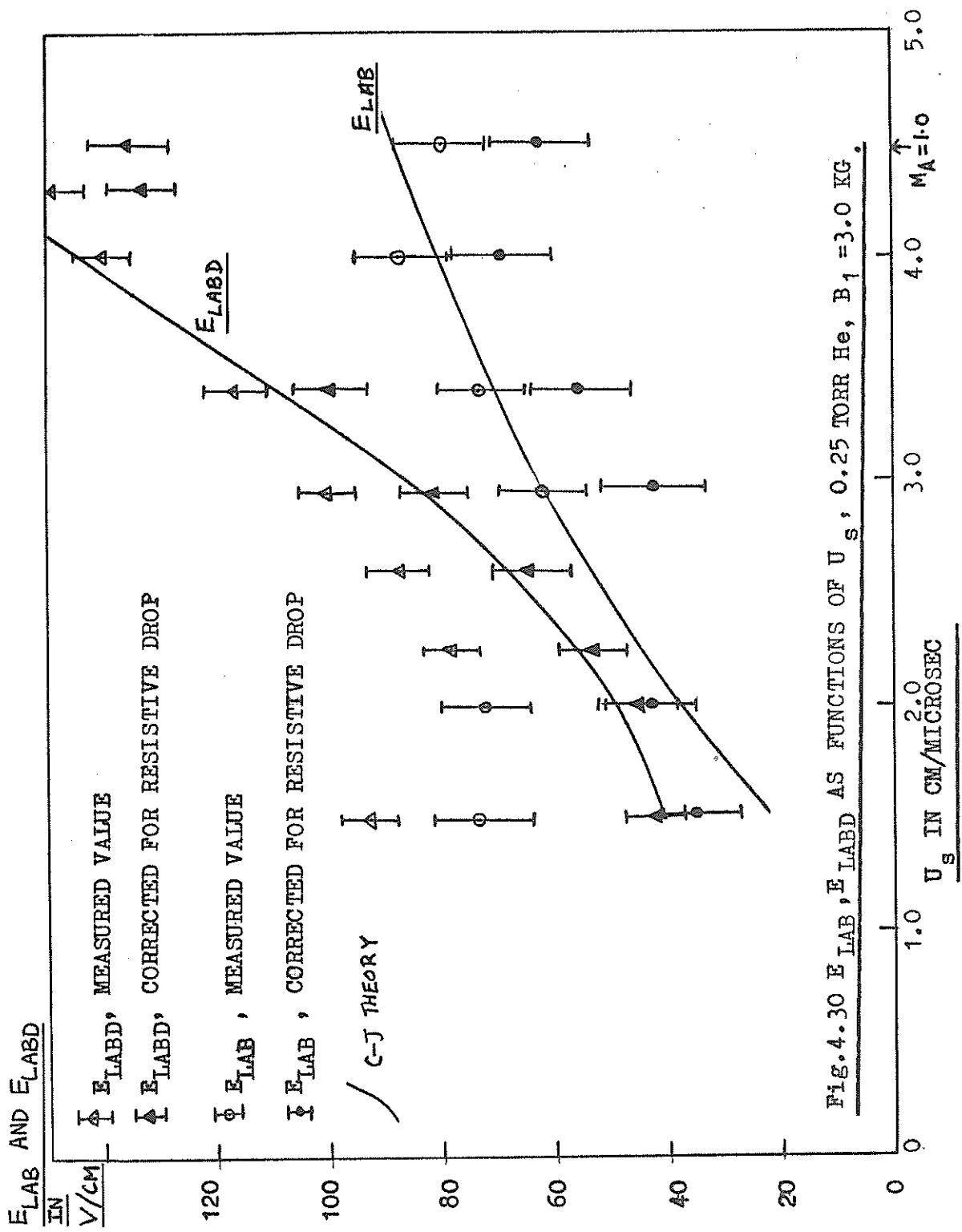


Fig. 4.30  $E_{LAB}$ ,  $E_{LABD}$  AS FUNCTIONS OF  $U_s$ , 0.25 TORR He,  $B_1 = 3.0$  KG.

Figure 4.26 illustrates the variation of  $V_1$  traces, at 0.1 torr argon and 5 KV; with different bias field values. At increasing values of the bias field, the period of positive  $V_1$  increased at the expense of the period of negative  $V_1$ .

#### 4.4.1 Electric field results

The voltages measured were converted into electric fields by dividing by the distance between the copper electrodes. These are denoted by  $E_{LAB1}$  and  $E_{LABD}$  for the downstream and upstream fields respectively. When  $B_1=0$ , no  $\vec{u} \times \vec{B}$  voltage should be measured ahead of the shock and  $E_{LAB1}$  can be ascribed to the resistive drop across the current sheet. This resistive drop field was measured to be almost a constant, namely,  $18.5 \pm 2$  V/cm, for 0.1 torr argon between the velocity range of 1.2 to 2.2 cm/microsec, as shown in Figure 4.27. For 0.25 torr helium, the resistive drop varied from  $32 \pm 2$  to  $18 \pm 2$  V/cm over the velocity range 1.8 to 3.2 cm/microsec.

If we assume that these resistive drops were the same when bias fields were applied, we can then subtract the resistive drop from each electric field measurement to obtain the  $\vec{u} \times \vec{B}$  component. Some results, using

this method, are presented in Figure 4.28 to Figure 4.31. The  $E_{LABD}$  results are in good agreement with the electric field behind the current sheet (calculated using equation 3-8), for the lower velocity range; but are lower than the expected values at the higher velocities (see Figure 4.29 to Figure 4.31).

In the  $E_{LAB1}$  measurements, the 0.25 torr helium results show good agreement both for  $B_1=0.5$  and  $B_1=3.0$  KG. The argon results, in general, show poorer agreement, except for 0.1 torr,  $B_1=0.27$ , where fairly good agreement was observed (see Figure 4.28). For the operating conditions of 0.2 torr argon,  $B_1=3.7$  KG, agreement between C-J theory and experiment was observed between 1.3 cm/microsec to 2.4 cm/microsec ( $M_A=1.6$ ). At higher velocities, the values of  $E_{LAB1}$  dropped below the C-J values, approaching the hydromagnetic value (i.e. zero) at 3.3 cm/microsec corresponding to  $M_A=2.1$ . The transition from the region of agreement to that of disagreement was very abrupt.

Some other results are presented in Table 4.3. The large relative errors for the low values of  $E_{LAB1}$  are due to the subtraction of the resistive drop field from the measured total value of the electric field. The

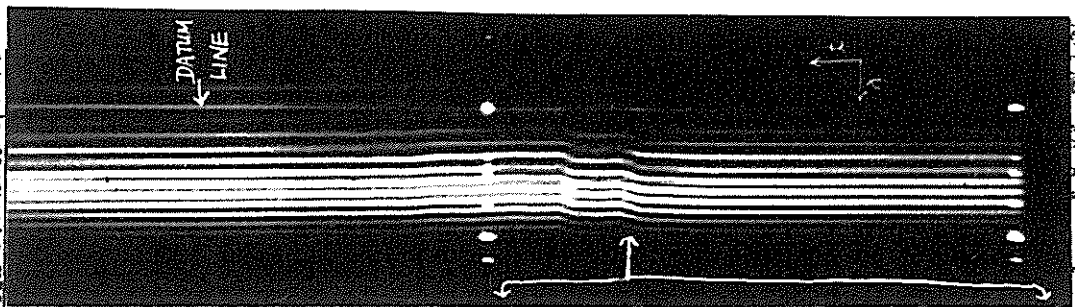
Table 4.3: Argon - electric field measurements

Measured					Theory - C-J
$P_1$ (torr)	$B_1$ (KG)	$U_s$ (cm/ $\mu$ s)	$M_A$	$E_{LAB1}$ (V/cm)	$E_{LAB1}$ (V/cm)
0.10	0.66	2.70	6.8	$3 \pm 5$	0
0.10	0.66	2.50	6.3	$3 \pm 5$	0
0.10	0.66	2.20	5.5	$7 \pm 5$	0
0.10	0.66	1.80	4.6	$24 \pm 5$	0
0.10	0.66	1.60	4.0	$22 \pm 5$	1.1
0.10	0.66	1.20	3.0	$15 \pm 5$	3.0
0.10	1.50	3.20	3.7	$7 \pm 5$	9.5
0.10	1.50	3.00	3.5	$8 \pm 5$	11.5
0.10	1.50	2.56	2.9	$22 \pm 5$	13.5
0.10	1.50	1.90	2.2	$36 \pm 5$	14.0
0.10	4.10	4.60	1.9	$20 \pm 5$	90.2
0.10	4.10	3.50	1.4	$20 \pm 5$	85.6
0.10	4.10	2.86	1.2	$27 \pm 5$	75.2
0.10	4.10	2.40	1.0	$54 \pm 5$	65.5
0.20	0.66	1.93	6.9	$2 \pm 5$	0
0.20	0.66	1.67	6.0	$19 \pm 5$	0
0.20	0.66	1.39	5.0	$19 \pm 5$	0
0.20	0.66	1.18	4.2	$12 \pm 5$	0.4
0.20	0.66	0.85	3.0	$9 \pm 5$	1.3

The measured value of  $E_{LAB1}$  has been corrected for the resistive drop.

main features of this Table are, that, when the theoretical solutions are near hydromagnetic (i.e.,  $E_{LAB1} \rightarrow 0$ ), the measured values of  $E_{LAB1}$  were consistently larger than the predicted values; whilst, when the

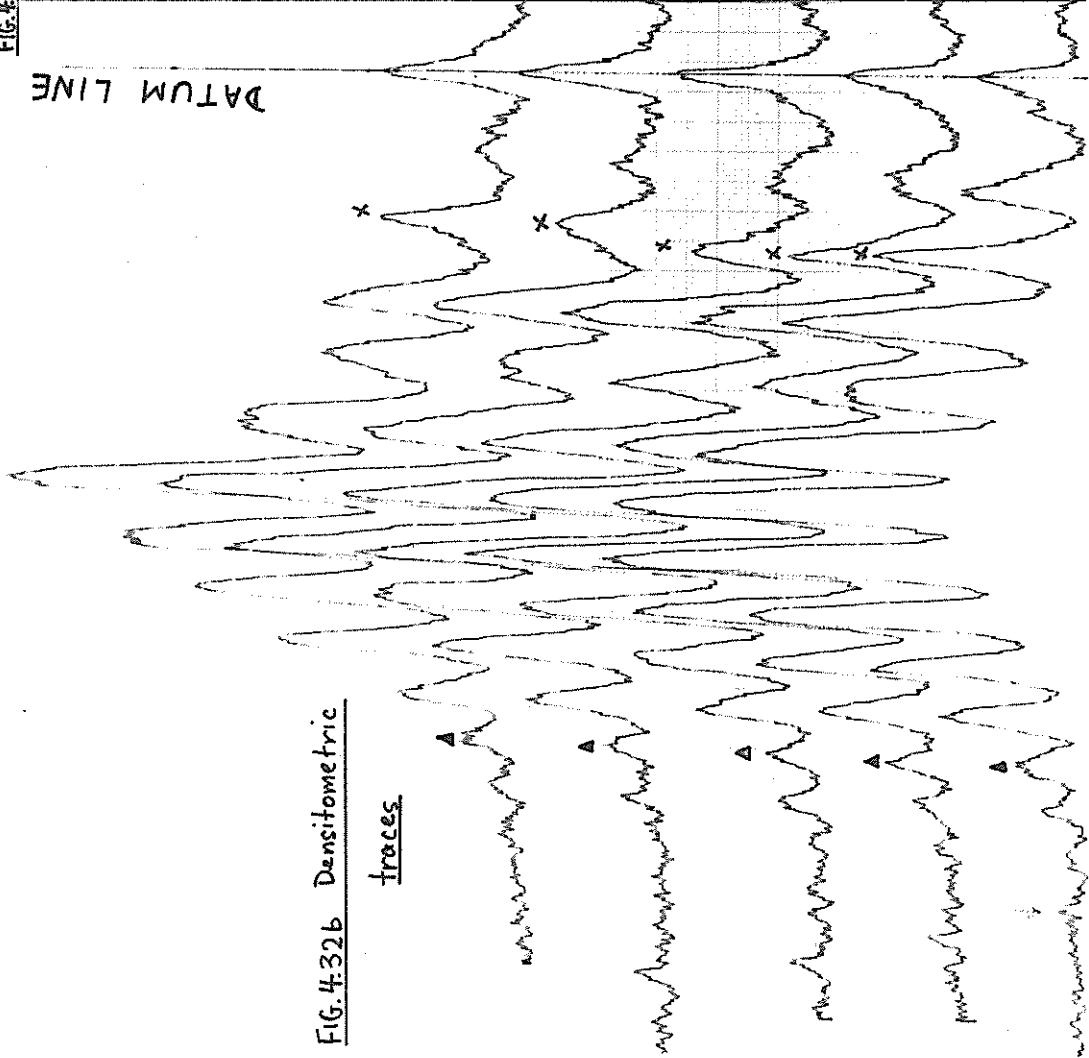
FIG. 4.32a Channelled Spectra



DATUM LINE

FIG. 4.32b Densitometric

traces



predicted values were large, the measured values were consistently too small.

#### 4.5 Electron density and heavy particle density measurements

##### 4.5.1 The channelled spectra measurements

Figure 4.32a is an example of a time resolved channelled spectra interferogram, printed from an HP4 original. The time sweep, with a total length of 20 microsec, was in the direction of the undeviated (no flow) spectral channels. The channels were closest together at the red end of the spectrum and furthest apart at the blue end. The direction towards the red end was the direction of increasing refractivity, corresponding to increasing heavy particle density. The reference features on the interferogram were the calibration spectrum (Hg-Cd-Zn) positioned at the start and in the middle of the sweep. The length of each spectrum line in the reference spectrum was the length of the spectrometer slit as recorded on the film. The seven prominent spectral lines in the calibration spectrum are, listing from the blue end:  $4046.6 \text{ \AA}^{\circ}$ ,  $4358.4 \text{ \AA}^{\circ}$ ,  $4678.2 \text{ \AA}^{\circ}$ ,  $4799.9 \text{ \AA}^{\circ}$ ,  $5085.8 \text{ \AA}^{\circ}$ ,  $5461.0 \text{ \AA}^{\circ}$ , and  $5780.0 \text{ \AA}^{\circ}$ . The datum line can be seen to pass through the  $4358.4$  line.



In making a densitometric record of the interferogram, the film was positioned with the help of the datum line, and first scanned along a channel to determine the 'straightness' of the no-flow channels. Notes were made on the regions of channel shifts regarding the clarity of the channels during the shift, and the number of scans required to cover the regions of interest. The calibration spectra and 3 to 5 no-flow scans were then recorded. Following this, the flow regions were scanned and recorded. An example of a densitometric record is shown in Figure 4.32b. This represents 5 scans in the first 1.0 microsec of flow of Figure 4.32a.

A number of problems were associated with the determination of the distance of the centre of a channel from the centre of the fixed spectral position which was approximated by the datum line (see Figure 4.32b). These are briefly listed.

1. Background light caused the centre of the fringe system to be displaced upwards with respect to the wings. The main effect was to displace the peaks from their original positions (i.e., positions in the absence of background light) by an amount depending on the steepness of the background envelope. It can be shown<sup>75</sup>

that the intensity maxima and minima are displaced in opposite directions. Thus provided both the maxima and the minima are used in the calculation, and provided the slope of the envelope is smooth and not too steep, the errors due to the displacements of the maxima and minima tend to cancel out. The experimental scatter will however be increased, though this can be minimized by smoothing out the scatter in the data.

2. In the region of abrupt channel shifts, the channels were often blurred; and in any case became asymmetrical and often hardly recognizable as simple peaks and troughs. The results in these regions invariably had large scatters.

3. Absorption lines in the exploding wire spectrum was another cause of non-simple peaks.

The channel spacing in the centre of the spectral range covered was of the order of  $100 \text{ \AA}$ , approximately 1 cm on the densitometric trace. The analysis of a large number of interferograms (about 50) showed a typical scatter of  $5 \text{ \AA}$  in the measurements due to a combination of all the errors. The average net channel shifts at the centre of the spectral range of the order of  $-100 \text{ \AA}$ , made up of  $-110 \text{ \AA}$  shift due to electrons and  $+10 \text{ \AA}$  due to the non-electronic species

(these figures were typical of 0.1 torr argon). This resulted in the determination of the electron density ( $N_e$ ) to better than 5 per cent. The measurements of the density ratio  $\Gamma$ , on the other hand, contained large probable errors. For helium, because of the low specific refractivity of the helium atom and ion, the typical positive component of the channel shift was of the order of  $2 \text{ \AA}$ , in 0.2 torr helium; and only a few usable values of  $\Gamma$  were obtained at the higher pressures (around 1.0 torr), where, because of the low shock speeds, the ionization fraction was of the order of a few per cent.

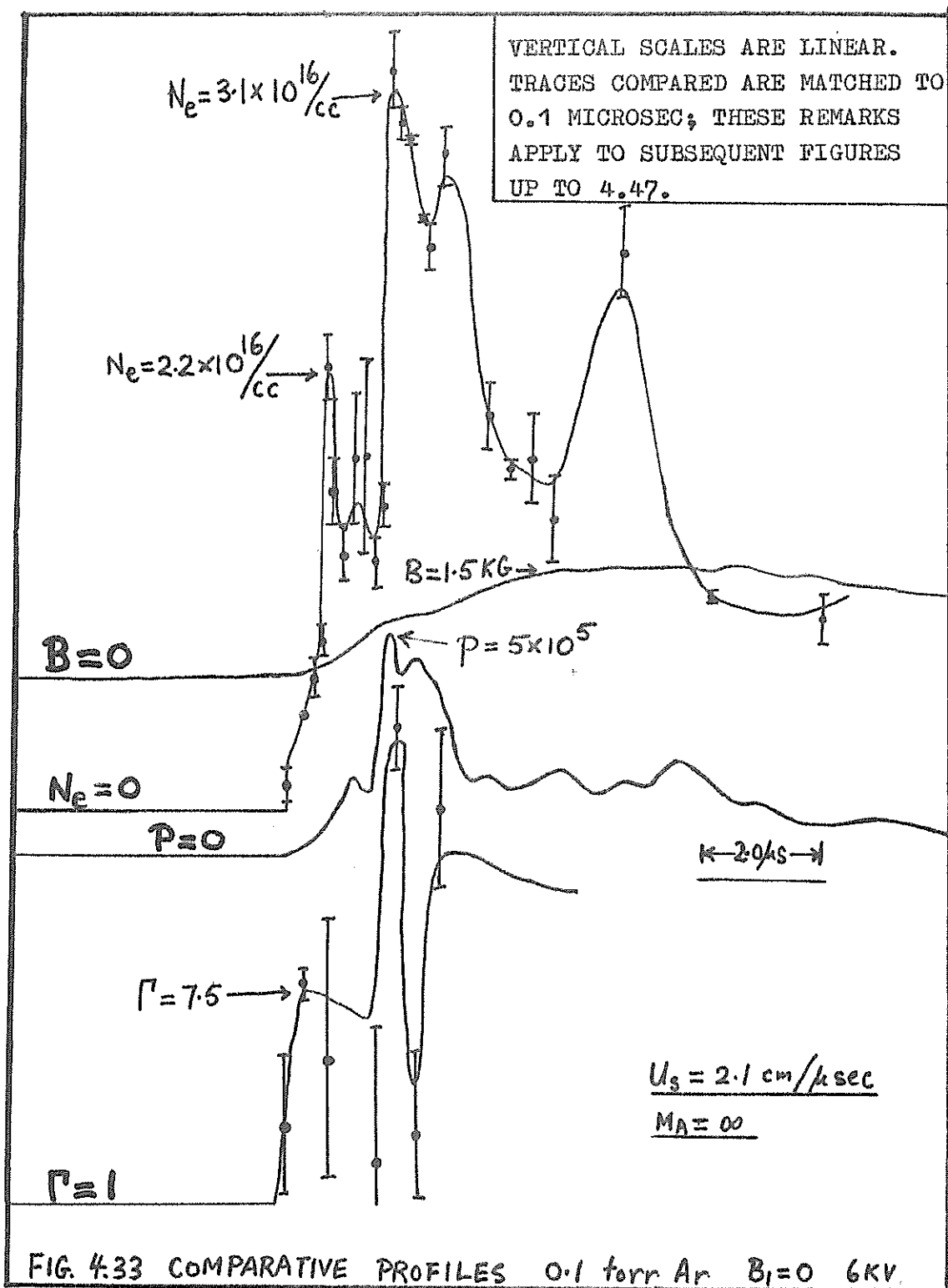
The data from the densitometric traces were fed into the programme described in section 3.3.4.4.3, for the calculation of  $N_e$  and  $\Gamma$ . The observation point of the interferometric record was at  $x=65 \text{ cm}$ , and was 3 mm ahead of the front face of a combination total pressure-magnetic field probe. The oscilloscopes monitoring the output of the pressure and magnetic probes were synchronized to the streak camera trigger. In the usual mode of operation, the oscilloscope traces started  $0.2 \pm 0.05$  microsec before the start of the streak. This time, plus the time of travel between the M-Z viewing position and the probe face was taken

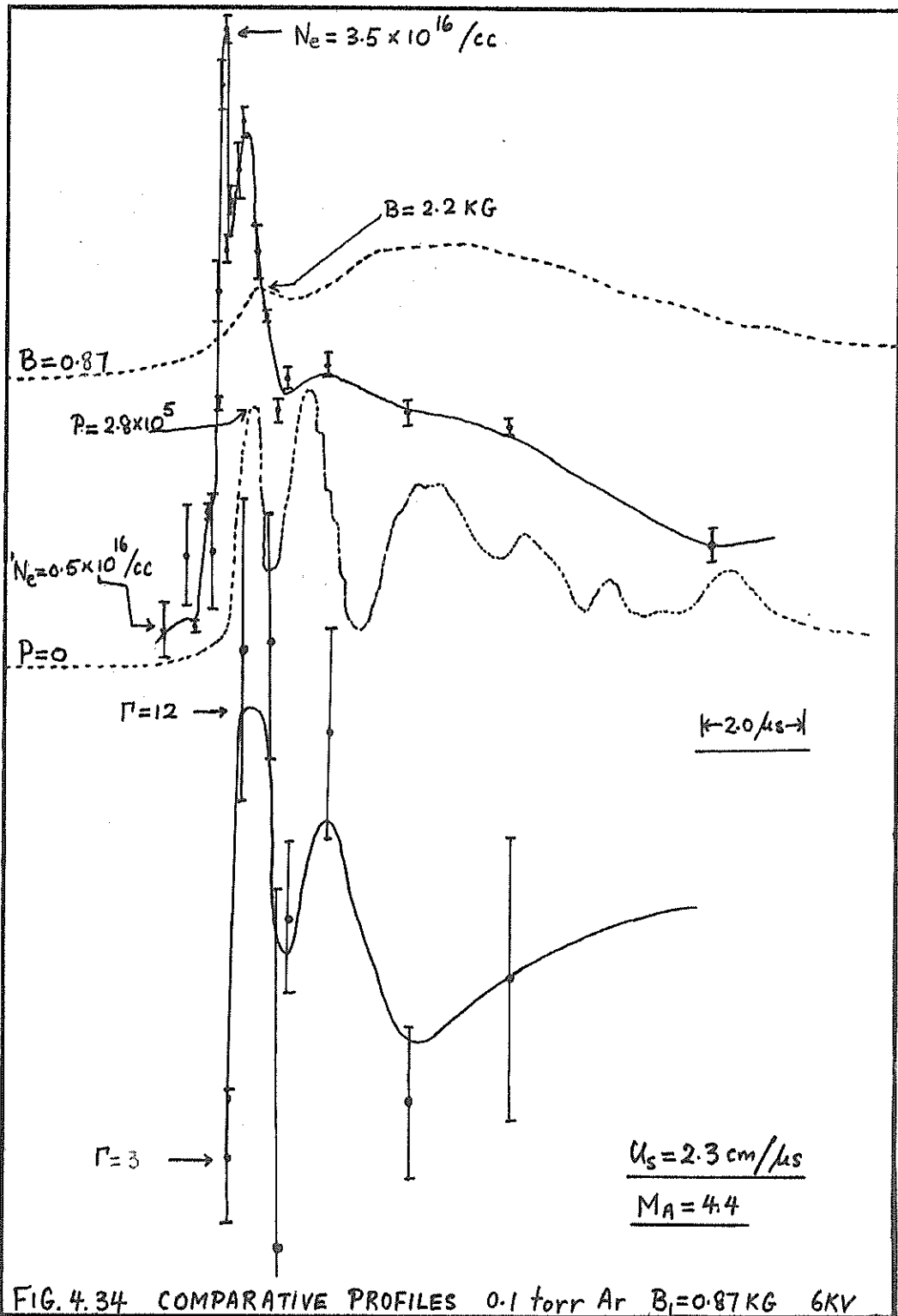
into account in comparing the P and B traces with the  $N_e$  and time functions. The P and B profiles presented here were direct tracings of the polaroid oscillograms projected with an episcope to provide a 4-time linear magnification. The points  $t=0$  on each set were matched with an estimated accuracy of 0.1 microsec.

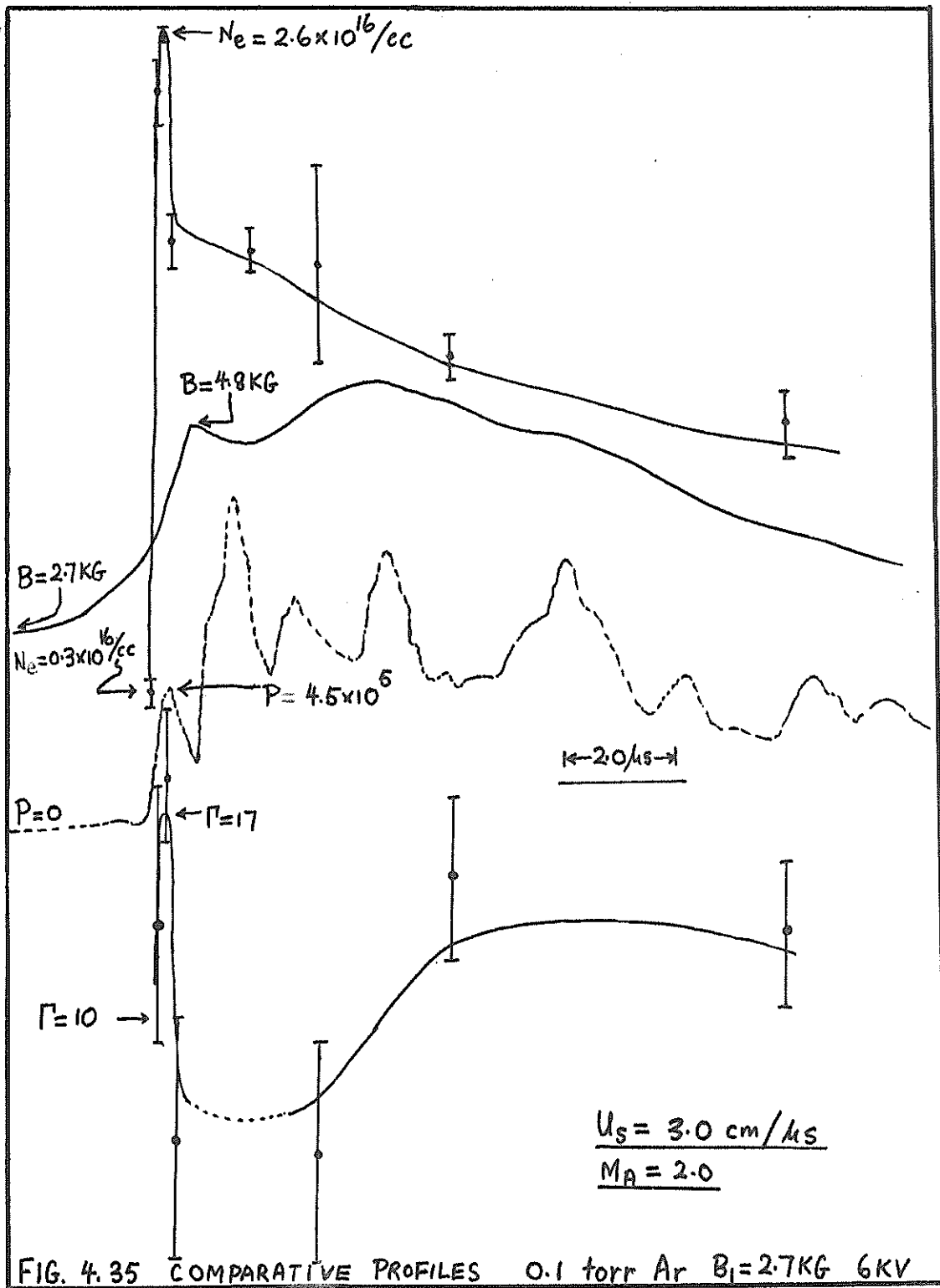
#### 4.5.1.1. Comparison of the $N_e$ , $\Gamma$ , P and B profiles

Fifteen sets of results are presented here. Figures 4.33 to 4.36 are of argon at 0.1 torr and with bias fields of from  $B_1=0$  to  $B_1=4$  KG. Figures 4.37 to 4.39 are at 0.2 torr argon and with bias field of from  $B_1=1.33$  KG to  $B_1=4$  KG. Figure 4.40 shows the effect of lowering the initial pressure to 0.075 torr with  $B_1=0$ . Figure 4.41 is of 1.0 torr helium and with  $B_1=0$ . Figures 4.42 to 4.45 are of helium at 0.25 torr and with bias field of from  $B_1=0$  to  $B_1=4.7$  KG, whilst Figures 4.46 and 4.47 are of 0.1 torr helium with  $B_1=0$  and  $B_1=.7$  KG respectively. In helium, results for  $\Gamma$  are presented only for the case of 1.0 torr.

The first important feature to be noticed in the  $N_e$  profile is that either a distinctive peak or a plateau always existed at the very front of the profile. In the 0.1 torr argon series, this peak is seen to be







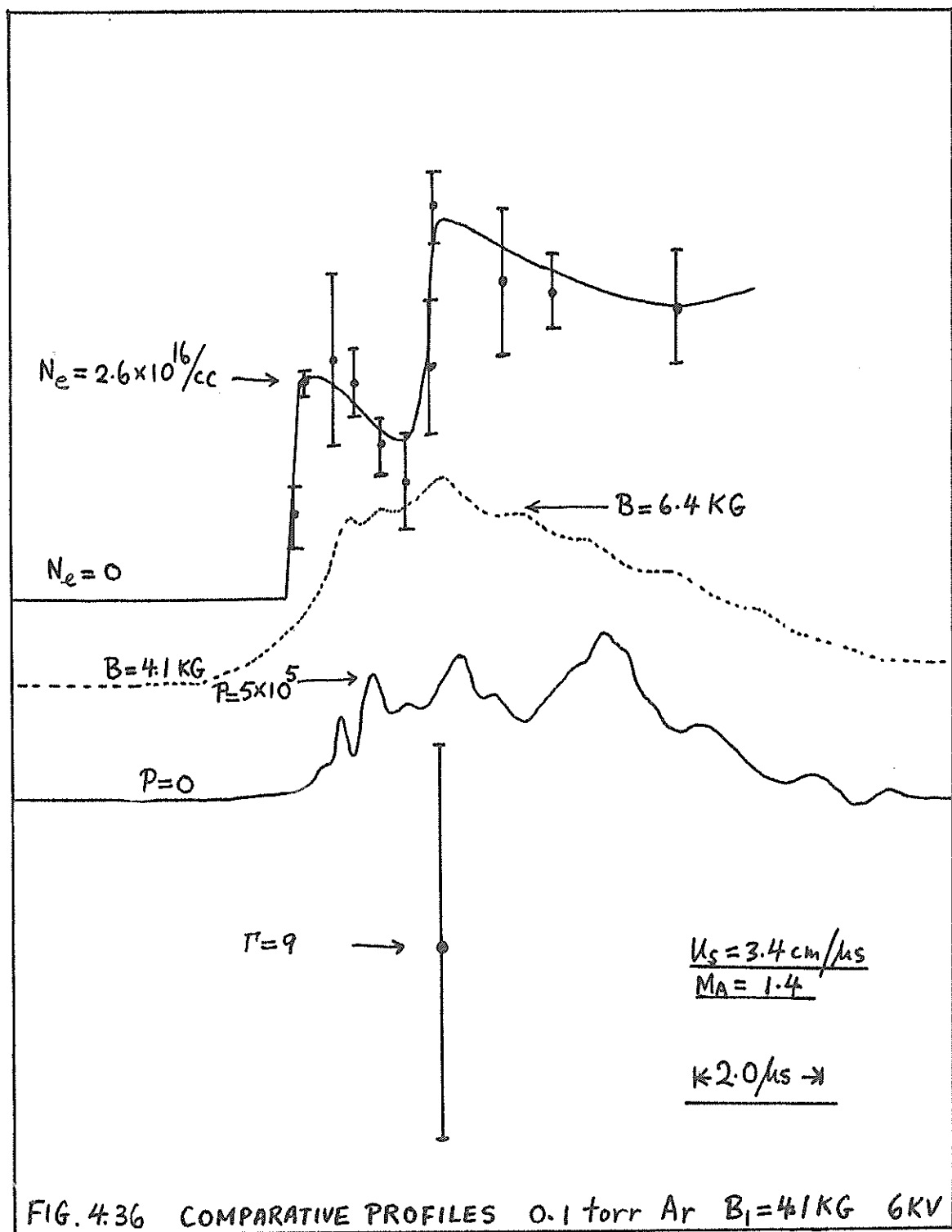
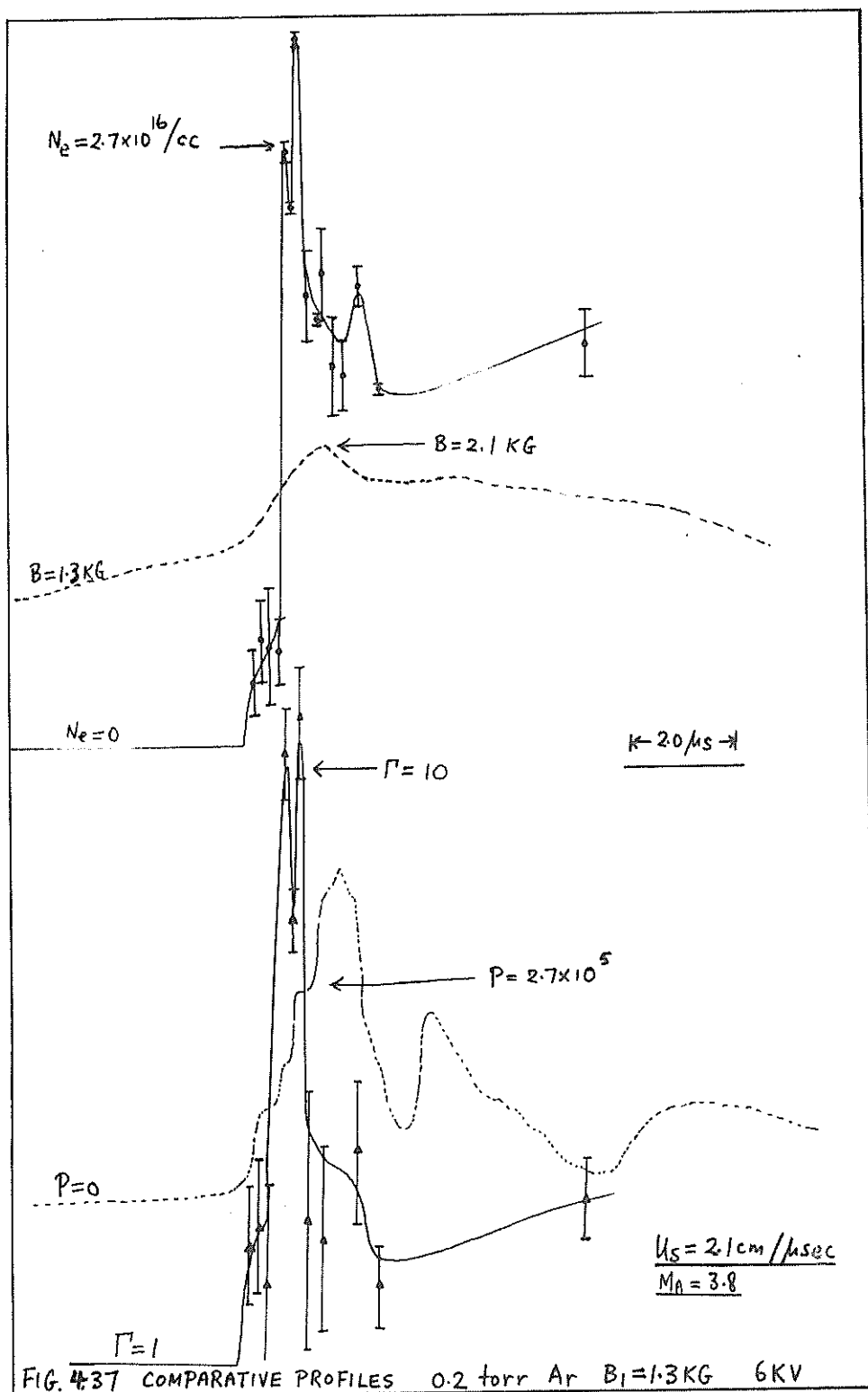


FIG. 4.36 COMPARATIVE PROFILES 0.1 torr Ar  $B_1 = 4.1 \text{ KG}$  6KV





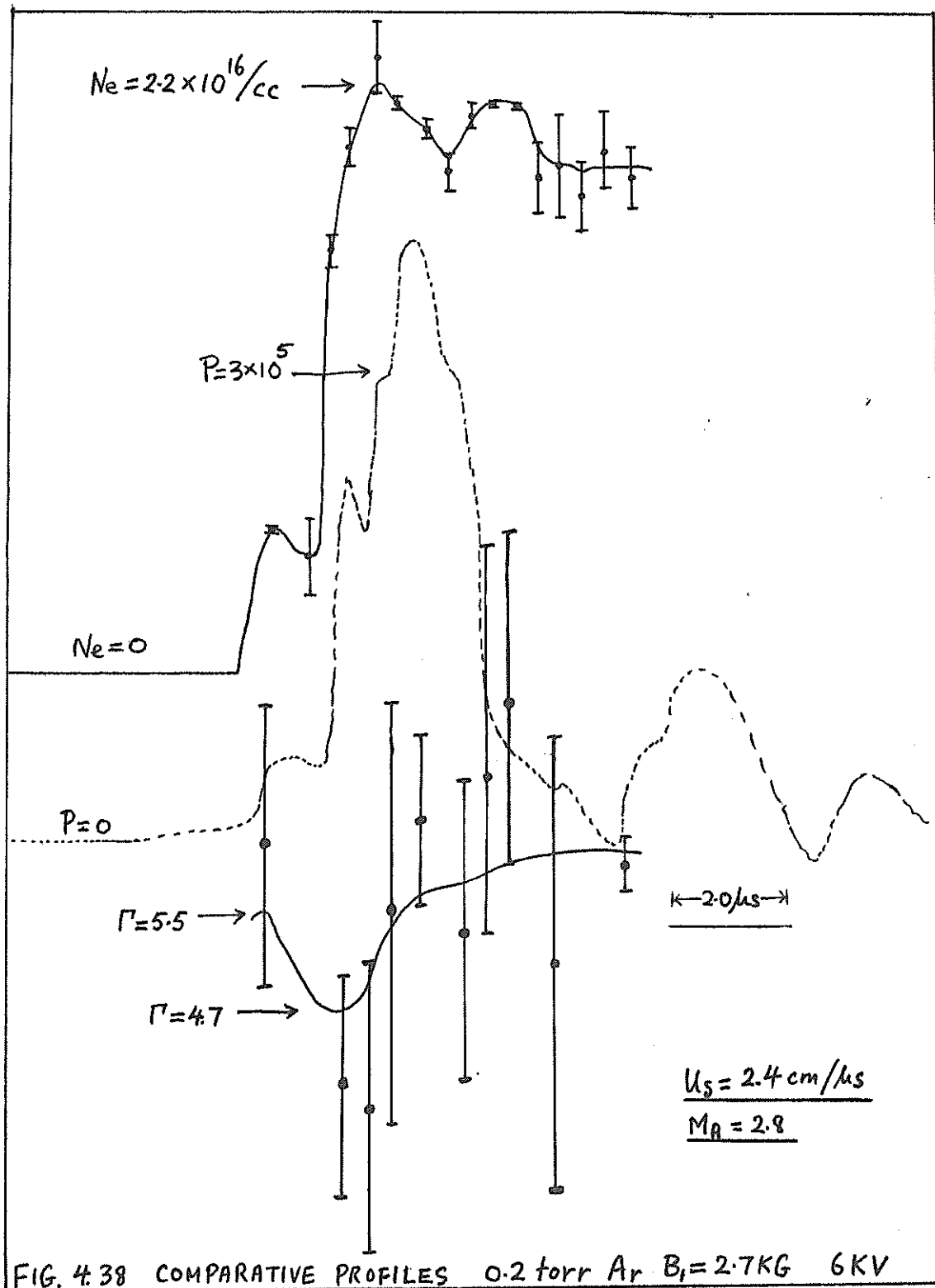


FIG. 4.38 COMPARATIVE PROFILES 0.2 torr Ar  $B_1 = 2.7 \text{ KG}$  6KV

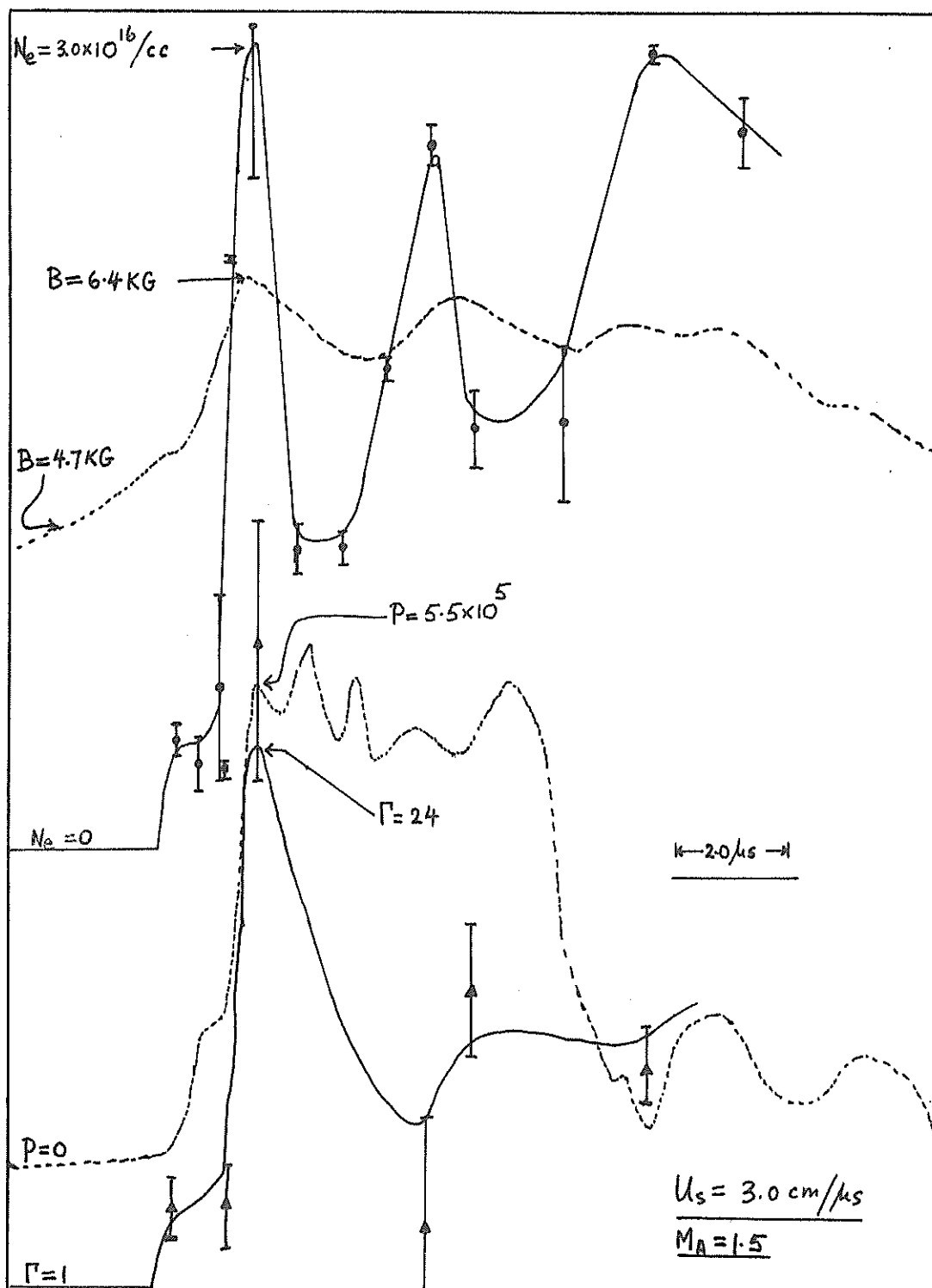
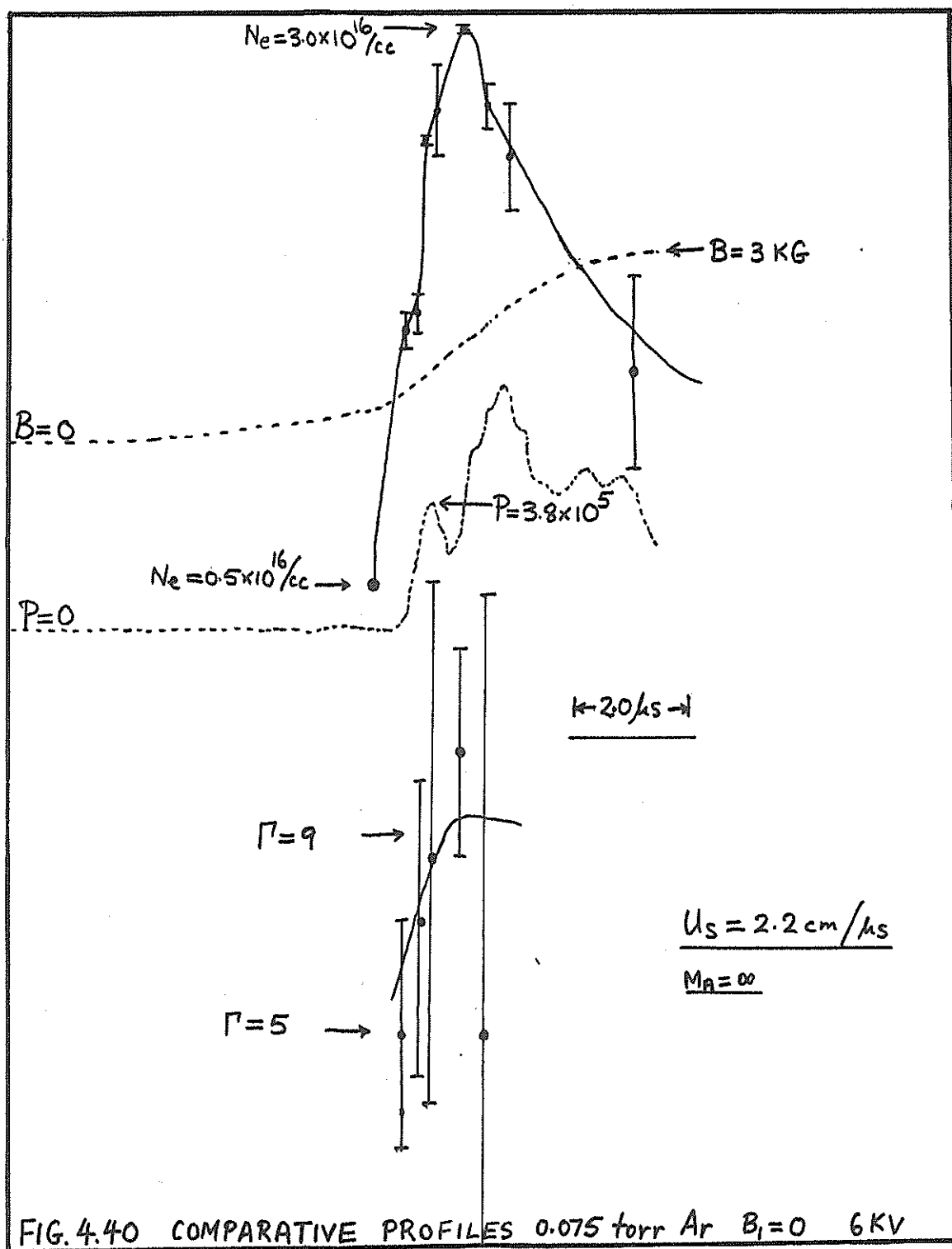
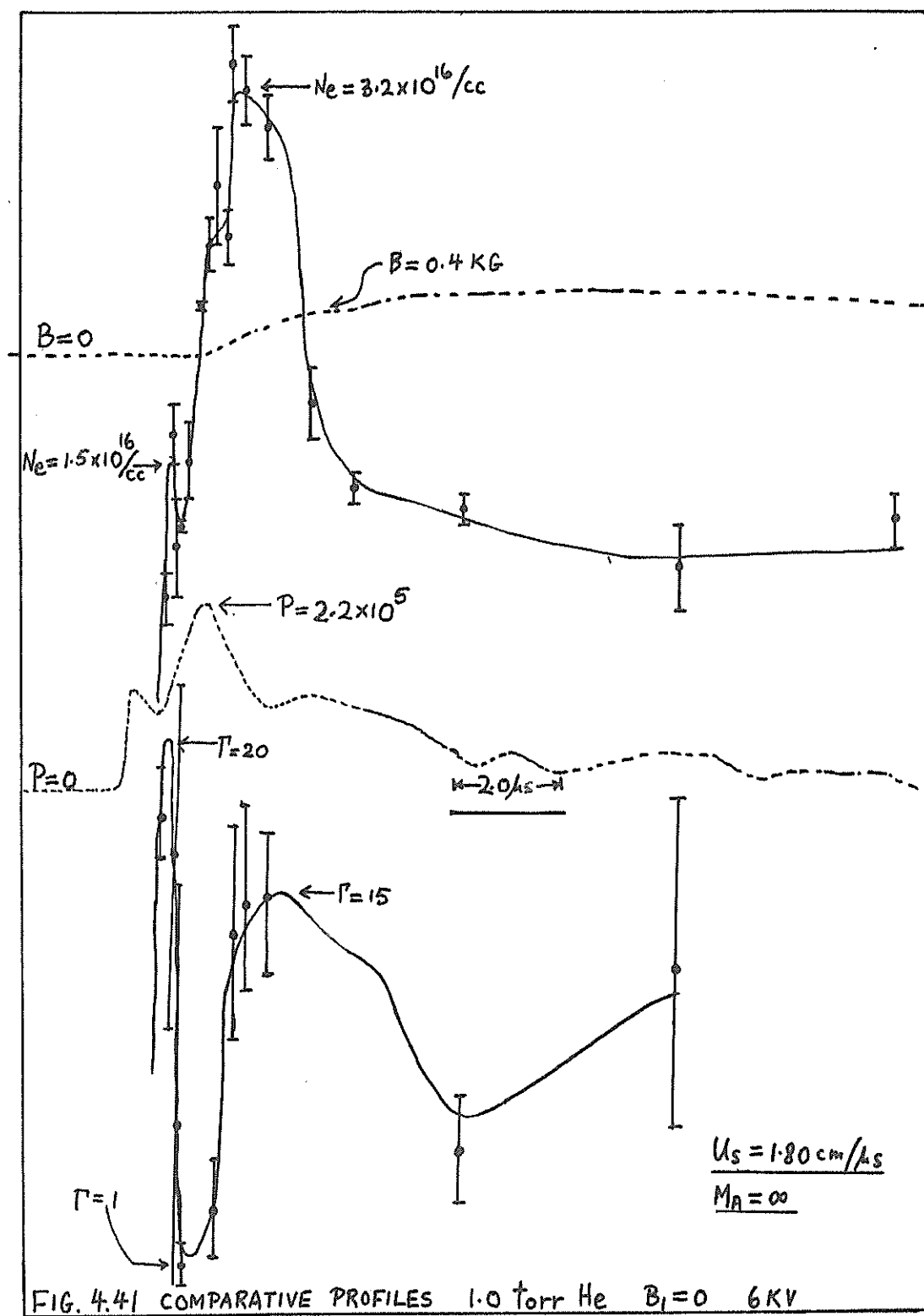


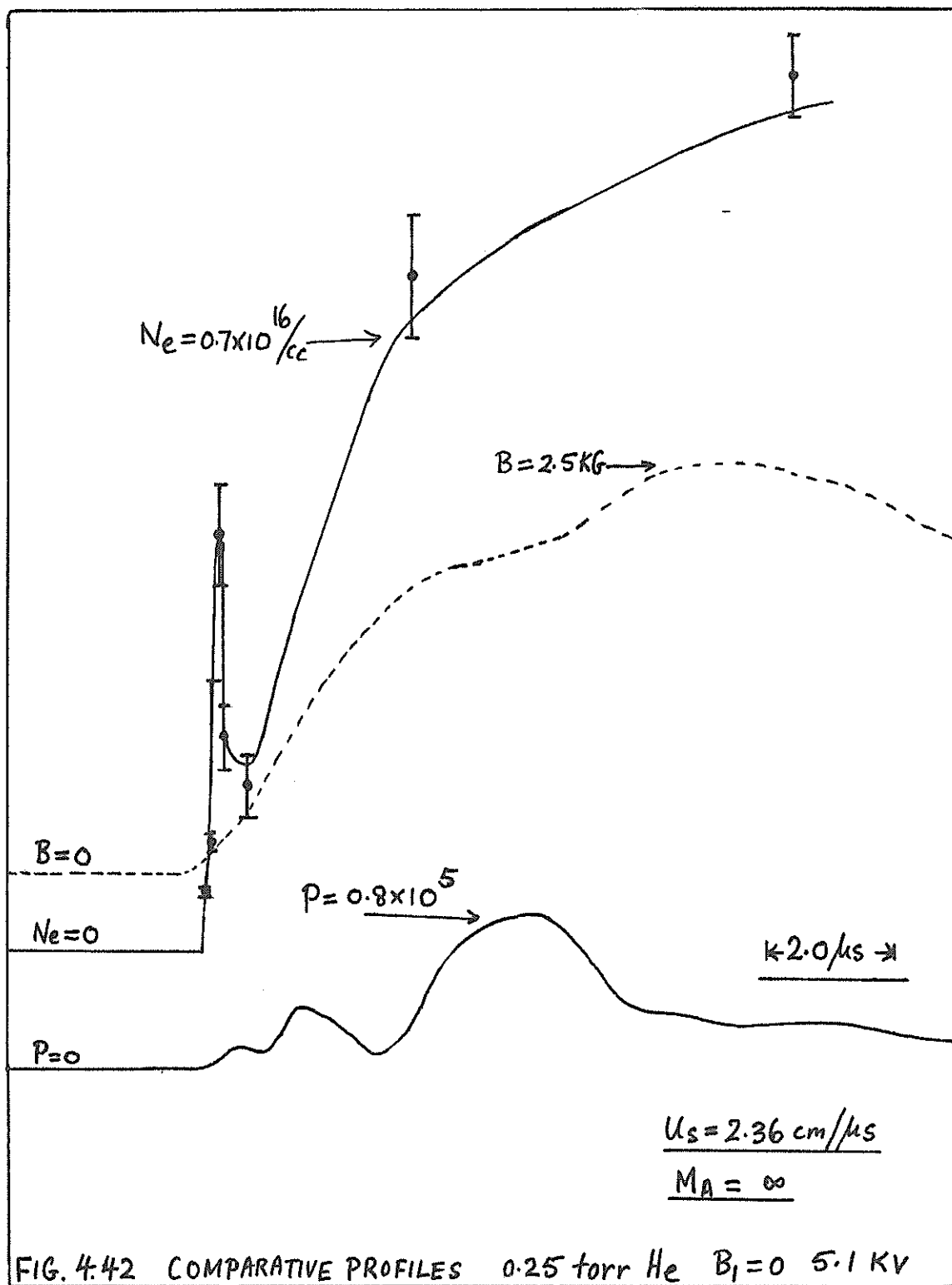
FIG. 4.39 COMPARATIVE PROFILES 0.2 torr Ar  $B_1 = 4.7 \text{ KG}$  6 KV

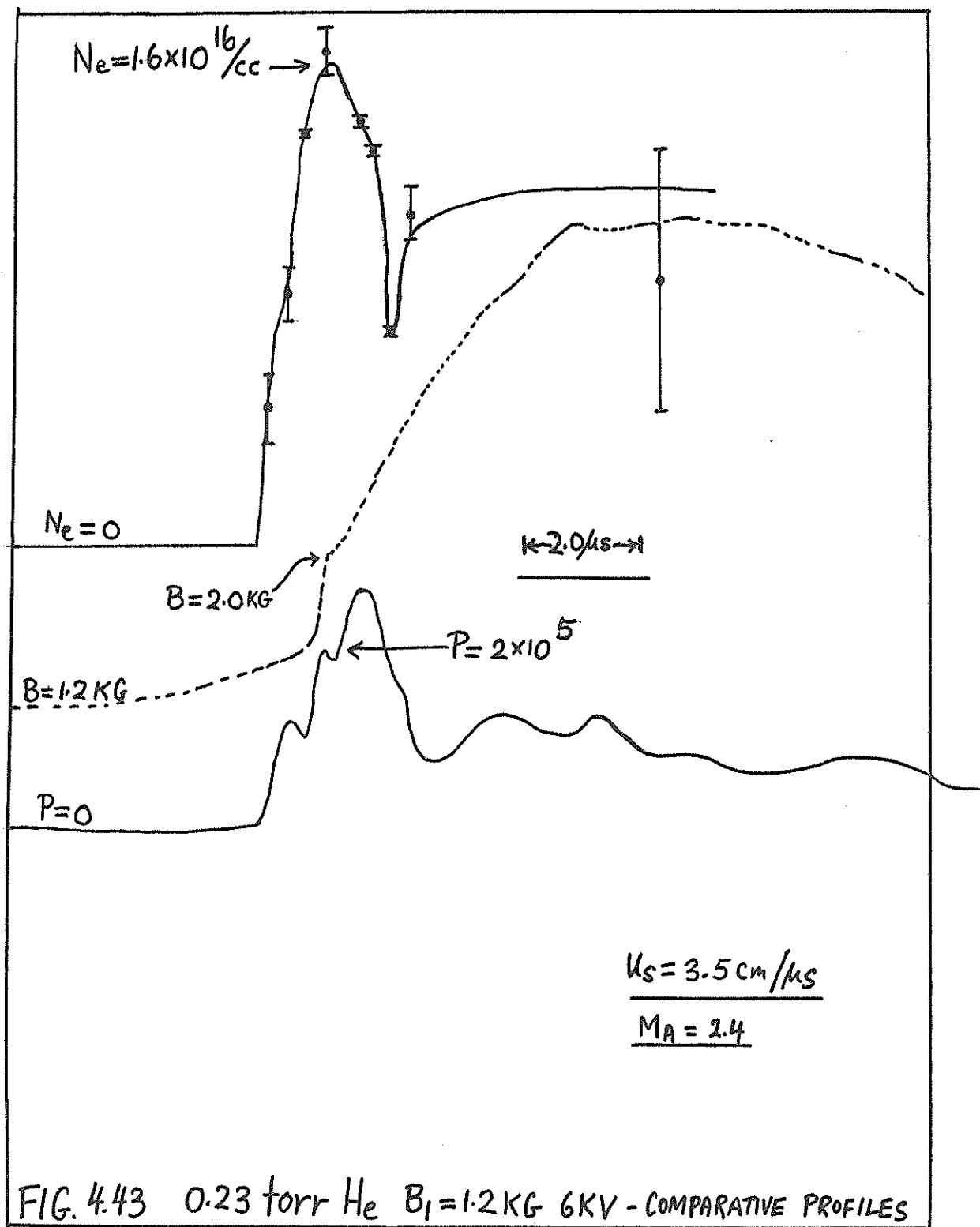


relatively small when  $B_1=0$ , becoming extremely sharp and prominent for the case  $B_1=0.87$  Kg and  $B_1=2.7$  KG; and then becoming less prominent again at  $B_1=4.7$  KG. The first peak in the total pressure probe output corresponded to this first peak in electron density in time as well as in relative amplitude. Comparing with the B signals, in the case of non-zero  $B_1$ , this first sharply peaked region corresponded to the shock-jump current region. The limited frequency response of the pressure and magnetic probes can also be seen in the comparison of the profiles. For example, in Figure 4.34, two narrow peaks, spaced about 0.3 microsec, are evident in the  $N_e$  profile. The fall time of the first of these peaks was 0.1 microsec, and the risetime of the second peak was 0.2 microsec. In the pressure profile, a double feature in the front region of the pressure pulse is just discernible having the right times as the  $N_e$  peaks, however, this feature did not separate into two distinct peaks. This is to be expected, since the fall time of the first peak, as measured from the  $N_e$  profile was 0.1 microsec, which was beyond the frequency response of the probe.

With large bias fields, in argon, the profiles developed three peaks of regular appearance separated

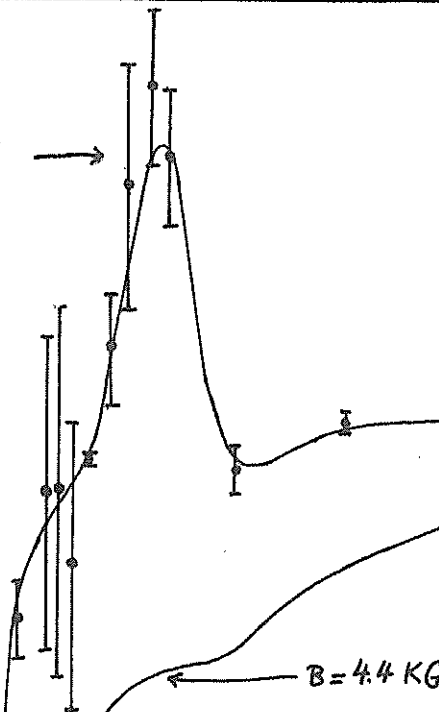








$$N_e = 1.2 \times 10^{16} / \text{cc}$$



$$B = 3.7 \text{ KG}$$

$$B = 4.4 \text{ KG}$$

$$P = 2.3 \times 10^5$$

$$N_e = 0$$

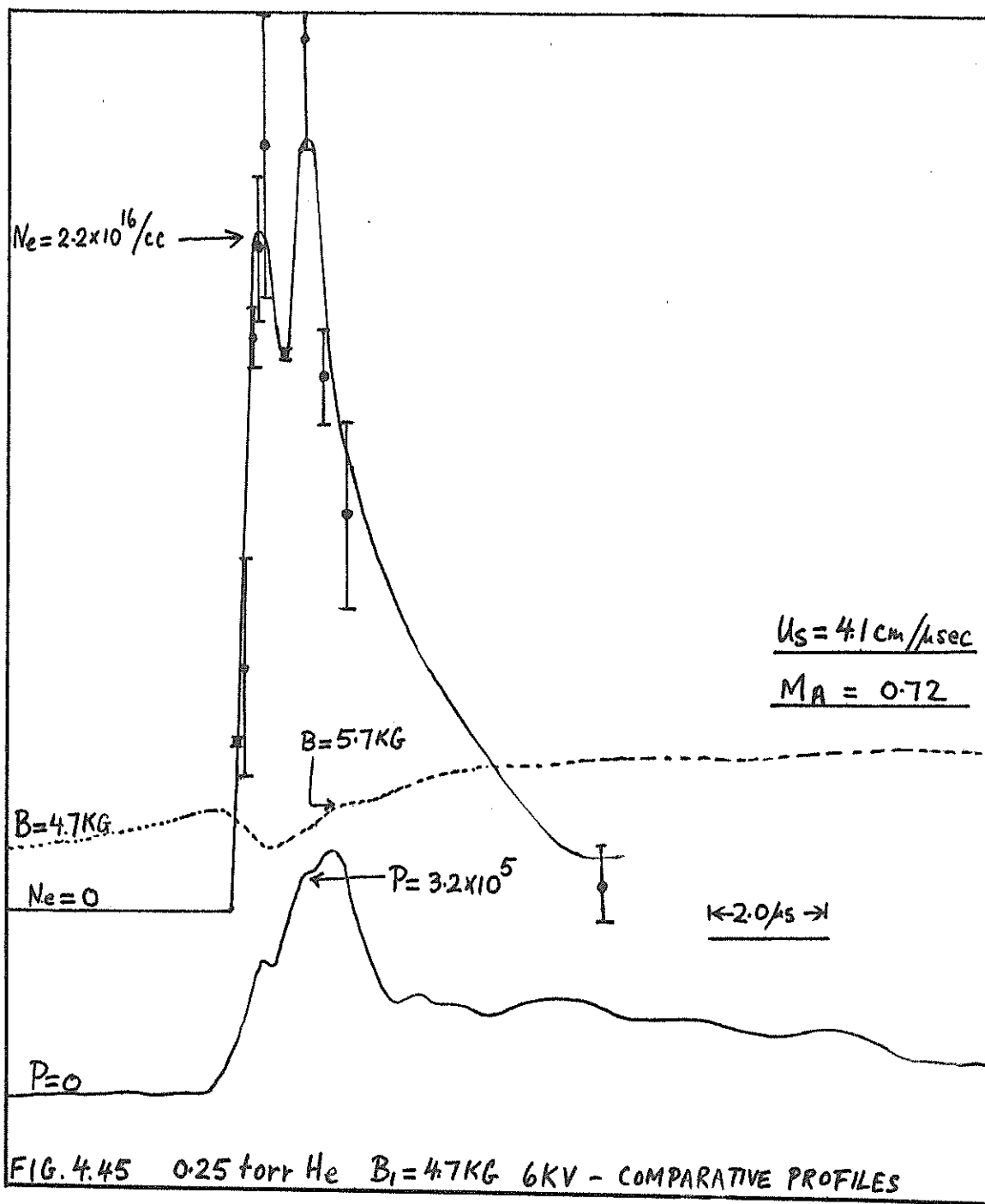
$$\leftarrow 2.0 \mu\text{s} \rightarrow$$

$$P = 0$$

$$u_s = 3.3 \text{ cm}/\mu\text{sec}$$

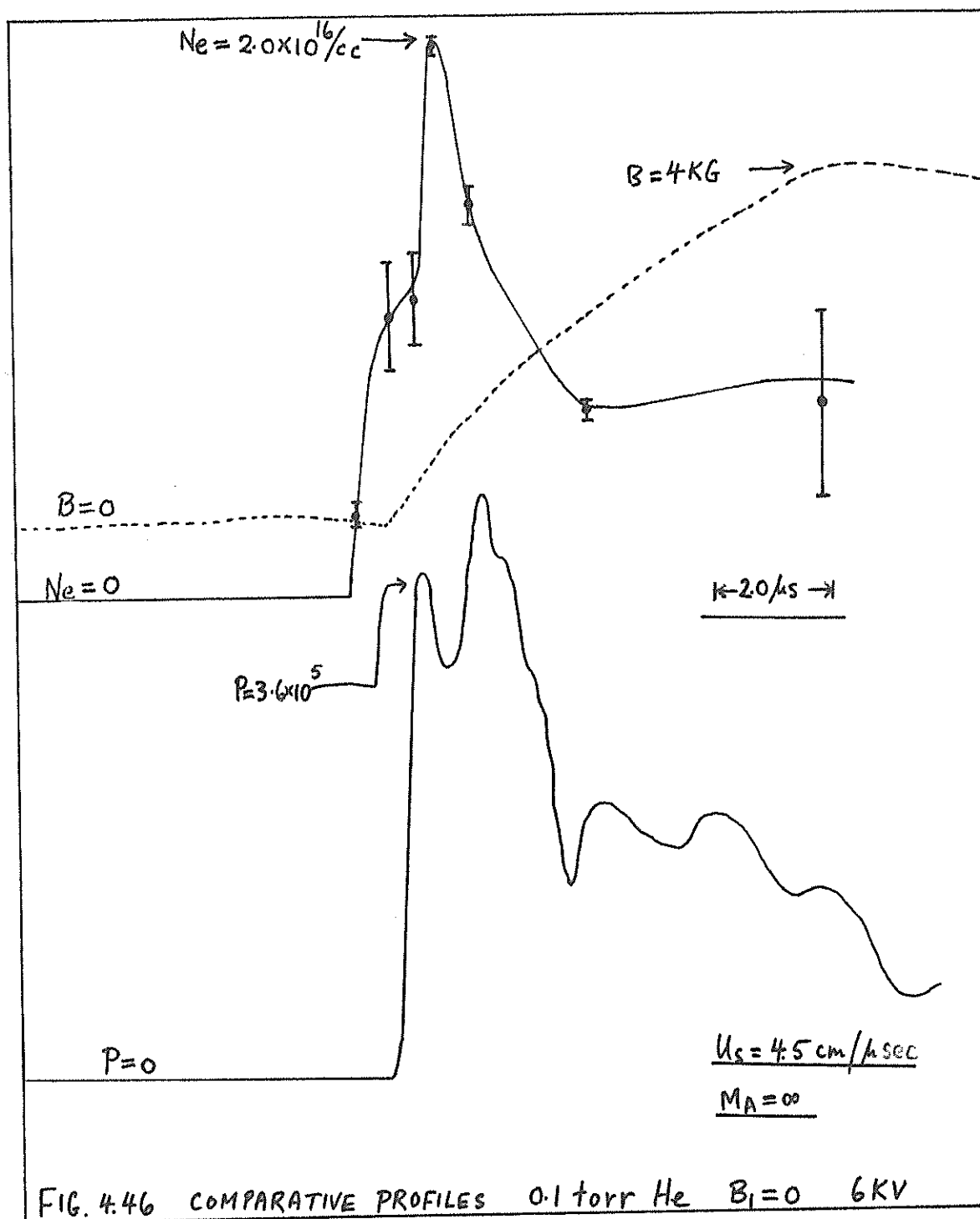
$$M_A = 0.73$$

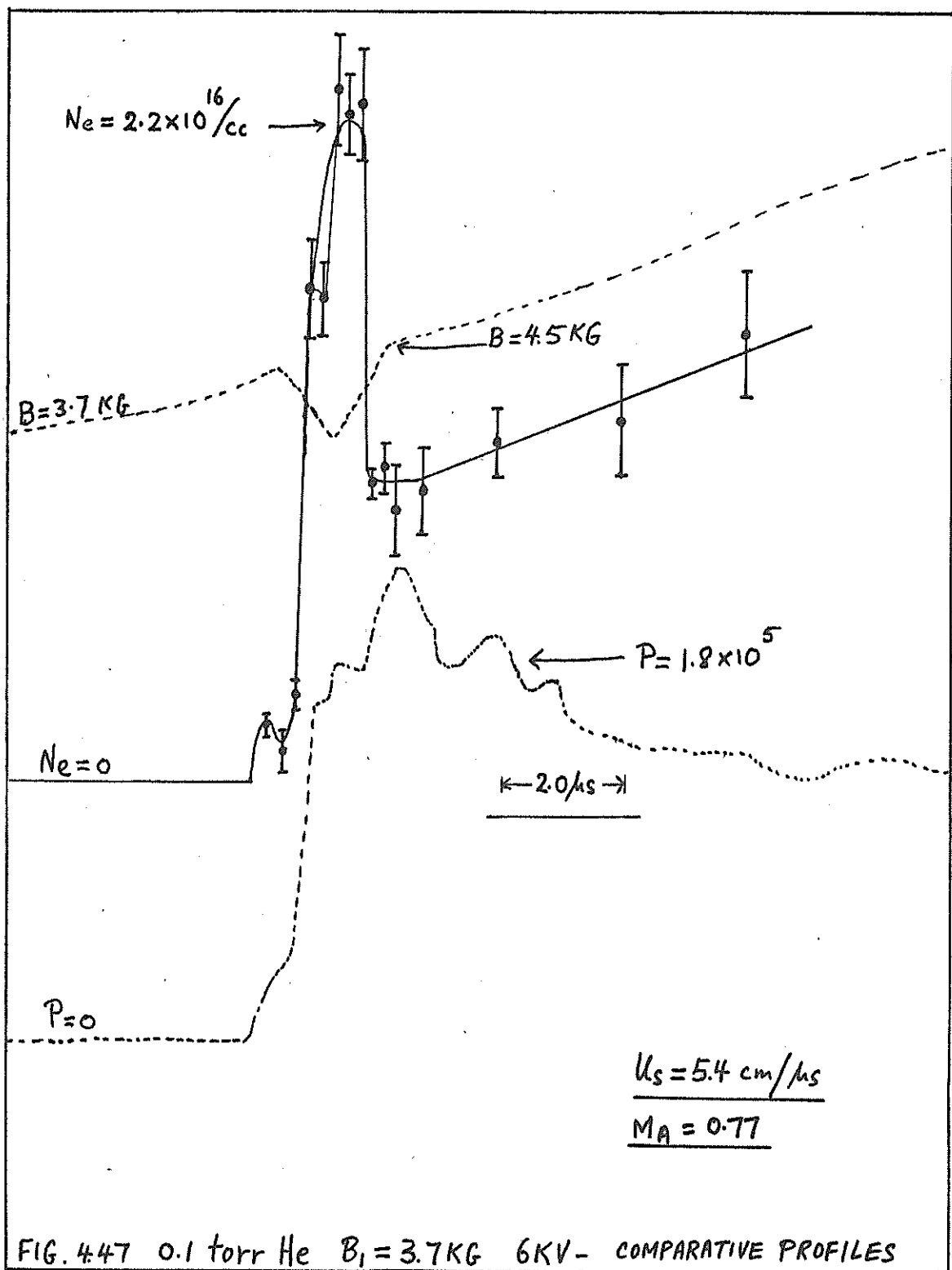
FIG. 4.44 0.25 torr He  $B_1 = 3.7 \text{ KG}$  6KV - COMPARATIVE PROFILES



by between 2 to 5 microsec. These peaks were reflected in the  $P$ ,  $B$  and  $N_e$  profiles; for example in Figure 4.36 of 0.1 torr argon with  $B_1=4$ . KG, and in Figure 4.39 of 0.2 torr argon with  $B_1=4.7$  KG. From the  $B$  profile of Figure 4.39, it is apparent that, after the initial shock-jump current, three or four regions of alternately forward and reverse current loops followed. Since the magnetic induction over this whole period remained at a large positive value, the current loops were localised loops, with the net current in the region being a positive one. In the case of 0.1 torr argon,  $N_e$  in the shock-jump region was less than in the succeeding peaks, whilst in the 0.2 torr argon case, the  $N_e$  in the shock-jump current region was larger than in the succeeding peaks.

In 1.0 torr helium, with  $B_1=0$ , a front peak of high  $\Gamma$  ( $20 \pm 5$ ) but low  $N_e$  ( $1.5 \times 10^{16}$  electrons per cc) had an ionization fraction of  $2.2 \pm 0.5$  per cent. This front peak (see Figure 4.41) was distinctly separated by about 1 microsec from a following region of lower  $\Gamma$  but higher  $N_e$ . In 0.25 torr helium, with  $B_1=0$ , this front  $N_e$  peak was about 0.1 microsec in width (Figure 4.42); and corresponds to a small pulse in the  $P$  profile entirely separated from the rest of the pressure pulse.





With a bias field, this front peak in  $N_e$  (see Figures 4.43 and 4.44) became much wider, and of larger amplitude than the separate following region. With the highest bias field of  $B_1=4.7$  KG (see Figure 4.45), the front peak separated into two. Unlike the corresponding high bias field shots in argon, however, the first peak carried reverse current; and the front region was not followed by regular peaks corresponding to current loops, as in the argon cases.

In 0.1 torr helium, with  $B_1=0$  (see Figure 4.46), the separated sharp  $N_e$  peak present in the 0.25 torr case, was not observed. Instead, a slow increase (risetime of 1 microsec) in  $N_e$  merged into a following peak. With a large bias field, see Figure 4.47, reverse current was again observed in the front peak.

#### 4.5.1.2 Summary of results and comparison with theory

The numerical results are summarized in two tables, Table 4.4 for argon and Table 4.5 for helium. Up to four quantities measured in each shot are compared with the C-J calculations. These values are  $N_e$  and  $\Gamma$  measured with the channelled spectra method, and the values of  $P$  and  $B$  monitored simultaneously. These values were measured from the region near the start of

Table 4.4: Argon results

No.	Experimental parameters				Measurements and comparison with theory					Agree- ment Index	No.
	P <sub>I</sub> Torr	B <sub>I</sub> KG	U <sub>s</sub> cm/μsec	N <sub>A</sub>	N <sub>e</sub> 10 <sup>16</sup> /cm <sup>3</sup>	Γ	P <sub>TM</sub> 10 <sup>5</sup> N/m <sup>2</sup>	B <sub>2</sub> KG			
1	0.10	0*	2.1±0.2	∞	2.2±0.2 (-81%)	13 ± 4 (15.5)	4.9±1.0 (-61%)	-	1/3	1	
2	0.10	0*	2.2±0.1	∞	4.0±0.3 (-70%)	40 ± 20(15.4)	6.5±1.5 (-57%)	-	0/2	2	
3	0.10	0.87±0.2	2.3±0.2	4.39	3.5±0.2 (-12%)	12 ± 3 ( 7.0)	2.8±1.5 (-56%)	2.2±0.2 (-46%)	2/4	3	
4	0.10	1.5 ±0.2	2.9±0.1	3.21	2.1±0.2 (-52%)	14 ± 4 ( 5.2)	-	3.7±0.2 (-34%)	0/3	4	
5	0.10	2.6 ±0.2	3.0±0.2	1.92	2.6±0.2 (-40%)	17 ± 4 ( 5.0)	4.5±0.9 (-20%)	4.8±0.3 (-19%)	2/4	5	
6	0.10	3.6 ±0.3	4.2±0.3	1.94	1.2±0.1 (-81%)	8 ± 4 ( 4.8)	5.0±1.0 (-64%)	5.5±0.5 (-30%)	0/3	6	
7	0.10	4.0 ±0.3	3.8±0.1	1.58	2.0±0.3 (-66%)	9 ± 3 ( 4.9)	5.1±1.5 (-50%)	6.8±0.5 (-15%)	2/3	7	
8	0.10	4.1 ±0.3	3.4±0.1	1.38	2.6±0.3 (-51%)	20 ± 9 ( 4.9)	5.0±1.0 (-37%)	6.4±0.4 (-14%)	1/3	8	
9	0.075	0*	2.2±0.1	∞	3.0±0.2 (-66%)	9 ± 3 (14.9)	3.8±0.6 (-66%)	1.4±0.2 ( - )	0/2	9	
10	0.20	1.0 ±0.2	1.6±0.1	3.72	2.5±0.5 (-54%)	4 ± 6 ( 4.9)	2.2±0.5 (-53%)	-	1/2	10	
11	0.20	1.3 ±0.3	2.1±0.1	3.76	2.7±0.1 (-54%)	10 ± 3 ( 4.9)	2.7±0.5 (-58%)	2.1±0.5 (-60%)	0/3	11	
12	0.20	2.6 ±0.1	2.4 0.1	2.75	2.2±0.1 (-69%)	5.5±1 ( 4.8)	3.0±0.5 (-64%)	-	1/3	12	
13	0.20	3.2 ±0.2	2.8±0.1	2.04	2.2±0.3 (-73%)	8 ± 3 ( 4.9)	5.1±1.5 (-56%)	4.9±0.5 (-30%)	0/3	13	
14	0.20	3.8 ±0.2	2.5±0.1	1.53	2.5±0.1 (-64%)	8 ± 3 ( 4.8)	4.0±1.0 (-56%)	5.2±0.5 (-30%)	1/3	14	
15	0.20	4.7 ±0.2	3.0±0.1	1.48	3.0±0.2 (-66%)	24 ± 9 ( 4.9)	5.5±1.0 (-58%)	6.4±0.3 (-25%)	1/3	15	

\* Indicates a pre-set value.

Table 4.5: Helium results

No.	Experimental parameters				Measurements and comparison with theory				Agreement Index	No.
	P <sub>l</sub> Torr	B <sub>l</sub> KG	U <sub>s</sub> cm/μsec	M <sub>A</sub>	N <sub>e</sub> 10 <sup>16</sup> /cm <sup>3</sup>	Γ	P <sub>TM</sub> 10 <sup>5</sup> N/m <sup>2</sup>	B <sub>2</sub> KG		
1	1.00	0*	1.80±0.2	∞	1.5±0.1 (-17%)	20.5	2.2±0.5 (-42%)	-	1/3	1
2	0.60	0*	2.20±0.1	∞	3.0±0.2 (-17%)	(7.5)	5.5±1.0 (+22%)	-	2/2	2
3	0.50	0*	3.00±0.2	∞	5.0±1.0 (-44%)	-	5.0±1.0 (-50%)	-	0/2	3
4	0.40	0*	3.00±0.1	∞	2.6±1.0 (-64%)	-	5.0±1.0 (-43%)	-	0/2	4
5	0.15	0*	3.50±0.1	∞	0.9±0.2 (-82%)	-	3.0±0.5 (-14%)	-	1/2	5
6	0.25	0*	2.36±0.1	∞	0.7±0.1 (-72%)	-	0.8±0.2 (-60%)	-	0/3	6
7	0.25	0.7±0.1	2.80±0.1	3.28	1.0±0.2 (+11%)	-	1.1±0.2 (-15%)	2.0±0.3 (-23%)	3/3	7
8	0.25	1.2±0.1	3.50±0.1	2.40	1.6±0.1 (+33%)	-	2.0±0.4 (+11%)	2.0±0.3 (-26%)	2/3	8
9	0.25	2.8±0.2	3.60±0.1	1.05	1.8±0.2 (+29%)	-	2.2±0.5 (+35%)	3.5±0.2 (-15%)	1/3	9
10	0.25	3.7±0.2	3.30±0.1	0.73	1.2±0.1 (+9%)	-	2.3±0.5 (+35%)	4.4±0.4 (-6%)	2/3	10
11	0.25	4.7±0.2	4.10±0.2	0.72	2.2±0.2 (0%)	-	3.2±0.6 (+23%)	5.7±0.5 (-3%)	3/3	11
12	0.10	0*	4.50±0.2	∞	2.0±0.2 (-49%)	-	3.6±0.6 (-25%)	-	1/2	12
13	0.10	1.4±0.1	3.60±0.1	1.33	0.7±0.2 (+17%)	-	0.9±0.2 (+22%)	2.0±0.4 (-20%)	3/3	13
14	0.10	2.4±0.2	4.70±0.2	1.02	1.6±0.3 (+23%)	-	1.6±0.4 (+23%)	3.3±0.4 (-3%)	3/3	14
15	0.10	2.9±0.2	4.80±0.2	0.86	1.7±0.2 (+21%)	-	1.4±0.3 (+17%)	3.5±0.2 (-10%)	3/3	15
16	0.10	3.7±0.2	5.50±0.2	0.77	1.9±0.2 (+27%)	-	1.8±0.4 (+20%)	4.5±0.5 (-4%)	2/3	16

\* Indicates a pre-set value.



the pressure pulse. This region was decided upon by a study of the profiles as discussed in the last section; and a decision was made in each case for the choice of the actual region in which the measurements were made. Whenever a shock-jump current was distinguishable, the peak values in that region were measured. The value of  $P_{TM}$  tabulated in the theory column is calculated from equation (3-45) and the theory developed in section 3.3.3.

The error attached to each measurement was estimated from a combination of calibration uncertainty, experimental scatter and the uncertainty involved in picking the peak value in the region decided upon as carrying the shock-jump current. For comparison of the measured value with the theoretical value, the quantity within brackets is used (see Table 4.4). In the  $\Gamma$  column, this quantity is the actual theoretical value; whilst in the  $N_e$ ,  $P_{TM}$  and  $B_2$  columns, this quantity is the difference between the measured value and the theoretical value, expressed as a percentage of the theoretical value. The negative sign indicates that the measured quantity is smaller than the theoretical value. As a summary of the relative agreement of the various sets of measured data when compared to the

theory, an 'agreement index' is also compiled. When a measured quantity has an uncertainty of more than 30 per cent of itself, it is not included in the index. The second number in the index indicates the number of quantities being compared, and the first number indicates the number of measured quantities that differ from their corresponding theoretical values by not greater than 25 per cent. It is immediately obvious that the measurements in helium with a bias field agree with theory better than the measurements in helium with no bias field; whilst the argon results show very poor agreement. For the  $N_e$  measurements, the argon shots, without exception, gave far lower values than the theory predicts; the disagreement being greatest when  $B_1=0$ . In helium, for the  $B_1=0$  cases, agreement is observed for the pressure range of 1.0 to 0.6 torr. Below 0.6 torr, the measured values are considerably below the gasdynamic calculations. However, when a bias field was applied, the measured  $N_e$  are in fair to good agreement with the C-J solutions.

The pressure measurements follow the same general trend, being too low by up to 65 per cent of the theoretical values for zero and small bias fields in argon. The disagreement is slightly less at higher

fields. In helium, the agreement is good over the whole range of operation, except for  $B_1=0$  with  $P_1=0.5$  to 0.15 torr, when the measured values were again low. The switch over from agreement to disagreement occurred when  $B_1$  was varied below 0.7 KG to zero. This appears to be connected with the extremely rapid change in the theoretical solutions in moving from the C-J regime into the hydromagnetic regime, the limit of which (when  $B_1=0$ ) is the pure gas solution.

The measured values of  $\Gamma$  are seen to have large uncertainties due to the experimental scatter. The measurements in 0.1 torr argon appear to be, in general, significantly larger than the predicted values, though agreement, within the limits of the large uncertainties, is observed for  $B_1=0$ ,  $U_s=2.0$  cm/microsec and for  $B_1=3.6$  to 4.0 KG. The measurements in 0.2 torr argon had a typical uncertainty of 40 per cent except for measurement no.12 with  $B_1=2.6$  KG which had an uncertainty of less than 20 per cent. Within this range of uncertainty, agreement with the theory is observed between  $B_1=1.3$  and 3.8 KG; but not at the highest bias field of 4.7 KG. These measurements do indicate that in the range of bias fields 1.3 to 3.8 KG the density ratios were between 5 to 10; with the range

narrowed to 4.5 to 6.5 for the point  $B_1=2.6$  KG,  
 $U_s=2.4$  cm/microsec.

In helium, no estimate of  $\Gamma$  was obtained except at the point  $B_1=0$ , 1.0 torr. However, it is noticed that, in the calculation of  $P_{TM}$  using equations (3-45), (3-41), (3-27) and (3-28), the state 2 quantities on which the coefficients of (3-30) depend are  $\Gamma$  and  $P_{B_2}$ . Hence, agreement with theory of both the quantities  $P_{TM}$  and  $B_2$  can be taken to be good indication that  $\Gamma$  is also in agreement. In helium, fairly good agreement in both  $P_{TM}$  and  $B_1$  is observed over the whole range of operation with a bias field.

The  $B_2$  measurements in argon were consistently lower than theory, the discrepancy with theory ranging from 46 per cent at  $B_1=0.87$  KG to 14 per cent at  $B_1=4.1$  KG for 0.1 torr; and from 60 per cent at  $B_1=1.3$  KG to 28 per cent at  $B_1=4.7$  KG for 0.2 torr. In helium, the measurements were again low compared with theory, the difference ranging from 23 per cent at  $B_1=0.7$  KG to 3 per cent at  $B_1=4.7$  KG for 0.25 torr; and from 20 per cent at  $B_1=1.4$  KG to 4 per cent at  $B_1=3.7$  KG for 0.1 torr.

It is noted that all the  $B_2$  measurements of Tables 4.4 and 4.5 and Tables 4.1 and 4.2 show a general

tendency for the disagreement with theory to be less at higher bias fields than at lower bias fields.

#### 4.5.2 Single wavelength Mach Zehnder Interferometry

Using the ruby laser ( $6943 \text{ \AA}$ ) as a shutter-light source, and integrating the refractivity effects of the plasma over the 20 cm width of the shock tube, we can expect, using the estimates of section 3.3.4.2, that the fringe shifts will be electron dominated. For example, considering 0.1 torr argon with  $\Gamma=5$  and 100 per cent single ionization, the fringe shift due to  $N_e$  would be 1, whilst that due to the argon ions of density  $N_{\text{ArII}}$  would be 0.04. In helium, considering the lowest ionization level that we expect to encounter in our experiment, namely, 5 per cent, corresponding to a speed of 2 cm/microsec in 1.0 torr with  $B_1=2.0 \text{ KG}$ , the  $N_{\text{HeI}}$  fringe shift (0.1) is still negligible compared to the  $N_e$  shift of 0.5. Because of the low level of ionization, there is the possibility of a region of unionized (less than 1/4 per cent ionization) helium (in the form of an incomplete gas shock of measurable thickness), in which the fringe shift is dominated by  $N_{\text{HeI}}$ . The fringe shift in such a region would be less than 0.05, and is unlikely to be detected.

The three prong pressure-magnetic probe assembly was positioned 6 cm downstream of the centre of the M-Z field of observation. Each of the three probes was 4 mm in diameter with 12 mm separating the centres. The probes were constructed mainly as timing devices, with only short backing rods. The risetime of each probe was 0.2 microsec; and the sensitivity of the middle probe was approximately half of that of the other two. The magnetic coils were of standard design and performance, as discussed in section 3.3.2.

The oscilloscopes used in monitoring the pressure and magnetic signals were calibrated to better than 2 per cent. These were triggered by a variable delay unit which itself was triggered either by the main discharge synchronising pulse, or by a photo-diode amplifier system focussed on the centre of the shock tube 24 cm upstream of the probe. The time of laser exposure relative to the start of each oscilloscope trace was checked from time to time with a 20 nsec photo-diode system, looking into the M-Z test beam through a narrow band  $6943^0 \text{ \AA}$  filter. It was found that all the oscilloscope sweeps started  $0.60 \pm 0.04$  microsec before the rising edge of the laser light pulse, the half width of which was less than 50 nsec. In each of

the shots analysed, the times between laser exposure and the arrival of the pressure and magnetic fronts at the probes were measured. These were then converted to distances on the interferogram by using the measured shock velocity. These distances were then used to correlate the start of the pressure and magnetic signals (as well as other prominent features such as the start of the expansion current) with the electron density structures exhibited by the interferogram. An estimated uncertainty of 3 to 8 mm was associated with these correlation studies.

A feature of these interferograms was that they were very reproducible. As we shall see, a large variety of features were observed under different operating conditions, including anode lead, cathode lead, straight and curved inclinations and anode and cathode layers. However, at each operating condition, the electron density features and their correlation to the pressure and magnetic probes were highly reproducible; for example, the angle of inclination of the pressure front or current front at one operating condition varied by less than 10 per cent from shot to shot.

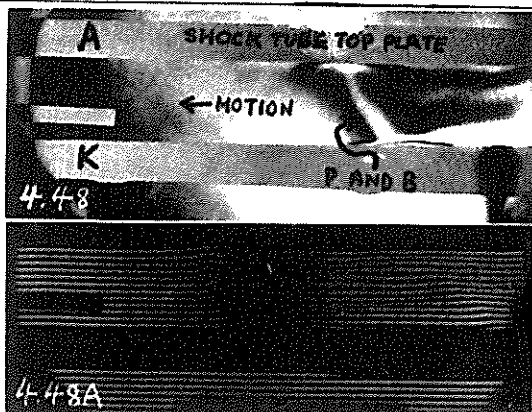


Fig.4.48 0.1 torr Ar,  
 $B_1=3.6$  KG, Infinite fringe  
(I.F.).

P and B fronts indicated.

Fig.4.48A Finite fringes

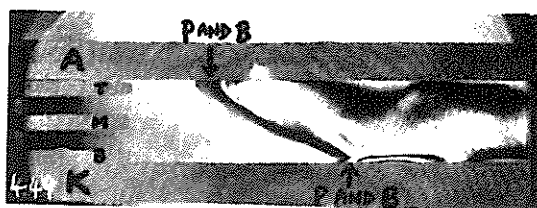


Fig.4.49 0.24 torr Ar,  
 $B_1=2.7$  KG (I.F.)

P and B fronts indicated.

$$U_s = 1.8 \text{ cm}/\mu \text{ sec.}$$

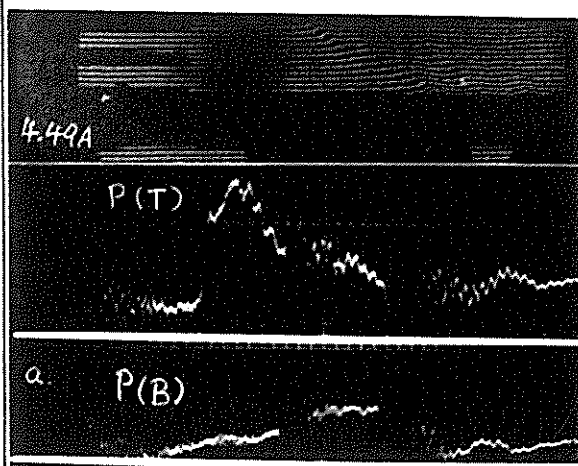


Fig.4.49A 0.3 torr Ar,  
 $B_1=3.6$  KG

a. P(T), output of top pressure probe.

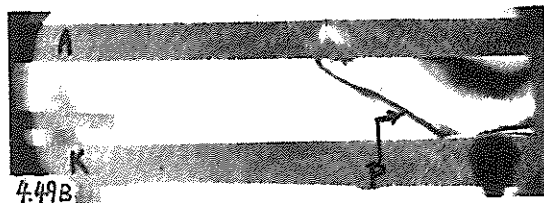
P(B), output of bottom pressure probe.

1  $\mu \text{sec}/\text{cm}$ .

same vertical sensitivity

Fig.4.49B 0.3 torr Ar,  
 $B_1=3.6$  KG (I.F.)

P front indicated.





#### 4.5.2.1 Argon interferograms

In argon, the most noticeable feature was an inclination of the pressure-current front of between 30 to 60° from the vertical, with the anode side leading. This was observed for the whole range of operation between 0.1 torr to 0.3 torr and with  $B_1=0$  to  $B_1=4$  KG. A list of the inclinations under different operating conditions will be given in the summary together with the helium results. In all cases observed, the effect of a strong magnetic field was to produce a sharply defined front.

Figure 4.48 shows the infinite fringe interferogram for 0.1 torr argon with  $B_1=3.6$  KG. The frontal region, about 1 cm thick has a sharply defined light structure embedded in a more diffused outer dark region. The central region had approximately 1 fringe shift (corresponding to  $1.6 \times 10^{16}$  electrons/c.cm) and extended as a uniform structure from anode to 1 or 2 mm above the cathode where it encountered a very thin and dense cathode layer having a peak density of about three fringe shifts ( $4.8 \times 10^{16}$  electrons/c.cm), the third fringe shift occurring so close to the cathode surface (less than  $\frac{1}{2}$  mm) that it is just perceptible on the interferogram. The start of the pressure and magnetic

pulse correlated with the sharply defined central light feature of the frontal region. At higher pressures, this front region became even more sharply defined as shown in Figure 4.49, of 0.24 torr argon with  $B_1 = 2.7$  KG. The front had a fringe shift of again one, over a thickness of 3 mm, with a region of fairly uniform density following it. The front was inclined at an angle of  $60^\circ$  from the vertical. The cathode layer was again prominent extending slightly past the main front giving the appearance of a small cathode 'foot'. The pressure and magnetic fronts were also similarly inclined and the measurements indicate that these fronts lay from 5 to 10 mm behind the start of the electron density front shown on the interferogram. This separation was just measurable experimentally.

The pressure probe profile correlated remarkably well with the electron density profile, particularly when the drive current had fallen to small values. This is illustrated by Figure 4.49A, where the fringe pattern was arranged for increasing refractivity in the downward direction, so that the upward shift represented electron density. The top pressure probe (Figure 4.49Aa) showed a pressure jump occurring over 0.2 microsec. Measurements show that this sharp rise

corresponded to the sharp fringe shift just below the anode. The slow rise of the pressure pulse (1 microsec) exhibited by the bottom pressure probe corresponded well to the 2.5 cm region of gradual fringe shift at the cathode region. The peak of the shift at both the anode and cathode regions was approximately 1 fringe, corresponding to an electron density of  $1.6 \times 10^{15}/\text{c.cm}$ .

It is noted that the single wavelength method of M-Z interferometry, as applied to this shock tube, cannot be expected to give quantitative estimates of  $N_e$  to better than 0.2 of a fringe shift ( $0.32 \times 10^{16}$  electrons/c.cm), using the finite fringe pattern; and to 0.3 of a fringe shift ( $0.48 \times 10^{16}$  electrons/c.cm), using the infinite fringe method. For example, the estimate of peak  $N_e$ , half way between the anode and the cathode in Figure 4.48 gives  $(1.6 \pm 0.5) \times 10^{16}$  electrons/c.cm; whilst the channelled spectra method gives a value of  $(1.2 \pm 0.1) \times 10^{16}$  electrons/c.cm.

#### 4.5.2.2 Helium interferograms

In helium, the pressure, current and electron density fronts were observed to have inclinations, with either the anode or the cathode side leading, depending on the shock tube operating parameters.



Fig.4.50 1.0 torr He,  $B_1=0$

(I.F.).

$x=25$  cm.  $U_s=2.2$  cm/ $\mu$  sec.

All horizontal axes of oscillograms: 1  $\mu$ sec/cm.

(T): indicates top probe

(B): indicates bottom probe.

P probes have same sensitivity

B probes have same sensitivity

Traces start 0.6  $\mu$  sec before exposure of the interferogram.

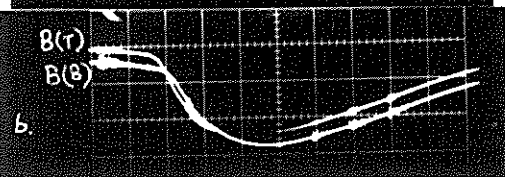
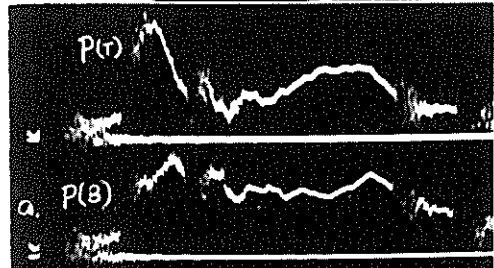


Fig.4.50A 1.0 torr He,  $B_1=0$

Finite fringes.

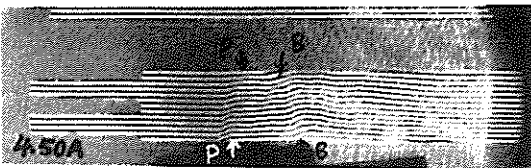


Fig.4.51 1.0 torr He,  $B_1=$

0.33 KG, Finite fringes.

$x=25$  cm.  $U_s=2.3$  cm/ sec.

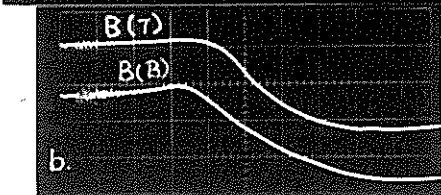
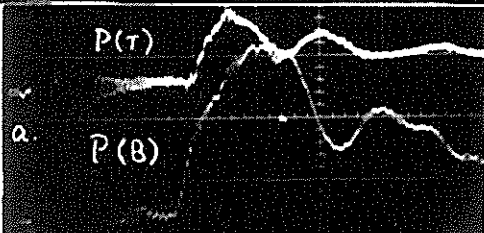
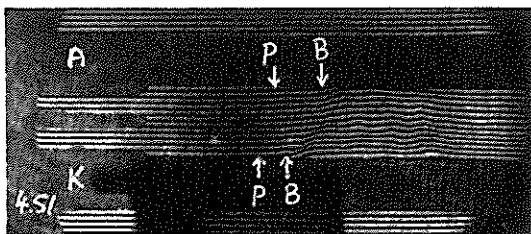
All horizontal axes of oscillograms: 1  $\mu$ sec/cm.

P and B fronts indicated on interferogram.

a. P outputs, same sensitivity

b. B outputs, same sensitivity

(Note cathode leading current sheet).



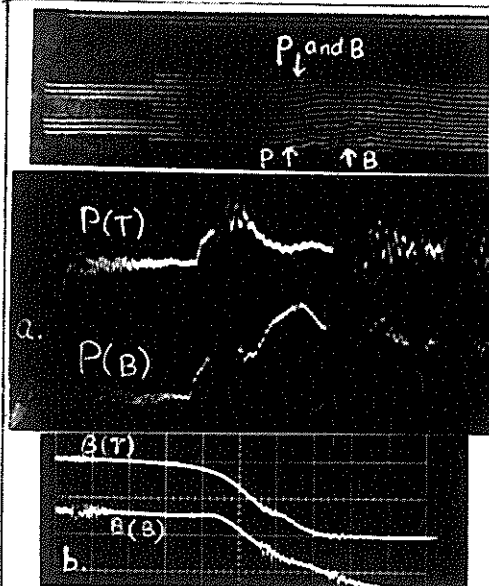


Fig.4.52 1.0 torr He,  $B_1 =$   
0.53 KG, Finite fringes.

$x = 25$  cm.  $U_g = 2.3$  cm/ $\mu$ sec.  
P and B fronts indicated on  
interferogram.

All horizontal axes of  
oscillograms: 1  $\mu$ sec/cm.

a. P outputs, same sensitivity  
b. B outputs, same sensitivity

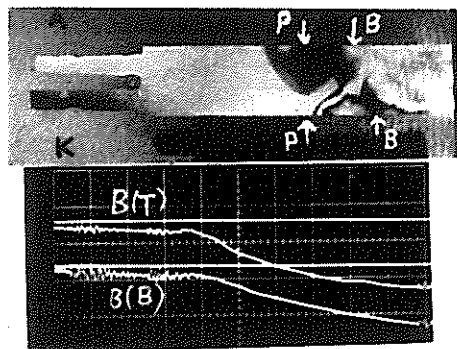


Fig.4.53 1.0 torr He,  $B_1 =$   
2.2 KG (I.F.).

$x = 25$  cm.  $U_g = 2.8$  cm/ $\mu$ sec.  
P and B fronts indicated on  
interferogram.

Fig.4.54A 1.0 torr He,  $B_1 =$   
3.6 KG (I.F.).

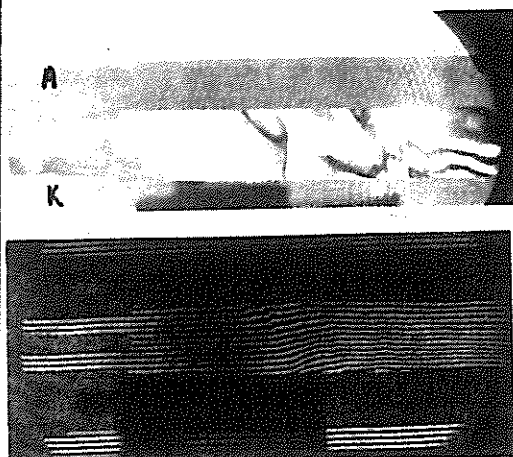


Fig.4.54B 1.0 torr He,  $B_1 =$   
3.6 KG, Finite fringes.

At  $x=25$  cm (centre of view), with  $B_1=0$ , a cathode leading pressure pulse (see Figure 4.50 and 4.50A with a fringe shift of 1 was followed by an anode leading current sheet with a fringe shift of  $2\frac{1}{2}$ ; with a separation of 1 cm in the anode region and  $2\frac{1}{2}$  cm in the cathode region. The pressure front position corresponds roughly to the first dark fringe shift in Figure 4.50. When a bias field was applied and increased in value (Figure 4.51 to 4.54), an anode leading initial front eventually developed corresponding to a distinguishable shock-jump current in the B trace. In this series at  $B_1=0.33$  KG, the pressure pulse had a slight cathode lead, with less than  $10^\circ$  inclination. The interferogram (Figure 4.51) did not reveal the presence of this pressure pulse, which at the cathode was about 1 cm and at the anode 2 cm ahead of the cathode leading fringe shift. This fringe shift corresponded to a cathode leading current front; as determined by the magnetic probes.

With further increase of  $B_1$  to 0.53 KG (see Figure 4.52), the pressure front (Figure 4.52a) was now almost vertical, whilst a diffuse anode lead developed at the current front (Figure 4.52b); this current front was close to the pressure front at the anode, but was some 2 cm behind the pressure front at the cathode.

The first fringe shift in the interferogram carried the diffuse current near the anode with the pressure front just behind; but no current flowed in that fringe shift near the cathode. Partitioning of the current was beginning to become evident on the B probe signal. The fringe shift appeared to be less sharp than the  $B_1=0$  case.

Above  $B_1=1$  KG, the anode lead had become very curved and of peculiar shape. This anode feature did not extend more than 5 mm below the anode plate at  $B_1=1$  KG; but by  $B_1=2.2$  KG, this anode structure had extended past the centre line between the plates. The pressure front corresponding to this interferogram (Figure 4.53), arrived at the same time at the top and bottom pressure probes; and was about 1 to 2 cm behind the front most region of the anode structure on the interferogram. The current sheet was a further 2 cm behind the pressure front and had a distinct anode lead. Figures 4.54A and 4.54B show the further development of the fringe shift structure at  $B_1=3.6$  KG. The electron density front was now vertical from the cathode almost to the anode; but, about halfway between the anode and cathode, a second feature developed,

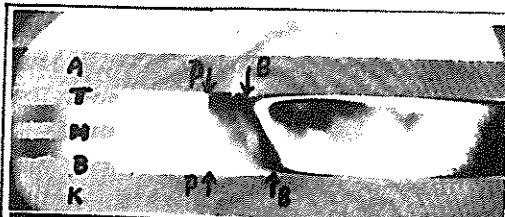


Fig.4.55 1.0 torr He,  $B_1=0$

(I.F.)

$x=65$  cm.  $U_s=1.9$  cm/ $\mu$ sec.

Positions of P and B fronts indicated on interferogram.

a. P(B) and P(M), output of bottom and middle pressure probes; sensitivity of P(B) is twice that of P(M).

1  $\mu$ sec/cm.

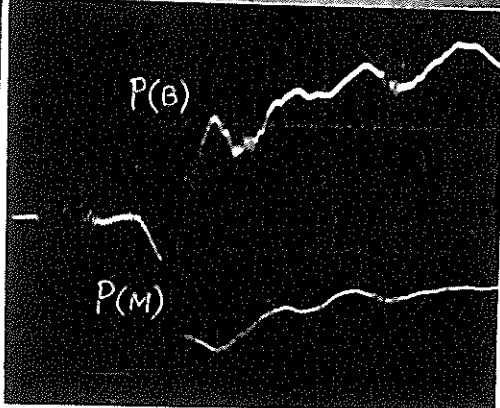


Fig.4.56 1.0 torr He,  $B_1=$

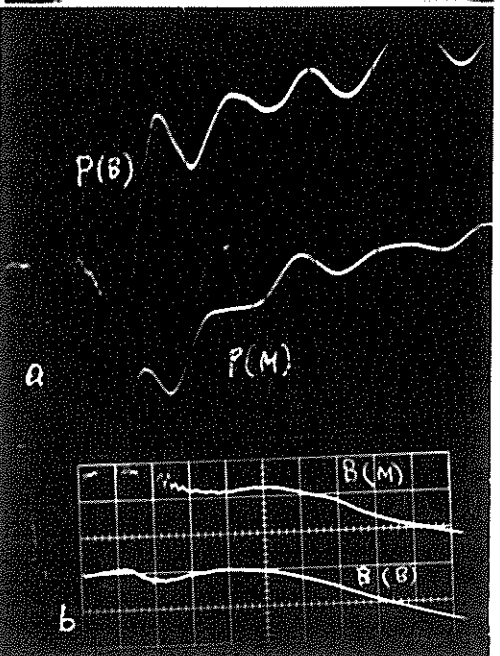
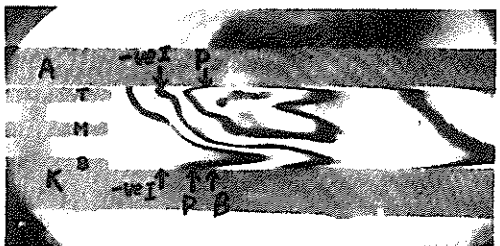
3.3 KG (I.F.)

$x=65$  cm.  $U_s=2.7$  cm/ $\mu$  sec.

Positions of P and positive B jump, and negative current (or negative B jump) are indicated on interferogram.

a. Sensitivity of P(B) twice that of P(M).

b. B(B) and B(M) have same sensitivity.





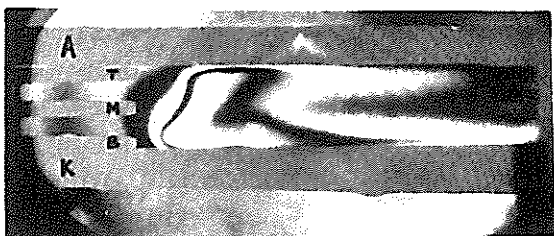
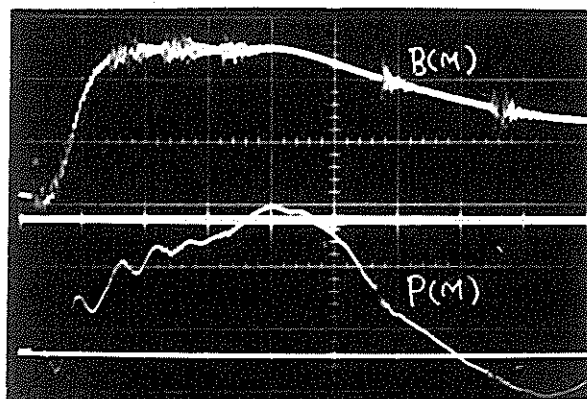
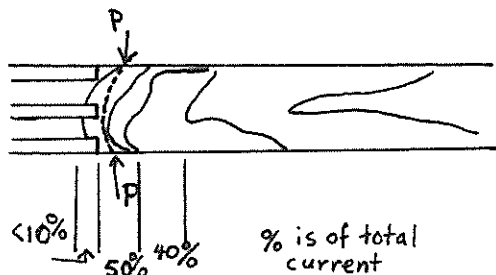


Fig.4.57 0.25 torr He,  
 $B_1 = 0$  (I.F.).

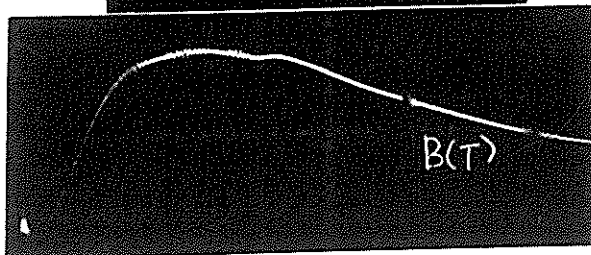
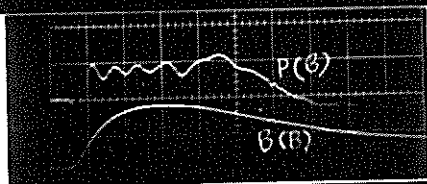
$x=65$  cm.  $U_g=3.2$  cm/ $\mu$ sec.

Accompanying sketch shows positions of current and pressure fronts relative to the features on the interferogram. (Accuracy  $\pm 2$  mm on the interferogram.)



All horizontal axes on the oscillograms: 1  $\mu$ sec/cm.

- a. Pressure signals, same vertical sensitivities.
- b. magnetic probe signals, same vertical sensitivities.



bending to an inclination of  $40^\circ$  to the vertical, forming the anode lead.

Further down the tube, at  $x=65$  cm, the electron density structures appear to become more uniform. At  $B_1=0$  the pressure pulses corresponding to Figure 4.55 show a vertical pressure front that was just in front of the first anode fringe shift in the interferogram. The current front had an anode lead, lying about 2 cm behind the pressure front and correlated well with the sharply defined structure (darkest line) that ran continuously from the anode to the cathode in the interferogram. With  $B_1=3.3$  KG, the pressure pulse was situated 2 to 3 cm behind the first fringe shift in Figure 4.56. The region just ahead of the pressure front contained a reverse current loop of about 5 KA. The shock jump current started 1 cm behind the pressure pulse.

At lower pressures, the interferograms look considerably different. For example, Figure 4.57 shows the electron density structure for 0.25 torr, with an accompanying sketch showing the pressure and magnetic fronts. The front-most electron density feature was the curved dark band with half a fringe shift and carrying less than 10 per cent of the total current.

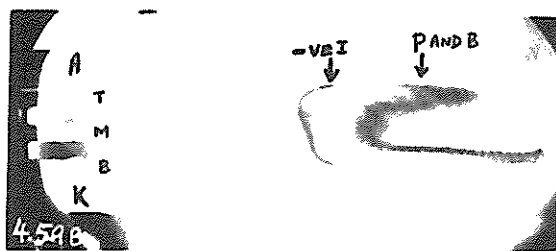
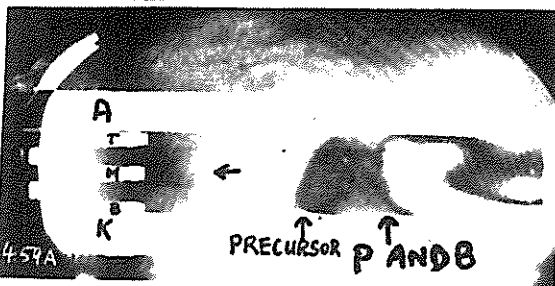
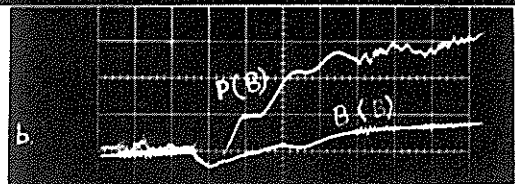
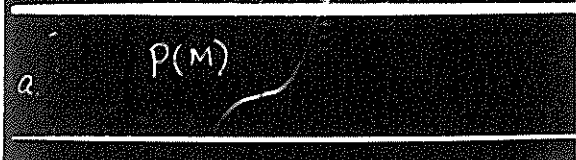
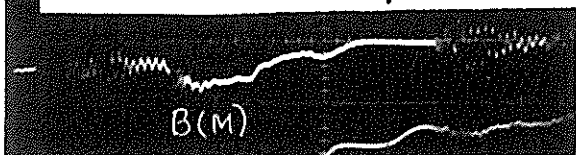
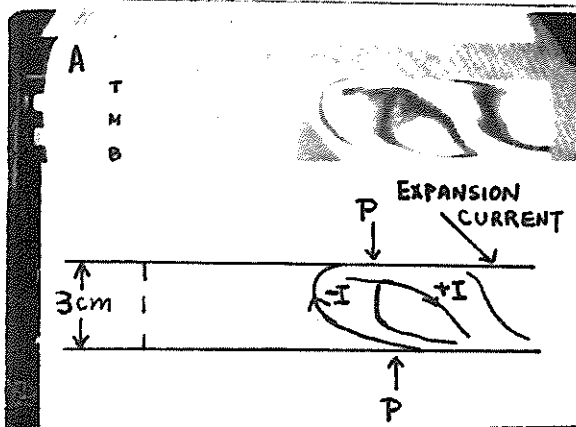


Fig.4.58 0.3 torr He,  
 $B_1 = 3.6$  KG (I.F.).

$x=65$  cm.  $U_s=3.5$  cm/ $\mu$  sec.  
Accompanying sketch shows  
positions of positive and  
negative current fronts  
and pressure features  
relative to features on  
the interferogram .

(Accuracy:  $\pm 2$  mm on the  
interferogram).

All horizontal axes:

$1/\mu$  sec/cm.

- a. P(B) has twice the  
vertical sensitivity as  
P(M).
- b. B(B) and B(M) have  
same vertical sensitivity.

Fig.4.59A 0.1 torr He,  
 $B_1 = 0$  (I.F.).

$x=65$  cm.  $U_s=4.4$  cm/ $\mu$  sec.  
P and B fronts indicated;  
also precursor ionization.

Fig.4.59B 0.1 torr He,  
 $B_1 = 3.6$  KG (I.F.).

$x=65$  cm.  $U_s=5.4$  cm/ $\mu$  sec.  
P and B fronts indicated.

The pressure front was embedded near the back of this curved band. Between the pressure front and the thin dark density contour, the fringe shift had increased by another half, and this region carried 35 per cent of the total current. The 2-cm region following this thin dark fringe contour had a fairly uniform electron density corresponding to 2 fringe shifts ( $3.2 \times 10^{16}$  electrons/c.cm). In this region 30 per cent of the current flowed. The fringe shift then decreased back to 1.

With a bias field of  $B_1 = 3.6$  KG (Figure 4.58), the current and pressure distributions are shown in the accompanying sketch. The thin curved dark density contour was determined to be the start of a region of negative current. The pressure front was roughly at the position of the vertical contour lying  $2\frac{1}{2}$  cm behind the thin curved front; and had a slight anode leading inclination of less than  $10^\circ$  from the vertical. The positive shock jump current lay 1 to 2 cm from the start of the pressure front and occupied some 2 cm. Following this was a 2 cm region of negligible current, behind which the expansion current started to flow. A central region of high density, with  $3.2 \times 10^{16}$  electrons/c.cm, is prominent, corresponding to the

enclosed island between the pressure front and the shock-jump current.

With 0.1 torr helium (Figure 4.59A) a region of precursor electron density extended 2 to 3 cm ahead of the pressure and current fronts which were at the same position. This position correlated with the thin dark density contour separating the precursor dark patch from the post shock (light) region of uniform electron density. With a bias field of  $B_1 = 3.6$  KG (Figure 4.59B), the correlation studies reveal the same gross features as the 0.3 torr case, except that the pressure pulse now lay further back, starting just before the expansion current region. The high density island, observed in the 0.3 torr case, was not present for the 0.1 torr case.

#### 4.5.2.3 Summary and discussion of interferograms

The study of the interferograms show that, although the pressure, magnetic field and electron density fronts show complex structures, a number of features can, in general, be distinguished. Firstly, there was an inclination from the vertical of the fronts, the angle of inclination being greater for argon than for helium. Secondly, there was an anode 'growth'

that was prominent in the 1.0 torr helium fronts when the bias field was increased to above  $B_1 = 1$  KG; this 'growth' was absent in the low pressure helium fronts and was present, but not prominent, in the argon fronts. Thirdly, there was a reverse current region that was present at large bias fields, which between 0.1 to 0.3 torr in helium, lay ahead of both the pressure and shock-jump current fronts. For 0.2 torr argon, this reverse current region lay behind the pressure and shock jump current regions as discussed in the channel spectra results. Finally, precursor electrons were observed for 0.1 torr helium with  $B_1 = 0$ .

As a summary, the Hall parameters  $\omega_e \tau_e$  and  $\omega_i \tau_i$ , and the radii of gyration  $r_{ge}$  and  $r_{gi}$  of the different discharge conditions are listed in Table 4.6 with the angles of inclination from the vertical. It is noted that the Hall parameters and the radii of gyration are calculated from the theoretical values of the temperatures, and the measured values of the electron densities and magnetic fields in the region of the inclined front. In addition, another parameter is listed, designed to give an indication of the relative magnitude of the ion drag effect at the cathode. This effect has to be considered because in the immediate

neighbourhood of the cathode ions can be expected to carry at least a fraction of the current from the discharge to the cathode<sup>86,43</sup>. The impact of the ions on the cathode results in a drag on the current sheet at the cathode side, which can be responsible for the anode lead. For consideration of the current sheet tilt, the quantity of importance is not the absolute value of the drag but the ratio  $R$  of the momentum per second lost to the cathode divided by the momentum increase per second of the entrained mass of the entire current sheet. If we assume that a fraction ' $f$ ' of the total current  $I$  is carried by the singly ionized ions, then the number of ions required to carry the current  $fI$  to the cathode is  $fI/e$ , where  $e$  is the electronic charge. If we further assume that on impact with the cathode, a neutral is reflected back into the flow (to satisfy the requirement of mass conservation) but that during the process the forward momentum of the original particle is completely lost to the wall, then the total momentum lost per second is  $fI(m/e) \times 1845A(q_1 - q_2)$ , where  $m$  is the electronic mass and  $A$  the atomic number of the ion; which we write as  $KfIA(q_1 - q_2)$  where  $K$  is a constant. Hence,

$$R = \frac{KfIA(q_1 - q_2)}{\rho_1 q_1 (q_1 - q_2)} \quad . \quad (4-1)$$

But for a given current  $I$ ,  $q_1$  is proportional to  $(\rho_1)^{-\frac{1}{2}}$  on momentum exchange basis (equation (2-72)). We therefore have:

$$R = \frac{KfIA}{\rho_1^{\frac{1}{2}}} \quad . \quad (4-2)$$

For constant values of  $I$  and  $f$ , we have  $R$  proportional to  $F$  where,

$$F = A \rho_1^{-\frac{1}{2}} \quad . \quad (4-3)$$

If ion impact on the cathode contributes significantly to current sheet tilt, then, on the assumption that  $f$  is a constant for a fixed  $I$ , we can expect the tilt to be related to the size of  $F$ . We include the value of  $F'$  in Table 4.6, which is the value of  $F$  normalized to 0.1 torr argon.



Table 4.6: Current sheet parameters

	$P_1$	$B_1$	$\omega_e \tau_e$	$\omega_i \tau_i$	$r_{ge}$	$r_{gi}$	$F'$	$\theta'$
	Torr	KG			mm	mm		o
$A_r$	0.1	0	0.7	0.003	0.01	17	1	50
	0.15	0	0.4	0.002	0.05	17	0.8	50
	0.1	3.3	1.5	0.005	0.02	5	1	40
	0.1	3.6	2.0	0.008	0.02	5	1	30
	0.24	2.7	0.5	0.002	0.01	2.5	0.6	58
$H_e$	0.1	3.6	0.5	0.01	0.01	0.8	0.3	5
	0.25	0	0.1	0.001	0.05	4	0.2	5
	0.3	3.6	0.5	0.01	0.01	0.8	0.17	25
	1.0	0	0.1	0.001	0.05	4	0.1	20
	1.0	0.33	0.15	0.002	0.03	2	0.1	-
	1.0	0.53	0.15	0.002	0.03	2	0.1	40
	1.0	1.6	0.2	0.003	0.03	2	0.1	35
	1.0	1.9	0.3	0.004	0.02	1.2	0.1	35
	1.0	2.2	0.4	0.005	0.02	1.0	0.1	30
	1.0	3.6	0.5	0.006	0.01	0.8	0.1	30
	1.0	3.4	0.2	0.003	0.01	1.0	0.1	40



The Hall drifts of both the electrons and the ions are in the direction of the shock propagation down the tube, the Hall drift being dependent on the Hall parameter. In the region of the anode, the electrons carry the current, and if the electron Hall parameter is of the order of 1, a Hall drift of the electron can occur there; the Hall drift force on an electron being transmitted to an ion through the Coulomb force, so that effectively, this force is considered to act on an electron-ion pair. In the region of the cathode, if ions carry the whole current, or part of the current, the Hall drift force is less than in the region of the anode, since the ion Hall parameter is smaller than the electron Hall parameter. This preferential anode drift, coupled with the ion impact drag, provides a possible mechanism for the current sheet tilt.

Once a tilt is initiated, the magnetic field behind the leading side increases, at the expense of that behind the lagging side. This non-uniformity tends to increase the tilt; and the situation would rapidly become unstable were it not for the restoring forces exerted by the gasdynamic flow on the current sheet. (These restoring forces are discussed at the end of the next section.) The steady tilt angle

observed at each operating condition must correspond to that angle at which equilibrium is achieved between the tilting and the restoring forces.

The current sheet tilt angles observed for helium are much less than those for argon. This is consistent with the fact that both the ion drag parameter and the electron Hall parameter are smaller for the helium current sheets. For the 1.0 torr helium series, the observed anode 'foot' gained increasing prominence with increasing bias field. The ion drag parameter is constant in this series, and this increasing prominence is consistent with the larger values of the electron Hall parameter, corresponding to the larger bias fields.

We have observed, in Figure 4.50, an anode leading current sheet driving a cathode leading pressure front. Though this is an unusual effect, it may be understood by considering the flow pattern in the region between the current sheet and the pressure front. In laboratory coordinates, the flow just ahead of the current sheet is directed normal to the plane of the current sheet (see Figure 4.60). If the pressure front is close to the current sheet, it can be expected to assume the shape of the current sheet. If the pressure front is some distance from the driving sheet, the flow in the region

between the front and the sheet cannot remain indefinitely in the direction of the normal to the sheet, because of the boundary conditions imposed by the presence of the cathode and anode. Depending on the distance of the pressure front from the driving current sheet, we may expect that the pressure front can be inclined at an angle different from that of the current sheet.

#### 4.6 The inclined pressure front and the shock solutions

The pressure, magnetic field and electron density correlation studies of section 4.5 have shown that, in argon, during the period of constant velocity propagation (and immediately after), the pressure, electron density and current fronts were all inclined from the vertical at an identical angle  $\theta$ , which varied from  $30^\circ$  to  $58^\circ$  over the range of observation.

We propose to treat the inclined pressure front as an inclined shock wave, i.e., the flow into the shock is inclined at an angle  $\theta$  to the shock normal. (The word inclined is used here in preference to the more usual word oblique, since we have already used the latter term to describe the relative orientation of the magnetic field and the flow direction.) In the shock

coordinates, the tangential component of flow into the shock is not affected by the shock jump, whilst the normal component  $q_1 \cos \theta$  is the component to be used in the shock relations. In the geometry of our shock tube, the magnetic induction is transverse to the component  $q_1 \cos \theta$ , and we can treat this shock as an inclined transverse ionizing shock, and apply the solutions, calculated earlier, to this situation; noting that, for a measured shock velocity of  $q_1$ , the velocity to be used is  $q_1 \cos \theta$ , which we denote by  $q_n$ .

Using this model, we can expect the measured quantities  $N_e$ ,  $B_2$ ,  $P_{TM}$  to be less than the theoretical values based on the shock velocity  $q_1$ .  $N_e$ ,  $\Gamma$  and  $B_2$  are obtained directly from the shock solutions corresponding to  $q_1 \cos \theta$ ; as are  $E_{LAB1}$  and  $P_2$ . The measured electric field, however, corresponds to  $E_{LABz}$  (the component of  $E_{LAB}$  in the z-direction), which is  $E_{LAB} \cos \theta$ . For the pressure probe measurement, we consider  $P_{G2x}$ , since the relationship between this quantity and  $P_{TM}$  has been calculated and shown in Figure 3.11b.

$P_{G2x}$  is the sum of  $P_2$  and  $P_{N2x}$ , the flow impact pressure in the x-direction which is calculated as follows. In Figure 4.60, the resultant velocity in

the post shock state, in shock coordinates, is shown as  $q_i$ . This is transformed to the velocity vector  $u_i^*$ ; and a vector construction, as indicated in Figure 4.60, shows that, independent of the values of  $\Gamma$  and  $\theta$ ,  $u_i$  is normal to the inclined shock front. We thus have,  $u_x = u_i \cos \theta$ , and

$$P_{N2x} = \rho_2 (u_i \cos \theta)^2 = \Gamma \rho_1 (u_i \cos \theta)^2. \quad (4-4)$$

For argon, we take  $\theta = 50^\circ$  for, all shocks into 0.2 torr and those into 0.1 torr with  $B_1$  from 0 to 1.5 KG; and  $\theta = 35^\circ$  for shocks into 0.1 torr at higher fields. For each of these values, a correction factor  $f_i$ , is computed. This factor is designed to convert the  $P_{TM}$  calculated from  $q_1$ , to the  $P_{TM}$  expected on the model of the inclined shock. For  $\theta = 50^\circ$  we have  $f_i = 0.34$ ; and for  $\theta = 35^\circ$ ,  $f_i = 0.61$ .

It is noticed that the correction is substantial. This is not surprising, and is largely due to the  $\cos^2 \theta$  dependence of  $P_{N2x}$ . The measured values of  $B_2$ ,  $E_{LAB}$ ,  $N_e$  and  $P_{TM}$  contained in Tables 4.1, 4.3 and 4.4 are compared to the re-evaluated theoretical values based on the inclined shock, in Tables 4.1X, 4.3X and 4.4X. The values of  $N_e$  are still low compared to the theoretical values except in the range 1.0 to 2.6 KG with 0.2 torr (Table 4.4X).

---

\* flow velocity in laboratory coordinates

Table 4.1X: Inclined shock correction of Table 4.1;  
 $A_r$  0.1 torr

Measured			Theory (C-J)	Comparison
$B_1$ (KG)	$q_n$ (cm/ $\mu$ s)	$B_2$ (KG)	$B_2$ (KG)	%
0.66	1.7	2.8 $\pm$ 0.3	3.3	-15
0.66	1.4	3.0 $\pm$ 0.3	2.7	-11
0.66	1.2	2.0 $\pm$ 0.2	2.3	-13
1.5	2.1	3.5 $\pm$ 0.4	4.2	-17
1.5	1.9	3.0 $\pm$ 0.3	3.8	-21
1.5	1.7	3.0 $\pm$ 0.3	3.5	-14
1.5	1.5	2.6 $\pm$ 0.3	3.1	-16
1.5	1.2	2.1 $\pm$ 0.2	2.6	-19
2.5*	2.1	5.4 $\pm$ 0.5	4.6	+17
2.7*	3.1	4.8 $\pm$ 0.5	6.1	-21
2.7*	2.5	4.7 $\pm$ 0.5	5.3	-11
2.7*	2.0	4.2 $\pm$ 0.4	4.5	- 7
2.7*	1.8	3.8 $\pm$ 0.4	4.3	-12
3.6*	2.9	5.2 $\pm$ 0.5	6.4	-19
4.1*	3.8	6.7 $\pm$ 0.7	8.1	-17
4.1*	2.8	6.3 $\pm$ 0.6	6.7	- 6
4.1*	2.3	4.9 $\pm$ 0.5	5.9	-17
4.1*	2.2	4.4 $\pm$ 0.4	5.7	-23

\* indicates that  $\theta$  is taken as  $35^\circ$ ; for the others,  $\theta$  is taken as  $50^\circ$ .

The measured values of  $P_{TM}$  are much closer to the re-evaluated theoretical values than to the theoretical values based on  $q_1$ , with typically less than 30 per cent disparity; the measured values being generally higher. For the  $B_2$  measurements, good agreement with the inclined shock values is obtained; as shown in Figure 4.21 and in Table 4.1X, in which agreement to better than 25 per cent is observed over the whole



Table 4.3X: Inclined shock correction for Table 4.3

Measured					C-J Theory
$P_1$ (torr)	$B_1$ (KG)	$q_n$ (cm/ $\mu$ s)	$M_A$	$E_{LAB1}$ (V/cm)	$E_{LAB1}$ (V/cm)
0.10	0.66	1.7	-4.3	3 $\pm$ 5	1
0.10	0.66	1.6	4.0	3 $\pm$ 5	1
0.10	0.66	1.4	3.5	7 $\pm$ 5	2
0.10	0.66	1.2	3.0	24 $\pm$ 5	3
0.10	0.66	1.0	2.5	22 $\pm$ 5	2
0.10	0.66	0.77	1.9	15 $\pm$ 5	2
0.10	1.50	2.1	2.4	7 $\pm$ 5	9
0.10	1.50	1.9	2.2	8 $\pm$ 5	9
0.10	1.50	1.7	2.0	22 $\pm$ 5	8.6
0.10	1.50	1.2	1.4	36 $\pm$ 5	8.3
0.10*	4.10	3.8	1.6	20 $\pm$ 5	73
0.10*	4.10	2.9	1.2	20 $\pm$ 5	63
0.10*	4.10	2.4	1.0	27 $\pm$ 5	54
0.10*	4.10	2.0	0.8	54 $\pm$ 5	48
0.20	0.66	1.2	4.4	2 $\pm$ 5	0.6
0.20	0.66	1.1	3.9	19 $\pm$ 5	4.5
0.20	0.66	0.9	3.2	19 $\pm$ 5	7.7
0.20	0.66	0.76	2.7	12 $\pm$ 5	8.0
0.20	0.66	0.54	1.9	9 $\pm$ 5	7.7

range. In Table 4.4X, good agreement is also observed except at two points (0.1 torr with  $B_1 = 0.87$  KG and 0.2 torr with  $B_1 = 1.3$  KG). Almost without exception, the measured values are lower than the inclined shock values.

The  $E_{LAB}$  comparison (See Table 4.3X), shows little difference from the previous comparison, the main points of difference remain unaltered.

Table 4.4X: Inclined shock correction for Table 4.4

		Comparison of measured and C-J Values									
No.	$q_n$	$N_e$ ( $10^{16}/\text{c.cm}$ )			$P_{TM}$ ( $10^5 \text{N/m}^2$ )			$B_2$ (KG)			AI
	cm/ $\mu\text{s}$	M	I-S	V-S	M	I-S	V-S	M	I-S	V-S	
1	1.4	2.2 $\pm$ 0.2	7.0	11.8	4.9 $\pm$ 1.0	4.1	12.5	-		0	1/2
2	1.4	4.0 $\pm$ 0.3	7.1	13.0	6.5 $\pm$ 1.5	5.1	15.0	-		0	0/2
3	1.9	3.5 $\pm$ 0.2	2.5	4.0	2.8 $\pm$ 0.5	2.1	6.4	2.2 $\pm$ 0.2	3.2	4.1	0/3
4	2.4	2.1 $\pm$ 0.2	3.1	4.4	-	-	-	3.7 $\pm$ 0.2	3.8	5.6	1/2
5	2.5*	2.6 $\pm$ 0.2	3.6	4.3	4.5 $\pm$ 0.9	3.6	5.6	4.8 $\pm$ 0.3	5.0	5.9	2/3
6	3.4*	1.2 $\pm$ 0.1	5.0	6.4	5.0 $\pm$ 1.0	7.5	14.1	5.5 $\pm$ 0.5	6.9	8.0	1/3
7	3.1*	2.0 $\pm$ 0.3	4.8	5.9	5.1 $\pm$ 1.5	6.0	10.2	6.8 $\pm$ 0.5	7.0	8.0	2/3
8	2.8*	2.6 $\pm$ 0.3	4.4	5.3	5.0 $\pm$ 1.0	4.7	7.9	6.4 $\pm$ 0.4	6.7	7.4	2/3
9	1.4	3.0 $\pm$ 0.2	5.3	8.8	3.8 $\pm$ 0.6	3.6	11.2	1.4 $\pm$ 0.2	0	0	1/2
10	1.1	2.5 $\pm$ 0.5	2.0	5.4	2.2 $\pm$ 0.5	1.6	4.7	-	-	4.5	1/2
11	1.4	2.7 $\pm$ 0.1	3.7	5.9	2.7 $\pm$ 0.5	2.2	6.5	2.1 $\pm$ 0.5	3.9	5.5	1/3
12	1.5	2.2 $\pm$ 0.1	3.5	7.0	3.0 $\pm$ 0.5	2.7	8.3	-	-	6.1	1/2
13	1.8	2.2 $\pm$ 0.3	4.8	8.1	5.1 $\pm$ 1.5	3.8	11.6	4.9 $\pm$ 0.5	5.7	6.9	1/3
14	1.6	2.5 $\pm$ 0.1	3.9	7.0	4.0 $\pm$ 1.0	3.0	9.1	5.2 $\pm$ 0.5	5.6	7.4	1/3
15	1.9	3.0 $\pm$ 0.2	5.2	8.8	5.5 $\pm$ 1.0	4.4	13.0	6.4 $\pm$ 0.3	7.2	8.8	2/3

M Measured quantity

V-S C-J value, based on measured shock velocity

I-S C-J value, based on normal component of shock velocity,  $U_s \cos \theta = q_n$ 

AI agreement index

For helium, the observed tilts of the pressure fronts are less than those of the current sheets, and over the range of observations, the observed tilts are less than  $15^\circ$ , and a typical figure of  $10^\circ$  can be used. Using this tilt angle, the correction to the shock solutions are: 1.5 per cent for the velocity, 1.5 per cent for  $E_{\text{LAB}}$ , 4 per cent for  $P_{\text{TM}}$ , less than 1.5 per cent for  $B_2$  and less than 10 per cent for  $N_e$ .

The restoring forces on the current sheet, mentioned earlier, are discussed now.

With the flow velocity vector pointing away from the anode, as shown in the Figure 4.60, a flow pattern (in laboratory coordinates), as indicated by the broad arrow, can be expected, with the anode region of lower density (and lower pressure) than the cathode region, resulting in a force against the tilt. This flow pattern was observed, e.g., in Figure 4.49. The association of the cathode layer and possible flow vortices with this flow pattern is a matter of speculation.

# EXPOSURES

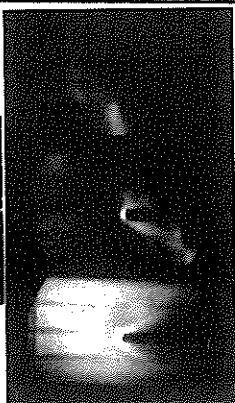
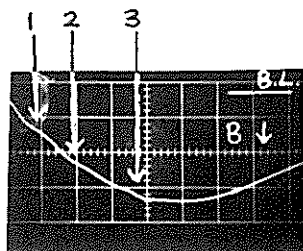


Fig.4.62 The bow shock in a large magnetic field

6x6cm tube

$x=63$  cm.  $U_s=4.0$  cm/ $\mu$  sec.

$t: 16, 17$  and  $19$   $\mu$  sec.

50 nsec exposure time.

B signal:  $1$   $\mu$ sec/cm,  
 $4$  KG/cm.

Fig.4.63 Streak photograph of Incomplete Separation

20x3 cm tube

$x=45$  cm.  $U_s=2.42$  cm/ $\mu$  sec.

All horizontal axes are identical:  $2$   $\mu$ sec/cm.

P trace:  $(0.5 \times 10^5 \text{ N/m}^2)/\text{cm}$ .

B trace:  $1.9$  KG/cm.

The horizontal axes of the streak and oscillogram are aligned for direct  $t$  comparison ( $\pm \frac{1}{2}$  small div).

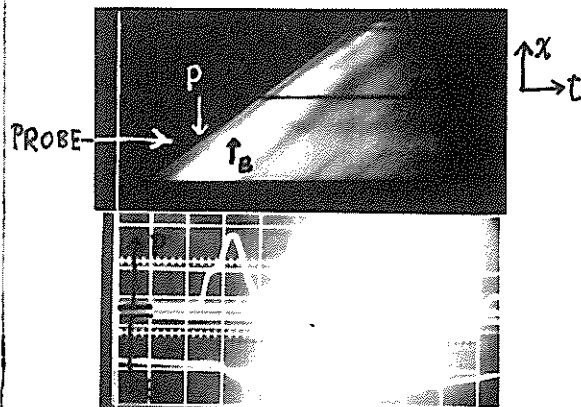


Fig.4.64 Framing photograph of Incomplete Separation.

$x=50$  cm.  $U_s=2.5$  cm/ $\mu$  sec.

$0.23$  torr He,  $B_1=2.9$ KG,  
(same conditions as 4.63).

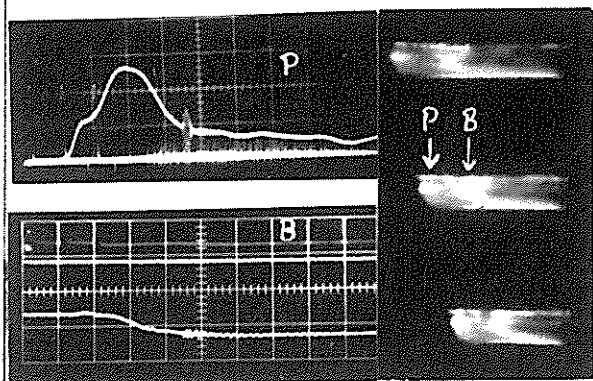
Horizontal axes of

oscillograms:  $1$   $\mu$ sec /cm.

same vertical scales as 4.63.

framing  $t: 18.5, 19.5, 20.5$   $\mu$ sec; 50 nsec exposure.

Framing time markers on P trace.



#### 4.7 Observation of the bow shock

The large width of the shock tube used in this series of experiments did not favour the observation of the bow shock, either with time resolved photography or with M-Z interferometry, since the luminosity and refractivity effects were integrated over 20 cm. The probe diameter was 0.6 cm and the overall path through the bow shock was not expected to be more than 3 cm.

However, framing photography observations in the 6 x 6 cm shock tube, mentioned in Chapter 3, showed the existence of a steady, detached bow shock, in both helium and air, over the pressure range of 0.07 to 0.4 torr, in the velocity range of 2 to 6 cm/microsec. The magnetic induction in the region of the observed bow shock ranged from low values (less than 1 KG) to 20 KG. The observed shock angle, Figure 4.61, ranged from 20 to  $35^{\circ}$ , and the detachment distance from  $\frac{1}{2}$  to over 1 probe diameter. An example is shown in Figure 4.62, where the three frames were taken at 16, 17 and 19 microsec after the start of the discharge. In the first frame, the front was just arriving at the probe, and in the third one, the front had past the probe head by a distance of 12 cm. The magnetic field at this time was 12 KG.

#### 4.7.1 Significance of the bow shock

For the example illustrated in Figure 4.62, at the time of the third frame, the magnetic speed  $b \approx 8$  cm/microsec, can be compared to the estimated flow speed ( $q_p$ ) and the isentropic sound speed- $a$  of 3 and 1 cm/microsec respectively. The shock angle  $\phi$  is approximately related to the flow Mach number  $M_f$  by the formula, relating the Mach angle to the Mach number,

$$\sin \phi = 1/M_f \quad . \quad (4-5)$$

If we take the small disturbance speed as  $(a^2 + b^2)^{\frac{1}{2}}$ , then the flow Mach number  $M_f \approx 0.4$ , and we do not expect to see a detached shock wave. If, on the other hand, we take the small disturbance speed as the isentropic sound speed- $a$ , we have the flow Mach number as 3 and hence expect a bow shock with  $\phi \gtrsim 20^\circ$ . The angle  $\phi$  is measured from Figure 4.62 as  $\phi \approx 25^\circ$ . Similar calculations over the whole range of observations up to 20 KG show that the shock angle was associated with the isentropic sound speed.

This is experimental evidence confirming the ohmic dissipation model and our choice of the small disturbance speed behind the transverse shock.

#### 4.8 Shock and non-shock effects

In any attempt to compare experimental results with a shock wave theory, it is necessary to recognize and attempt to understand the non-shock effects; i.e., effects observed with the shock wave that are not included in the equilibrium shock calculations. Among the most commonly discussed effects of this class include the lack of local thermodynamic equilibrium behind the shock wave, and precursors attributed to electron diffusion from the shock front, photo-ionization, and electric breakdown waves. The experiments described above suggest the possibility of precursor reverse current loops and 'post-cursor' reverse current loops in 'biased' electromagnetic shock tubes, associated with the decoupling of the back emf, due to the shock wave motion in the bias field, from the driving current. To develop this concept further, we need to examine more closely the coupling and decoupling of the pressure front and current sheet during the various phases of operation, as well as under different operating conditions.

#### 4.8.1 Observation of a pure gas separation

In helium, with a bias field, at the normal operating voltage range of 5-7 KV, the region immediately behind the pressure front was often observed to be gasdynamic, with the bias field value unchanged through it. An example of this is seen in Figure 4.18 of section 4.2, in which the operating conditions were: 5.1 KV helium at 0.25 torr, with  $B_1 = 1.9$  KG. The first 'step' in the pressure pulse, of 0.7 microsec duration was gasdynamic. The distribution of pressure and current with distance for a similar operating point ( $B_1 = 2.5$  KG) has been shown in Figure 4.17b. A gasdynamic region in the first part of the pressure pulse preceded by a 3 cm region of reverse current ahead of the shock front can be seen.

When the drive voltage was reduced, this gasdynamic region gained prominence. Figures 4.63 and 4.64 show streak and framing photographs, together with synchronised pressure and magnetic probe records of a shock wave propagating in 0.23 torr helium with  $B_1 = 2.9$  KG and a condenser voltage of 2.5 KV. A region of 1.2 microsec (3 cm) following the start of the pressure rise was gasdynamic (Figure 4.63a); the magnetic field rise through it being less than 5 per cent of the



bias field (Figure 4.63b). On the streak photograph, a comparison with the probe signals leads to the identification of the first luminosity front as the pressure front; and the brighter streak, 1.2 microsec behind this first luminosity front, as the start of the magnetic field jump. The estimated positions of the pressure and current fronts, are indicated on the framing photographs.

The pressure measured by the probe in the gasdynamic region can be approximated to  $P_{G2}$ , the total gas pressure in the freestream (refer Figure 3.11b). For a gasdynamic shock we may write (3-36) as:

$$P_{G2} = W \frac{(\Gamma-1)^2}{\Gamma} + W \left( \frac{2}{\gamma+1} \right) \quad (4-6)$$

Taking  $\gamma = 1.67$  for the gasdynamic region, the peak density ratio ( $\Gamma$ ) is calculated to be  $3.1 \pm 0.6$ .

Assuming that the second pressure feature (Figure 4.64a) corresponds to the ionizing shock transition, the measured value of the peak pressure is taken as  $P_{TM}$ , which is then related to  $P_{G2}$ , using the bow shock solutions of Figure 3.11b. This enables a value of  $\Gamma$  to be calculated; and it is  $7 \pm 1.5$ , compared to C-J theoretical value of 4.0, and a hydromagnetic value of less than 1.5. The value of the peak shock jump

magnetic field, measured 0.3 microsec after the pressure peak, is  $3.4 \pm 0.3$  KG, compared to a C-J theoretical value of 3.5 KG.

These measured values are in agreement with the assumption that the gasdynamic region was an incomplete gasdynamic shock serving as an 'onset' region for ionization. In such a region, the conductivity is insufficient for the magnetic field to interact with the gas, so that the initial shock is entirely governed by viscosity and heat conductivity. It is of interest to note that at 2.5 cm/microsec, a helium atom has a kinetic energy (and an equal thermal energy) of 13 ev compared to an ionization potential of 24.5 ev. An argon atom at the same speed has a kinetic energy of 130 ev compared to an ionization potential of 15.8 ev. When the thermal energy is large compared to the ionization energy, we can infer that the onset region is small, and vice versa. On this basis, in our range of experiment, the gasdynamic shock region for argon can be expected to be smaller than the helium gasdynamic region.

This difference was observed. In argon, no gasdynamic shock was detected in the period of steady propagation; whereas in helium, gasdynamic shocks

separated from the ionizing shocks by up to 3 cm were observed during periods of constant drive.

#### 4.8.2 Reverse current loops and the back emf

For a steady ionizing shock to exist, the shock jump relations require an increase in magnetic induction across the jump, corresponding to a current flow in the positive direction through the transition (see Figure 2.1 for coordinates). The post shock electric field, transformed to the laboratory coordinates,  $E_{LAB2}$  ( $= q_1 B_2 - q_2 B_2$ ) points in the positive direction, but is a back emf since its effect on the driving circuit is to reduce the current from the value that would flow in the absence of the shock impedance. We can thus consider  $E_{LAB2}$  as driving a reverse current through the shock transition even during the period of steady propagation. This reverse current flows through the condenser, and for the existence of the steady shock wave, the gross forward drive current must exceed this reverse current by an amount at least equal to that required for the shock jump magnetic induction. This requirement is additional to the requirement of momentum balance, which has already been discussed in section 2.7.

Assuming that both the flow and current sheet moves at the same velocity  $u_p = q_1 - q_2$ ; we have, for the total back emf of the shock front-current sheet system,

$$\begin{aligned} T_{\text{emf}} &= B_D u_p \\ &= (B_2 + B_e) u_p = B_2 u_p + B_e u_p \\ &= S_{\text{emf}} + C_{\text{emf}} \end{aligned}$$

Here  $B_e$  stands for the increase in magnetic induction from the post shock value to the final value in the expansion current;  $S_{\text{emf}}$  is the back emf associated with the shock motion, and  $C_{\text{emf}}$  is that associated with the current sheet motion. In the absence of a bias field, we have  $S_{\text{emf}} = 0$ . (We note that  $T_{\text{emf}}$  is the quantity  $E_{\text{LABD}}$ , whose measurement is described in section 4.4.1.)

During the period of steady drive, our observations indicate strong coupling between the current sheet and shock front (as it must to provide effective drive). There is however a difference in the degree of this coupling between the argon and the helium systems. This is evidenced in the more diffuse nature of the current sheet in helium and in our conclusion of poorer coupling in the case of helium from the comparison of measured shock speeds with those predicted from momentum balance.

When the current drive decreases, our comparative profiles of Figures 4.15 to 4.17 indicate a rapid decoupling of the current sheet from the shock front in both the biased and the unbiased cases (e.g.,  $t = 26.2$  and  $t = 28.2$  microsec in Figure 4.15; and  $t = 14.2$  and  $t = 28.2$  microsec in Figure 4.16). By the time the condenser voltage has dropped to zero, the remnant positive flux in the shock tube, associated with the reduced, but still appreciable current, would, if it remained coupled to the condenser circuit, begin to assume the role of a generator, discharging its remnant energy into the condenser bank. However, at this time, this remnant flux becomes decoupled from the condenser circuit, forming a closed loop of flux decoupled from both the shock front and the condenser circuit. In both the presence and absence of a bias field, this loop encloses positive but decreasing flux, and hence, the induced current encircling it is a positive one. The forward end of this region is identifiable, in our comparative profiles, as a diffuse positive current sheet that moved backwards. In the unbiased case (Figure 4.15); the backward speed was faster than in the biased case (Figure 4.16); but the rate of decay of the current amplitude was greater in the biased case.

Returning to the shock front, in the unbiased case when the current sheet decouples from it, the shock wave becomes purely gasdynamic, propagating into a field-free region. In the biased situation, in the absence of the driving current (or a substitute force), there is no external current flow to sustain a forward current (necessary for the shock jump field), in opposition to the back emf. The post shock  $B_2$  must therefore decrease rapidly to the value of the bias field. This is observed between  $t = 28.2$  to  $t = 32.2$  on Figure 4.1, where in this time the velocity had dropped from 2.5 to 1.6 cm/microsec. The total pressure amplitude had decreased by less than 25 per cent over this period of time. Since the total pressure is proportional to  $\rho_2$  and  $q_1^2(1-\frac{1}{F})^2$ , this indicates that the density ratio in the pressure front had increased by a factor greater than two. The energy released from the dissolution of the magnetic field must be deposited in the pressure front, so that between  $t = 28.2$  and  $t = 32.2$  microsec, this energy and the energy from the loss in kinetic energy, after accounting for the energy imparted to newly swept-in gas, must be added to the gas enthalpy. This, and the increased density

ratio, are consistent with the transition from an ionizing shock to a gasdynamic shock.

Such a situation as that at  $t = 32.2$  is not a steady gasdynamic shock, however, because the motion of the conducting gas behind it has still an induced emf associated with it, the direction of which is such as to oppose the motion. This necessitates a flow of current in such a direction as to tend to exclude the bias field from the interior region of the shocked gas. Consequently a reverse current flows in the region behind the pressure front. This was observed in the comparative profiles (Figure 4.16,  $t = 36.2$ ).

We have seen that the  $S_{\text{emf}}$  can be considered as generating a reverse current, during the period of constant drive, which is coupled through the condenser circuit. The question now arises whether, during this period, this back emf can become decoupled, or partially decoupled from the driving circuit. Such a decoupling will manifest itself as a region of decreased magnetic field in the vicinity of the shock front. This was observed in helium for the larger values of bias field and velocity in the range of our operation, but not for the cases when either the velocity, or the bias field, was small. This difference is consistent with the back

emf model, since the combination of a large field and a large velocity gives rise to a large back emf. The fact that this frontal reverse current was not observed in argon, but in helium, is also consistent with this model since the argon current sheet was observed to couple more strongly to the shock front. This strong coupling in argon makes it more unlikely for the  $S_{emf}$  to decouple from the  $C_{emf}$  with the result that the current of the two back emfs takes the same path, which has to be through the condenser circuit.

One effect of this reverse current front is to reduce the electric field  $E_{LAB1}$  ahead of the ionizing shock, because, as observed from ahead of the shock wave, this reverse current has a negative resistive drop. In helium, at  $B_1 = 3.0$  KG, at the high velocities (above 3 cm/microsec), the measured values of  $E_{LAB1}$ , corrected for the positive resistive drop, are significantly lower than the predicted values. At the lower velocity range (below 2 cm/microsec) the values are a little too high. With the low bias field of 0.05 KG, the values of  $E_{LAB1}$  are also typically larger than the predicted values. The region where the values of  $E_{LAB1}$  are significantly low, was just that region where frontal reverse current loops were



observed; the difference between measured and theoretical values was small enough to be completely attributable to the reverse current resistive drop.

In argon, the  $E_{LAB1}$  measurements follow the same general trend, being low for high fields and high velocities (e.g., Table 4.3X; 0.1 torr,  $B_1 = 4.1$  KG,  $q_n = 3.8$  and  $2.9$  cm/microsec, and Figures 4.28 and 4.29). No frontal reverse current was observed, however, but instead, reverse loops were observed behind the shock-jump current, for a combination of a high bias field and high shock velocity. It may be speculated that these loops are due to a combination of the  $S_{emf}$  and the anode to cathode flow pattern; the fringe pattern on the interferogram (Figure 4.49) has the same approximate periodicity as the magnetic probe signal. The observation of such possible reverse loops in argon also corresponds with the low measured values of  $E_{LAB}$ , though it is unlikely that the difference of 50 V/cm at  $B_1 = 4.1$  KG,  $q_n = 3.8$  cm/microsec can be accounted for simply by this effect.

## CHAPTER 5

### CONCLUSIONS

#### 5.1 Experimental verification of the C-J model

The Kunkel-Gross-Champman-Jouguet hypothesis, originally applied to normal ionizing shock waves, was adapted for the operation of our transverse planar electromagnetic shock tube. This was made possible by the choice of an ohmic dissipation model for the flow behind the transverse shock wave, in preference to the usual dissipationless model. In such an ohmic dissipation-controlled flow, the small disturbance speed is the isentropic sound speed. The experimental observation of the bow shock in the presence of large magnetic fields and the measurement of the bow shock angles confirmed this choice of the small disturbance speed.

Limits based on structural consideration were applied to the transverse C-J theory. According to these limits, the ionizing C-J solutions are not applicable above a magnetic Mach number  $M_A$  in the neighbourhood of 4.5, when shock behaviour becomes hydromagnetic. Also, in the limit of vanishing

magnetic fields corresponding to very large values of  $M_A$ , the shock solutions become gasdynamic. Solutions using this model were obtained and compared with the experimental results.

In the experiments, a new method of Mach Zehnder interferometry, using multi-channel spectra, was employed. This method provided greater accuracy, in the determination of the electron and heavy particle densities, than was available using conventional M-Z techniques. An approximate probe theory was developed to account for the influence of the bow shock on the probe measurements of the transverse magnetic field and the pressure. The main results of this theory were that, in the ionizing C-J regime, the magnetic field measured by our coil was a little less than the freestream transverse field; and that the pressure recorded by the probe was approximately equal to the difference between the total stagnation pressure and the freestream magnetic pressure. The electric field ahead of the shock wave was also measured.

In the course of the experiments, two effects were observed that had to be considered, before a comparison of the measured quantities with the theoretical quantities could reasonably be made. The

first of these was a pressure front tilt that varied from  $35^{\circ}$  to  $58^{\circ}$  in argon, and from  $0^{\circ}$  to  $15^{\circ}$  in helium. Treating the pressure front as an inclined shock, the flow velocity into the shock was not just the measured shock velocity, but depended also on the angle of tilt. For argon, this correction was substantial; for helium, small. The second effect observed was a reverse current loop that preceded the helium pressure front when the operation of the shock tube was consistent with a large back emf due to the shock motion. In argon, this precursor current loop was not observed, but instead, alternate reverse and forward loops were observed following the shock jump current. One effect of these reverse loops was to reduce the electric field ahead of the shock wave.

In helium, over the  $M_A$  range of 0.7 to 3.3, fair to good agreement was observed for the four quantities compared, namely, the electron density, the magnetic field, the pressure and the electric field ahead of the shock. The electron density measurements were on the high side (typically less than 25 per cent), the magnetic field on the low side (typically less than 20 per cent), and the pressure measurements on the high side (typically less than 25 per cent). The electric

field measurements, taken between  $M_A = 0.5$  to  $M_A = 6.5$  were slightly high in the low back emf region, and slightly low in the high back emf region, these latter low values being attributable to the reverse current loops. Thus, general agreement was observed, for helium, in the ionizing C-J regime. For the unbiased cases, corresponding to the gasdynamic limit, serious disagreement was observed, both the electron density and the pressure measurements being generally far too low.

In argon, the inclined shock corrections were applied. Over the  $M_A$  range of 1 to 3.7, the agreement of the pressure and magnetic field measurements with the C-J theory was comparable with the helium results in both magnitude and direction. The electron density measurements were not in such good agreement, however, the typical disagreement being more than 30 per cent and on the low side. In addition the density ratio measurements, subject to large uncertainties, were also in general agreement. The electric field measurements also follow the same general trend as the helium results, being high for low shock emfs, and low for those shots with high shock emfs. However, the disagreement in the latter case was more serious than

in the corresponding helium case, and was probably too large to be purely attributable to the negative resistive drop of the reverse current loop. In argon, as in helium, the electron density measurements in the gasdynamic limit were in serious disagreement with the gasdynamic theoretical values.

In comparing the experimental results with the C-J theoretical values, it should be noted that the hydromagnetic solutions should be considered at the same time, in case the experimental results may agree just as well, or better, with the hydromagnetic solutions. In such a case, the hydromagnetic calculations are preferred, since they are in general easier to make. For distinguishing between the two models, in the  $M_A$  range up to 4.5, the magnetic field is not a good quantity, since the two models give solutions within 10 per cent of each other. The electric field ahead of the shock is a good quantity to compare, since the hydromagnetic model requires this field to be zero whereas the C-J ionizing theory requires a non-zero field up to  $M_A = 4.5$  approximately. However, the measurement of this field involves at least two uncertain quantities, namely, the current sheet resistive drop, for which our subtraction

procedure, based on the 'unbiased' resistive drop may not be justifiable; and reverse current loops. Bearing these in mind, we find that, over our experimental range within the C-J regime, the experimental results do not indicate a hydromagnetic shock, except for the case of argon with 0.2 torr and  $B_1 = 0.37$ , where the observed values of the electric field (corrected for resistive drop) approached zero in the region of  $M_A = 2$ , instead of at  $M_A = 4.5$ . This was, however, precisely the region where the reverse current loops, behind the shock-jump current, became prominent. That the shock wave in this region had not 'prematurely' become hydromagnetic was shown by the density ratio and pressure probe measurements. At  $M_A = 2$ , the hydromagnetic solution requires a density ratio of 3 compared to the C-J value of 4.9. The measured density ratio indicates a value not less than 5. Moreover, the value of the pressure  $P_{TM}$ , based on a density ratio of 3 is less than half the C-J theoretical value whereas the measured value of  $P_{TM}$  was 20 to 30 per cent above the C-J value. Thus, in our experimental range of the C-J regime, the C-J solutions are in considerably better agreement, with the experimental observations, than the hydromagnetic solutions.

If now we look at the gasdynamic solutions, we note that these require a much larger density ratio, electron density and  $P_{TM}$ . In helium, the measured values of the electron density and  $P_{TM}$  are on the high side of the C-J solutions, likewise, the argon measurements of the density ratio and  $P_{TM}$ . This indicates that the disagreement between our experimental results and the C-J theory is in the direction of the gasdynamic solution rather than in the direction of the hydromagnetic solution. In view of this general trend, the discrepancy, posed by the low measured value of the electron density, in the case of argon, is probably an exception; explainable, perhaps, in terms of the de-ionizing effect due to the ion-neutral exchange process at the cathode. We also observe that, in the unbiased case, the measurements do not agree with the gasdynamic solutions. This is almost certainly due to the existence of the magnetic field in the post shock gas immediately following the small incomplete shock region.

Summarizing, the experiments have shown that, in the ionizing C-J regime, the C-J solutions were in fair to good agreement with the measured shock properties in



helium; and, when the inclined shock effect was taken into account, similar agreement was observed for the argon shock.

## 5.2 The identification of a shocked 'gas sample'

The comparison of experimental measurements with an equilibrium shock-jump theory is based on two assumptions; firstly, the existence of a shock-jump region, of measureable thickness, separate from any following region of expansion or compression, and secondly, local thermodynamic equilibrium (LTE) within the shock-jump region. Generally, the first of these assumptions has to be satisfied, for the comparison to be at all meaningful; whereas, depending on the degree of departure from LTE, approximate agreement may still be observable between the experimental measurements and equilibrium predictions. From our study of the comparative distributions of the pressure and magnetic field, and the correlation study on the pressure, electron density and magnetic field fronts, we are in a position to discuss the validity of this first assumption, in our transverse planar shock tube.

We have established that a well defined and reproducible pressure pulse propagated down the shock tube, over the entire range of operation. Associated

with this pressure pulse were three features of current, that were classified as, a diffuse current, a shock jump current and an expansion current. Current-free regions in the pressure pulse were identified. These are significant to the concept of a separated shock-jump region, and will be discussed below.

It is important to immediately distinguish between two classes of separation. The first of these is the incomplete gas shock, that was observed in helium (the lighter gas) both with and without a bias field; and which served as an ionization 'incubation' region for the onset of the ionizing shock. The observation of this incomplete shock does not imply a separated ionizing shock; and, in fact, as the shock speed is increased, so that the thermal energy of the shocked gas greatly exceeds its ionization potential, this region should lose prominence, and become not measurable.

The other class, is what we shall term complete separation, which is defined as the separation of the complete ionizing shock from the expansion current. In the 'unbiased' case, such a separated complete shock is gasdynamic, with no magnetic field in it, and with its properties calculable from gasdynamic shock-jump theory (including ionization effects). With a shock

wave propagating into a bias field, this separated complete shock is ionizing, with a shock jump current through it, as determined by the choice of the shock-jump closing relation.

In the above context, our experimental observations of the constant drive period, showed that, when the bias field was zero, no complete separation was observed, in both argon and helium. For small values of the bias field, current partitioning (i.e., into two separate regions of shock-jump and expansion current) was not observed; but for values within the C-J regime, current partitioning was observed, usually with a region of zero, or negligible, current separating the two regions of current flow. Moreover, (1) the magnitude of the first magnetic field jump, (2) the thinness of this jump region (manifested by magnetic signal, streak photography and M-Z interferometry), and (3) the correlation of the magnetic and pressure signals, provide sufficient evidence that the current partitioning was indeed to be associated with the separation of the shock front from the expansion current. The region between the partitioned currents generally extended over a distance of 2 to 4 cm, and was a region

of uniform magnetic field, and relatively uniform electron density and total pressure.

One now questions why a complete separation is observable in the case of large bias fields, and not in the case of small or zero bias fields. For an explanation, we consider the expansion current, whose leading edge moves relative to the shocked gas at the small disturbance speed. In the biased case, according to the C-J model, the shock-jump current deposits an amount of energy and momentum in the shock front, which is just sufficient to constrain the flow out of the shock to have the local small disturbance speed. The expansion current is thus prevented from 'invading' into the shock front. Without a bias field, a gasdynamic shock tends to develop, with the flow speed, out of the shock, typically a third of the post-shock sound speed. The expansion current must therefore, necessarily, overtake the shock front. The presence of the current in the shock front will then alter the momentum and energy balance from that prevailing in its absence; whilst at the same time the interaction can be expected to also alter the characteristics of the front part of the expansion

current. This could account for the appearance of the diffusion current region.

This same argument also applies to the case of small bias fields, i.e., when the magnetic Mach number extends past the C-J hydromagnetic limit of 4.5. In this case, the flow speed out of the shock is also subsonic and not sufficient for the shock front to keep ahead of the expansion current.

Therefore, in the presence of an expansion current, we expect, and observed, complete separation, only in the C-J regime.

One other experimental observation should be noted here, concerning complete separation. In the unbiased cases, when the drive current decreased, the expansion current was observed to rapidly decouple from the shock front, leaving a complete gasdynamic shock to propagate ahead. During this decoupling, the gasdynamic 'slug' increased in length, and the shock velocity and total pressure amplitude decreased only slightly. This could well be one method for producing a high velocity gasdynamic shock, with complete separation, since the decoupling action is expected to remain just as efficient at high velocities, as it was in our relatively low velocity shocks.

It is possible, however, that at high velocities, this method of decoupling may not be necessary, since the characteristics of shock-current propagation may then be different from the C-J model. Specifically, if the temperature of the post shock gas is sufficiently high an expansion current may not be required, and a gasdynamic shock, with complete separation, could be propagated with steady drive.

The apparently contradictory experimental observations of Hoffman<sup>20</sup> and Sorrell<sup>81</sup> may be discussed from this point of view. Hoffman's observations suggest that separation was more likely to occur at low current sheet Mach number, specifically, around the operating condition of 0.475 torr hydrogen at a shock speed of 2.4 cm/microsec. Sorrell, on the other hand, observed separation at 0.46 torr hydrogen in the shock speed range of 8 to 11.4 cm/microsec; but not below 8 cm/microsec. (Both the experiments were in the absence of bias fields.) There is little doubt, that, at a speed of 2.4 cm/microsec, an incomplete shock of measurable thickness would precede the complete ionizing shock. At higher shock velocities, and in heavy gases at low velocities, the incomplete shock region would be smaller; so that

Hoffman's conclusion, that, a low Mach number in a light gas favours separation, may really be applicable to an incomplete separation; rather than to the separation of a complete shock. Sorrell's experiments, on the other hand, suggest that, at high post-shock temperatures ( $115,000^{\circ}$  K), the expansion current may not dominate the shock front-current relationship in the same C-J manner as it did in our range of relatively low temperatures.

In summary, we distinguish between incomplete and complete separation. The former was observed in helium shocks, both with and without bias field. During the constant drive period, complete separation was observed in both argon and helium shocks, propagating into a bias field, in the C-J regime; but was not observed for shocks propagating into zero or small magnetic fields.

REFERENCES

1. L.C. Wood, J. Fluid Mech. 22, 44 (1965).
2. B. Miller, Phys. Fluids 10, 9 (1967).
3. L.S. Levine, Phys. Fluids 11, 1479 (1968); also Columbia University Plasma Laboratory Report 36 (1967).
4. J.B. Heywood, Phys. Fluids 9, 1150 (1966).
5. R.A. Gross, Rev. Mod. Phys. 37, 724 (1965).
6. R.M. Patrick and E.R. Pugh, Phys. Fluids 8, 636 (1965).
7. R.G. Fowler, J.S. Goldstein and B.E. Clotfelter, Phys. Rev. 82, 879 (1951).
8. A.C. Kolb, Phys. Rev. 107, 345 (1957).
9. R.M. Patrick, Phys. Fluids 2, 589 (1959).
10. H.H. Teh and S. Lee, Int. J. Electronics 22, 193 (1967).
11. A.C. Kolb, Phys. Rev. 112, 291 (1958).
12. M.H. Brennan, I.G. Brown, D.D. Millar, C.N. Watson-Munro, J. Nuclear Energy C5, 229 (1963).
13. M. Camac, A.R. Kantrowitz, M.M. Litvak, R.M. Patrick and H.E. Petschek, Nuclear Fusion (1962), Supplement Pt.2, p.423.
14. M. Yasuhara, Phys. Fluids 11, 2567 (1968).
15. W.R. Ellis and R.G. Jahn, J. Plasma Phys. 3, Pt.2, 189 (1969).
16. R.T. Taussig, Phys. Fluids 9, 421 (1966).
17. R.T. Taussig, Phys. Fluids 10, 1145 (1967).



18. N.H. Kemp and H.E. Petschek, Phys. Fluids 2, 599 (1959).
19. F. Fishman and H. Petschek, Phys. Fluids 5, 1188 (1962).
20. A.L. Hoffman, J. Plasma Phys. 1, Pt.2, 193 (1967).
21. R.H. Lovberg, in Proc. of the Sixth International Conference on Ionization Phenomena in Gases, Paper IX, p.235 (1963).
22. L. Liebing, Phys. Fluids 6, 1035 (1963).
23. J.R. MacLelland, A.S. Mackenzie and J. Irving, Phys. Fluids 9, 1613 (1966).
24. A.C. Ekbreth, K.E. Clark and R.G. Jahn, AIAA 11, 2125 (1968).
25. R.G. Fowler and E.B. Turner, Phys. Fluids 4, 544 (1961).
26. G.C. Vlases, J. Fluid Mech. 16, 82 (1963).
27. G.C. Vlases, Phys. Fluids 7, 1358 (1964).
28. H.K. Messerle, Bull. Am. Phy. Soc. (1968); also B. Campbell, H.K. Messerle, S. Ludvik and A.D. Stokes, Sydney University Department of Electrical Engineering Report EC-67-11 (1967).
29. M.H. Brennan, J.A. Lehane, D.D. Millar and C.N. Watson-Munro, Aust. J. of Phys. 16, 340 (1963).
30. W. Marshall, Proc. Roy. Soc. (London) A233, 367 (1955).
31. J.B. Helliwell and D.C. Pack, Phys. Fluids 5, 738 (1962).
32. C.K. Chu, Phys. Fluids 1, 1349 (1964).
33. A.G. Kulikovskii and G.A. Lyubimov, Soviet Phys. - Doklady (English translation) 4, 1195 (1960).

34. C.E. Moore, Atomic Energy Levels (United States Bureau of Standards Circular 467, 1949).
35. H. Griem, Plasma Spectroscopy (McGraw-Hill, New York, 1964), p.140.
36. H. Drahwin and P. Felenbok, Data for Plasmas in Local Thermodynamic Equilibrium (Gauthier Villars, Paris, 1965).
37. J.K. Wright, Shock Tubes (Methuen, London, 1961), p.19.
38. A.G. Kulikovskii and G.A. Lyubimov, Soviet Phys. - Doklady (English translation) 4, 1185 (1960).
39. R.M. May and T. Tendys, Nuclear Fusion 5, 144 (1965).
40. T.E. Allen and S.E. Segre, J. Nuclear Energy, Part C, Plasma Phys. 6, 153 (1964).
41. G.E. Perona and W.I. Axford, Phys. Fluids 11, 294 (1968).
42. W.B. Kunkel and R.A. Gross, 'Hydromagnetic Ionizing Waves' in Plasma Hydrodynamics (Stanford University Press, Stanford, California, 1962), p.58.
43. R.B. Johansson, Phys. Fluids 8, 866 (1965).
44. R.T. Taussig, Phys. Fluids 8, 1616 (1965).
45. M.D. Cowley, J. Plasma Phys. 1, Pt.1, 37 (1967).
46. K.O. Friedrichs and H. Kranzer, Notes on Magneto-Hydrodynamics VIII, Nonlinear Wave Motion (Institute of Mathematical Sciences, New York University, New York, 1958).
47. S.R. Kholev and D.S. Poltavchenko, Soviet Phys. - Doklady (English translation) 5, 356 (1960).
48. G.H. Allen, A.N.U. Honours Report (1967).
49. L.E. Kalikman, Elements of Magnetogasdynamics (translated by Scripta Technica, Inc., W.B. Sanders, Philadelphia, 1967), p.77.

50. A. Kantrowitz and H.E. Petschek, in Plasma Physics in Theory and Application, edited by W.E. Kunkel (McGraw Hill, New York, 1966), p.153.
51. L. Spitzer, Jr., Physics of Fully Ionized Gases (Interscience, New York, 1962).
52. S.I. Pai, Magnetogasdynamics and Plasma Dynamics (Wien-Springer Verlag, 1962).
53. S.I. Pai, in Proceedings of the 5th Midwestern Conference on Fluid Mechanics (University of Michigan, 1957), p.251.
54. M.R. Osborne, Technical Report No.5 (Computer Centre, Australian National University, Canberra, 1966).
55. W.H. Heiser, appendix to Magnetohydrodynamic Shock Waves by J.E. Anderson (MIT Press, Cambridge, 1963), p.211.
56. R.J. Sandeman, 'The Development of the Current Sheet in a Planar Electromagnetic Shock Tube', Paper 25, AINSE, Sixth Australian Plasma Physics Conference (1967) (unpublished).
57. S. Lee, 'Matching of an Electromagnetic Shock Tube with a Transmission Line Condenser Bank', Paper 27, AINSE, Sixth Australian Plasma Physics Conference (1967) (unpublished).
58. R.A. Fitch and N.R. McCormick, Proc. Inst. Elect. Engrs. 106A, Supplement No.2, 117 (1959).
59. D.G. Fearn and E.R. Wooding, J. Sci. Instruments 44, 571 (1967).
60. E.L. Neau, 'A Low Inductance Megampere Switch', Sandia Laboratory Report SC-TM-65-553 (Albuquerque, 1965).
61. R.H. Huddleston and S.L. Leonard, Plasma Diagnostics (Academic Press New York, 1965).
  - a. S.L. Leonard, p.9.
  - b. R.H. Lovberg, p.69.

62. E. Grives, T. Moulin and E. Robert, IEEE Transactions on Nuclear Science, p.47 (1964).
63. J. Cooper, J. Nuclear Energy Pt.C 5, 285 (1963).
64. L.A. Ferrari and M.S. Zucker, Rev. Sci. Instruments 40, 925 (1969).
65. B. Miller, Rev. Sci. Instruments 37, 7 (1966).
66. A. Seigelman and F. Mintz, J. Ac. Soc. Amer. 27 (1955).
67. C.T. Chang, Phy. Fluids 4, 1085 (1961).
68. W.H. Rudderlow, J. Applied Phys. 39, 1 (1968).
69. H.W. Liepmann and A. Roshko, Elements of Gasdynamics (John Wiley and Sons, New York, 1965).  
a. p.168; b. p.98; c. p.47.
70. J. Lukasiewicz, National Aeronautical Establishment, Canada, Report 15 (1952).
71. J.N. Bradley, Shock Waves in Chemistry and Physics (Methuen, London, 1962), p.112.
72. R.A. Alpher and D.R. White, Phys. Fluids 2, 162 (1959).
73. C.W. Allen, Astrophysical Quantities (Oxford University Press, London, 1963).
74. J.H. van Vleck, Electrical and Magnetic Susceptibilities (Oxford University Press, London, 1932), p.225.
75. R.J. Sandeman, 'The Use of Channelled Spectra in Two Beam Interferometry' - to be published.
76. Hildebrand, Introduction to Numerical Analysis (McGraw Hill, New York, 1956), p.49.
77. J. Topping, Errors of Observation and Their Treatment (Chapman and Hall, London, 1962), p.23.

78. F.B.A. Frungel, High Speed Pulse Technology Vol.I  
(Academic Press).
79. IBM System/360, Scientific Subroutine Package  
(360A-CM-03X) Version III, p.160.
80. A. Jeffrey, Magnetohydrodynamics (University  
Mathematical Texts, Oliver and Boyd,  
Edinburgh and London, 1966).
81. F.Y. Sorrell, Phys. Fluids 12, 1218 (1969).
82. R.J. Stalker and D.L. Plumb, Nature 218, 789 (1968).
83. J.E. Anderson, Magnetohydrodynamic Shock Waves  
(MIT Press, Massachusetts, 1963), p.33.
84. T.E. Drummond Plasma Physics (McGraw Hill,  
New York, 1961), p.172.
85. S.I. Pai and E.T. Kornowski, in Engineering  
Aspects of Magnetohydrodynamics, edited by  
C. Manna and N.W. Mather (Columbia University  
Press, New York, 1962), p.97.
86. K. Thom, J. Norwood and N. Jalufka, Phys. Fluids 7,  
Supplement S67 (1964).

# NOMENCLATURE

MKS units are used throughout the thesis except where otherwise specified.

Only the more commonly used symbols appear in this list. The page (or Figure) listed with each symbol indicates the page (or Figure) in which the symbol first appears, or is best defined. Where a symbol is used to denote different quantities in different parts of the thesis (only a few symbols are used in this way, e.g., the symbol 'R'), no confusion should be caused, as the quantity is defined before its usage.

		<u>Page</u>
$\vec{J}$	vector current density	3
$\vec{B}$	vector magnetic induction	3
$R_m$	magnetic Reynolds number	5
$\mu$	permeability	5
$\sigma$	electrical conductivity	5
$u$	fluid velocity, laboratory coordinates	5
$E$	electric field	11
$\Gamma$	density ratio, usually $\rho_2/\rho_1$	10
$\beta$	magnetic induction ratio, usually $B_2/B_1$	10
$E_{LAB}$	electric field ahead of shock, laboratory coordinates	12

$\rho$	density	14
$P$	pressure	14
$e$	internal energy	14
$q$	flow velocity in shock coordinates	15 also Fig.2.1
$U_s$	shock velocity, laboratory coordinates	Fig.2.1
$h$	enthalpy per unit mass	15
$R$	gas constant = $k/M_w$	17
$k$	Boltzmann constant	17
$M_w$	molecular weight	17
$\alpha_r$	rth ionization fraction	18
$\bar{E}_r$	excitation energy per rth ionized ion	18
$I_r$	total ionization energy per rth ionized ion	18
$Z_r$	rth partition function	18
$\delta_r$	reduction of ionization potential	18
$T$	temperature	17
$\gamma$	defined in (2-19)	21
$m$	mass of the electron	18
$\nu$	viscosity	23
$\chi$	heat conductivity	23
$\nu_m$	magnetic viscosity	23
$a$	gasdynamic sound speed (isentropic, unless otherwise stated)	28

$c_s$	slow magneto-acoustic speed	28
$c_f$	fast magneto-acoustic speed	28
$c_A$	Alfven speed	31
$b$	magnetic speed	31
$c$	small disturbance speed	34
$S$	entropy	37
$\omega_i$	ion gyration radius	39
$\omega_e$	electron gyration radius	39
$\tau_i$	ion-ion collision relaxation time	39
$\tau_e$	electron-electron collision relaxation time	39
$\omega_e \tau_e$	electron Hall parameter	39
$\omega_i \tau_i$	ion Hall parameter	39
$A$	mass number of atom	39
$n_e$	number density of electrons	39
$n_i$	number density of ions	39
$Z$	ionic charge	39
$M_A$	magnetic Mach number $q_1/b_1$	46
$W$	momentum flux into shock	46
$P_B$	magnetic pressure $B^2/2\mu$	47
$\Gamma_G$	pure gas value of $\Gamma$ -strong shock limit	47
$B_D$	drive field corresponding to total drive current	49 also Fig.2.4
$B_T$	total field at 'magnetic piston'	49 also Fig.2.4
$\beta_D$	ratio of $B_D/B_1$	50



$J$	current density (per unit y-width)	52
$J_S$	shock jump $J$	52
$J_E$	expansion $J$	52
$J_D$	total $J$	52
$\rho_D$	Debye radius	54
$I_H$	ionization potential of the hydrogen atom	54
$Z_S$	shock tube dynamic impedance	71
$L'$	inductance per unit length	73
$g$	shock tube inter-electrode gap	65
$w$	shock tube width	65
$E_{LABD}$	electric field observed at input terminals of shock tube	77
$R$	ohmic resistance of current sheet	77
$U_p$	flow velocity in laboratory coordinates	77
$RC$	$1/e$ decay time	81
$P_N$	Newtonian impact pressure	92
$P_G$	total gas pressure, sum of $P_N$ and $P$	92
$P_T$	total pressure, sum of $P_G$ and $P_B$	92
$q_p$	flow velocity in bow shock coordinates	94
$P_{TM}$	resultant total pressure on the stagnation point of the pressure probe $\approx P_{T03} - P_{B2}$	105
$B_M$	magnetic induction observed by coil $\approx B_2$	107

subscript p	post shock quantity transformed to bow shock coordinates	94
subscript 1	ambient quantity	94
subscript 2	post shock quantity in shock coordinates	94
subscript 3	post bow shock quantity in bow shock coordinates	94
subscript 0	stagnation quantity	98
subscript 03	post bow shock stagnation quantity	98
$r_p$	ratio $P_2/P_{B2}$	96
$r_N$	ratio $P_{N2}/P_{B2}$	96
Y	pressure ratio	96
$\Gamma_3$	ratio of state 3 and state 2 densities	96
$Y_3$	ratio of state 3 and state 2 pressures	96
M	sonic Mach number $q_1/a$	115
$\mu_r$	refractivity of gas	117
$\lambda$	wavelength	117
$\delta$	change in optical path	117
$\delta'$	fractional fringe shift	119
A, B	Cauchy coefficients	118
$N_e$	electron number density, equivalent to $n_e$	119
$N_{ArI}, N_{ArII}$	number density of neutral argon, and singly ionized argon, respectively	119

$N_{\text{HeI}}, N_{\text{HeII}}$	number density of neutral helium and singly ionized helium respectively	119
$t_d$	characteristic flux diffusion time	107
HM	hydromagnetic	151
$E_{\text{LAB1}}$	same as $E_{\text{LAB}}$	155
$\theta$	angle of inclination of shock front from the vertical	189
$q_n$	normal component of flow velocity into the inclined shock = $q_1 \cos \theta$	190
$f$	fraction of current carried by ions to the cathode	184
$\theta'$	angle of inclination of the current sheet from the vertical	Table 4.6
$R$	ratio of the momentum loss per second to the cathode and the momentum flux into the shock	184
$F$	ion drag parameter	185
$F'$	$F$ normalized to value at 0.1 torr Argon	185
$M_f$	flow Mach number	197
$\phi$	bow shock angle	Fig. 4.61
$E_{\text{LAB2}}$	post shock electric field, transformed to laboratory coordinates	202
$T_{\text{emf}}$	sum of $S_{\text{emf}}$ and $C_{\text{emf}}$	203
$S_{\text{emf}}$	shock back emf, equivalent to $E_{\text{LAB2}}$	203

$C_{emf}$	expansion current back emf	203
$B_e$	$(B_D + B_1 - B_2)$	203

LIST OF TABLES

		<u>Page</u>
3.1	Specific refractivity of plasma species	118
4.1	$B_2$ measurements - Argon 0.1 torr	151
4.2	$B_2$ measurements - Helium	152
4.3	$E_{LAB}$ measurements - Argon	157
4.4	Comparison of $N_e$ , $\Gamma$ , $P_{TM}$ and $B_2$ - Argon	166
4.5	Comparison of $N_e$ , $\Gamma$ , $P_{TM}$ and $B_2$ - Helium	167
4.6	Current sheet parameters	186
4.1X	Inclined shock correction of Table 4.1	192
4.3X	Inclined shock correction of Table 4.3	193
4.4X	Inclined shock correction of Table 4.4	194

LIST OF FIGURES

		<u>Page</u> <u>Facing</u>
2.1	Schematic of the Transverse Electromagnetic Shock Tube	15
2.2	Flow Model of the Transverse Ionizing Shock Wave	29
2.3	Values of $\Gamma$ and $M_A$ in the Hydromagnetic Limit of the Transverse Ionizing C-J Model	48
2.4	'Structureless' Momentum Balance Model	49
Solutions of the Transverse C-J Model, 0.1 torr Ar: (2.5-2.11)		
2.5	$\Gamma$ as Function of $U_s$	59
2.6	$B_2$ as Function of $U_s$	60
2.7	$E_{LAB}$ as Function of $U_s$	60
2.8	Temperature as Function of $U_s$	60
2.9	$J_D$ as Function of $U_s$	61
2.10	$N_e$ as Function of $U_s$	61
2.11	Ratio of Specific Heats as Function of $U_s$	62
2.12	Hydromagnetic Solutions of $\Gamma$ and $\beta$	62
3.1a	Coordinates for Magnetic Field Computation	65
3.1b	Magnetic Field Distribution - $B_y$	65
3.1c	Magnetic Field Distribution - $B_x$	65
3.1d	Magnetic Field Distribution - $B_z$	65

Page  
Facing

3.2	Planar Electromagnetic Shock Tube - A section	66
3.3	The Shock Tube - A photograph	66
3.4	Shock Tube Circuit and Control Electronics	70
3.5	Bias Bank Magnetic Field	77
3.6	Equivalent Circuit for Shock Tube Voltages	77
3.7	Rogovsky Coil	80
3.8	Coil Calibration	80
3.9a	Bow Shock on Probe	94
3.9b	One-dimensionalized Detached Shock	94
3.10a	Bow Shock, Flow and Field Components	100
3.10b	Geometrical Construction of Field Lines	100
3.11a	Bow Shock and Stagnation Density and Pressure ratios	99
3.11b	Bow Shock Pressures	99
3.12	Combination Total Pressure and Magnetic Probe	109
3.13	Pressure Measuring Circuit	111
3.14	Low Frequency Probe Calibration	111
3.15	Atmospheric Pressure Driven Shock Tube for Probe Calibration	114
3.16	Pressure Record of Probe at End Port	114
3.17	Optical set up for Single Wavelength M-Z interferometry	117

	<u>Page</u> <u>Facing</u>
3.18 Channel Spectra M-Z Interferometry	123
3.19 Fringe Number Schematic - $\lambda\Delta P$	127
Comparison of Streak, Pressure and Magnetic Field Signals (4.1 to 4.5):	
4.1 0.1 torr Ar, $B_1 = 0$ , 5 KV, $x = 26$ cm	134
4.2 0.1 torr Ar, $B_1 = 2.5$ KG, 5 KV, $x = 31$ cm	134
4.3 0.25 torr He, $B_1 = 0$ , 5 KV, $x = 70$ cm	134
4.4 0.25 torr He, $B_1 = 2.5$ KG, 5 KV, $x = 63$ cm	134
4.5 0.1 torr Ar, $B_1 = 2.5$ KG, 5 KV, $x = 80$ cm	134
Velocity measurements (4.6-4.14):	
4.6 Velocity-Time Relationship, 0.1 torr Ar, $B_1 = 0$ , 5 KV	136
4.7 Velocity-Time Relationship, 0.1 torr Ar, $B_1 = 2.5$ KG, 5 KV	136
4.8 $U_s$ as Function of Ambient Pressure, Ar, $B_1 = 0$ , 6 KV	137
4.9 $U_s$ as Function of $B_1$ , 0.1 torr Ar, 6 KV	137
4.10 $U_s$ as Function of $B_1$ , 0.2 torr Ar, 6 KV	137
4.11 $U_s$ as Function of Condenser Voltage, 0.1 torr Ar	137
4.12 $U_s$ as Function of Condenser Voltage, 0.2 torr Ar	137
4.13 $U_s$ as Function of Ambient Pressure, He, $B_1 = 0$ , 6 KV	137



4.14	$U_s$ as Function of $B_1$ , 1.0 torr He, 6 KV	137
------	--	-----

Comparative x-t Profiles of Total Pressure,  
Magnetic Field and Luminosity (4.15-4.17b):

4.15	0.1 torr Ar, $B_1 = 0$ , 5 KV	142
4.16	0.1 torr Ar, $B_1 = 2.5$ KG, 5 KV	144
4.17a	0.25 torr He, $B_1 = 0$ , 5 KV	146
4.17b	0.25 torr He, $B_1 = 2.5$ KG, 5 KV	147

Pressure and Magnetic Field Traces - Illustrating  
Technique of  $B_2$  Measurement (4.18-4.20):

4.18	0.25 torr He, $B_1 = 1.9$ KG, 5 KV, $x = 65$ cm	148
4.19	0. torr Ar, $B_1 = 2.5$ KG, 5 KV, $x = 14$ cm	148
4.20	0.1 torr Ar, $B_1 = 2.5$ KG, 5 KV, $x = 40$ cm	148

$B_2$  as Function of  $U_s$  - Experimental Values  
(4.21-4.23):

4.21	0.2 torr Ar, $B_1 = 0.66$ KG and $B_1 = 3.7$ KG Comparison with C-J; Also Inclined Shock Correction	150
4.22	0.25 torr He, $B_1 = 0.66$ KG	150
4.23	0.25 torr He, $B_1 = 1.5$ KG, 3.0 KG	150

Pre-Shock and Post-Shock Voltage - Oscillograms  
(4.24-4.26):

4.24	0.25 torr He, $B_1 = 0$ , Condenser Voltage Varied	151
------	---	-----

4.25	0.1 torr Ar, $B_1 = 1.5$ KG, Condenser Voltage Varied	153
4.26	0.1 torr Ar, 5 KV, $B_1$ Varied	153

$E_{LAB}$  and  $E_{LABD}$  as Functions of  $U_s$  (4.27-4.31):

4.27	0.25 torr He, 0.1 torr Ar, $B_1 = 0$	155
4.28	0.1 torr Ar, $B_1 = 2.7$ KG	155
4.29	0.2 torr Ar, $B_1 = 3.7$ KG	155
4.30	0.25 torr He, $B_1 = 3.0$ KG	155
4.31	0.25 torr He, $B_1 = 0.5$ KG	155
4.32a	Channelled Spectra	158
4.32b	Densitometric Traces	158

Channelled Spectra M-Z Results; Comparative Time Profiles of  $N_e$ ,  $\Gamma$ , B and P (4.33-4.47):

4.33	0.1 torr Ar, $B_1 = 0$ KG, 6 KV	163
4.34	0.1 torr Ar, $B_1 = 0.87$ KG, 6 KV	163
4.35	0.1 torr Ar, $B_1 = 2.7$ KG, 6 KV	163
4.36	0.1 torr Ar, $B_1 = 4.7$ KG, 6 KV	163
4.37	0.2 torr Ar, $B_1 = 1.3$ KG, 6 KV	163
4.38	0.2 torr Ar, $B_1 = 2.7$ KG, 6 KV	163
4.39	0.2 torr Ar, $B_1 = 4.7$ KG, 6 KV	163
4.40	0.075 torr Ar, $B_1 = 0$ , 6 KV	163

4.41	1.0 torr He, $B_1 = 0$ , 6 KV	164
4.42	0.25 torr He, $B_1 = 0$ , 5.1 KV	164
4.43	0.23 torr He, $B_1 = 1.2$ KG, 6 KV	164
4.44	0.25 torr He, $B_1 = 3.7$ KG, 6 KV	164
4.45	0.25 torr He, $B_1 = 4.7$ KG, 6 KV	164
4.46	0.1 torr He, $B_1 = 0$ , 6 KV	165
4.47	0.1 torr He, $B_1 = 3.7$ KG, 6 KV	165

Single Wavelength M-Z Interferometry, P, B and  $N_e$ , Correlation Studies (4.48-4.59B); I.F. = Infinite Fringe

4.48	0.1 torr Ar, $B_1 = 3.6$ KG (I.F.)	175
4.49	0.24 torr Ar, $B_1 = 2.7$ KG (I.F.)	175
4.49A	0.3 torr Ar, $B_1 = 3.6$ KG	175
4.49B	0.3 torr Ar, $B_1 = 3.6$ KG (I.F.)	175
4.50	1.0 torr He, $B_1 = 0$ (I.F.)	178
4.50A	1.0 torr He, $B_1 = 0$	178
4.51	1.0 torr He, $B_1 = 0.33$ KG	178
4.52	1.0 torr He, $B_1 = 0.53$ KG	178
4.53	1.0 torr He, $B_1 = 2.2$ KG (I.F.)	178
4.54A	1.0 torr He, $B_1 = 3.6$ KG (I.F.)	17'
4.54B	1.0 torr He, $B_1 = 3.6$ KG	17
4.55	1.00 torr He, $B_1 = 0$ (I.F.)	180
4.56	1.00 torr He, $B_1 = 3.3$ KG (I.F.)	180

	<u>Page</u> <u>Facing</u>
4.57      0.25 torr He, $B_1 = 0$ (I.F.)	180
4.58      0.3 torr He, $B_1 = 3.6$ KG (I.F.)	181
4.59A     0.1 torr He, $B_1 = 0$ (I.F.)	181
4.59B     0.1 torr He, $B_1 = 3.6$ KG (I.F.)	181
4.60      Geometry of the Inclined Shock Wave	187
4.61      Bow Shock Angle	187
4.62      Observation of Bow Shock with Large Magnetic Fields	196
Observation of an Incomplete Separation - Luminosity, P and B Correlation (4.63-4.64):	
4.63      Streak photograph	196
4.64      Framing photograph	196